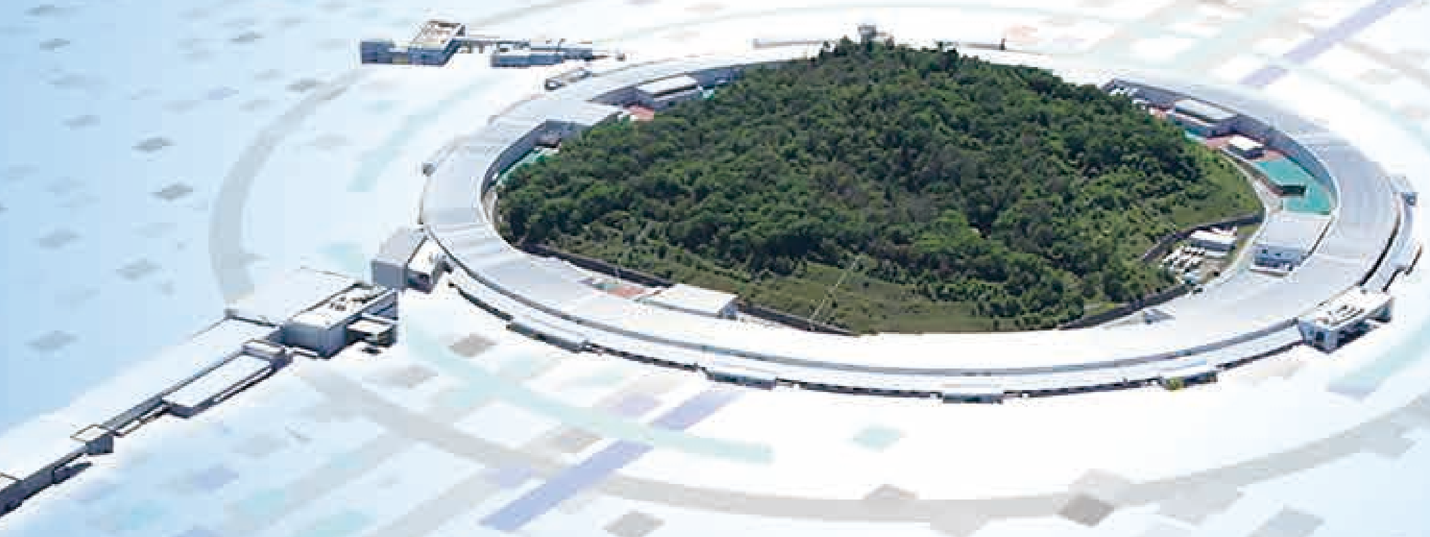

SPring-8 SACLA Research Frontiers 2015

ISSN 1349-0087
SPring-8 Document D2016-010

SPring-8/SACLA
Research Frontiers 2015

CONTENTS

Life Science

Physical Science

Chemical Science

Earth & Planetary Science

Industrial Applications

Note: The principal publication(s) concerning each article is indicated with all author's names in italics in the list of references.

PREFACE

Today, the SPring-8 campus operates both the SPring-8 and SACLA facilities and offers a unique environment where the two can be used synergistically.

In this volume, Prof. Jian-Ren Sen of Okayama University has contributed an important article on the radiation-damage-free structure of photosystem II revealed by femtosecond X-ray pulses at SACLA. His group has also contributed an excellent article on the detailed structures of the light-harvesting complex on plant photosystem I revealed at SPring-8. Readers will learn of the characteristics of the SPring-8 and SACLA facilities in both articles. Users of SPring-8 have performed high-level research in a wide range of fields, including life, physical, chemical, earth/planetary and engineering sciences, and representative users report the essence of their results in this volume. Two comprehensive review articles have been contributed by two active SPring-8 users, Prof. Chikashi Toyoshima of the University of Tokyo and Prof. Katsuya Shimizu of Osaka University. In addition, six excellent articles contributing to the life, physical and chemical science chapters have been provided by active users of SACLA.

The SPring-8 facility welcomed over 15,000 users in 2015. In 2015, 9,423 users conducted 1,317 experiments at the 26 public beamlines, and 5,858 users performed 552 experiments at the 19 contract beamlines. The operation time of the storage ring in 2015 was 4,805 h and the user time was 4,034 h. In addition, the SACLA X-ray free electron laser facility welcomed 1,079 users, who conducted 68 experiments at the two beamlines in 2015. The total operation time in 2015 was 6,483 h and the user time was 3,924 h.

A number of SPring-8 and SACLA users were awarded prizes in 2015 and 2016 for their achievements in science and technology. Prof. Hideo Hosono (Tokyo Institute of Technology) was awarded the Japan Prize in 2016 for his achievement in the creation of unconventional inorganic materials with novel electronic functions based on nanostructures. Prof. Susumu Kitagawa (Kyoto University) was awarded the Japan Academy Prize in 2016 for the creation and application of porous metal complex materials. Prof. Zenji Horita (Kyushu University) and Prof. Hisanori Shinohara (Nagoya University) were respectively awarded the Medal with Purple Ribbon in Fall 2015 and Spring 2016.

I am very grateful to the many authors and experts who contributed their papers to this volume. Special thanks are given to Dr. Naoto Yagi and the members of the editorial board for their constant effort.

土肥義治
Yoshiharu Doi
President
Japan Synchrotron Radiation Research Institute (JASRI)

EDITOR'S NOTE

Here I am happy to present to you another issue of SPring-8/SACLA Research Frontiers, which covers the outstanding scientific outcomes achieved at SPring-8 and SACLA in 2014 and 2015. Articles in a wide range of scientific fields are included. Most notably, there are more reports each year on experiments performed at SACLA. Articles in SACLA New Apparatus, Upgrades & Methodology describe new technical developments, but more importantly, there are six excellent articles in Life Science, Physical Science and Chemical Science, proving that SACLA is a versatile experimental tool for leading-edge science.

Because the scope of the science covered by SPring-8 and SACLA is rapidly expanding, a small change has been made to the index in this issue. This year, the scientific articles are sorted in five major categories. To help readers find articles of their interest, a keyword or key phrase is given to each article. This was not an easy task, since they must attract the attention of readers in particular fields but should not be too specific for readers with a wide scientific interest. The editors put their heads together to find adequate words and phrases. I hope this change will be helpful for all readers.

The review articles in this issue were contributed by Prof. Toyoshima of the University of Tokyo and Prof. Shimizu of Osaka University. These reviews summarize the progress of their work in structural biology and superconductivity research, respectively, in recent years. It is clear that the experimental techniques developed at SPring-8 have greatly accelerated advances in these important scientific fields.

Copies of SPring-8/SACLA Research Frontiers will be sent on request. The full text is also available on the SPring-8 website (*http://www.spring8.or.jp/*). For the list of publications produced by SPring-8 users and staff, please visit the publication database at *http://www.spring8.or.jp/en/science/publication_database/*. Further detailed information on the current and historical status of SPring-8, such as the numbers of submitted and conducted proposals, the budget, and publications, is also available (*http://www.spring8.or.jp/en/about_us/spring8data/*).

Representing the editors, I extend my appreciation to those who have recommended outstanding research results suitable for publication in SPring-8/SACLA Research Frontiers. I would also like to express my sincere gratitude to the users and staff of SPring-8 and SACLA for contributing their reports to this issue.

Naoto Yagi
- Editor in Chief -
Japan Synchrotron Radiation Research Institute (JASRI)

EDITORIAL BOARD

SCIENTIFIC FRONTIERS

Review Article

Structural Biology of the Sodium Pump

P-type ATPases are ATP-powered ion pumps, and include Ca^{2+}-ATPase, Na^+,K^+-ATPase, among others. Best understood structurally and biochemically is Ca^{2+}-ATPase from sarcoplasmic reticulum of fast twitch skeletal muscle (sarco(endo) plasmic reticulum Ca^{2+}-ATPase 1a, SERCA1a). Since our publication of the first crystal structure of SERCA1a in 2000, which was the first ion pump structure determined at near atomic resolution, the pump has been a continuous source of excitement, as crystal structures of new reaction intermediates always show large and unexpected structural changes. In the P-type ATPase reaction cycle, there are two major states, E1 and E2 [1] (Fig. 1(a)). The E1 state has high affinity for cations to be transferred from the cytoplasm into the extracellular medium (or lumen). In this state, SERCA1a binds two Ca^{2+} with high affinity, whereas Na^+,K^+-ATPase bind three Na^+. In the E2 state, the transmembrane cation binding sites bind these ions with low affinity and counter ions with high affinity. That is, SERCA1a binds 2 or 3 H^+ with high affinity, whereas Na^+,K^+-ATPase binds two K^+. The crystal structures show that very large rearrangements of three cytoplasmic domains and 10 transmembrane helices take place during the reaction cycle. A 110° rotation of the A-domain accompanying the transition from E1P → E2·Pi is one of the largest domain movements ever observed as far as the authors are aware (Fig. 1(b)). For SERCA1a, crystal structures have been determined using BL41XU for most of the reaction intermediates, nearly covering the entire reaction cycle. We can now describe a quite detailed scenario for the active transport of Ca^{2+} by this ATPase [1]. In 2013, we published a long awaited E1 structure with and without sarcolipin [2], a regulatory protein in skeletal and heart atrial muscles. As we have already published a review article [3] on this crystal structure, here we focus on our other target, the Na^+,K^+-ATPase, which, as we have described, transports three Na^+ out and two K^+ into the cytoplasm per molecule of ATP hydrolysed (Fig. 1(a)). Na^+,K^+-ATPase is expressed in all animal cells and plays critical roles in many fundamental processes in life, notably excitation of nerve cells and

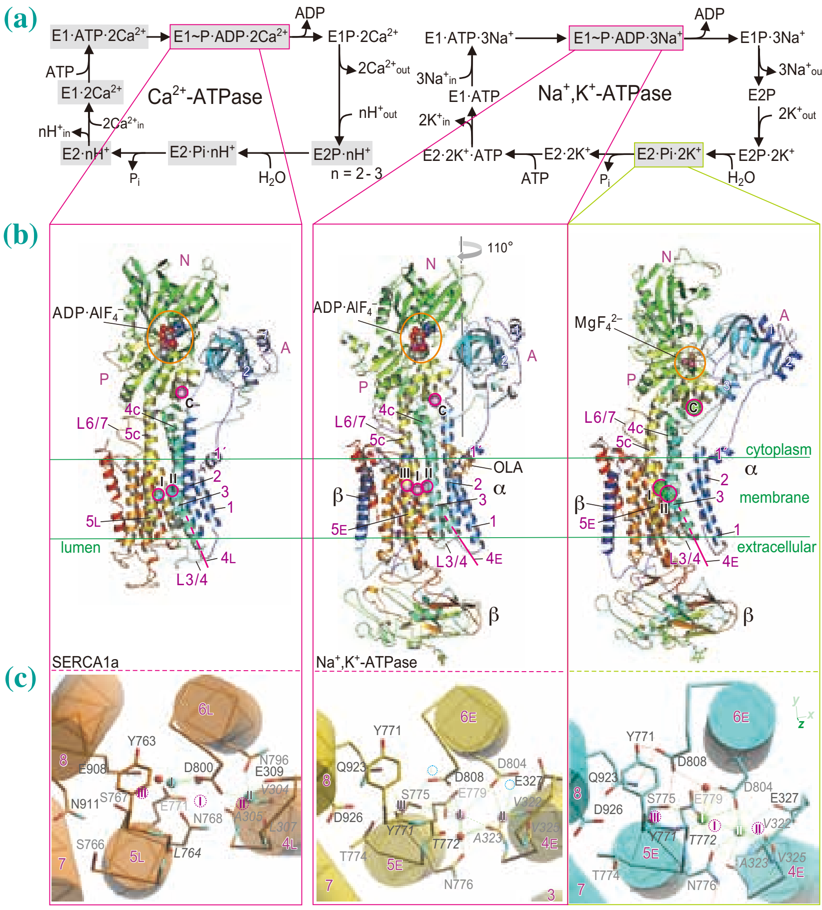

Fig. 1. **(a)** The reaction cycle and crystal structures of Na^+,K^+-ATPase in comparison with those of SERCA1a. The intermediates of which crystal structures have been published are shaded (top panel). **(b)** The Na^+ (or K^+) under the P-domain (c) has a regulatory role. **(c)** The bottom panels show the transmembrane cation binding sites viewed from the cytoplasm. Small violet spheres represent Na^+, cyan ones Ca^{2+}, green ones K^+ and red ones water. Dotted circles in cyan indicate the positions of bound Ca^{2+} in SERCA1a and purple ones bound Na^+ in Na^+,K^+-ATPase.

contractions of heart muscle. As a consequence, Na^+,K^+-ATPase is implicated in many diseases, such as high blood pressure, neurological disorders and cancers. It is the target of digitalis-like compounds (now called cardiotonic steroids (CTS)), which have been prescribed for more than two centuries for treatment of heart failure and arrhythmias. Furthermore, Na^+,K^+-ATPase may function as a docking station, regulated by endogenous CTS. In fact, a number of proteins have been reported to interact with Na^+,K^+-ATPase. Since Na^+,K^+-ATPase is up regulated in certain cancer types, it has been gathering attention as a new anti-tumor target [4].

Compared to Ca^{2+}-ATPase, structural elucidation of Na^+,K^+-ATPase lags far behind. Na^+,K^+-ATPase is a substantially more complex pump than SERCA1a, consisting of α and β subunits and an auxiliary FXYD protein. The α-subunit is the catalytic subunit, with a very similar architecture to SERCA1a, has four distinct domains: cytoplasmic actuator (A), phosphorylation (P) and nucleotide binding (N) domains and a transmembrane domain. The β-subunit is considered to be the molecular chaperone of the α-subunit and is heavily glycosylated; this subunit is unique to Na^+,K^+-ATPase and H^+,K^+-ATPase. The FXYD protein is a tissue specific regulator for fine tuning of catalytic activity and stability (Fig. 1(b)). The first crystal structure of this ATPase was published in 2007 by Morth *et al.* [5]. It showed an $E2{\cdot}2K^+{\cdot}Pi$ state at only 3.5 Å resolution and lacked information on most of the β-subunit. We published a 2.4 Å resolution structure for the same state two years later [6] and provided a description of nearly the entire pump, including details of K^+-coordination. This crystal structure gave answers to several fundamental questions, such as, why Na^+,K^+-ATPase countertransports K^+ whereas Ca^{2+}-ATPase does not, even though almost the same residues are present in the binding sites (reviewed in [7]).

Crystal structure of Na^+, K^+-ATPase in the $E1{\sim}P{\cdot}ADP{\cdot}3Na^+$ state

Nevertheless, Na^+-bound structures are far more important, because Na^+,K^+-ATPase is essentially a Na^+-pump: only Li^+ and H^+ can partially substitute for Na^+, but K^+ can be replaced with many monovalent cations, including even Na^+, and organic cations. Of particular interest is where the third Na^+ site, specific to Na^+,K^+-ATPase is located. Furthermore, the affinity of Na^+,K^+-ATPase for Na^+ is very low (~ mM K_d; 15 mM from charge transfer), compared to that of SERCA1a for Ca^{2+} (μM to sub-μM). K^+ has a higher affinity and converts the ATPase into the E2 state. Yet, Na^+,K^+-ATPase strictly transfers only Na^+, rejecting K^+ and Ca^{2+}, in the forward direction. The turnover number of the ATPase is even larger than that of SERCA1a. Explanations about these differences awaited crystal structures of the E1 species with bound Na^+. We recently succeeded in determining crystal structures of this ATPase in $E1{\cdot}AlF_4^-{\cdot}ADP$ with three bound Na^+ at 2.8 Å resolution using BL41XU [8]. This structure is thought to represent the transition state ($E1{\sim}P{\cdot}ADP{\cdot}3Na^+$) that precedes the occluded $E1P[3Na^+]$ state. We chose this state, as the cytoplasmic gate is at a closed position, with $3Na^+$ already occupying the transmembrane cation binding sites, to evade problems that arise from the low affinity for Na^+.

The crystal structures show three Na^+ bound in the transmembrane region (Fig. 1(b,c)) and exhibit several distinct structural features. It is understandable that K^+ has a high affinity for the Na^+-binding sites, as thermal movements will slightly alter the conformations of the coordinating side chains allowing larger ions to bind. In fact, site I appears large enough to accommodate K^+ (Fig. 2). To minimise such movements, three strategies appear to be used. The first one is the use of main chain carbonyls for coordination. Indeed, the Na^+-binding sites are highly offset to the M5-side compared to the Ca^{2+}-binding sites in SERCA1a for this purpose, although the coordinating residues are almost identical to those in SERCA1a (Fig. 1(c)). The second is the

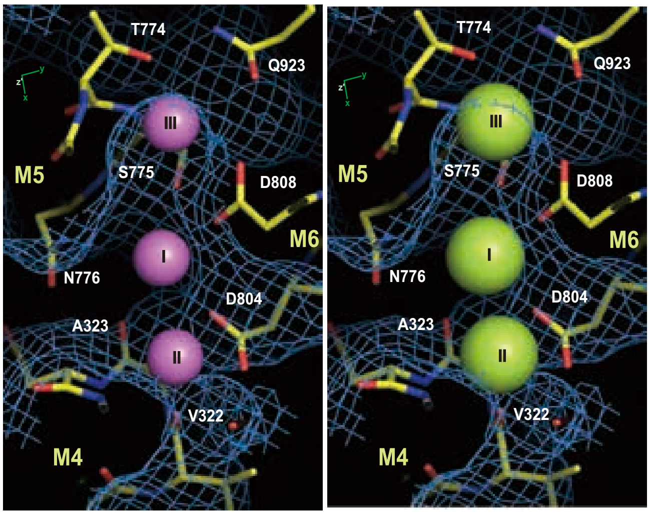

Fig. 2. Continuous cavity connecting three Na^+-binding sites. Na^+-accessible surface (blue nets) with three Na^+ (violet spheres) and K^+ (green spheres) placed in the Na^+-binding sites.

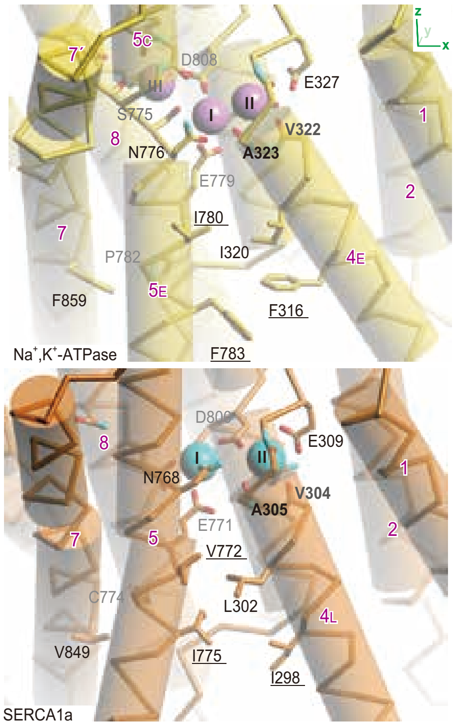

Fig. 3. Enlarged views of the transmembrane region of Na$^+$,K$^+$-ATPase (yellow) and SERCA1a (orange) around the cation-binding sites. Viewed approximately parallel to the membrane. M5 consists of two halves (M5C and M5E) in Na$^+$,K$^+$-ATPase but is contiguous in SERCA1a. Residue names with underscores indicate that they are substituted with bulkier residues in Na$^+$,K$^+$-ATPase.

sharing of a carboxyl group by two adjacent sites. The bindings of the three Na$^+$ are all sequential and co-operative. The binding of the first Na$^+$ to site III creates site I. Sites III and I share the carboxyl group of Asp808 and sites I and II share that of Asp804. Coordination of Na$^+$ will fix the orientation of the carboxyl group in a position suitable for binding of the right-sized ion (i.e. Na$^+$) but not larger ions (i.e. K$^+$). In this way, thermal movements of the coordinating residues can be effectively reduced. The third is the juxtaposition of the transported ions. The very short distance (3.4 Å) between Na$^+$ at sites I and II indicates that larger K$^+$ or divalent cations (e.g. Ca^{2+}) cannot bind because of the physical size and/or electrostatic repulsion (Fig. 2). This is achieved by bringing site II closer to site I by tilting the extracellular half of M4 (M4E) larger than in SERCA1a (Fig. 3). As a result, the main chain carbonyl of Ala323, corresponding to Ala305 dedicated to site II in SERCA1a, now contributes to site I in Na$^+$,K$^+$-ATPase. A large space formed between M4E and M5 should be filled with bulkier hydrophobic residues. Indeed, Ile and Val in SERCA1a are replaced by Phe and Leu in Na$^+$,K$^+$-ATPase (Fig. 3).

Another conspicuous strategy is that only the binding of the right-sized ion (i.e. Na$^+$) to site III allows productive phosphoryl transfer from ATP. Site III is highly confined so as to accommodate only Na$^+$ (ionic radius = 0.95 Å) and not K$^+$ (1.33 Å) (Fig. 2). However, as it is located in the hinge between the two halves of the M5 helix (M5C and M5E) (Fig. 3), K$^+$ appears to be able to bind if M5C moves 10° or so towards M7. As M5C is integrated into the P-domain (Fig. 1(b)), it controls the position of the P-domain. That is, for phosphoryl transfer from ATP to the invariant Asp residue in the P-domain to take place, a proper arrangement of the three cytoplasmic domains is necessary. Such an arrangement is realised only by the binding of the right sized ion (i.e. Na$^+$) to site III. It should be noted that the orientation of M5C also determines the inclination of M4E, through the L6/7 loop and the M3 helix.

Thus, we now see the really intricate maneuvers that Na$^+$,K$^+$-ATPase uses for selecting Na$^+$. In view of this, the Ca^{2+} binding sites in SERCA1a appear very primitive. Yet, SERCA1a rigorously selects Ca^{2+}, even in a milieu of 10,000 times more concentrated Na$^+$, which has a very similar ionic radius (0.95 *vs* 0.99 Å). This will mean that charge balance is critical in maintaining the binding sites with right geometries or in causing proper structural changes for creating the binding sites.

Visualization of the substitution process of K$^+$ bound to Na$^+$,K$^+$-ATPase

It is well established that two K$^+$ bind sequentially to the empty cation binding sites after the release of three Na$^+$ into the extracellular medium (Fig. 1(c)), but to which site the first K$^+$ binds was unknown. It is also well established that the two bound K$^+$ can be substituted with K$^+$ congeners in two (fast and slow) phases in the presence of Pi, and only a half of the bound K$^+$ is substituted in the fast phase. To explain these experimental findings, Forbush proposed a "flickering gate model" [9], in which only K$^+$ at the "fast" site can be substituted with congeners, such as Rb$^+$ and Tl$^+$. Such a sequential binding/release model implies that the "fast" site must be the site for the last (i.e. second) K$^+$ to bind. Conventional kinetics experiments using radio isotopes cannot answer which of the two binding sites is the "fast" site, but X-ray crystallography could, using Tl$^+$ or Rb$^+$ as the substituent, because they have larger atomic numbers and significant anomalous scattering cross-sections. Indeed, Fourier difference and anomalous difference maps calculated from diffraction data collected at BL41XU from the crystals of Na^+,K^+-ATPase in E2·MgF_4^{2-}·2K^+ (a stable analogue of E2·Pi·2K^+) soaked in a buffer containing either Tl^+ or Rb^+, showed clear peaks at the K^+-binding sites (Fig. 4(a)) [10]. By changing the time of incubation, we clearly showed that site II is the "fast" site. Thus, we have demonstrated that X-ray crystallography can provide spatial resolution to kinetics measurements.

Then the obvious question to be addressed is how these ions are gated. We have already elucidated the gating mechanism of SERCA1a for Ca^{2+} in the E1 state, but it could be entirely different for the counter ions in the E2 state. In the case of Na^+,K^+-ATPase, there may be different gating mechanisms for Na^+ and K^+ on the cytoplasmic and extracellular sides respectively. We would like to know the movements of the gating segment and the residues participating. With crystals of Na^+,K^+-ATPase in E2·MgF_4^{2-}·2K^+, such information can be obtained by analysing the temperature factors of all atoms of the protein at once. This is because thermal movements of an atom can be separated into two components: one from anisotropic collective movements of a segment (e.g. an α-helix) on which that particular atom is located, and the other from random isotropic movements of that atom. The answer is again quite clear: the M3 and M4 helices move together and work as a swing door to the ion pathway (Fig. 4(b,c)). The movements predicted by the temperature factor analysis were very similar to those caused by ouabain binding to the E2·MgF_4^{2-}·2K^+ crystal [11], indicating that such movements are indeed possible. Thus, we demonstrated that it is possible to predict how a gate will open from a crystal structure with the gate closed.

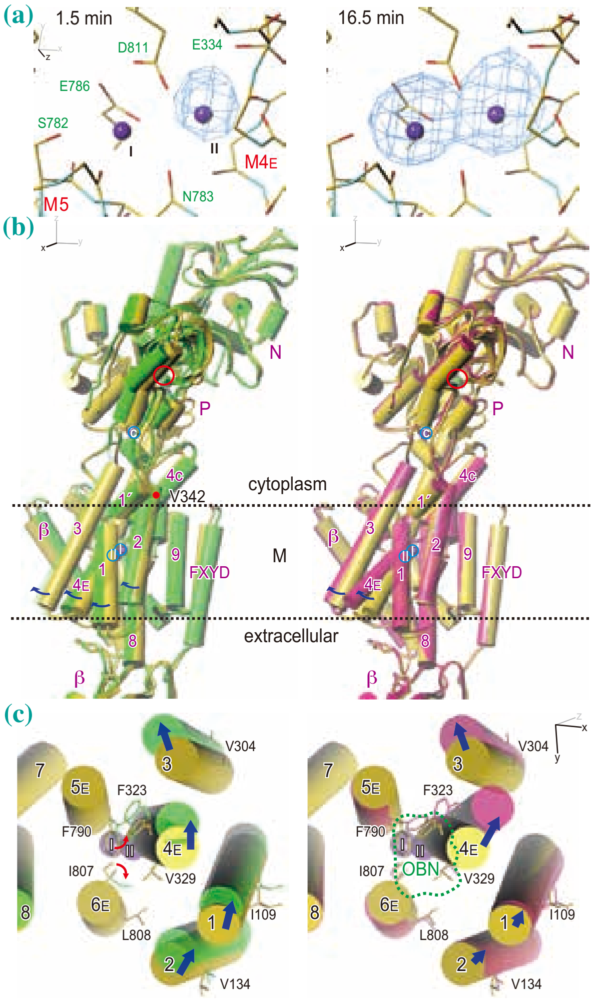

Fig. 4. Sequential substitution of bound K^+ with Tl^+ and segmental movements of Na^+,K^+-ATPase in the E2·2K^+·MgF_4^{2-} crystal. **(a)** $|F_{obs}(Tl^+)| - |F_{obs}(K^+)|$ difference Fourier maps from crystals soaked in a buffer containing Tl^+ for 1.5 min and 16.5 min. **(b)** and **(c)** Superimpositions of the atomic models of the ATPase in the 'average' (yellow) and 'open' (light green) or ouabain-bound (pink) forms. Viewed from the M1 to M10 direction (b) or from the extracellular side (c). Small red arrows in (c) indicate likely conformation changes of the side chains to open the ion pathway.

Chikashi Toyoshima*, Haruo Ogawa and Ryuta Kanai

Institute of Molecular and Cellular Biosciences, The University of Tokyo

*E-mail: ct@iam.u-tokyo.ac.jp

References

[1] C. Toyoshima: Arch Biochem Biophys. **476** (2008) 3.
[2] C. Toyoshima *et al*.: Nature **495** (2013)260.
[3] C. Toyoshima and F. Cornelius: Curr. Opinion Struct. Biol. **23** (2013) 507.
[4] I. Prassas, E.P. Diamandis: Nat. Rev. Drug Discov. **7** (2008)926.
[5] J.P. Morth *et al*.: Nature **450** (2007) 1043.
[6] T. Shinoda *et al*.: Nature **459** (2009) 446.
[7] C. Toyoshima *et al*.: Structure **19** (2011)1732.
[8] R. Kanai *et al*.: Nature **502** (2013) 201.
[9] B. Forbush *et al*.: J. Biol. Chem. **262** (1987) 11116.
[10] H. Ogawa, F. Cornelius, A. Hirata and C. Toyoshima: Nat. Commun. **6** (2015) 8004.
[11] H. Ogawa *et al*.: Proc. Natl. Acad. Sci. USA **106** (2009) 13742.

Review Article

High-Pressure Research on Superconductivity at SPring-8

Although superconductivity is known as a very rare phenomenon that occurs in a limited number of compounds, many superconductors have been found and synthesized under high-pressure conditions. Actually, almost half the elements in the periodic table become superconductors under ambient and high-pressure conditions.

Pressure changes the distance between atoms and can also change the structure. Thus, the properties of a material, such as superconductivity, can be controlled via the pressure. To study and uncover the potential of materials, the use of a high pressure can be a very effective and powerful methods. Here we review our high-pressure research on superconductors and related materials at SPring-8.

1. Beamline improvement for multipurpose measurements: XRD, electrical resistivity, and Raman scattering under a high pressure and low temperature

A newly developed system for simultaneous X-ray diffraction (XRD) and Raman scattering spectroscopy measurements was installed in the upstream experimental hutch of BL10XU. The crystal structure at high pressures is one of the most important points in the study of the high-pressure phenomena of materials, such as pressure-induced insulator-to-metal transition, superconductivity, and so on. However, when data for the crystal structure and electrical resistance have been obtained in separate experiments and compared, discrepancies have been found between them in not only the pressure but also the pressure condition such as the pressure hydrostaticity. To solve this problem, resistance measurements at a high pressure and low temperature were performed on the diffraction measurement stage in the experimental hutch of BL10XU.

1-1. New simultaneous measurement system in BL10XU

Figure 1 shows the system in the experimental hutch of BL10XU. The X-ray diffractometer consists of a flat imaging plate detector (IP) and a horizontally rotating ω-goniometer on a heavy-duty *y*–*z* stage. High-pressure and low-temperature experiments are performed using a helium-gas-flow-type 4 K cryostat combined with a helium-gas-driven membrane diamond anvil cell (DAC). To minimize the vibration of the sample in the DAC caused by the cold head due to the motion of the refrigerator, a bundle of flexible copper wires is used as the heat link between the cold stage and the DAC.

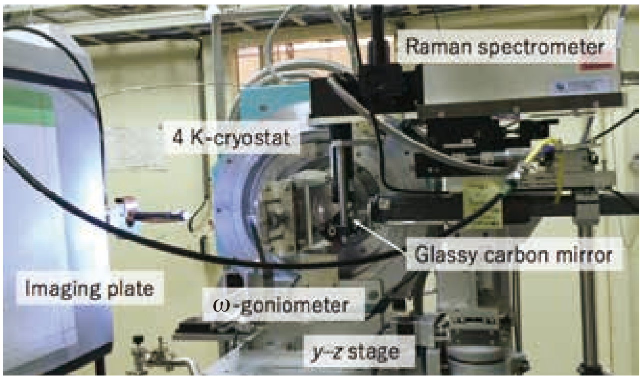

Fig. 1. Photograph of the cryostat equipped with Raman scattering and resistance measurements equipment used in high-pressure studies.

The cryostat has two transparent windows: one is for the synchrotron X-ray beam input (upstream) and the other is for diffraction measurements (downstream). The micro-Raman scattering spectroscopy system was installed in the up-stream. The objective lens of the Raman microscope has a long working distance, and the laser beam and Raman signal are introduced on-axis to the input X-ray beam by using a glassy carbon mirror that is transparent to X-rays.

The optics of the Raman spectroscopy system and pressure control system were installed outside of the experimental hutch and they are connected by optical fibers and stainless-steal high-pressure gas tubes, respectively. This allows us to simultaneously obtain XRD and Raman scattering spectra from samples under precise pressure control.

1-2. Electrical measurement setup in high-pressure device (DAC)

A pair of ~1/3 carat diamond anvils with an 8-degree beveled design, a top surface diameter of 50 or 100 μm, and a culet of 300 μm is routinely used. When performing an electrical resistance measurement at high pressure, the insulation of the metal gasket is essential. Figure 2 shows the typical arrangement of the gasket and electrodes we use (in this figure, the sample was lithium). The rhenium gasket is pre-indented to ~30 μm thickness and a thin part of the indent is removed. An insulating material powder (such as diamond, c-BN, or Al_2O_3) is placed in the gasket and a sample hole of 30–50 μm diameter is made at the center of the gasket. The electrodes deposited on the upper diamond consist of a bottom layer of titanium (Ti) and a top layer of copper (Cu). The deposited electrodes with the sample and with platinum (Pt) foil electrodes on the insulating layer. The electrical resistance is measured by the conventional four-terminal method with an AC current.

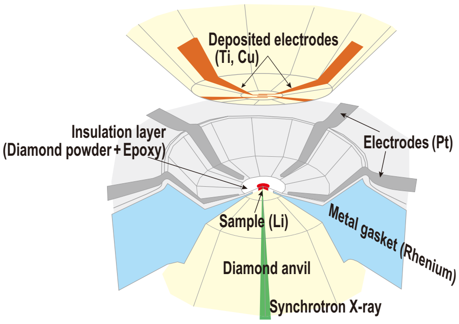

Fig. 2. Schematic of the sample (Li) and the electrode in the DAC.

2. Examples of results

In this section, recent works on superconductivity and structural studies carried out at BL10XU are reviewed.

2-1. Pressure-induced superconductivity, metal-to-insulator transition, and re-entrant metal phase of *lithium*

We previously reported that the superconducting transition temperature of lithium is enhanced by pressure from a low temperature of 0.4 mK under ambient condition to 20 K [1]. A theoretical calculation predicted the possible formation of an insulating or semiconducting state of lithium at ~100 GPa [2]. Here we report the dramatic changes in the electrical and structural properties of lithium upon applying pressure.

An anomalous increase in the electrical resistivity at 25 K was observed with increasing pressure as shown in Fig. 3, where the vertical broken lines indicate the structural phase boundaries at the same temperature determined by *in situ* XRD studies. When the pressure reached ~70 GPa, the electrical resistivity abruptly increased by about five orders of magnitude and saturated at ~94 GPa. It was found that the huge increase in the electrical resistivity is accompanied by a structural transition from cI16 to higher-pressure phases named hp-I (Li-VI) and hp-II (Li-VII) [3].

At further compression up to 137 GPa, the electrical resistivity decreased by about four orders of magnitude at a pressure of 100–120 GPa, indicating closure of the band gap as shown in Fig. 4. At the same time (at 120 GPa), a structural transition from Li-VII to a new phase (Li-VIII) was observed. The temperature dependence of the resistivity changed from negative to positive, indicating a transition from a semiconductor to metal. In addition, a drop in the resistance (which may indicate superconductivity) was also observed at ~10 K [4].

This study demonstrated the existence of a semiconductor phase between two distinct metallic phases as shown in Fig. 4. The compressed light alkali metal Li has contributed to broadening our understanding of metals.

2-2. Incommensurate structural phase in molecular *iodine*

Solid iodine is a typical diatomic molecular crystal, for which it has been reported that metallization occurs at 16 GPa and molecular dissociation occurs at 21 GPa [5,6]. Iodine changes its structure from a diatomic molecular crystal to a single atomic metal under pressure. However, in a recent hydrostatic pressure experiment that used helium as a pressure medium, a new structural phase (phase-V) was observed at a pressure around 24–28 GPa [7]. Phase-V takes an incommensurate structure before dissociation from the molecule to the atomic metal. We consider that this intermediate phase of iodine may be one of the keys to clarifying the pressure-induced phenomena of molecular crystals. Here we report electrical resistance measurements of phase-V as a function of temperature down to 6 K while simultaneously performing XRD measurements. A gas-membrane-type diamond anvil cell (MDAC) made of nonmagnetic CuBe alloy was used. The iodine sample was treated in water- and oxygen-free argon gas in a glove box and placed into the gasket without a pressure-transmitting medium. Pressure was determined by the ruby fluorescence method at a low temperature as well as at room temperature. The electrical resistance was measured by an ac four-terminal method with evaporated Pt electrodes at a typical current of 500 nA. The pressure was applied at room temperature. The iodine transformed completely into phase-V at 24 GPa even without a pressure-transmitting medium. Vibration of the refrigerator used in the experiment was suppressed to less than 10 micron. A synchrotron X-ray beam was accurately focused onto the sample at the 20-micron gap between two electrical probes and the diffraction was collected by an imaging plate detector. During the cooling of the MDAC, the pressure, electrical resistance, and diffraction spectra were monitored at

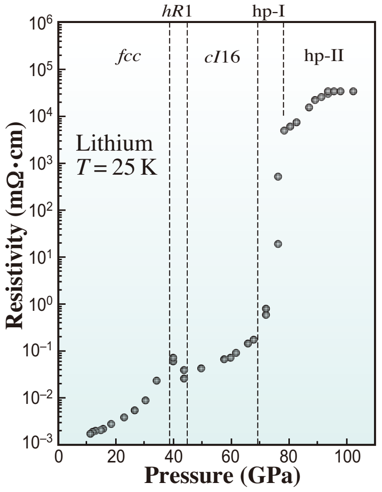

Fig. 3. Resistivity of lithium at high pressure measured with XRD.

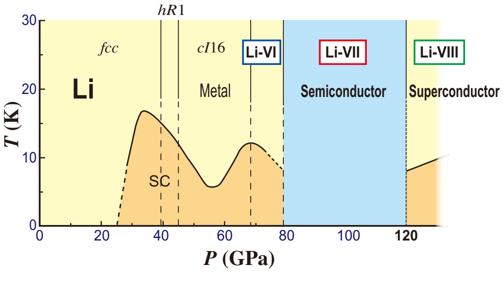

Fig. 4. Temperature-pressure phase diagram of lithium. SC: superconducting phase. The vertical lines indicate the structural phase boundary at 25 K.

same time and are shown in Fig. 5. The resistance decreased with decreasing temperature down to 6 K, suggesting that phase-V is metallic. The search for superconductivity at a lower temperature in phase-V is ongoing.

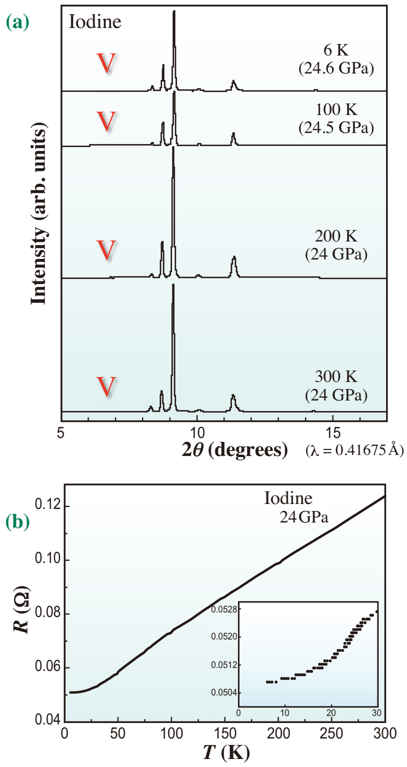

Fig. 5. **(a)** XRD spectra of iodine in phase-V at different temperatures and **(b)** temperature dependence of the electrical resistance at a fixed pressure of 24 GPa.

2-3. *Calcium*, the highest temperature superconducting element, and its structure

We have reported the highest temperature superconductivity for an element, which calcium (Ca) was with a transition temperature of 29 K at 216 GPa. At ambient pressure and temperature, Ca forms an *fcc* structure (Ca-I). With increasing pressure, successive phase transitions to Ca-VII were experimentally observed as shown in Fig. 6(a). The high-pressure phase Ca-VII has been suggested to be the host-guest structure already reported for the highest temperature superconducting phase of Ba [8,9]. We performed powder XRD and electrical resistance measurements of Ca under high pressure in order to search for the high-pressure phase of Ca-VII with the host-guest structure and superconductivity.

A Ca sample was set in a DAC for XRD measurements and pressurized up to 241 GPa at room temperature. High-quality powder patterns of Ca in the high-pressure region above 200 GPa were obtained. The structure of Ca-VII was determined by this XRD experiment combined with a density functional theory calculation and was found to be an unusual host-guest-type structure [10].

Figure7 shows the superconducting transition temperatures of elements in the periodic table as heights, including Ca with the highest temperature. The height is proportional to the highest (maximum) superconducting temperature ever observed for each element. Most of the maxima were recorded at ambient pressure, but the remainder were observed at higher pressures. In addition, for some of the elements, superconducting transition temperature T_c continues to increase with the pressure. According to this figure, the high-T_c elements are located at near the horizontal edges of the table. One of the ultimate goals of superconductivity research is the experimental realization of metallic hydrogen as a room-temperature superconductor. This is expected to occur above a pressure of 450 GPa, which has never been achieved for hydrogen.

We reported our recent research towards achieving metallic hydrogen in the next two subsections.

2-4. Transition to *metallic fluid hydrogen* at high temperature and high pressure

Hydrogen is expected to metallize and show high-temperature superconductivity at a very high pressure of ~500 GPa. On the other hand, hydrogen under high temperature and high pressure (HTHP) condition is also expected to be metallic in the fluid phase, which is realized in giant planets such as Jupiter and Saturn. In previous shock-pressure experiments, the metallic behavior of fluid hydrogen was observed [11]. However, the transition boundary and the properties of metallic fluid hydrogen have not yet been clarified. Thus, we generated a static HTHP condition and examined the region of stability of hydrogen using a laser heated diamond anvil cell (LHDAC).

We heated hydrogen under a high pressure with an infrared laser and examined the heating efficiency by considering the relationship between the temperature and the laser power. XRD and Raman spectroscopy measurements were performed before and after the laser-heating experiments and they showed that no chemical reaction occurred between hydrogen and surrounding materials. The results show anomalies in the heating efficiency, which are likely to be due to the phase transition of hydrogen from a diatomic fluid to a monoatomic fluid in the pressure range 82–106 GPa as shown in Fig. 8. These results are in good agreement with the previously proposed plasma phase transition boundary [12]. This technique is expected to help us experimentally to realize the solid metallic phase of hydrogen.

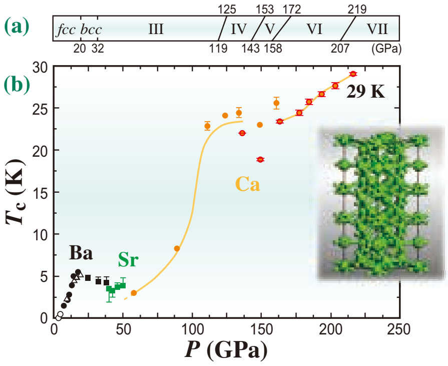

Fig. 6. **(a)** Structural transitions and **(b)** superconducting temperature of Ca at high pressure.

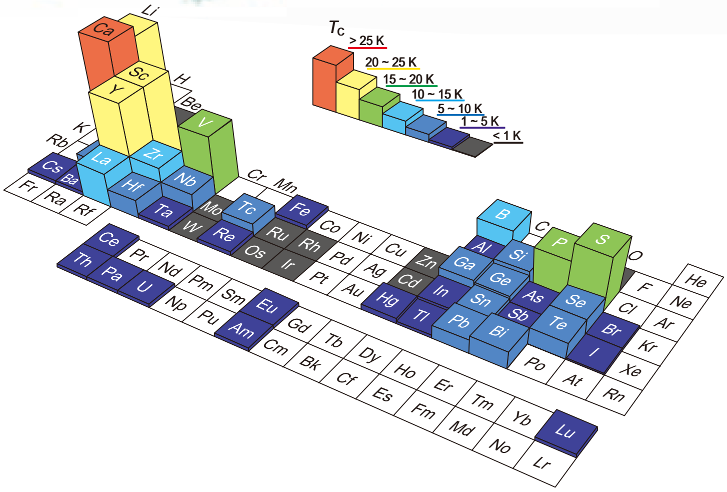

Fig. 7. 3D periodic table of elements, where the heights represent superconducting temperatures.

2-5. Structure of *sulfur hydrides* with superconductivity above 200 K

Superconductivity above 200 K was recently reported in highly compressed hydrogen sulfide (H_2S) [13]. It has been proposed that this material decomposes into elemental sulfur and a hydride with a higher hydrogen content, which is responsible for the high-temperature superconductivity [14]. We measured the crystal structures of the superconducting phases of hydrogen sulfide and deuteride sulfide in their normal (at room temperature) and superconducting states by XRD measurements combined with electrical resistance measurements.

H_3S and D_3S were compressed to 150 GPa in a DAC by a previously reported process [12] and cooled to 10 K in a cryostat. The resistivity was monitored throughout the cooling process. The critical temperature and zero resistivity were observed at around 180 K. The collected XRD data showed good agreement with the theoretically predicted sulfur atom position in the structures of the $R3m$ and $Im\bar{3}m$ phases and pure sulfur (β-Po structure). The position of the hydrogen atoms cannot be determined from the XRD measurements as the hydrogen atom is a weak scatterer. No difference was observed between the spectra obtained at 10 K and room temperature, and from the pressure dependence of the transition, we can conclude that the highest critical temperature of 200 K corresponds to the $Im\bar{3}m$ phase as shown in Fig. 9 [15].

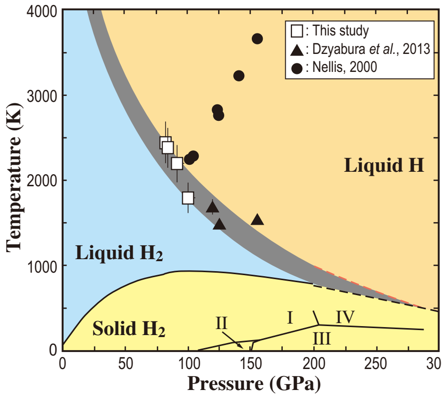

Fig. 8. Phase diagram of hydrogen. The gray area is the theoretically proposed transition line.

3. Summary

The benefit of simultaneous measurements in high-pressure experiments, especially in the high-pressure region, is worth noting. This is because when some physical properties are measured in separate experiments, it is not guaranteed that the samples are under exactly the same pressure, stress, and temperature conditions. In order to demonstrate the relationship between the crystal structure and electrical characteristics, simultaneous XRD and electrical resistance measurements of the same sample are the most straightforward solution.

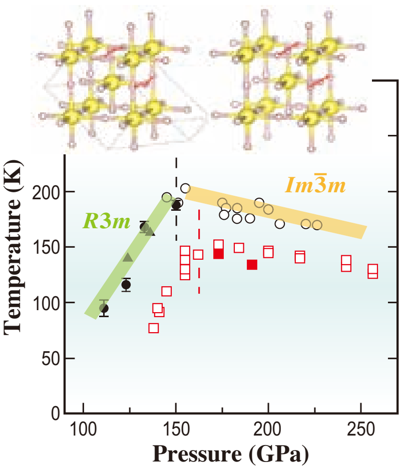

Fig. 9. Pressure dependence of the superconducting transition temperature T_c of H_3S (black) and D_3S (red).

Katsuya Shimizu[a] and Yasuo Ohishi[b]

[a] Osaka University
[b] Japan Synchrotron Radiation Research Institute (JASRI)

E-mail: shimizu@stec.es.osaka-u.ac.jp, ohishi@spring8.or.jp

References

[1] K. Shimizu *et al*.: Nature **419** (2002) 597.
[2] J.B. Neaton and N.W. Ashcroft: Nature **400** (1999) 141.
[3] T. Matsuoka and K. Shimizu: Nature **458** (2009) 186.
[4] T. Matsuoka *et al*.: Phys. Rev. B **89** (2014) 144103.
[5] A.S. Balchan and H.G. Drickamer: J. Chem. Phys. **34** (1961) 1948.
[6] N. Sakai *et al*.: J. Phys. Soc. Jpn. **51** (1982) 1811.
[7] K. Takemura *et al*.: Phys. Rev. Lett. **45** (1980) 881.
[8] M.I. McMahon *et al*.: Phys. Rev. B **61** (2000) 3135.
[9] R.J. Nelmes *et al*.: Phys. Rev. Lett. **83** (1999) 4081.
[10] H. Fujihisa *et al*.: Phys. Rev. Lett. **110** (2013) 235501.
[11] S.T. Weir *et al*.: Phys. Rev. Lett. **76** (1996) 1860.
[12] K. Ohta *et al*.: Sci. Rep. **5** (2015) 16560.
[13] A.P. Drozdov *et al*.: Nature **525** (2015) 73.
[14] D. Duan *et al*.: Sci. Rep. **4** (2014) 6968.
[15] M. Einaga *et al*.: Nat. Phys. (2016) doi:10.1038/nphys3760.

Radiation damage-free structure of photosystem II at 1.95 Å resolution revealed by femtosecond X-ray pulses at SACLA

Oxygenic photosynthesis utilizes light energy from the sun to convert carbon dioxide and water into carbohydrates, thereby providing chemical energy required for sustaining life on the earth. During this process, molecular oxygen is evolved as a by-product by the splitting of water at the first step of a series of electron transfer reactions, which transformed our atmosphere into an oxygenic one that enabled aerobic life to evolve and flourish as we enjoy today. This water-splitting reaction is catalyzed by photosystem II (PSII), a membrane-protein complex consisting of 17 trans-membrane subunits and 3 peripheral, hydrophilic subunits with a total molecular mass of 350 kDa for a monomer.

In order to reveal the water-splitting mechanism, it is essential to solve the structure of PSII, especially the catalytic center for water-splitting. After decades of extensive studies, the structure of PSII dimer was solved at resolutions gradually increased up to 1.9 Å in 2011 with X-rays of SPring-8 [1-3], which made PSII the largest membrane protein complex with its structure solved beyond 2.0 Å resolution. In this high resolution structure, the detailed organization of the catalytic center for water-splitting was clearly elucidated, which showed that it is a Mn_4CaO_5-cluster organized in a distorted chair form (Fig. 1(a)). The distorted structure suggested that it is unstable in some extent, and this is considered to be one of the most important features required for the catalytic activity. Since the water-splitting reaction proceeds through an S-state cycle composed of four steps, and each step is driven by the absorption of one photon causing a slight structural re-arrangement of the catalyst, the distorted, unstable structure should allow such structural changes to occur easily.

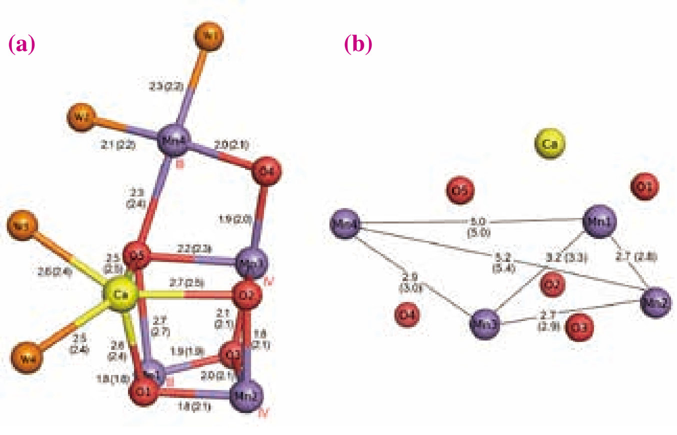

Fig. 1. **(a)** Structure of the Mn_4CaO_5-cluster. Inter-atomic distances of the XFEL-structure at 1.95 Å are shown in Å, with the corresponding distances obtained in the previous synchrotron radiation (SR) structure shown in parentheses. **(b)** Comparison of the Mn-Mn distances between those obtained by XFEL and SR (parentheses).

The reasons causing the distortion in the structure of the Mn_4CaO_5-cluster are two-folds: One is that the Ca-O distances are slightly longer (2.3–2.5 Å) than the typical Mn-O distances (1.8–2.1 Å), making the cubane core asymmetric; the other one is that, among the five O atoms bridging four Mn ions, four O atoms have normal Mn-O distances, whereas the 5th O (O5) atom has unusually longer distances to its nearby Mn ions in the range of 2.4–2.7 Å (Fig. 1(a)). This suggested that the O5 atom binds weakly to the Mn ions, and therefore may be cut out during the reaction, providing one of the substrates for O=O bond formation.

However, the high-resolution structure of PSII described above was solved with SPring-8 beamlines, and a possibility was raised that the structure has suffered some radiation damage, causing elongation of the Mn-Mn and Mn-O distances. Indeed, previous EXAFS as well as theoretical (QM/MM) studies based on the X-ray structure have suggested slightly shorter Mn-Mn distances, which hampered unambiguous elucidation of the structure and reaction mechanism.

In order to eliminate the radiation damage and solve the PSII structure at an atomic resolution, we utilized femtosecond XFEL pulses from SACLA to collect the X-ray diffraction data (**BL3**), which allowed collection of the diffraction data before radiation damage occurs (diffraction before destruction). Since PSII is an extremely large membrane protein complex, its crystal diffracts very weakly, and small crystals have been shown to have a very low resolution (4.5–5.5 Å) with the XFEL pulses [4]. Thus, we used large PSII crystals, and adopted an approach in which, the diffraction data was collected by irradiating one point of the crystal with one XFEL pulse, then translating the crystal by 50 μm to enable collection of the diffraction image from a fresh, undamaged volume of the crystal (Fig. 2) [5]. In this way, a full data set was collected by use of more than 100 large PSII crystals, and we collected two independent data sets from two different batches of crystals. Both data sets were analyzed at 1.95 Å resolution, and the atomic distances were taken from the average of the two structures [5].

Our results showed that most of the Mn-Mn distances were shortened by 0.1–0.2 Å (Fig. 1(b)),

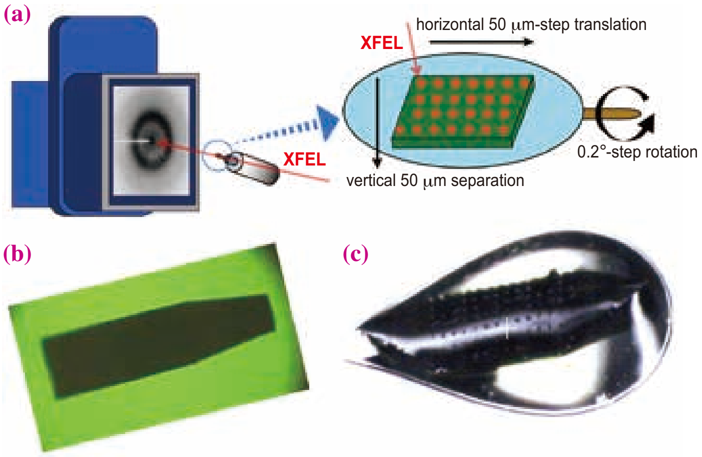

Fig. 2. **(a)** Schematic drawing of the XFEL-diffraction experiment. Still diffraction images were recorded from different spots of large PSII crystals, and the crystals were rotated by 0.2° between every two consecutive images over a range of 180°. Adjacent irradiation spots were separated by 50 μm in the horizontal direction for any rotational angle. Translation in the vertical direction was varied depending on the rotational angle so that the irradiation spots were separated by at least 50 μm in the vertical direction, too. **(b)** and **(c)** A picture of the PSII crystal before (b) and after the XFEL diffraction experiment (c). The path where the XFEL beam passed through became hollowed out, resulting in footprints of the irradiation spots by the XFEL beam which were well separated.

suggesting the elimination of the radiation damage. The O5-Mn1 and O5-Mn4 distances became 2.7 and 2.3 Å, respectively. Compared with the previous structure, these distances were slightly changed. However, they are still extremely longer than the typical Mn-O distances. Based on the Mn-O and Mn-ligand distances, we also assigned the valences of the four Mn ions to be (Mn1, Mn2, Mn3, Mn4)=(III, IV, IV, III) (Fig. 1(a)) [5].

The above results indicated that the unusual feature of the O5 atom is retained in the damage-free structure, suggesting that the O=O bond formation occurs in the area involving the O5 site. Based on this and other theoretical studies, a reaction mechanism was proposed in which, the O5 atom may move closer either to Mn4 or Mn1 upon one electron transfer from the S_1-state to S_2-state, resulting in two types of structures, namely, one with an open space between O5 and Mn1 (right-side open) (Fig. 3(a)) and the other one with an open space between O5 and Mn4 (left-side open) (Fig. 3(b)). These two types of structures have been shown to be in a quasi-equilibration in the S_2-state, which may enable an additional water (O atom) to come into either of the open spaces upon transition from S_2 to the higher S-state. Thus, the O=O bond formation may proceed either in the right-side or left-side between O5 and the newly inserted water (O atom) (Fig. 3) [5].

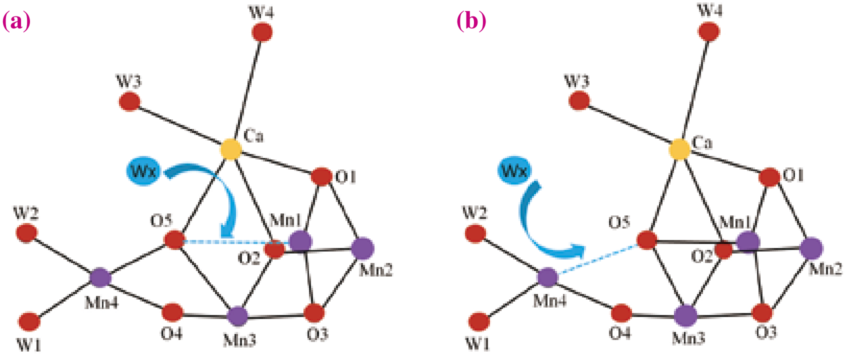

Fig. 3. Proposed mechanism for the O=O bond formation. **(a)** The O5 atom moved toward Mn4, resulting in an open space between O5 and Mn1 (right-side open), allowing a new water molecule (Wx) to come in and form the O=O bond between O5. **(b)** The O5 atom moved toward Mn1, resulting in the left-side open structure and allows a new water molecule to come in and form the O=O bond.

Jian-Ren Shen*, Fusamichi Akita and Michihiro Suga

Photosynthesis Research Center, Okayama University

*E-mail: shen@cc.okayama-u.ac.jp

References

[1] A. Zouni *et al*.: Nature **409** (2001) 739.
[2] N. Kamiya and J.-R. Shen: Proc. Natl. Acad. Sci. USA **100** (2003) 98.
[3] Y. Umena *et al*.: Nature **473** (2001) 55.
[4] C. Kupitz *et al*.: Nature **513** (2014) 261.
[5] *M. Suga, F. Akita, K. Hirata, G. Ueno, H. Murakami, Y. Nakajima, T. Shimizu, K. Yamashita, M. Yamamoto, H. Ago and J.-R. Shen: Nature* ***517*** *(2015) 99.*

Energy transfer pathways revealed from structural analysis of the plant PSI-LHCI supercomplex

Photosystem I (PSI) is one of the two photosystems functioning in oxygenic photosynthesis by various photosynthetic organisms ranging from cyanobacteria to eukaryotic algae and higher plants. It absorbs light energy from the sun to initiate a series of electron transfer reactions starting from electron donors plastocyanin or cytochrome c_6 to iron-sulfur centers, which is finally utilized to reduce NADP$^+$ to NADPH required for the reduction of carbon dioxide into sugars. The electrons used by PSI come from water through the water-splitting reaction catalyzed by photosystem II (PSII). In this way, the two photosystems work in series to extract electrons from water to reduce carbon dioxide, thereby converting light energy into chemical energy indispensable for sustaining life on the earth.

The reaction center of PSI performing light-induced charge separation and electron transfer reactions is largely conserved from prokaryotic cyanobacteria to higher plants, and is designated the PSI core. The PSI core from cyanobacteria contains 9 transmembrane and 3 peripheral subunits together with 127 cofactors (including 96 chlorophylls (Chls)), and exists as a trimer with a total molecular mass of around 1068 kDa. The structure of cyanobacterial PSI core has been analyzed at 2.5 Å resolution in 2001 [1]. On the other hand, PSI core from higher plants exists as a monomer and is surrounded by 4 trans-membrane light-harvesting complex I (LHCI) subunits Lhca1-Lhca4, forming a PSI-LHCI supercomplex with a total molecular mass over 600 kDa. One of the distinct features of this supercomplex is that the energy absorbed by LHCI is transferred to the PSI core with an extremely high efficiency (over 95%). The structure of higher plant PSI-LHCI supercomplex has been solved up to 3.3 Å resolution [2-4]. However, this resolution was not high enough to reveal the exact location and detailed organization of a vast number of cofactors including more than 150 Chls, which hampered an unambiguous elucidation of the principles underlying the highly efficient energy transfer pathways.

In order to improve the crystal resolution, we purified the PSI-LHCI supercomplex from pea leaves with a modified procedure, and screened the crystallization conditions extensively. As a result, we were able to solve the structure of PSI-LHCI at a 2.8 Å resolution with X-rays from beamlines **BL41XU** and **BL44XU** [5]. Our structure showed that the whole complex contained 16 subunits, among which, 12 subunits belong to the PSI core whereas 4 are LHCI subunits (Lhca1-Lhca4) (Fig. 1(a) and 1(b)). Within the 12 core subunits, PsaM and PsaX found in the cyanobacterial PSI core were not present whereas 2 subunits (PsaG and PsaH) unique to higher plant PSI were found [5].

In addition to the protein subunits, a total of 205 cofactors were identified in the PSI-LHCI supercomplex. These included 155 Chls (143 Chls a and 12 Chls b), 35 carotenoids [26 β-carotenes (BCRs), 5 luteins (Luts), and 4 violaxanthins (Vios)], 10 lipids [6 phosphatidylglycerols (PGs), 3 monogalactosyldiacylglycerols (MGDGs), and 1 digalactosyldiacylglycerol (DGDG)], 3 Fe_4S_4 clusters, 2 phylloquinones, and several water molecules (Fig. 2). Among these cofactors, 98 Chls a, 22 BCRs, 5 lipids (3 PGs, 1 MGDG, and 1 DGDG), 3 Fe_4S_4 clusters, and 2 phylloquinones are located in the PSI core, which

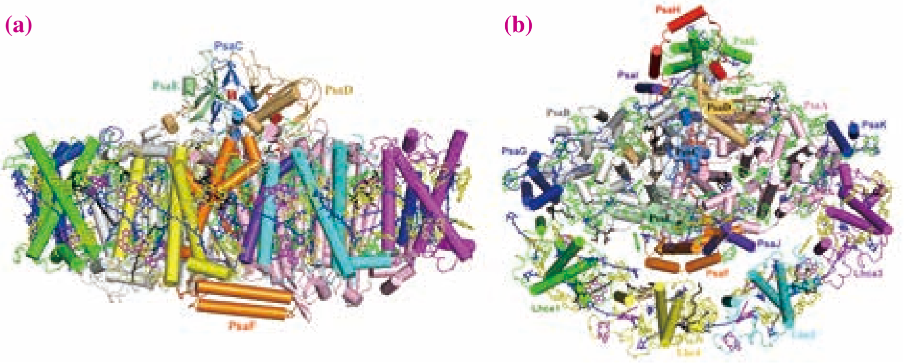

Fig. 1. Overall structure of the plant PSI-LHCI supercomplex.
(a) Side view; **(b)** Top view from the stromal side.

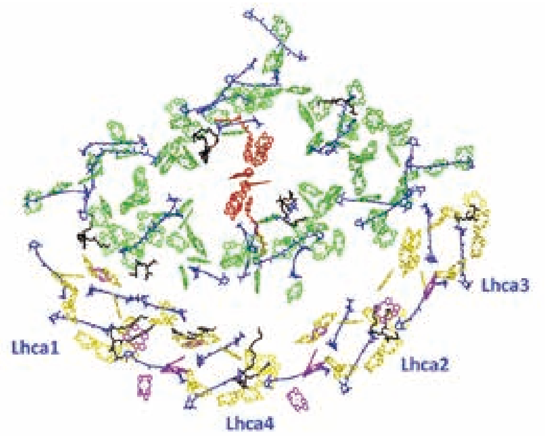

Fig. 2. Arrangement of pigments and other cofactors in the PSI-LHCI supercomplex with the same top view as in Fig. 1(b). Color codes: green, Chls a of PSI core complex; yellow, Chls a of LHCI; magenta, Chls b of LHCI; blue, carotenoids; black, lipids; red, cofactors of the electron transfer chain (Chls a, phylloquinones, and Fe_4S_4 clusters).

is largely comparable to the 96 Chls, 22 BCRs and 4 lipids found in the cyanobacterial PSI core structure, although several Chla were found to be in slightly different positions or orientations.

The most significant feature of the plant PSI-LHCI supercomplex is the presence of 4 LHCI subunits that function to harvest light energy efficiently. Our study revealed the detailed structures of these subunits and the organization of pigments they bind for the first time. Thus, we identified the location of 45 Chl a, 12 Chl b, and 13 carotenoids in these 4 subunits, and the interaction sites within the Lhca subunits and between each of the Lhca subunit and PSI core. We found that each of the LHCI subunits binds 1 BCR, 1 Lut and 1 Vio, with an additional Lut located between Lhca1 and Lhca4. The binding of Vio to LHCI was demonstrated for the first time, as was the difference between Chl a and b within LHCI. The presence of Vio in LHCI suggested its role in photoprotection, since it is well known that this carotenoid is involved in the “xanthophyll-cycle” in LHCII functioning in photoprotection. The “gap region” between the LHCIs and PSI core are filled with “red Chls”, which is a dimer of Chl a with a lower energy absorption level due to the strong interaction between the 2 Chl a monomers. Each of the 4 Lhca subunits binds one red Chl dimer, and these red Chls may have important roles in the energy transfer from LHCIs to the PSI core, as well as the binding of LHCIs to the PSI core.

Based on our structure, 4 plausible pathways for the energy transfer from LHCIs to the PSI core were deduced (Fig. 3(a)). Among these 4 pathways, Chls in Lhca1 and Lhca3 in the 2 sides of the Lhca belt have short distances to the PSI core Chls, offering 2 efficient energy transfer pathways (Fig. 3(b) and 3(c)). Chls in Lhca2 interact with PSI core Chls with a slightly longer distance, providing another energy transfer pathway (Fig. 3(c)). Chls in Lhca4 have a much longer distance to the PSI core, and therefore may not be able to transfer their energy directly but have to pass through Lhca1 in the lumenal side to transfer their energy to the core.

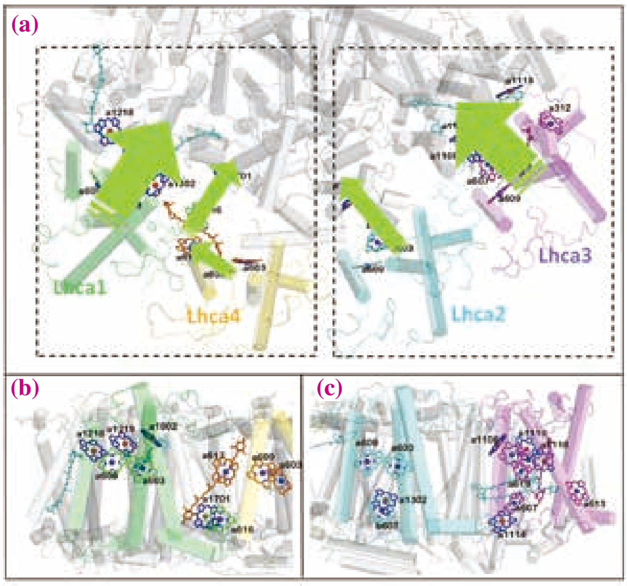

Fig. 3. Plausible energy transfer pathways from LHCI to the PSI core. **(a)** Overall view of the 4 energy transfer pathways from LHCI to the PSI core, with a top view from the stromal side. The green, thick arrows indicate efficient energy transfer pathways from Lhca1 and Lhca3 to the PSI core, whereas thin arrows indicate less efficient pathways from Lhca2 to PSI core, and from Lhca4 through Lhca1 to the core. **(b)** and **(c)**. Detailed interactions among the pigments involved in the energy transfer pathways indicated in panel (a). Side view of the boxed areas with dashed lines in the left (b) and right (c) sides of panel (a).

Michihiro Suga and Jian-Ren Shen*

Photosynthesis Research Center, Okayama University

*E-mail: shen@cc.okayama-u.ac.jp

References

[1] P. Jordan *et al.*: Nature **411** (2001) 909.
[2] A. Ben-Shem *et al.*: Nature **426** (2003) 630.
[3] A. Amunts *et al.*: Nature **447** (2007) 58.
[4] A. Amunts *et al.*: J. Biol. Chem. **285** (2010) 3478.
[5] *X. Qin, M. Suga, T. Kuang, J.-R. Shen: Science* ***348*** *(2015) 989.*

Visualization of agonistic and inhibitory DNA recognition by Toll-like receptor 9

Our bodies often face dangers from bacterial and viral invasions. Pathogenic microorganisms (bacteria, viruses, fungi, and parasites) threaten us continuously but we are equipped with powerful defense mechanisms. The innate immune system is the first line of defense against pathogenic microorganisms by detecting certain kinds of microbial products as a sign of danger and activating the downstream immune response. The Toll-like receptors (TLRs) are among the best-known receptors in the innate immune system and recognize a wide variety of microbial products. Dr. Beutler and Dr. Hoffmann won the Nobel Prize in Physiology or Medicine 2011 for their discovery concerning the activation of innate immunity by TLRs [1,2]. TLRs have received significant attention due to their critical roles in the innate immune system. TLRs are type I transmembrane receptors consisting of an extracellular leucine-rich repeat (LRR) domain, a transmembrane domain, and an intracellular Toll IL-receptor (TIR) domain. The LRR and TIR domains are responsible for ligand recognition and signaling, respectively. To date, 10 TLRs (TLR1 to TLR10) have been identified in humans and each TLR recognizes a distinct type of molecule commonly found in microorganisms that cause disease (Fig. 1). TLR9 recognizes CpG-DNA, a DNA sequence with a cytosine-phosphate-guanine dinucleotide (CpG) motif that is specific to bacterial and viral DNA [3,4]. The activation of TLR9 by CpG-DNA leads to the release of interferon and inflammatory cytokines. TLR9 thereby has the potential to be a target for vaccine adjuvants or therapeutic agents for viral infections and allergy diseases. Although TLR9 has been studied extensively since its discovery in 2000, the way it functions, especially from a structural viewpoint, remains unknown.

A research group at the Graduate School of Pharmaceutical Sciences of the University of Tokyo used brilliant synchrotron X-rays at SPring-8 beamline **BL41XU** and KEK to determine the crystal structures of the LRR domain of TLR9 in three forms: unliganded, inhibitory DNA-bound, and CpG-DNA-bound forms [5].

In the ring-shaped monomer structure of TLR9, its N- and C-termini directly interact (Fig. 2(a)). In the crystal structures, the unliganded and inhibitory DNA-bound forms of TLR9 are monomeric (Figs. 2(a) and 2(b)). Upon ligand binding, TLR9 and the CpG-DNA complex form a 2:2 complex with the CpG-DNA wedged between the two TLR9 protomers in an extended conformation (Fig. 2(c)). The dimerization of TLR9 brings the two C-termini in close proximity and induces the association of the intracellular TIR domain, leading to the activation (Fig. 3), while the unliganded and inhibitory DNA-bound forms of TLR9 are unable to associate the TIR domain.

The CpG-DNA binds to the groove formed at the lateral face of the ring structure near the N-terminus in one protomer and simultaneously to the lateral face of the C-terminal side of the other protomer; thus, it acts as a molecular glue to bridge the two TLR9 molecules and induce the activated form. The bases of the CpG motif are accommodated in the groove and engage in multiple specific interactions with TLR9, which define the specificity of the TLR9 toward the CpG dinucleotide. In addition, the flanking regions of the CpG motif further strengthen the interaction between TLR9 and CpG-DNA.

The inhibitory DNA binds to the concave surface of TLR9 to form stem-loop structures with three or four intramolecular base pairs. The high affinity of the inhibitory DNA is achieved mainly through the recognition of the backbone of the stem-loop

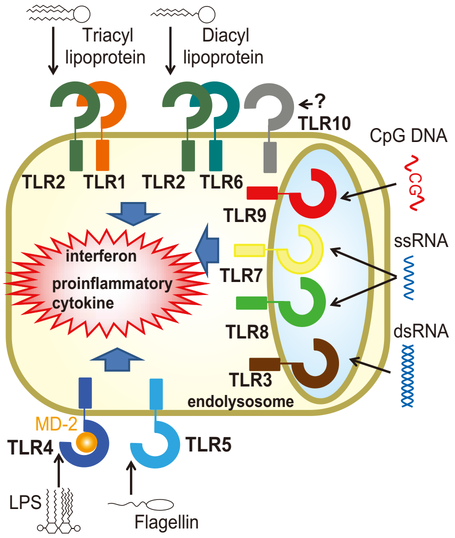

Fig. 1. Schematic illustration of human TLR signaling. TLR3 and TLR7–9 localize at the endosome, where they sense microbial and host-derived nucleic acids, whereas TLR5 and heterodimers of TLR2 and TLR1 or TLR6 are expressed at the cell surface. TLR4 localizes at both the plasma membrane and the endosome. TLR signaling is initiated by ligand-induced dimerization of receptors. TLR signaling induces proinflammatory cytokines and type I interferons.

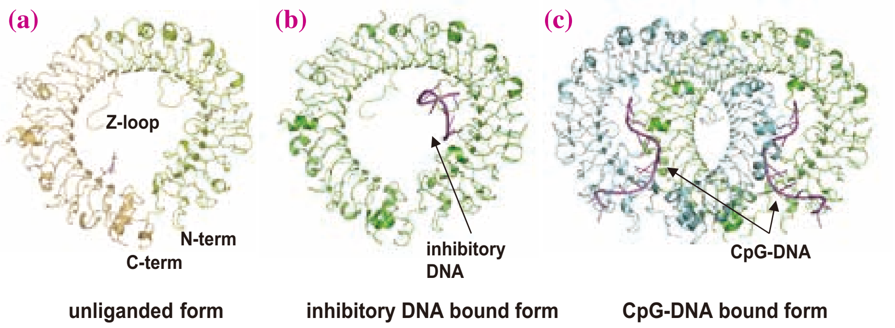

Fig. 2. Structures of TLR9 in the unliganded **(a)**, inhibitory DNA-bound **(b)**, and CpG-DNA-bound **(c)** forms. Bound DNA is shown in sticks in purple. The N- and C-terminal halves of TLR9 are shown in green and brown, respectively, in (a). The two protomers in the dimer are shown in green and cyan in (c).

structures. Since the binding site for the inhibitory DNA partially overlaps with that for agonistic CpG-DNA, inhibitory DNA competes for the binding site with agonistic CpG-DNA and thereby inhibits the TLR9 activation.

These structural analyses enable us to understand the detailed agonistic CpG-DNA and inhibitory DNA recognition and the activation mechanism of TLR9, which also open a new avenue for developing novel therapeutic agents targeting TLR9.

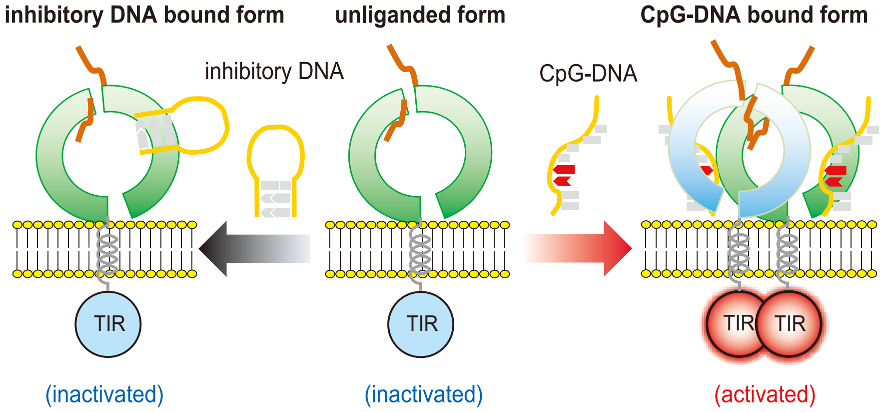

Fig. 3. Schematic regulation mechanism of TLR9 by CpG-DNA and inhibitory DNA. The unliganded, inactivated form of TLR9 (middle panel) transforms into the activated form (right panel) upon the binding of CpG-DNA. Upon the binding of inhibitory DNA, TLR9 remains inactivated (left panel).

Toshiyuki Shimizu

Graduate School of Pharmaceutical Sciences,
The University of Tokyo

E-mail: shimizu@mol.f.u-tokyo.ac.jp

References

[1] A. Poltorak *et al*.: Science **282** (1998) 2085.
[2] B. Lemaitre *et al*.: Cell **86** (1996) 973.
[3] H. Hemmi *et al*.: Nature **408** (2000) 740.
[4] S. Bauer *et al*.: Proc. Natl. Acad. Sci. USA **98** (2001) 9237.
[5] *U. Ohto, T. Shibata, H. Tanji, H. Ishida, E. Krayukhina, S. Uchiyama, K. Miyake and T. Shimizu: Nature* ***520*** *(2015) 702.*

Crystal structures of the human adiponectin receptors

Adiponectin is an antidiabetic adipokine secreted from adipose tissue. Plasma adiponectin levels are reduced in obesity and type 2 diabetes, while the replenishment of adiponectin reportedly ameliorated the abnormal glucose and lipid metabolism in mice.

We previously reported the expression cloning of the complementary DNAs encoding adiponectin receptors 1 and 2 [1]. Adiponectin receptors 1 and 2 (AdipoR1 and AdipoR2) are predicted to contain seven transmembrane helices, with an internal amino terminus and an external carboxy terminus, which is the opposite topology to G-protein-coupled receptors (GPCRs). Therefore, AdipoRs are expected to have different structures from those of GPCRs. AdipoR1 and AdipoR2 serve as the major receptors for adiponectin *in vivo*, with AdipoR1 activating the 5'AMP-activated protein kinase (AMPK) pathways and AdipoR2 activating the peroxisome proliferator-activated receptor (PPAR) α pathways (Fig. 1), leading to the increased expression of target genes such as molecules involved in fatty-acid combustion including acyl-CoA oxidase (ACO) and energy dissipation including uncoupling protein 2 (UCP2) [2]. Thereby, they regulate glucose and lipid metabolism, inflammation, and oxidative stress *in vivo*. Recently, the small-molecule AdipoR agonist AdipoRon was shown to ameliorate diabetes and increase exercise endurance while simultaneously prolonging the shortened lifespan resulting from obesity [3].

For crystallization, AdipoR1 and AdipoR2 were optimized by deleting their N-terminal tails because the full length human AdipoRs tended to aggregate. We then used the Fv fragment of an anti-AdipoR monoclonal antibody that recognizes a conformational epitope of both AdipoR1 and AdipoR2 and the lipidic mesophase method for crystallization [4]. Finally, we successfully determined the crystal structures of human AdipoR1 and AdipoR2 at 2.9 and 2.4 Å resolutions, respectively [5]. Data collection was performed on beamlines **BL32XU** at SPring-8, X06SA at the Swiss Light Source, and I24 at the Diamond Light Source. X-ray diffraction data were collected by the helical data collection method with a beam size of 1 × 10 μm (horizontal × vertical) on beamline BL32XU.

The AdipoR proteins contain the N-terminal intracellular region (NTR), a short intracellular helix (helix 0), a seven transmembrane (7TM) domain, and the C-terminal extracellular region (CTR) (Fig. 2). The Fv fragment is bound to the NTR. The seven transmembrane helices (I–VII) are connected by three intracellular loops (ICL1–3) and three extracellular loops (ECL1–3). ECL3 has a central short α helix, while ICL3 has another short α helix immediately following helix VI.

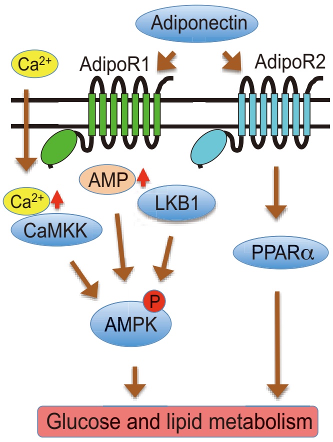

Fig. 1. Schematic representation of adiponectin signaling. Adiponectin induces extracellular Ca^{2+} influx by AdipoR1, which is necessary for the subsequent activation of Ca^{2+}/calmodulin-dependent protein kinase kinase (CaMKK). Adiponectin also increases the concentration of cellular AMP. Both CaMKK and AMP/LKB1 are necessary for adiponectin-induced full AMPK activation via AdipoR1. Adiponectin activates PPARα pathways via AdipoR2. Thereby, they regulate glucose and lipid metabolism.

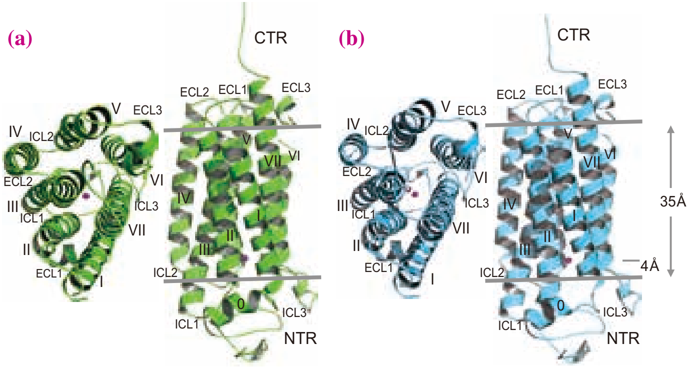

Fig. 2. Overall structures of AdipoR1 and AdipoR2. **(a)** Structure of AdipoR1 with 2.9 Å resolution. **(b)** Structure of AdipoR2 with 2.4 Å resolution. The structures of their complexes with Fv fragments were determined, but the Fv fragments are omitted here for clarity. The structures are viewed from the extracellular side (left) and parallel to the membrane (right). The NTR, helix 0, transmembrane helices I–VII, the ECL, the ICL, and the CTR of AdipoR1 **(a)** and AdipoR2 **(b)** are indicated. A zinc ion and a water molecule are represented by magenta and pink spheres, respectively.

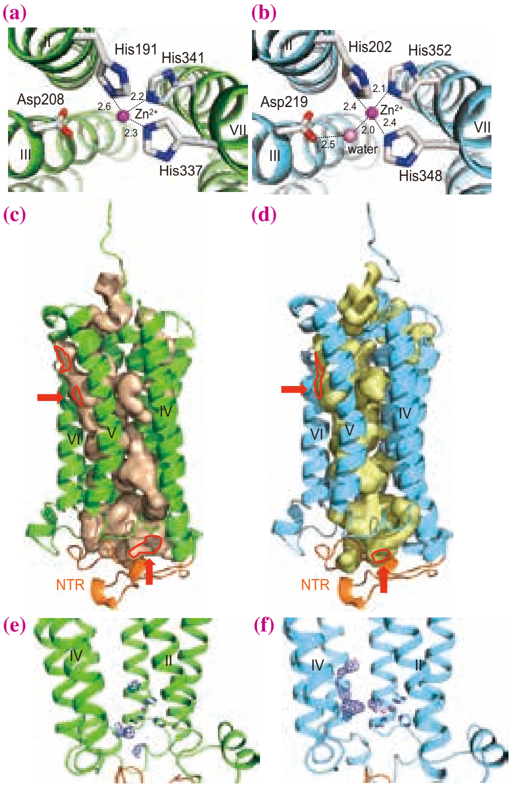

Fig. 3. The zinc-binding sites and cavities of AdipoR1 and AdipoR2. **(a, b)** Coordination of the zinc ion (magenta sphere) by three His residues of AdipoR1 **(a)** and AdipoR2 **(b)**, viewed from the cytoplasmic side. A water molecule (pink sphere) is also coordinated to the zinc ion and is fixed by D219 in AdipoR2. **(c, d)** Cavities of AdipoR1 **(c)** and AdipoR2 **(d)**. The red arrows indicate the openings of the cavities. **(e, f)** Extra electron density maps in the cavities of AdipoR1 **(e)** and AdipoR2 **(f)**, contoured at 0.5 s and 1 s, respectively. The NTR is colored orange. The openings of the cavities are bordered in red.

The seven transmembrane helices of AdipoR form a helix bundle. As viewed from the outside of the cell, the seven transmembrane helices in the helix bundle are arranged circularly in a clockwise manner from helix I to helix VII (Fig. 2). The structures of the AdipoR1•Fv complex and the AdipoR2•Fv complex are quite similar. As compared with the GPCR structures, the AdipoR1/R2 structures lack kinked transmembrane helices, while helix V is slightly curved due to the three Gly residues (Figs. 3(c,d)). In addition, a DALI search revealed that the AdipoR1 and AdipoR2 structures share no similarity with other protein structures in the Protein Data Bank. Consequently, we concluded that the AdipoR1 and AdipoR2 structures are novel.

AdipoR1 and AdipoR2 have two major characteristic structures in their transmembrane domain. One is a zinc ion and the other is a cavity. We found a zinc ion bound within the 7TM domain at a site located in the inner membrane leaflet. The zinc ion is coordinated by three His residues of AdipoR1/R2 at zinc–nitrogen distances of 2.1–2.6 Å (Figs. 3(a,b)). The zinc ion is thus located approximately 4 Å deep from the inner surface of the plasma membrane (Fig. 2). Furthermore, a water molecule is bound between the zinc ion and the side-chain carboxylate group of D219 of AdipoR2. Thus, the zinc ion has a tetrahedral coordination. We also found a large internal cavity surrounded by the 7TM helices, including the zinc-binding site, in both the AdipoR1 and AdipoR2 structures (Figs. 3(c,d)). The cavities extend from the cytoplasmic surface to the middle of the outer lipid layer of the membrane, and contain unidentified extra electron densities, which are weaker than those of the protein (Figs. 3(e,f)). In the cavity of AdipoR2, extra electron densities are observed along with helices III, V, and VI. In contrast, in the cavity of AdipoR1, even weaker electron densities are observed on the cytoplasmic side of the cavity. These weak electron densities might be relevant to the substrates/products of the hypothesized hydrolytic activities of AdipoR1/AdipoR2.

In summary, this study revealed that the structural and functional characteristics of AdipoR1 and AdipoR2 are completely different from those of GPCRs, and therefore the AdipoRs represent an entirely novel type of receptor. The present crystal structures are expected to provide a strong basis for the development and optimization of adiponectin agonists, such as AdipoRon.

H. Tanabe[a,b,c,d], T. Yamauchi[e,f,g], T. Kadowaki[e,f]
and S. Yokoyama[a,b,d,*]

[a] RIKEN Systems and Structural Biology Center/Yokohama
[b] Dept. of Biophysics and Biochemistry,
The University of Tokyo
[c] RIKEN Center for Life Science Technologies/Yokohama
[d] RIKEN Structural Biology Laboratory/Yokohama
[e] Dept. of Diabetes and Metabolic Diseases, The Univ. of Tokyo
[f] Dept. of Integrated Molecular Science on Metabolic Diseases,
The University of Tokyo
[g] JST/CREST

*E-mail: yokoyama@riken.jp

References

[1] T. Yamauchi *et al*.: Nature **423** (2003) 762.
[2] M. Iwabu *et al*.: Nature **464** (2010) 1313.
[3] M. Okada-Iwabu *et al*.: Nature **503** (2013) 493.
[4] H. Tanabe *et al*.: J. Struct. Funct. Genomics **16** (2015) 11.
[5] *H. Tanabe, Y. Fujii, M. Okada-Iwabu, M. Iwabu, Y. Nakamura, T. Hosaka, K. Motoyama, M. Ikeda, M. Wakiyama, T. Terada, N. Ohsawa, M. Hato, S. Ogasawara, T. Hino, T. Murata, S. Iwata, K. Hirata, Y. Kawano, M. Yamamoto, T. Kimura-Someya, M. Shirouzu, T. Yamauchi, T. Kadowaki and S. Yokoyama: Nature* **520** *(2015) 312.*

Absolute slowness encoded in the circadian clock protein KaiC

Intracellular events are rhythmically regulated by an oscillator with a 24 h period (circadian clock) to adapt to daily changes in the environment on Earth. The slowness of the clock oscillator is one of the characteristics distinguishing it from well-known faster chemical oscillators (with periods of seconds or minutes) [1], raising a fundamental question about the origins of slow but ordered rhythms. We thus searched for determinants of the circadian period using a protein-clock system: the cyanobacterial circadian clock can be reconstituted in a test tube by mixing three clock proteins, KaiA, KaiB and KaiC, with adenosine triphosphate (ATP) [2].

We found that the activity of ATP hydrolysis (ATPase) in KaiC is a determinant of the oscillatory frequency (reciprocal of the period). As the ATPase activity of KaiC itself is increased by a series of single amino acid replacements in KaiC (Fig. 1), the frequency of the *in vitro* protein-clock system (Fig. 1(a)) as well as that of the *in vivo* system (Fig. 1(b)) increased in a well-correlated manner. We thus conducted X-ray crystallographic studies of KaiC [3] at beamline **BL44XU** to search for the structural origins of the slow ATPase orchestrating the frequency of the intracellular events in cyanobacteria.

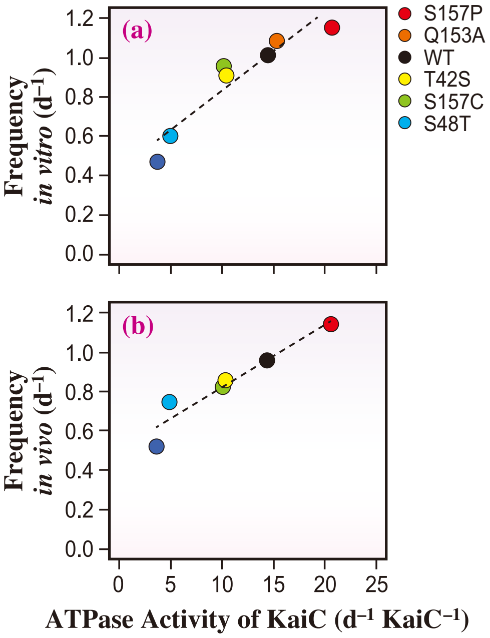

Fig. 1. ATPase activity of KaiC governing the frequencies of both protein-clock rhythms in a test tube **(a)** and intracellular rhythms **(b)**. These figures are reproduced from Ref. 3.

We identified two structural factors slowing the ATP hydrolysis reaction to the circadian time scale (Fig. 2(a)). The first is an unusual positioning of a lytic water molecule surrounding a γ-phosphate of ATP in the crystal structure with the $P2_12_12_1$ space group (right inset in Fig. 2(a)). The lytic water molecule is sequestered from an ideal position to attack a phosphorus atom of the γ-phosphate by hydrogen bonding to the carbonyl oxygen atom of F199 and to the nitrogen atom (N_η) of R226 (Fig. 2(b)). In another crystal structure with the $P3_121$ space group, the lytic water molecule is positioned farther from the γ-phosphate of ATP than that in the $P2_12_12_1$ crystal structure (right inset in Fig. 2(a)). The impact of these two different states on ATPase activity was studied by introducing KaiC mutations perturbing their relative stability (S157P, Q153A, and S157C in Fig. 1). On the basis of the experimental evidence, we conclude that the water positions in both states are basically unfavorable to the ATP hydrolysis (right inset in Fig. 2(a)) as they deviate considerably from the ideal position, similarly to the behavior of other hyperactive enzymes (right inset in Fig. 2(a)), and that the position in the $P3_121$ crystal structure is much more unfavorable than that in the $P2_12_12_1$ crystal structure.

The second is peptide isomerization, one of the slowest reactions in protein chemistry. The coupling of ATP hydrolysis to a *cis-trans* isomerization is clearly reflected in the crystal structure of a KaiC hexamer harboring ATP-bound and adenosine diphosphate (ADP)-bound subunits asymmetrically. In the pre-hydrolysis state, the peptide bond between D145 and S146 mainly adopted the *cis*-conformation, whereas, in the post-hydrolysis state, the peptide completely adopted the *trans*-conformation (left inset in Fig. 2(a)). Our molecular dynamics simulations indicate that the pre-hydrolysis state should overcome a barrier of 14 to 16 kcal·mol^{-1} for *cis-trans* isomerization itself and a barrier of 11 to 17 kcal·mol^{-1} for ATP hydrolysis [3].

The two structural origins uncovered in the present study indicate an unexpectedly high energy barrier upon ATP hydrolysis concomitant with peptide isomerization (Fig. 3). Assuming a frequency factor of 10^{12} s^{-1}, the barrier can be estimated to be approximately 22 kcal·mol^{-1} using the rate constant of 0.5 h^{-1} (12 ATP d^{-1}) at 30°C. Our results show that the circadian time scale is designed in the atomic structure of KaiC to regulate the efficiency of ATP hydrolysis.

An analogous mechanism may be found in other organisms, because all of the key factors such as

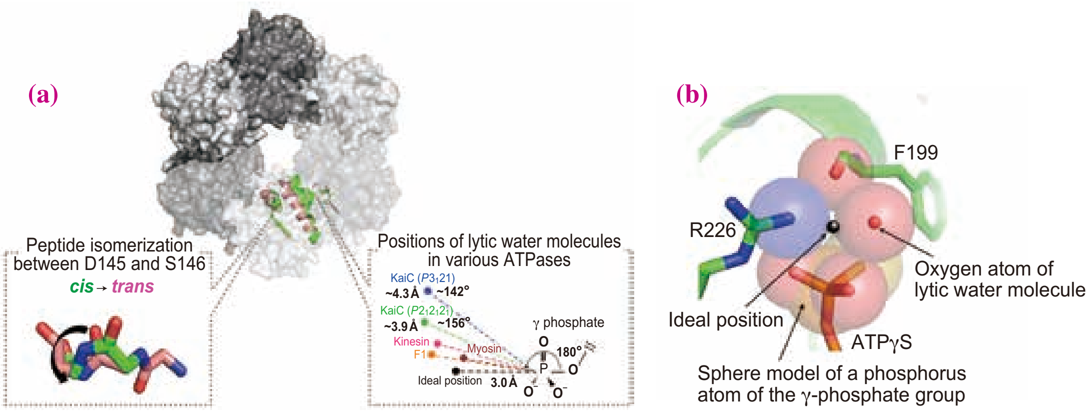

Fig. 2. Structural origins of slowness in a KaiC hexamer. **(a)** Unusual positioning of a lytic water molecule relative to ATP (right inset) and coupling of the peptide isomerization with the ATP hydrolysis reaction (left inset). **(b)** Steric hindrance surrounding a γ-phosphate of ATP. The black filled circle represents the ideal position for a lytic water molecule to attack a phosphorus atom of the γ-phosphate of ATP. Van der Waals radii of the oxygen atom of the lytic water molecule, a carbonyl oxygen atom of F199, N_η of R226, and a phosphorus atom of the γ-phosphate group of ATP γS are drawn using sphere models.

the water molecule, ATP and peptide isomerization are ubiquitously shared and available for achieving absolute slowness. In mammals, the accepted model of the circadian clock is the transcriptional and translational oscillation (TTO); the clock proteins negatively regulate their own expression, thereby producing rhythmic transcription and translation. However, the slowness of the TTO model is often questioned because the transcriptional and translational events can proceed within minutes [4]. Recently, a circadian clock independent of the TTO in mammals was reported [5]. In the future, a structural analysis focusing on the slowness and the correlation with the period of a chemical reaction (the ATP hydrolysis reaction in this study) might reveal the design principle of the circadian clock.

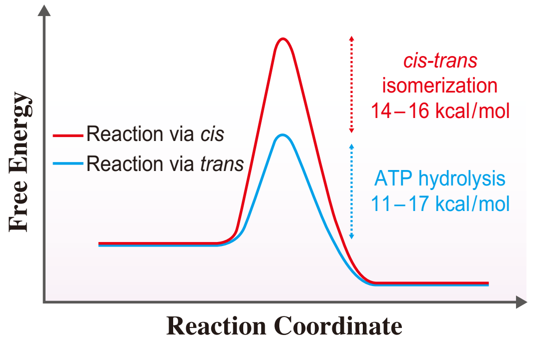

Fig. 3. Circadian time scale encoded in the atomic structure of KaiC. The pre-hydrolysis state with the *cis*-conformation (red line) overcomes a higher energy barrier (exceeding 22 kcal·mol^{-1}) during the reaction than that with the *trans*-conformation (blue line).

Jun Abe[a], Atsushi Mukaiyama[a,b] and Shuji Akiyama[a,b,*]

[a] Research Center of Integrative Molecular Systems (CIMoS), Institute for Molecular Science
[b] Dept. of Functional Molecular Science, SOKENDAI, The Graduate University for Advanced Studies

*E-mail: akiyamas@ims.ac.jp

References

[1] K.I. Agladze *et al.*: Nature **308**, (1984) 834.
[2] M. Nakajima *et al.*: Science **308** (2005) 414.
[3] *J. Abe, T.B. Hiyama, A. Mukaiyama, S. Son, T. Mori, S. Saito, M. Osako, J. Wolanin, E. Yamashita, T. Kondo and S. Akiyama: Science* ***349*** *(2015) 312.*
[4] B. Schwanhäusser *et al.*: Nature **473** (2011) 337.
[5] J.S. O'Neill and A.B. Reddy: Nature **469** (2011) 498.

Grease matrix method for serial femtosecond crystallography using XFELs

Using femtosecond X-ray pulses from X-ray free-electron lasers (XFELs), serial femtosecond crystallography (SFX) offers a route to overcome radiation damage to small protein crystals via the "diffraction-before-destruction" approach. A single-pulse X-ray exposure will completely destroy small individual crystals; therefore, fresh specimens must be supplied for subsequent X-ray pulses to continue data acquisition (Fig. 1). Diffraction signals up to a few angstroms in resolution can be obtained from even submicrometer-size crystals, thereby greatly reducing the difficulty of producing large crystals. SFX has expanded the window for obtaining room temperature structures of proteins. More recently, it has also been applied in time-resolved studies of light-driven structural changes and chemical reaction dynamics.

SFX is contingent on a reliable and tractable supply of protein crystals to complete the data collection. Tens of thousands of diffraction patterns from specimens in random orientations are required to obtain a structure. At SACLA (SPring-8 Angstrom Compact Free Electron Laser), SFX has been carried out using a diverse application platform for hard X-ray diffraction in SACLA (DAPHNIS) system, which consists of a sample chamber, injectors and an MPCCD detector [1]. Liquid jet injection of small protein crystals is often exploited for serial sample loading. A continuous flow of the liquid-jet injectors at a relatively high speed (~10 m/s) consumes 10–100 mg of the protein sample; consequently, the applicability of SFX to proteins with low expression or poor crystallization is limited. Although a rather large amount of sample is needed to form a continuous jet stream, less than 0.01% of the crystals are typically exposed to X-ray pulses. On the other hand, the microextrusion of specimens using viscous media such as monoolein, which is used for the crystallization of membrane proteins in the lipidic cubic phase (LCP), can maintain a stable stream at a low flow rate of 0.02 – 0.5 μl/min, which helps to reduce sample consumption (~0.3 mg) [2]. However, this approach is probably limited to proteins crystallized in the LCP. A more universal method that is applicable to a wide variety of proteins is essential to firmly establish SFX.

In this study, we introduce an oil-based grease matrix as a generic carrier of protein microcrystals for SFX using XFELs [3]. In protein X-ray crystallography, a mineral oil is used as a versatile cryoprotectant for a wide variety of proteins without serious damage to crystals. A grease matrix provides maximum adaptability for most classes of proteins with a straightforward sample-loading procedure, protection against the cracking and dissolution of protein crystals due to various physical or chemical events such as osmotic shock arising from the properties of other viscous media (e.g., hydrogels), and preservation of the aqueous environment of the native protein molecules. We successfully applied a grease-matrix carrier to various proteins including lysozyme, glucose isomerase, thaumatin and fatty acid–binding protein type 3 (FABP3) in SFX experiments and obtained electron density maps beyond 2 Å resolution using less than 1 mg of micrometer-size protein crystals.

We performed the SFX experiments using femtosecond X-ray pulses from SACLA. Each X-ray pulse delivered ~7×10^{10} photons within a 10 fs duration (FWHM) to the samples with a grease matrix. The experiments were carried out using a DAPHNIS at **BL3**. We suspended protein microcrystals in the grease medium. An aliquot of the sample was loaded into a syringe. We used storage solutions of microcrystals of the proteins lysozyme (size 7–10 μm, Fig. 2(a)), glucose isomerase (10–30 μm), thaumatin (10–30 μm) and FABP3 (10–20 μm). For SFX data

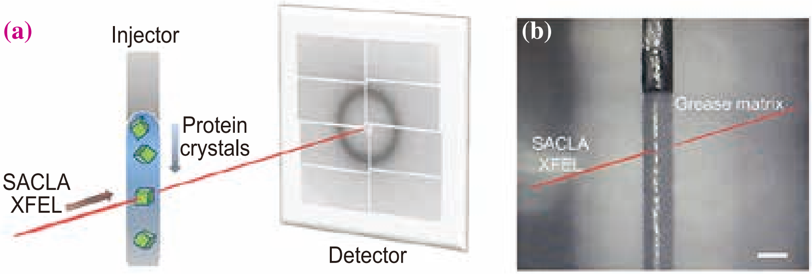

Fig. 1. Serial femtosecond crystallography. **(a)** Fresh nano/microcrystals are supplied for subsequent X-ray pulses to continue data acquisition. **(b)** Sample extrusion of the grease matrix through a syringe needle. Grease matrix was extruded as a continuous column to intersect with the XFEL beam. Scale bar represents 240 μm.

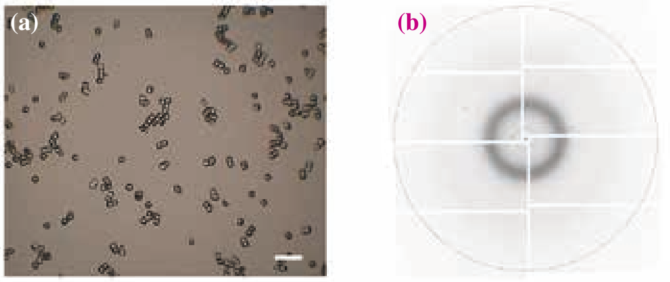

Fig. 2. **(a)** Lysozyme microcrystals used for SFX measurements. Scale bar represents 40 μm. **(b)** Typical XFEL single diffraction pattern from grease matrix. The resolution at the edges corresponds to ~1.6 Å (dashed circle).

collection, we used a sample volume of ~30 μl (10^7 crystals/ml). The grease matrix containing randomly oriented protein microcrystals was continuously delivered to the 1.5-μm (FWHM)-diameter focal spot of the XFEL radiation using a syringe injector with a 110-μm-i.d. needle installed in a diffraction chamber with a helium atmosphere. The sample flow rate was 0.5 $\mu l \cdot min^{-1}$. The grease formed a stable flow for all protein samples (Fig. 1(b)). Diffraction patterns were collected using a custom-built multiport CCD.

We collected single-pulse X-ray diffraction patterns of microcrystals from the four different proteins (Fig. 2(b)). With the SACLA running at a 30 Hz repetition rate, ~100,000 diffraction patterns were collected within 1 h using a sample volume of less than 30 μl. We successfully indexed and integrated 8,000–30,000 patterns for each of the proteins. Lysozyme, glucose isomerase, thaumatin and FABP3 crystals yielded data sets beyond 2.0 Å resolution. We determined the room-temperature crystal structures of lysozyme (PDB ID: 3WUL), glucose isomerase (4W4Q), thaumatin (3WXS) and FABP3 (3WXQ) at 2.0, 2.0, 2.0 and 1.6 Å, respectively. We were able to observe clear electron density maps; an example is shown here for lysozyme (Fig. 3). An increase in the crystal hit rate (indexed patterns/collected diffraction patterns) can be achieved with increased crystal number densities, which would, however, cause multiple sample hits in one shot and complicate the indexing procedures. We found that a crystal number density of ~10^7 was suitable for SFX data collection under our experimental conditions using the 110-μm-i.d. needle and a 0.5 $\mu l \cdot min^{-1}$ flow rate.

In summary, using a grease matrix as a general carrier of protein microcrystals for serial sample loading in SFX, we successfully obtained room-temperature structures beyond 2 Å resolution from four different proteins in 7 – 30 μm microcrystals using less than 1 mg of a sample. More recently, using the grease matrix technique, Yamashita and coworkers have demonstrated a single isomorphous replacement with anomalous scattering (SIRAS) phasing for a Hg-derivatized luciferin-regenerating enzyme [4]. In addition, we have successfully determined the structure of native lysozyme with single-wavelength anomalous diffraction (SAD) by utilizing the weak anomalous signals of sulfur and chlorine [5]. One of the major challenges of phasing in SFX is to improve the signal-to-noise ratio. This technique using the matrix with low background scattering noise will contribute significantly to measuring weak anomalous signals for *de novo* phasing from SFX data. Our grease matrix-based approach should be applicable to a wide range of proteins as well as inorganic nanocrystals to facilitate investigations to determine structures with atomic resolution using single-pulse exposure.

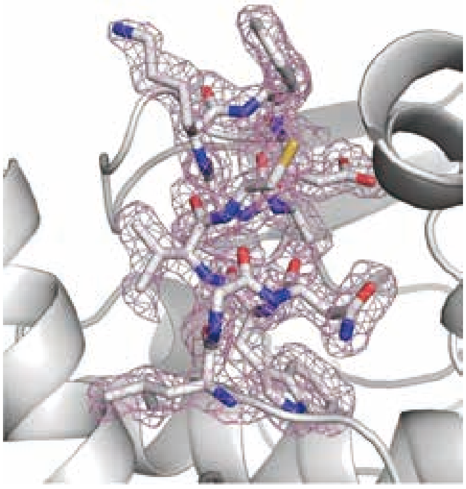

Fig. 3. Close-up view of the lysozyme structure with a $2F_o$ -F_c electron density map contoured at the 1.0σ level.

Michihiro Sugahara[a,*], Eriko Nango[a] and So Iwata[a,b]

[a] RIKEN SPring-8 Center
[b] Graduate School of Medicine, Kyoto University

*E-mail: msuga@spring8.or.jp

References

[1] K. Tono *et al*.: J. Synchrotron Rad. **22** (2015) 532.
[2] U. Weierstall *et al*.: Nat. Commun. **5** (2014) 3309.
[3] *M. Sugahara, E. Mizohata, E. Nango, M. Suzuki, T. Tanaka, T. Masuda, R. Tanaka, T. Shimamura, Y. Tanaka, C. Suno, K. Ihara, D. Pan, K. Kakinouchi, S. Sugiyama, M. Murata, T. Inoue, K. Tono, C. Song, J. Park, T. Kameshima, T. Hatsui, Y. Joti, M. Yabashi and S. Iwata: Nat. Methods* ***12*** *(2015) 61.*
[4] K. Yamashita *et al*.: Scientific Rep. **5** (2015) 14017.
[5] T. Nakane *et al*.: Acta Crystallogr. D Biol. Crystallogr. **71** (2015) 2519.

De novo phasing with serial femtosecond crystallography at SACLA

Phase determination has been a major problem in protein crystallography. The protein crystal structure is very informative for understanding the functions of proteins; however, it is difficult to solve the protein structure using μm-size protein crystals, especially membrane protein crystals.

The high brilliance X-ray pulses of the X-ray free electron laser (XFEL) are anticipated to enable crystal structure determination using microcrystals. Serial femtosecond crystallography (SFX) [1] is a new method of structure determination, where single-pulse diffraction patterns are collected from a liquid flow of microcrystals using X-ray pulses of the XFEL. Data collection by SFX will reduce the time spent on the optimization of protein crystallization conditions because large crystals are no longer required. However, structure determination by SFX has mainly been restricted to the molecular replacement method. Thus, the development of *de novo* phasing using protein microcrystals for XFEL has been anticipated.

The single-wavelength anomalous dispersion (SAD) method is the most common experimental phasing method in protein crystallography. Barends *et al*. succeeded in *de novo* phasing by the SAD method with lysozyme crystals using the SFX method at LCLS in 2014 [2]. About 60,000 single-pulse patterns, which were required for the structure determination, were collected using 8.5 keV X-rays in order to measure the anomalous dispersion of Gd ions soaked in lysozyme crystals. Another reason for this X-ray energy was because the maximum available photon energy at LCLS was 9.5 keV. Heavy atoms such as Hg, Se, Pt, and Au are most commonly used in protein phase determination at synchrotron radiation facilities. The absorption edges of these atoms are near 12.4 keV. Such a high photon energy, which is advantageous in high-resolution *de novo* structure determination, is available at SACLA. We are developing an effective *de novo* phasing method using protein microcrystals and the high photon energy XFEL of SACLA [3].

In order to carry out phasing by SFX at SACLA, we prepared microcrystals of native luciferin regenerating enzyme (LRE) and a Hg derivative. The microcrystals were crystallized by a batch method using PEG3350 as a precipitant. Hg-derivative crystals were obtained by soaking native microcrystals in stock solution containing 1 mM HgO. Before SFX data collection, the solution including the microcrystals was mixed with a grease matrix in order to increase the viscosity [4]. The SFX experiment was performed at **BL3** of SACLA. The mixture solution was extruded from the syringe injector system in a DAPHNIS chamber [5] at room temperature. The photon energy was tuned to 12.6 keV, which is near the absorption edge of the Hg atom. We collected 133,958 and 583,291 images for the native and Hg-derivative crystals, respectively. For the native crystals, 26,238 images (20%) were preselected on the basis of the diffraction intensity

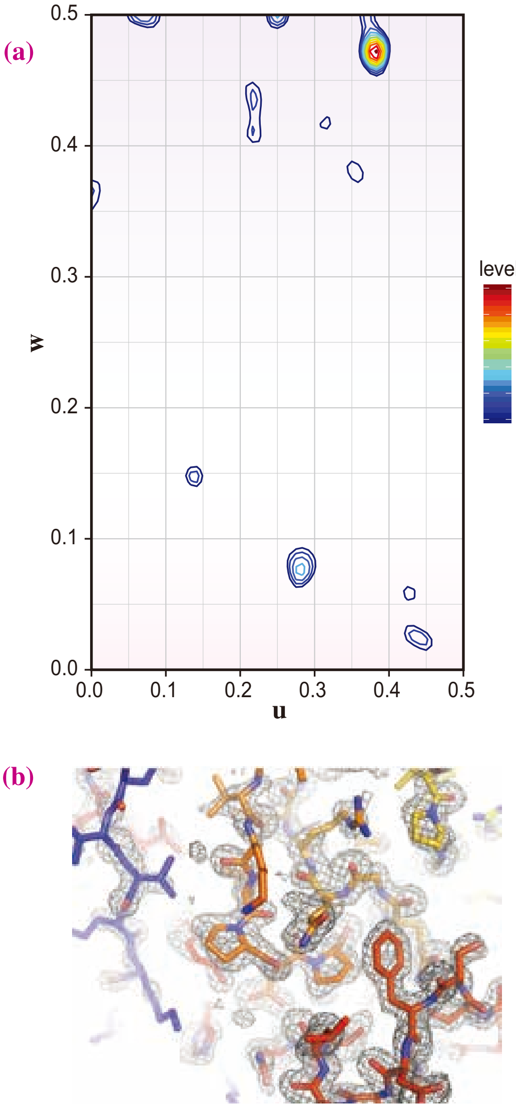

Fig. 1. **(a)** The v = 1/2 Harker section of isomorphous difference Patterson map. **(b)** A refined model of LRE and SIRAS electron density map produced by SHELXE. The electron density map is contoured at 1.0σ. These maps were calculated with 10,792 and 10,000 indexed patterns of native and Hg-derivative LRE crystals, respectively.

and 10,792 patterns of these (41%) were indexed. For the Hg-derivative crystals, we selected 298,061 (51%) images and 85,747 patterns of these (29%) were indexed. Diffraction patterns were processed using the CrystFEL software suite [6]. Monte Carlo integration for the native and Hg-derivative crystals yielded mean SFX multiplicities of 222 at 1.5 Å resolution and 908 at 1.6 Å resolution, respectively. We attempted phasing by the SAD method using all the Hg-derivative data, but this was unsuccessful.

Although SAD phasing was unsuccessful, we succeeded in phase determination by the SIRAS method using 10,792 native and 10,000 Hg-derivative images with a mean multiplicity of 106. The phase calculations and improvements were carried out using the SHELX C, D, and E programs. An isomorphous difference Patterson map showed a significant peak corresponding to the position of the Hg atom at 8.1σ (Fig. 1(a)). When the correct hand was used, an electron density map that was readily interpretable using a mean FOM of 0.615 was obtained and 197 residues were modeled with CC = 27%. Automatic model building was then performed using ARP/wARP with REFMAC5. 304 out of 308 residues were modeled with satisfactory accuracy (R_{work} = 22.3% and R_{free} = 27.6%) (Fig. 1(b)).

In order to examine the quality of the *de novo* phasing, we tested the SIRAS phasing protocol using different numbers of native and derivative patterns. We evaluated the phase quality using the correlation coefficient (CC) between the experimental electron density map given by SHELXE and the Fc map calculated using the final refined structure mentioned above. When the CC value was greater than 0.65, the trial was judged a success. More than 5,000 native patterns and 8,000 derivative patterns were required but in total at least 18,000 patterns were needed for successful phasing (Fig. 2).

In this study, we showed that the combination of Hg-derivative and native crystals enabled *de novo* phasing using SIRAS with a much smaller number of crystals than that required for the SAD method. *De novo* phasing was achieved using data collected in only two hours. The reduction in the amount of data required for structure determination is very important to make the best use of the limited beam time of XFEL because there are only two XFEL facilities in the world, SACLA and LCLS.

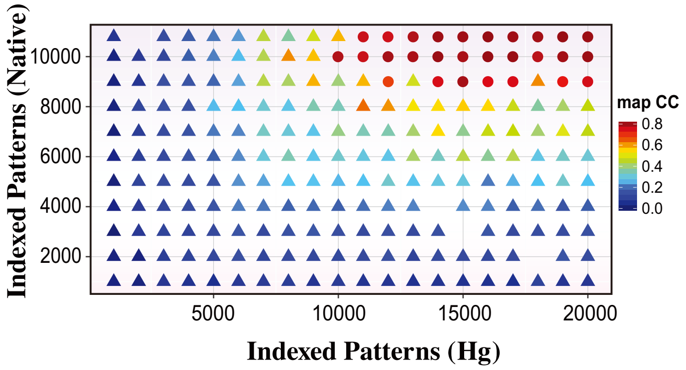

Fig. 2. Phase quality (CC) as a function of the numbers of native and derivative indexed patterns. The success and failure of phasing are represented as circular and triangular symbols, respectively. The CC between the experimental electron density map and the Fc map is indicated by the color. Some data points are missing because SHELXE failed to trace the map.

Toru Nakatsu[a,b,*], Keitaro Yamashita[b] and So Iwata[b,c]

[a] Department of Structural Biology, Kyoto University
[b] RIKEN SPring-8 Center
[c] Department of Cell Biology, Kyoto University

*E-mail: nakatsu@pharm.kyoto-u.ac.jp

References

[1] H.N. Chapman *et al.*: Nature **470** (2011) 73.
[2] T.R.M. Barends *et al.*: Nature **505** (2014) 244.
[3] *K. Yamashita, D. Pan, T. Okuda, M. Sugahara, A. Kodan, T. Yamaguchi, T. Murai, K. Gomi, N. Kajiyama, E. Mizohata, M. Suzuki, E. Nango, K. Tono, Y. Joti, T. Kameshima, J. Park, C. Song, T. Hatsui, M. Yabashi, S. Iwata, H. Kato, H. Ago, M. Yamamoto and T. Nakatsu: Sci. Rep.* **5** *(2015) 14017.*
[4] M. Sugahara *et al.*: Nat. Meth. **12** (2015) 61.
[5] K. Too *et al.*: J. Synchrotron Rad. **22** (2015) 532.
[6] T.A. White *et al.*: J. Appl. Cryst. **45** (2012) 335.

X-ray diffraction patterns from flagellar axonemes of *Chlamydomonas*

Cilia and flagella are motile organelles found in various types of eukaryotes. Their scaffold, called the axoneme, is composed of nine doublet microtubules (doublets) surrounding a pair of singlet microtubules and forms highly regular arrays of such axonemal components on doublets as dynein arms and radial spokes [1]. Within the axoneme, dynein arms generate shear between adjacent doublets, and this shear is then converted into complex three-dimensional waveforms. The mechanism of this conversion has remained a long-standing unresolved issue. The investigation of this mechanism requires structural information at near-atomic-level resolution.

Because X-rays have such short wavelengths (approximately 0.1 nm), X-ray diffraction techniques can potentially reveal the structures of biomolecules or their assemblies at an atomic resolution. X-ray diffraction is particularly useful when the target molecules are periodically arranged because X-rays scattered by periodic arrays interfere with each other and generate strong signals. In addition, the high penetration of X-rays allows the technique to be applied to functioning natural structures in an aqueous environment. An axoneme with its highly arranged components is therefore a potentially suitable target for X-ray diffraction.

A useful model system for experiments on the structure and function of eukaryotic cilia and flagella is provided by a genus of green algae, *Chlamydomonas*, because of the high homology of axonemal components with humans and a large repertoire of axoneme mutants [2]. Using *Chlamydomonas*, we explored the spatial arrangement of axonemal components under physiological conditions by small angle X-ray fiber diffraction. The axonemes were oriented in a physiological solution by continuous shear flow and were exposed to intense and stable X-rays generated in the synchrotron radiation facility SPring-8 at beamline **BL45XU** [3].

Flow alignment of flagellar axonemes

We used the apparatus designed for the spatial arrangement of fibrous biological materials [4] to apply shear flow to a suspension containing flagellar axonemes of *Chlamydomonas*. The apparatus for shear flow alignment consisted of two round coverslips (diameter 17 mm) that faced each other across a small gap (0.1–0.35 mm) filled with a suspension of axonemes (Fig. 1). The suspension was held in place by surface tension. One of the coverslips remained stationary while the other was rotated by a motor. X-ray beams were directed at a point close to the edge of the coverslips where the shear rate was nearly at its greatest. The continuous shear flow at this point caused the axonemes to align with the shear.

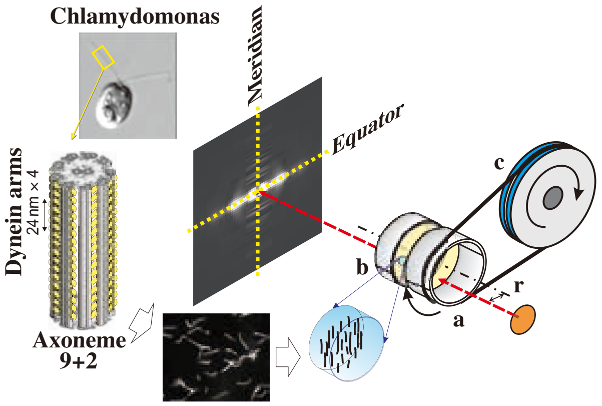

Fig. 1. Experimental system used for the shear flow alignment of axonemes of *Chlamydomonas*. The X-ray beam passes through an area 6 mm off the center (**r**) of a pair of tubes (**a** and **b**). The suspension of axonemes (2–5 mg/ml) is placed in the gap (0.1–0.35 mm) between the two parallel discs. The highlighted area schematically shows the alignment of axonemes under shear flow and in the beam. One of the discs (**a**) is rotated by a DC motor (**c**).

The diffraction pattern of the axonemes comprised two series of reflections: equatorial and meridional (Fig. 2). The very intense equatorial reflections occurred in the direction perpendicular to the longitudinal axes of the axonemes. The weaker meridional reflections were ladder-like reflections aligned along the meridian. When viewed along the meridian, the peaks of the meridional reflections were sharp and well-separated from each other and could be indexed to a basic axial repeat of 96 nm, which was the periodicity of the radial spokes and inner dynein arms. Although the first-order reflection at 1/96 nm^{-1} was too close to the beamstop and not clearly recognizable, reflections were observed up to the 12th (at 1/8 nm^{-1}, Fig. 2(a)) and 24th (at 1/4 nm^{-1}, Fig. 2(b)) orders. The diffusive layer-line reflections (4nm-LL arrow) were observed at 1/4 nm^{-1}; these were the first microtubule-based reflections.

Assignment of diffractions to axonemal components

The interpretation of signals in reciprocal space is not always straightforward and requires knowledge of the theory of diffraction, although the basic theory of diffraction from axonemes has been provided and the diffraction pattern of the axonemes has been calculated

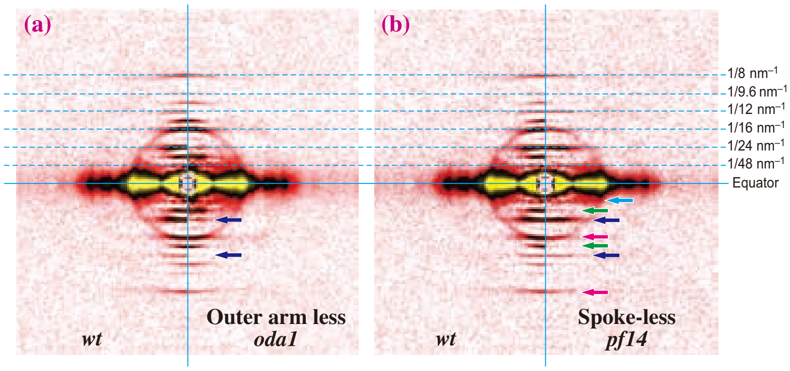

Fig. 3. Diffraction patterns from axonemes of wild-type and mutant strains of *Chlamydomonas* in the presence of 1 mM ATP and 100 μM vanadate. **(a)** Wild-type in the left half and *oda1* in the right half. Blue arrows: 4th and 8th (of 96 nm repeat) meridional reflections. **(b)** Wild-type in the left half and *pf14* in the right half. The meridional part of the second reflection (1/48 nm^{-1}, cyan arrow) becomes weaker in *pf14*, but its off-meridional part is clearly visible. Green arrows: 3rd and 7th meridional reflections. Magenta arrows: 6th and 12th meridional reflections.

[5]. We have taken an advantage of using axonemes of *Chlamydomonas* flagella, namely, the availability of a variety of mutants lacking specific axonemal components. The use of these mutants allows us to discuss directly the origin of observed reflections. We recorded diffraction patterns from axonemes of *oda1* (lacking the whole outer dynein arm) and *pf14* (lacking radial spokes). Diffraction patterns from mutant axonemes exhibited a systematic loss/attenuation of meridional/layer line reflections, making it possible to determine the origin of various reflections (Fig. 3).

The 1/24 and 1/12 nm^{-1} meridional reflections of *oda1* were much weaker than those of the wild-type (blue arrows in Fig. 3(a)), suggesting that the outer dynein arms were the main contributor to these reflections. The weaker 1/32 and 1/13.7 nm^{-1} meridional reflections from *pf14* (green arrows in Fig. 3(b)) compared with that from the wild-type suggested that these reflections mainly came from the radial spokes.

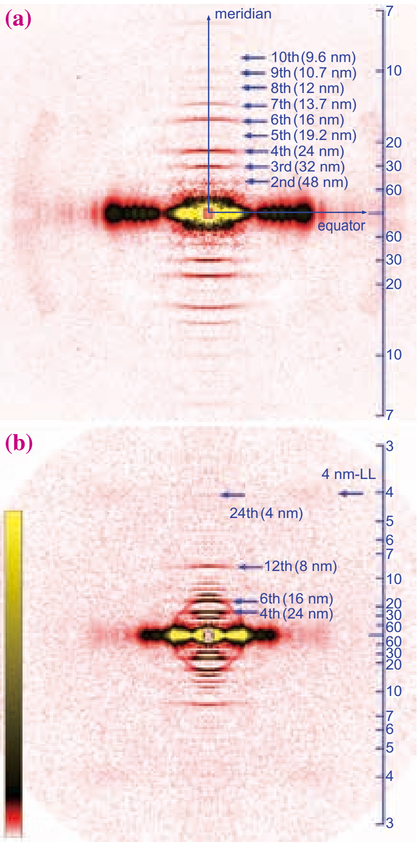

Fig. 2. Diffraction patterns from flow-oriented axonemes of wild-type *Chlamydomonas* flagella. **(a)** The pattern was recorded with a long specimen-to-detector distance (3.5 m) and a long X-ray wavelength (0.15 nm) (long-camera settings); sum of 50 frames (0.7 s exposure each). **(b)** The pattern was recorded with a short specimen-to-detector distance (2 m) and a short X-ray wavelength (0.09 nm) (short-camera settings); sum of 40 frames (0.8 s exposure each).

X-ray diffraction allows the extraction of structural information from unfixed biological materials that remain functional in an aqueous environment. Because of the noninvasive nature of the technique, dynamic or time-resolved measurements are possible, and the structures of a single axoneme sample can be compared before and after experimental intervention. This first detailed description of axoneme reflections presented here should serve as a basis for further X-ray diffraction studies to monitor the action of the constituent proteins in functional axonemes.

Shiori Toba[a,†] and Kazuhiro Oiwa[a,b,*]

[a] Advanced ICT Research Institute, National Institute of Information and Communications Technology
[b] Graduate School of Life Science, University of Hyogo

*E-mail: oiwa@nict.go.jp

[†] Present address: Department of Genetic Disease Research, Osaka City University Graduate School of Medicine

References

[1] T. Ishikawa: Cilia **4** (2015) 3.
[2] S.K. Dutcher: J. Eukaryot Microbiol. **47** (2000) 340.
[3] *S. Toba, H. Iwamoto, S. Kamimura and K. Oiwa: Biophys J.* ***108*** *(2015) 2843.*
[4] T. Sugiyama *et al*.: Biophys J. **97** (2009) 3132.
[5] H. Iwamoto *et al*.: Cell Motil Cytoskeleton **65** (2008) 563.

Imaging the airway surface to test Cystic Fibrosis treatments

The genetic condition Cystic Fibrosis affects the body in a number of ways, most devastatingly in the form of progressive early-fatal lung disease. This lung disease is largely caused by an inability to effectively clear inhaled debris and bacteria along the airway surface and out of the lungs. Key to this clearance is the airway surface liquid (ASL) that lines the airways at a depth of only a few microns, enabling cilia along the airway surface to beat in coordination, transporting mucus and debris away from the lungs. In Cystic Fibrosis, the ASL is dehydrated and decreased in depth, compromising these mechanisms. A variety of existing and new airway treatments aim to increase this ASL depth to reverse the defective transport processes, but it is difficult to verify treatment success *in vivo*. Some treatment testing is done using excised airway epithelium sections, or airway tissue cultures, but these do not completely model the state of the airway *in vivo*. Other tests examine changes in lung function, but these quantify overall lung health, and these measures typically do not change until several months after treatment delivery, meaning that treatment testing can be very slow and logistically difficult.

In this project, we developed and applied a non-invasive method of airway imaging to observe treatment-induced changes in the ASL depth in mouse airways in real time [1,2]. This new method enables immediate, quantitative and direct feedback on treatment effectiveness in airways while they are in normal operation within the body.

These measurements were enabled by phase contrast, a mode of X-ray imaging that reveals not only bone structure, but also details of soft tissue structures like the airways. This method analyses the phase of the X-ray wavefield and has been developed at high coherence synchrotron sources. Quantitative sample images can be reconstructed by relating variations in X-ray phase to the refractive properties of the sample. The significant difference in refractive properties between tissue and air means the air-filled lungs and airways are particularly suited to phase contrast X-ray imaging.

We utilized the high flux of the undulator synchrotron beamline **BL20XU** to capture short exposure image sequences of the airway surface in mice. In order to track micron-sized changes in the airway surface liquid depth, the selected field of view was 721 micron by 497 micron. To avoid blur from respiratory motion, exposures were only 100 ms long and image capture was synchronized to the end of expiration (the most stationary point of the breath cycle), achieved using a small animal ventilator. The mouse was anaesthetized during the experiment and its health was remotely monitored using temperature and ECG. In order to best reveal the details of the airway, fur was removed from the neck area surrounding the relevant airways.

We have also used this set-up to image the motion of inhaled particles along the surface of the airways [3]. For those experiments, we visualized the phase effects by introducing a distance of approximately 1 meter between the animal and the detector. This mode of phase contrast imaging is referred to as "propagation-based", and results in edge-enhancement at the air/tissue interfaces, as well as at the edges of any inhaled or resident particles.

While there is this strong edge enhancement seen at the air to liquid boundary, the ASL-tissue boundary is too subtle and is not visible in the propagation-based phase contrast image, as seen in Fig. 2(a). Therefore propagation-based phase contrast is not sufficiently sensitive to differentiate the airway surface liquid from the underlying tissue. In order to increase the sensitivity of the system, we introduced a fine grid immediately upstream of the mouse, as seen in Fig. 1. By tracking sample-induced distortions to the grid-and-airway image (Fig. 2(b)), we can extract a 'differential' contrast image (Fig. 2(c)). This differential image is more sensitive to subtle changes in the refractive index of the sample, and hence the ASL-tissue boundary can be located (Fig. 2(c)). This type of phase contrast imaging can be referred to as single-grid imaging and can use an absorption [4] or phase [5] grid, or a random phase object like a piece of paper, to provide a reference pattern at the detector.

Single-grid phase contrast X-ray imaging satisfies the requirements of this application in that it is both sufficiently sensitive to differentiate ASL from tissue and sufficiently fast to avoid image blur often present in a living animal. Importantly, only a single exposure is required to capture the relevant detail of the ASL depth. In comparison, some phase contrast techniques require multiple and/or long exposures to reconstruct an image, rendering them incompatible with respiratory motion and (non-repetitive) biological changes, present in this situation (and exaggerated with such a small field of view).

To measure ASL depth a reference image of the

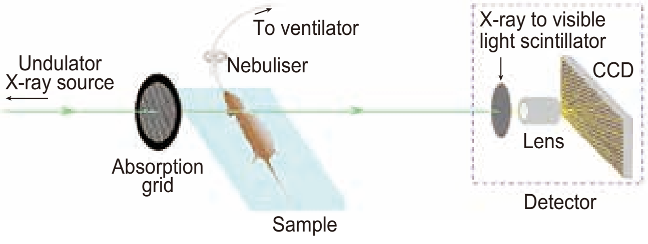

Fig. 1. Experimental setup.

grid was captured before the mouse was introduced to the field of view. Airway-and-grid images could then be locally compared to the reference grid-only image using a local cross-correlation to track how far each part of the image is transversely shifted due to the presence of the sample [4]. As seen in Fig. 2(b), these shifts are usually of the order of 0 to 8 pixels, hence the peak of the cross-correlation is interpolated to measure shifts with precision better than one pixel [5]. The magnitude of these shifts in a given direction is then plotted across the image to provide a differential image, as seen in Fig. 2(c) where shifts in the vertical direction are shown. The differential images can then be integrated together and scaled to give the total tissue thickness [4], shown in Fig. 2(c), which looks more like a conventional X-ray image.

Once the mouse was positioned in the X-ray beam, images were captured at time points separated by 3 min, with the first data point immediately prior to treatment delivery. The treatment, delivered as an aerosol, was a combination of 7% hypertonic saline (HS) and HS-P308, a long-acting epithelial sodium channel blocker (P308; Parion Sciences, Durham, NC) used at a concentration of 1 mM. The same volume of isotonic saline was used as a control. Ten images were taken at each time point to minimize variability and avoid problems with motion blur. ASL depth measurements were made by manually tracing both the tissue-to-ASL and ASL-to-air interfaces in the vertical differential contrast images (e.g., Fig. 2(c)), then measuring the distance between these traces in software, taking the average of all (roughly 3000) measurements along the length of the airway edge available in the image. Because the isotonic saline produced minimal changes, it was difficult to definitively measure the ASL depth in these images, hence the distance between the uppermost boundary of the cartilage and the ASL-to-air boundary was measured as an indicator of changes in ASL depth, as shown in Fig. 3(a). A statistically significant increase in surface position was observed for time points greater than 6 min from HS-P308 treatment delivery, with no return-to-normal observed within the imaging period ($p < 0.05$, repeated-measure ANOVA). There was also an increase in ASL depth noted at 9 and 12 min post-treatment-delivery, indicating treatment had been effective for that period.

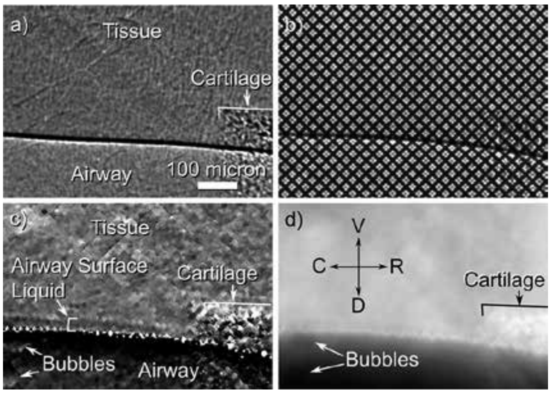

Fig. 2. **(a)** Propagation-based phase contrast X-ray imaging of the airway surface is not sufficiently sensitive to differentiate tissue from airway surface liquid. **(b)** When a grid is placed in front of the airway, sample-induced distortions can be tracked to recover **(c)** a differential image that shows the airway surface liquid. **(d)** The projected thickness of the airway can also be reconstructed, with reference directions shown as V=ventral, D=dorsal, C=caudal and R=cranial.

This imaging technique can now be used to test the effectiveness and duration of effect of new airway rehydrating treatments in animal models *in vivo*. Future studies will use repeat-imaging over extended periods of time in the same animals to assess long-term treatment effects [3], different animal models of CF to assess differences in treatment effect with disease, and will compare different methods of treatment delivery. None of these types of studies are possible with previous techniques used to measure the airway surface liquid.

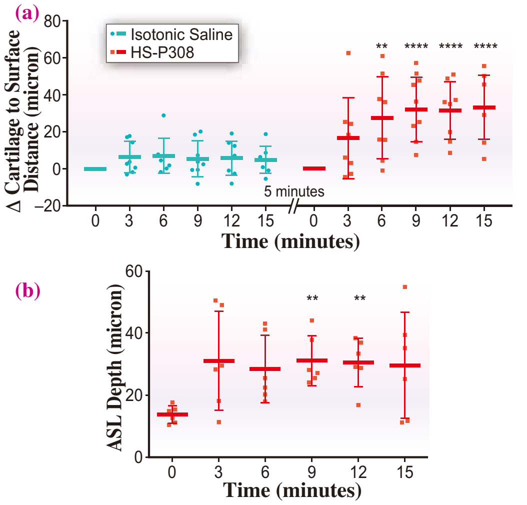

Fig. 3. Measurements of **(a)** airway surface position and **(b)** ASL depth, with stars indicating statistical significance (** indicates $p \leq 0.01$ and **** indicates $p \leq 0.0001$), with treatment delivered immediately after $t = 0$ minutes. Horizontal bars indicate mean measurement at that time point, with tails showing the standard deviation in measurements.

K. Morgan[a,b,*], M. Donnelley[c], D. Parsons[c] and K. Siu[a]

[a] School of Physics and Astronomy, Monash University, Australia
[b] Institute of Advanced Studies & Chair of Biomedical Physics, Technische Universität München, Germany
[c] Women's and Children's Hospital, North Adelaide & Robinson Institute, University of Adelaide, Australia

*E-mail: kayemorgan7@gmail.com

References

[1] *K.S. Morgan, M. Donnelley, N. Farrow, A. Fouras, N. Yagi, Y. Suzuki, A. Takeuchi, K. Uesugi, R. Boucher, K. Siu, D. Parsons: Am. J. Resp. Crit. Care Med.* ***190*** *(2014) 469.*
[2] K.S. Morgan *et al.*: PLoS ONE **8** (2013) e55822.
[3] M. Donnelley *et al.*: J. Synchrotron Rad. **21** (2014) 768.
[4] K.S. Morgan *et al.*: Opt. Express **19** (2011)19781.
[5] K.S. Morgan *et al.*: Opt. Lett. **38** (2013) 4605.

Distribution analyses of trace metallic elements in oral mucosal tissues using high-energy SR-XRF

Various noble and base metal alloys are used for dental restoration. Even dental alloys, which have high corrosion resistance, undergo slight dissolution of the alloy elements. The eroded metallic elements cause the acute, chronic, and allergic reactions. Therefore, the detection and analysis of the distribution and chemical state of trace metallic elements in the oral mucosa or surrounding tissues are necessary to reveal the relationship between the dissolved metallic elements and histopathological changes. However, because the concentration of such eroded metallic elements in the oral mucosa is quite low, a highly sensitive analytical method is required. In addition, biopsy specimens have limited availability and mainly are required for histopathological diagnosis. Therefore, analysis of the elements should be carried out nondestructively. The author's group have applied the synchrotron radiation X-ray fluorescence (SR-XRF) analysis to detect trace metallic elements in various biomedical specimens [1-5].

Silver-based alloys (Ag-Pd-Au-Cu alloy, Ag-In-Sn-Zn alloy) are widely used for metallic dental restoration in Japan. To detect the K lines of Pd, Ag, In, and Sn, high energy (>25 keV) incident X-rays are required. Beamline **BL37XU** in SPring-8 provides high energy X-rays with high flux, enabling the detection of trace alloy elements used in dental restoration. Oral mucosal tissue was fixed in formalin, embedded in paraffin and thinly sliced. The slice was mounted on polyimide film (Kapton®, 12.5 μm*t*) and analyzed using SR-XRF at BL37XU. The incident X-rays (30 keV) were focused into $2 \times 4\,\mu m^2$ and the specimen was scanned in the X-Y direction to obtain two-dimensional elemental distribution images. The scanning steps were varied from 5 μm to 50 μm depending on the scanning area.

Figure 1 shows typical images of elemental distribution in the oral mucosa and histopathological images obtained with hematoxylin-eosin (H-E) staining. Accumulated spots of Zn, Cu, and Ag were observed inside the mucosa. Figure 2 shows the detailed distribution images of the white rectangular region in Fig. 1. Localization of Ag and Pd could be observed in narrow vicinal regions. The XRF spectrum at the localized spots of these elements (white arrow in Fig. 2) is shown in Fig. 3. Clear peaks due to Ag, Pd, Au, Zn, and Cu can be identified. Zn and Cu are essential trace elements in the human body, while Ag, Pd, and Au are not endogenous elements in the mucosa. This mucosa was derived from an oral lichenoid lesion (OLL). An OLL is one of the commonly observed oral mucosal diseases, and the eroded metallic elements from dental restoration are suspected to be one of the causal factors of OLL. Ag-Au-Pd-Cu alloy is most commonly used for dental metallic restoration in Japan. Therefore, the elements detected in the mucosa are suspected to derive from the dental metallic restoration. Including this case, the authors analyzed six OLL tissues using SR-XRF, and the accumulation of dental alloy elements was detected in all the tissues [3,4].

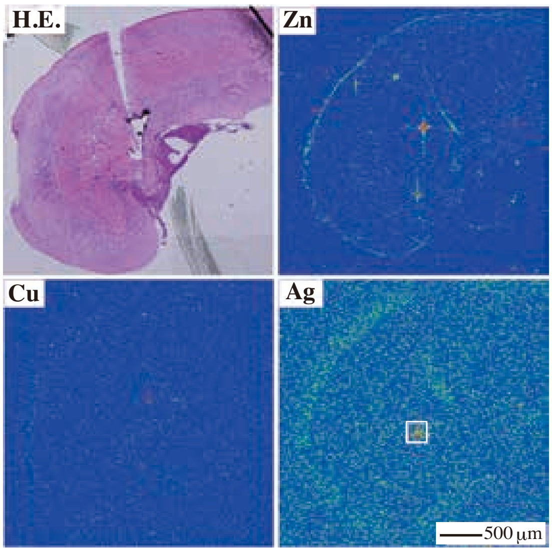

Fig. 1. H-E stained histopathological image and SR-XRF elemental distribution images of OLL specimen.

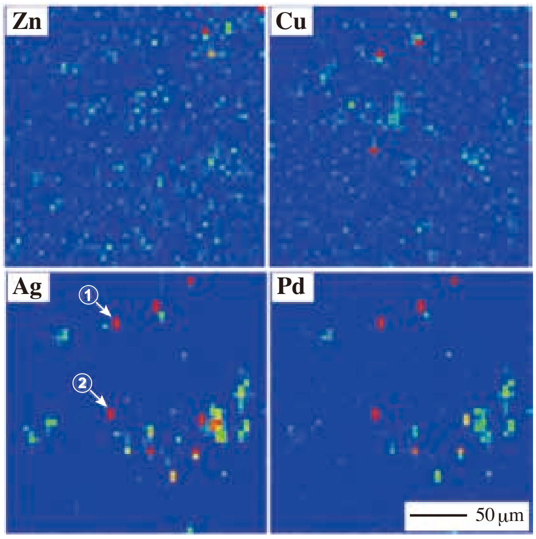

Fig. 2. Detailed elemental distribution images of the white rectangular region in Fig. 1.

In current diagnosis of eroded metal related symptoms (e.g., metal allergy and OLL), causal metal species are predicted by the skin patch test using various metal salt solutions. However, patch tests are not reliable because of their false positive/negative reactions. The identification of causal metallic elements by SR-XRF analysis would provide more reliable information and could be used to prescribe the removal of the causative restoration; this is a simple and innovative treatment. In addition, the author's group applied SR-XRF to the estimation of metallic ion penetration into skin and the development of a novel metal allergy patch test using metal nanoparticles [1]. Thus, SR-XRF analysis of biomedical specimens will provide useful information concerning the effects of trace metallic elements in various tissues.

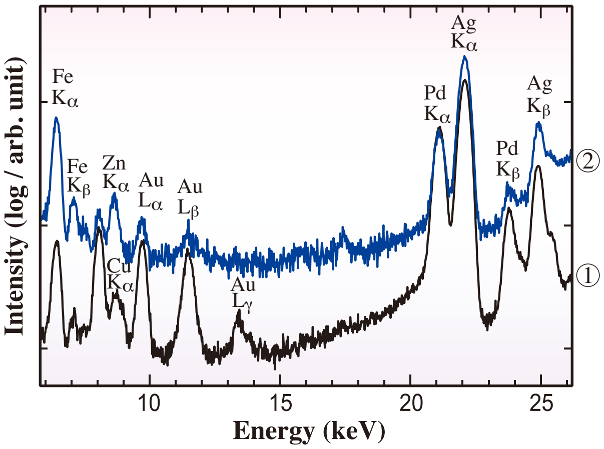

Fig. 3. Fluorescence X-ray spectra of the spots marked by the arrows in Fig. 2.

Motohiro Uo[a,b]

[a] Advanced Biomaterials Department, Tokyo Medical and Dental University
[b] Department of Materials Engineering, The University of Tokyo

E-mail: uo.abm@tmd.ac.jp

References

[1] T. Sugiyama *et al.*: J. Nanobiotechnology **12** (2014) 1.
[2] M. Uo *et al.*: Jpn. Dent. Sci. Rev. **51** (2015) 2.
[3] T. Sugiyama *et al.*: Biometals **28** (2015) 11.
[4] *T. Sugiyama, M. Uo, T. Wada, D. Omagari, K. Komiyama, S. Miyazaki, C. Numako, T. Noguchi, Y. Jinbu, M. Kusama and Y. Mori: Sci. Rep.* **5** *(2015) 1.*
[5] T. Sugiyama *et al.*: Bone Rep. **3** (2015) 40.

Structural mouthpart interaction evolved already in the earliest lineages of insects

Hexapoda (insects in the broad sense) evolved an astonishing diversity of mouthparts tailored to use different resources of food. For example, dragonflies and crickets use biting-chewing motions of their mandibles to chop food particles, true bugs evolved piercing-sucking mouthparts to suck fluids from plants, flies evolved sponging mouthparts, and moths and butterflies evolved the unique proboscis to siphon mostly nectar of flowers [1,2]. Although mouthparts *functionally* interact in nearly all insects to process food, many winged insects evolved a *structural* interaction resulting in the formation of new mouthpart types [1]. Corresponding structural changes are radical and morphologically very different to each other, a comparable diversity and complexity of mouthparts is not present in any other arthropod group. It is unclear when this major trend in insect evolution – structural mouthpart interaction (SMI) – evolved for the first time.

In order to assess this question, we used synchrotron μCT (SR-μCT) imaging setups to investigate the mouthpart anatomy of Collembola and Diplura - ancient, tiny, soil-living insects. High resolution SR-μCT was done at the beamline **BL47XU** using a stable beam energy of 8 keV in absorption-contrast mode. The tomography system consists of a full field X-ray microscope with Fresnel zone plate optics. The field of view and the effective pixel size are 0.11 mm × 0.11 mm and 82.6 nm × 82.6 nm, respectively.

Collembolan and dipluran mouthparts show a specific and unusual type of SMI, based on an articulatory point between the mandible and the maxilla [3]. In Diplura, the contact point is formed by an articulatory stud of the maxillary stipes ("STST"; Fig. 1(a,b)). This stud is a short, upraised prominence, and is supported by two internal stipital strengthening ridges. The dorsal ridge originates at the base of the stud and extends along the inner stipital wall to fuse with the ventral stipital ridge [3]. The tip of the stud is in contact with a slight concavity at the posterior outer wall of the mandible [3].

The newly found SMI in Collembola also is composed of a stipital stud (STST) that originates at the median anterior (dorsal) wall of the stipes (Fig. 1(c,d)). As in Diplura, this stud is supported by two strengthening ridges, one spanning from the base of the stud to the opposite side of the maxillary stipes where it fuses with the second strengthening ridge [3].

The stipital studs of the maxillae in Collembola

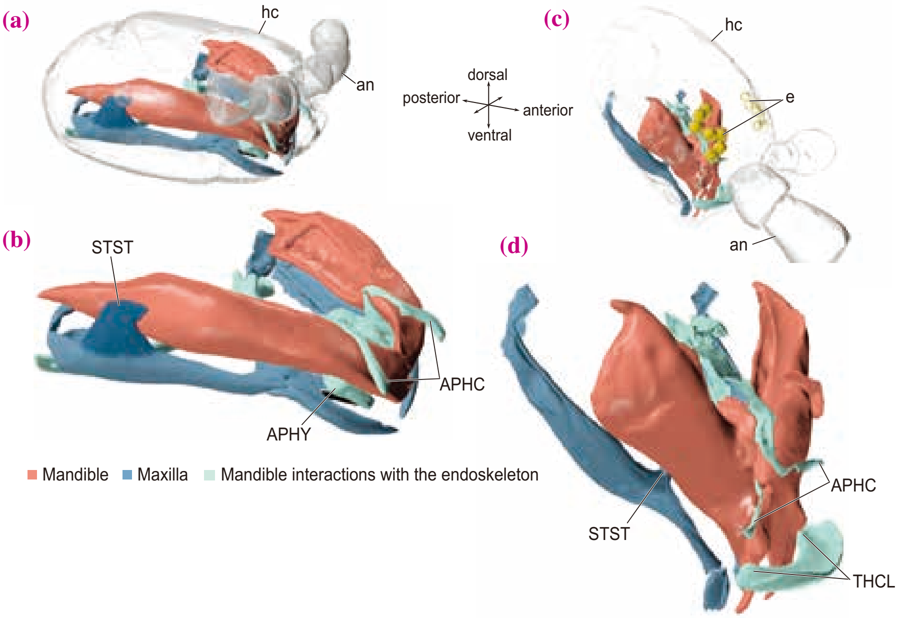

Fig. 1. Overview of dipluran and collembolan mouthpart organisation illustrated with 3D reconstructions of SR-μCT data. **(a)** Dorsolateral view of a dipluran to indicate the location of the mandible-maxilla hypopharynx complex in the head capsule. **(b)** Same as (a) with head capsule removed. Note the stipital stud (STST) embracing the posterior part of the mandible and the apodemes of head capsule (APHC) and hypopharynx (APHY) embracing the anterior inner part of the mandible. **(c)** Dorsolateral overview of the mouthpart location within the collembolan head. **(d)** Same as in (c) with head capsule removed. Note the stipital stud (STST) contacting the mandible to prevent posterior sheering out of the mandible. The thickening of the clypeus (THCL) prevents lateral sheering out of the mandibles, while the apodemes of head capsule (APHC) and hypopharynx (APHY, not shown) embrace the anterior inner part of the mandibles just like in Diplura. Additional abbreviations: an, antenna; e, eye; hc, head capsule.

and Diplura are most probably homologous [3]. In both groups, these articulatory studs are located on the dorsal side of the stipes and are supported by a conspicuous configuration of two strengthening ridges at the inner side of the stipes that show the same arrangement. These ridges reinforce the stipital studs to counter loads imposed on the maxilla during mandible movement. The two modes of mandible-maxilla interaction in Collembola and Diplura are thus the first examples of a structural mouthpart interaction in ancestrally wingless insects.

This result has important implications for our understanding of insect mouthpart evolution (Fig. 2). The presence of a homologous SMI in Collembola and Diplura implies the presence of this basic principle in stemgroup representatives of the entire Hexapoda (insects in the widest sense; Fig. 2). It remains unclear until which point SMIs are exhibited in the stemline of early insects before this principle occurs again in more derived winged insects (Fig. 2). However, the biting-chewing mouthpart type with mandibles connected to the head via articulations, as shown in jumping bristletails, can no longer be attributed as the plesiomorphic condition in insects [3]. Rather, we suggest that a "light" form of entognathy with an enlarged subgenal area, probably overgrowing the mouthparts laterally to some extend, might be ancestral. In this scenario, the mouthparts probably already interacted with each other due to some form of structural coupling. Exposed (Ectognathous), structurally uncoupled mouthparts are a derived groundplan feature of silverfish and winged insects.

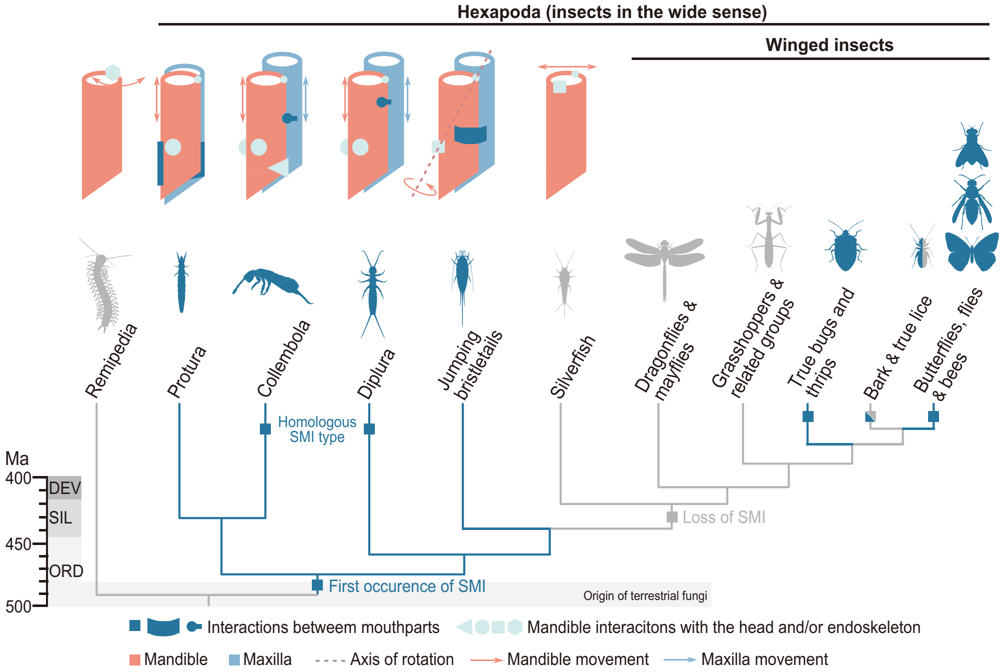

Fig. 2. Evolution of structural mouthpart interactions in insects mapped on a transcriptome based phylogenetic tree and divergence time estimate [4]. Shapes of mouthparts and articulation points are shown as simplified models, mandible and maxilla movements with red and blue arrows respectively. Note that the same forms of interaction points indicate putative homologous structures across taxa. Also note the differing SMI solutions to achieve mandible stabilization during food uptake in Protura, Collembola, Diplura and jumping bristletails. The common ancestor of insects (Hexapoda) most probably already possessed a mandible-maxilla SMI. The occurrence of SMI can be correlated with the origin of fungi during the Ordovician, one of the principal diets of recent Collembola and Protura. In bristletails, an anterior mandibular articulation (dicondyly) evolved, which made other supporting or stabilizing structures obsolete during the further evolution of dicondyly in silverfish and winged insects. Structural mouthpart interaction again occurs in extant true bugs and thrips, lice, and large parts of bees, butterflies and flies, where parts of the mouthparts function as guiding structures for other mouthparts or even fuse together. The occurrence of these new mouthpart types again can be correlated with the evolution of food sources such as diverse plant and animal fluids.

Alexander Blanke[a,*] and Ryuichiro Machida[b]

[a] School of Engineering, University of Hull, UK
[b] Sugadaira Montane Research Center,
University of Tsukuba

*E-mail: a.blanke@hull.ac.uk

References

[1] D. Grimaldi and M.S. Engel: Evolution of the Insects (Cambridge University Press, 2005)
[2] C.C. Labandeira: Annu. Rev. Ecol. Syst. **28** (1997) 153.
[3] *A. Blanke, P.T. Rühr, R. Mokso, P. Villanueva, F. Wilde, M. Stampanoni, K. Uesugi, R. Machida, B. Misof: Proc. R. Soc. B* ***282*** *(2015) 20151033.*
[4] B. Misof *et al.*: Science **346** (2014) 763.

Ferromagnetically coupled stellated cuboctahedral spin nanocage

The self-assembly of small molecular “building blocks” into ordered polyhedral structures, inspired by biological systems, is a highly attractive prospect [1]. In particular, metal-organic polyhedra, discrete molecular architectures constructed through the coordination of metal ions and organic ligands, have recently attracted attention owing to their potential for a variety of applications, such as gas storage, guest recognition, delivery, and catalysis [2]. Here, we introduce our recent study of a synthetic metal-organic spin polyhedron with a nanosized discrete molecular architecture and a cyanide-bridged magnetic Fe_{42} nanocage comprising 18 high-spin Fe^{III} ions and 24 low-spin Fe^{II} ions [3]. An important characteristic of the polyhedron is that it is a mixed-valent $Fe^{III}{}_{18}Fe^{II}{}_{24}$ compound and contains 18 ferromagnetically coupled Fe^{III}($S = 5/2$) ions as vertices, yielding the highest ground state spin number ($S = 45$) of any molecule ever prepared.

Green single crystals of $[\{Fe^{II\text{-}LS}(Tp)(CN)_3\}_{24}\{Fe^{III\text{-}HS}(H_2O)_2\}_6\{Fe^{III\text{-}HS}(dpp)(H_2O)\}_{12}(CF_3SO_3)_6]\cdot 18H_2O$ (**1**$\cdot 18H_2O$; LS = low-spin, HS = high-spin, Tp = hydrotris(pyrazolyl)borate, dpp = 1,3-di(4-pyridyl)propane) were obtained by the reaction of $Fe(CF_3SO_3)_2$, dpp, L-ascorbic acid, and $Li[Fe(Tp)(CN)_3]$ in H_2O. The crystal structure revealed by synchrotron radiation at beamline **BL02B1** in collaboration with Dr. Kunihisa Sugimoto (JASRI) is shown in Fig. 1. Each octahedral $\{Fe(Tp)(CN)_3\}$ unit is connected to three Fe ions by three cyanide anions. The Fe ions are further ligated with water and dpp to obtain octahedral $\{Fe(NC)_4(H_2O)_2\}$ and $\{Fe(NC)_4(dpp)(H_2O)\}$ coordination spheres, where the Fe centers are in a weakly distorted octahedral environment with axial water molecules. Thus, 24 $\{Fe(Tp)(CN)_3\}$, 12 $\{Fe(NC)_4(dpp)(H_2O)\}$, and 6 $\{Fe(NC)_4(H_2O)_2\}$ building units are symmetrically formed in an octahedral (cubic) symmetry space around a central point, providing the cube cage with a separation of 1.96 nm between the most distant Fe ions.

Moreover, the 18 $Fe^{III\text{-}HS}$ ions in compound **1** can be identified as the vertices of a highly symmetric entity known as a stellated cuboctahedron (Fig. 2). Namely, 12 Fe^{III} centers in $\{Fe(NC)_4(dpp)(H_2O)\}$ units are defined as the vertices of the cuboctahedron, all sides of which are 7.85 Å long. Six square windows of the cuboctahedron are stellated with 24 isosceles triangles, each having side lengths of 6.83, 6.83, and 7.85 Å, whose six vertices are defined by Fe^{III} ions in the $\{Fe(NC)_4(H_2O)_2\}$ units. To date, only one stellated metal-organic polyhedron with metal ion vertices, i.e., diamagnetic $Pd_{18}L_{24}$ stellated cuboctahedron, has been reported [4]. On the other hand, the $[Fe^{III}{}_{18}Fe^{II}{}_{24}]$ stellated cuboctahedron consists of Fe^{III} metal spin centers as vertices with tridentate cyanide complex ligands, $[Fe(Tp)(CN)_3]$, as opposed to organic tripyridyl ligands; thus, compound **1** is the first example of a

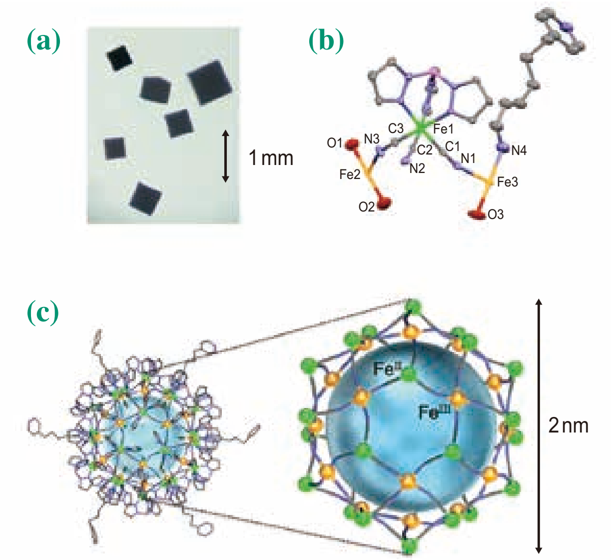

Fig. 1. **(a)** Photo of cubic crystals consisting of Fe_{42} metal-organic polyhedra. **(b)** Asymmetric unit of Fe_{42} metal-organic polyhedra with thermal ellipsoids at 30% probability. Hydrogen atoms, counterions, and solvent molecules are omitted for clarity. **(c)** Molecular structure of an Fe_{42} nanocluster molecule clarified at beamline BL02B1 by single-crystal structure analysis. Fe^{II} and Fe^{III} atoms are shown as green and orange spheres, respectively.

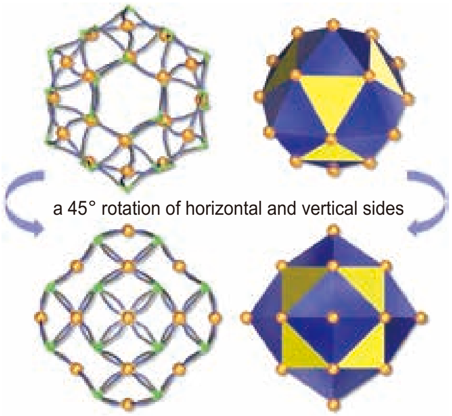

Fig. 2. Schematic view of the stellated cuboctahedron formed by eighteen trivalent iron atoms ($Fe^{III\text{-}HS}$: orange spheres) bearing magnetism. All face-center positions of square faces in the yellow cuboctahedron are capped to have blue stellation, showing beautiful and high symmetry of molecular shape.

stellated metal-organic spin polyhedron.

The magnetic properties of compound **1** indicate the existence of predominantly ferromagnetic interactions. The magnetization data in the range of 300–30 K can be fitted to the Curie–Weiss law, yielding C = 83.2 cm^{3}mol^{-1}K and θ = 6.7 K. The magnetization (M) at 2 K immediately increases at low fields, and then steadily increases with $H > 15$ kOe to reach a near saturation value of 88.4 μ_B at 50 kOe (Fig. 3), which is in good agreement with the expected value of 90 μ_B (with g = 2.0) for a ground state of S_T = 90/2. This magnetization behavior is significantly higher than the Brillouin curve corresponding to 18 non-interacting S_{Fe} spins (S = 5/2), but fits with the Brillouin curve for one S = 45 center (with g = 2.0). These data support the maximum spin state possible, S = 45, which is the largest spin ground state number of any molecule ever prepared. Nowadays, competitive research studies are conducted in the field of molecular magnetism, with the aim to artificially generate magnetic molecules with huge spins as nanoscale permanent magnets. Our findings will provide a deeper understanding of the magnetic behavior on the intermediate scale between molecular and bulk objects.

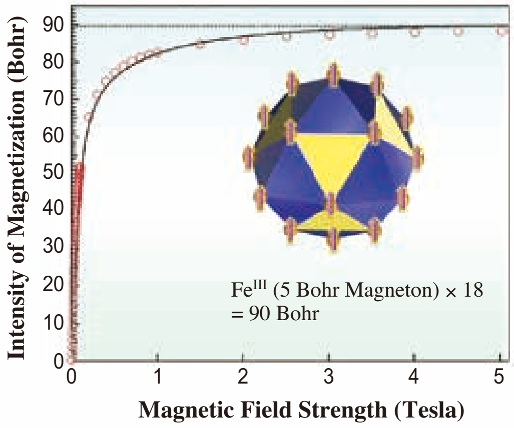

Fig. 3. Magnetic characteristics of the Fe_{42} metal-organic spin polyhedron and schematic arrangement of atomic magnets. Upward arrows indicate atomic magnets. Red circles are experimental values and the black curve is a theoretical prediction, which show a good agreement.

Soonchul Kang and Osamu Sato*

Institute for Materials Chemistry and Engineering,
Kyushu University

*E-mail: sato@cm.kyushu-u.ac.jp

References

[1] P.F. Damascene *et al.*: Science **337** (2012) 453.
[2] D.J. Tranchemontagne *et al.*: Angew. Chem. Int. Ed. **47** (2008) 5136.
[3] *S. Kang, H. Zheng, T. Liu, K. Hamachi, S. Kanegawa, K. Sugimoto, Y. Shiota, S. Hayami, M. Mito, T. Nakamura, M. Nakano, M.L. Baker, H. Nojiri, K. Yoshizawa, C. Duan and O. Sato: Nat. Commun.* ***6*** *(2015) 5955.*
[4] Q.-F. Sun *et al.*: Nat. Chem. **4** (2012) 330.

Imaging and controlling all-in/all-out magnetic domains in pyrochlores

The pyrochlore lattice can be described as a cubic lattice of tetrahedra, joined by shared vertices (Fig. 1(a,b)). In the compounds $A_2B_2O_7$ of interest, magnetic ions B are located at these vertices and it is impossible to satisfy all their interactions if the exchange is antiferromagnetic. As a result, several magnetic states may co-exist at the same energy. One particular case is the so-called "all-in/all-out" magnetic structure: in the presence of uniaxial magnetic anisotropy along <111> all the magnetic moments on the vertices of a given tetrahedron will point either towards the center or away from it. Consequently, if one sets the orientation of a given magnetic moment, the orientation of all the others is decided. Therefore only two different states – corresponding to the two choices for the original orientation – can describe the magnetic structure: all-in/all-out (AIAO) or all-out/all-in (AOAI) as shown in Fig. 1 [1]. The AIAO and AOAI states are time-reversal symmetric of each other, which we may define as opposite *pseudo-orientation*. They can also be described as differently oriented zinc-blende crystals of magnetic hedgehog monopoles (Fig.1(c)) or face-centered crystals of magnetic octupoles. They are thus expected to host unconventional opposite magnetic behaviors [2], such as opposite linear magnetostriction, opposite linear magneto-capacitance or opposite quadratic terms in the magnetization. Suitable experimental means to image and control the AIAO and AOAI magnetic domains are therefore much needed.

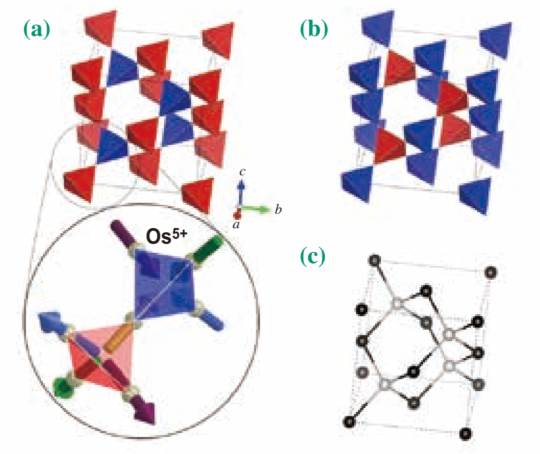

Fig. 1. **(a)** All-in/all-out and **(b)** all-out/all-in magnetic order on the pyrochlore lattice; both configurations are time-reversal symmetric of each other. All Os spins are located at the vertices of the tetrahedra and point either towards the center of the blue tetrahedra or away from the center of the red tetrahedra, as shown in the magnified region. **(c)** Equivalent zinc-blende lattice [1].

In this work, we experimentally investigated the compound $Cd_2Os_2O_7$: the AIAO ordering of the spins of the $5d^3$ Os^{5+} ions was previously reported below $T_N = 225$ K [3], along with a continuous metal-insulator transition [4]. In order to distinguish the AIAO order from the AOAI, i.e. to measure the *pseudo-orientation*, we performed polarized resonant X-ray microdiffraction at beamline **BL19LXU**. The structure factor of space-group forbidden $0\ 0\ 4n+2$ Bragg reflections at the Os L_3 resonance (10.871 keV) is the sum of two components: a non-magnetic part due to the anisotropic tensor of susceptibility (ATS) and the screw axis along c, F_{ATS}; and a magnetic part due to the spin order, F_m. The diffracted intensity results from the interference of these two components. The key point is that the sign of F_m is opposite in AIAO and AOAI while that of F_{ATS} is constant. Since both F_{ATS} and F_m are polarization-dependent, we defined the contrast in diffraction for right-handed (I^+) and left-handed (I^-) circular polarization as the flipping ratio $FR = (I^+ - I^-)/(I^+ + I^-)$. We demonstrated that the sign of FR is opposite in opposite types of domains, which could be used to distinguish AIAO from AOAI. The FR was measured experimentally using a diamond phase plate upstream of the sample to control the handedness of the incident beam. A pair of Kirkpatrick-Baez mirrors was used to focus the X-ray beam to a 500 × 500 nm² spot on the sample, which was raster scanned.

The resulting maps measured over the (001) and {001} adjacent facets of the sample are shown in Fig. 2(a-f). Stripe-like patterns of opposite FR sign were observed, indicating the coexistence of AIAO and AOAI domains within the same crystal. The typical size of the magnetic domains was a few tens of microns. We note that these results are the first experimental imaging of AIAO and AOAI magnetic domains in the pyrochlore lattice. At the interface between opposite magnetic domains, magnetic domain walls (DW) could be observed. From the analysis of the DW orientations on the different facets, we could suggest two families of planes for the DW: {(113), $(11\bar{3})$, $(1\bar{1}3)$, $(\bar{1}13)$ and circular *hkl* permutations}, and {(011), $(01\bar{1})$ and circular *hkl* permutations}. The observation of DW is consistent with other experimental measurements, such as the finite conductivity at low temperature (attributed to transport along the DW) and the remnant magnetization below the antiferromagnetic ordering temperature (attributed to magnetic ordering of the frustrated spins in the DW).

Finally we showed that we could control the

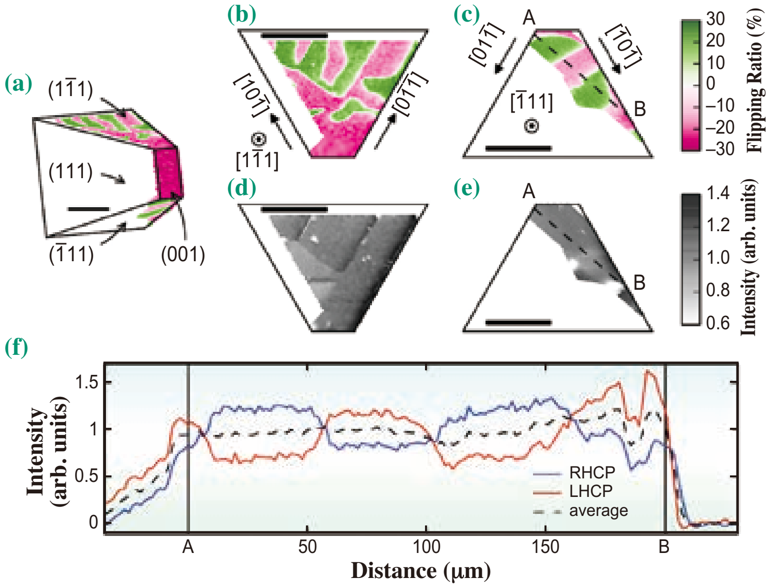

Fig. 2. **(a)** FR map at the 0 0 10 reflection, as measured experimentally by rastering the sample in a plane perpendicular to the scattering vector. The ideal crystal is outlined and the orientation of the facets is shown. Opposite signs of the FR indicate opposite pseudo-orientations of the magnetic domains (AIAO *vs* AOAI). **(b, c)** FR maps and **(d, e)** normalized intensity on the top (1 $\bar{1}$ 1) and bottom ($\bar{1}$ 1 1) facets after correction of the projection, respectively. The intensity is normalized to the average value on each facet to outline the deviation from the average structure. All scale bars are 100 mm across. **(f)** Line scan across the bottom ($\bar{1}$ 1 1) facet, indicated by the AB dashed line in **(c, e)**, for both right- and left-handed circular polarization and their average [1].

orientation of the AIAO and AOAI domains by using a magnetic field-cooling procedure and orienting the field along a <111> direction. We showed that using a double magnets setup we could reverse the domain distribution by reversing the direction of the magnetic field while cooling through T_N, as illustrated in Fig. 3. The possible origins of the coupling to the external field are the domain-dependent piezomagnetism and non-linear magnetization mentioned earlier, as well as the presence of uncompensated spins on the {111} facets.

Our results show that AIAO/AOAI magnetic domains can be measured in real space and their distribution controlled. This paves the way for future investigation of pyrochlore lattices with all-in/all-out magnetic ordering.

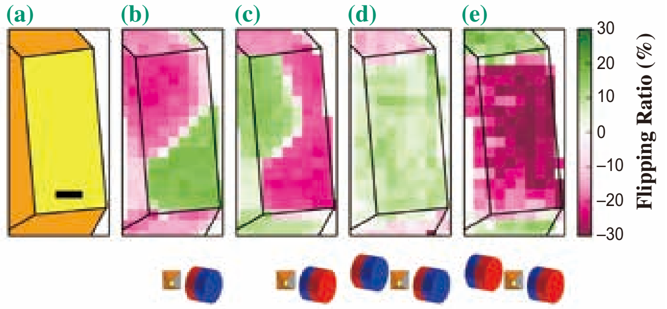

Fig. 3. **(a)** Sketch of the sample view in the geometry used, the central rectangle is the (0 0 1) facet. The scale bar is 25 mm across. **(b–e)** Maps of the FR across the sample at the 0 0 10 reflection at 100 K for different field cooling conditions, as sketched in the lower panels. The North pole of the cylindrical permanent magnets is indicated in red, the magnetic field at the surface of the magnets is 0.4 T. The surface of the magnet is also parallel to the ($\bar{1}$ $\bar{1}$ 1) facet, indicated in light grey in the sketch [1].

Samuel Tardif[a,b]

[a] Université Grenoble Alpes, INAC-MEM, France
[b] CEA, INAC-MEM, France

E-mail: samuel.tardif@gmail.com

References

[1] *S. Tardif, S. Takeshita, H. Ohsumi, J. Yamaura, D. Okuyama, Z. Hiroi, M. Takata and T. Arima: Phys. Rev. Lett.* ***114*** *(2015) 147205.*
[2] T. Arima: J. Phys. Soc. Japan **82** (2013) 013705.
[3] J. Yamaura *et al.*: Phys. Rev. Lett. **108** (2012) 247205.
[4] A. Sleight *et al.*: Solid State Commun. **14** (1974) 357.

Competition and collaboration between magnetism and superconductivity: Electronic structures of ferromagnetic superconductors UGe_2, URhGe, and UCoGe

Superconductivity is one of the most fascinating platforms for condensed matter physicists. The superconducting state is a significant quantum-mechanical phenomenon, and it can be observed macroscopically. Furthermore, its fundamental understanding is required subject for its technological applications such as superefficient electrical-transport systems and ultrahigh-speed maglevs. Conventionally, magnetic fields and magnetism have been considered as enemies of superconductivity: for example, a high magnetic field simply suppresses superconducting states in most superconductors. This stereotype has been defied in recent years by the discovery of some rare-earth and actinide compounds that exhibit coexisting magnetic ordering and superconductivity. In particular, the discovery of ferromagnetic superconductors in some uranium-based compounds motivated us to reconsider the relationship between magnetism and superconductivity [1].

In the present study, we have revealed the electronic structures of the uranium-based ferromagnetic superconductors UGe_2, UCoGe, [2] and URhGe [3] by angle-resolved photoelectron spectroscopy (ARPES) by using soft X-rays at beamline **BL23SU**. We found that U 5*f* electrons in these compounds have an essentially itinerant character, and they exhibit both ferromagnetic orderings and superconducting states. These results further infer that the magnetic instability might be a possible glue of superconducting electrons, which are referred to as Cooper pairs. Magnetism and superconductivity are not enemies and help each other in these compounds.

Figure 1 shows the crystal structures of UGe_2, URhGe, and UCoGe. UGe_2 has a body-centered orthorhombic structure while URhGe and UCoGe have a simple orthorhombic structure. An interesting point is that they have similar zigzag chains of uranium atoms, and these characteristic structures are considered to be the origin of their unique physical properties. Although it is generally believed that the U 5*f* electrons in these compounds have itinerant characters, other scenarios such as a completely localized model or the dualism of U 5*f* states have also been proposed. ARPES is one of the most powerful experimental methods for revealing the electronic structures of solids. In particular ARPES with soft X-ray synchrotron radiation is suitable for studying the bulk electronic structures of U 5*f* states.

Figure 2 summarizes the ARPES spectra and the results of the band structure calculations of UGe_2, URhGe, and UCoGe [2-4]. Their overall band structures and the results of the band calculations in an energy scale of a few electronvolts are shown in Figs. 2(a, b, c). All samples are in paramagnetic phases. Contributions from U 5*f* states exist in the vicinity of E_F. They exhibit strong momentum dependences, suggesting that they form itinerant quasi-particle bands in these compounds. In the spectra of URhGe and UCoGe, Rh 4*d* or Co 3*d* bands exist on the high-binding-energy side, which have finite hybridizations with U 5*f* states. There are some good correspondences between the experimental ARPES spectra and the results of the band structure calculation.

Figures 2(d, e, f) show the electronic structures and the results of band structure calculations in the vicinity of E_F. The spectra have been divided by the Fermi-Dirac function convoluted by the instrumental

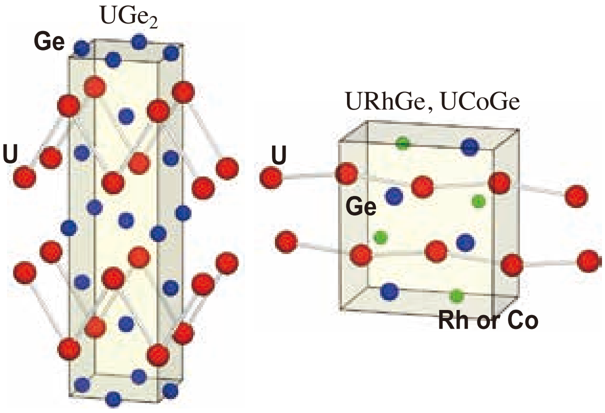

Fig. 1. Crystal structures of UGe_2, URhGe, and UCoGe.

energy resolution to show the states at E_F more clearly. These electronic structures in the vicinity of E_F have a particular importance since they govern their Fermi surfaces, which determine the transport properties of materials. The comparison between ARPES spectra and their simulations based on the band structure calculations exhibits both agreement and disagreement. In particular, the electronic structures just below E_F exhibit very complicated behaviors in both the experiments and calculations, and the agreement is not as good as in the cases of band structures in an energy scale of eV order. Figures 2(g, h, i) show the Fermi surfaces of these compounds obtained by the band structure calculations. They have very complicated three-dimensional shapes. This is due to the low-symmetry nature of their crystal structures, which removes the degeneracies of bands. On the other hand, the experimental band structures in the vicinity of E_F exhibit considerable deviation from the calculation. This suggests that the shapes of the Fermi surfaces of these compounds are qualitatively different from the results of calculations, possibly due to the finite electron correlation effect in the complicated band structures of the low-symmetry crystals.

All these results suggest that band structure calculations with all U 5*f* electrons treated as being itinerant are a good starting point to describe their overall electronic structures, but the topologies of their Fermi surfaces are considerably different from those obtained by calculations. The possible origins of these discrepancies are the very complicated band structures of these compounds due to the low-symmetry nature of their crystal structures and the weak but finite contributions from the electron correlation effect. To account for the contributions from the electron correlation effect, it is essential to include the dynamical nature of U 5*f* electrons in the low-symmetry crystals.

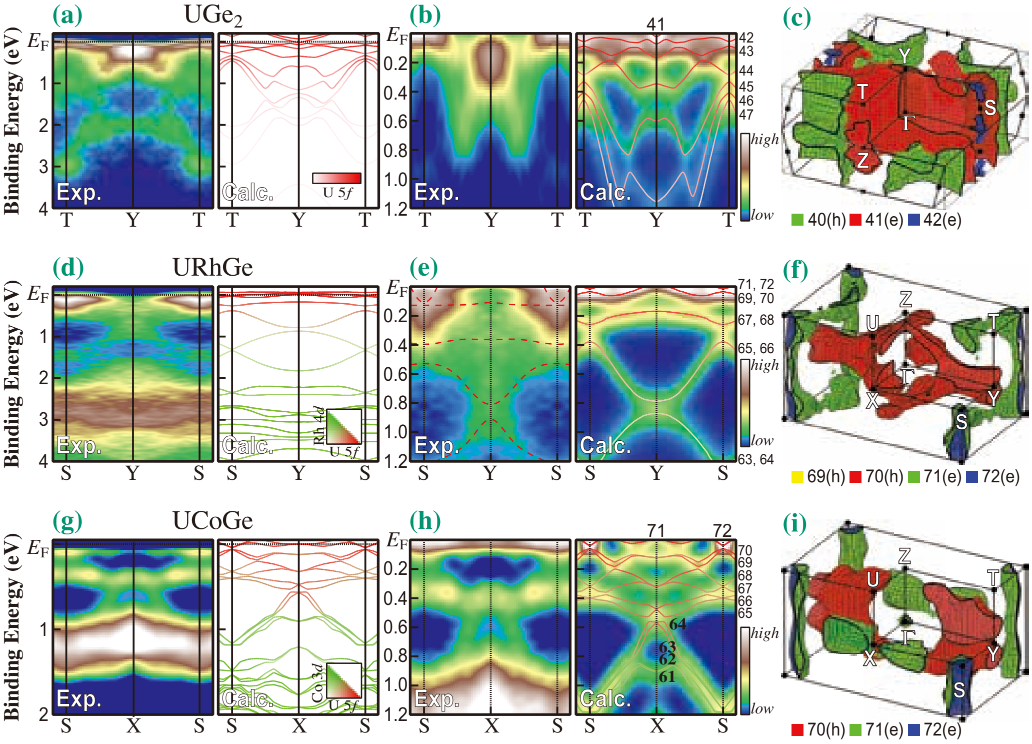

Fig. 2. ARPES spectra and the results of band structure calculations of UGe$_2$, URhGe, and UCoGe [2-4].

Shin-ichi Fujimori

Condensed Matter Science Division, JAEA

E-mail: fujimori@spring8.or.jp

References

[1] D. Aoki and J. Flouquet: J. Phys. Soc. Jpn. **81** (2012) 011003 .
[2] *S. Fujimori, T. Ohkochi, I. Kawasaki, A. Yasui, Y. Takeda, T. Okane, Y. Saitoh, A. Fujimori, H. Yamagami, Y. Haga, E. Yamamoto and Y. Ōnuki: Phys. Rev. B* ***91*** *(2015) 174503.*
[3] S. Fujimori *et al.*: Phys. Rev. B **89** (2014) 104518.
[4] *S. Fujimori, Y. Takeda, T. Okane, Y. Saitoh, A. Fujimori, H. Yamagami, Y. Haga, E. Yamamoto and Y. Ōnuki: J. Phys. Soc. Jpn.* ***85*** *(2016) 062001.*

Linking phonons in $SrFe_2As_2$ to magnetic fluctuations

The discovery of superconductivity in the iron pnictide materials [1] provided a new class of high-temperature superconductor that could be compared with the more-well-known cuprates. Initial investigations suggested that, like the cuprates, the high T_c of the pnictide materials could not be explained by conventional phonon-mediated pairing. None-the-less, the measured phonon dispersion in the pnictides was in surprisingly poor agreement with *ab initio* density functional (DFT) based phonon calculations. This failure appeared in several ways (see e.g. [2]) including the tendency of the non-magnetic calculations to get the wrong energies for many of the phonon modes for the samples above T_N and a tendency for calculations including magnetic order to indicate a much stronger splitting than was observed below T_N (see also Fig. 3). In fact, no phonon splitting at finite momentum transfer had been observed prior to the present work, despite calculations suggesting such splitting should be several times larger than instrumental resolution. Thus, while the phonon structure of the pnictides appeared conventional in that there were no broad modes, no large softening, and no strong temperature dependence, the dispersion was also anomalous in that it was surprisingly different than calculations.

Experimentally, careful investigation of phonons in magnetically ordered pnictides has been hampered by the twinning of materials below T_N. Investigations of twinned materials showed that the few-meV splitting predicted by calculation was certainly *not* present, but finer details might have been obscured by the presence of twin structure. Therefore, we undertook [3] to make single-domain samples of one iron-pnictide, $SrFe_2As_2$, as shown in Fig. 1: a small amount of pressure was used to preferentially select the shorter lattice constant at the structural transition (a slight distortion of the material from tetragonal to orthorhombic occurs at T_N = 200 K). This led to single domain samples below T_N, as was confirmed by X-ray diffraction. Phonon measurements at **BL35XU** and **BL43LXU** [4] then showed that while the splitting induced by the magnetic-order was smaller than calculated, it was clearly visible, as seen in Fig. 1(c,d).

The surprising phonon results, small splitting below T_N, and anomalous dispersion above T_N, can be interpreted self consistently, and quantitatively, by allowing for the presence of magnetic fluctuations. In particular, if one considers [3] the response of an atom in a harmonic potential with an effective force constant fluctuating randomly between two values, one finds the frequency response has two clear lines when the mean dwell time is longer than the inverse splitting of modes, but then collapses into a single line at the average value when the mean dwell time becomes small, as seen in Fig. 2. The measured phonon response is then qualitatively explained as follows: above T_N, the magnetic fluctuations are fast enough that all lines that are collapsed, and one sees what is essentially the average response; meanwhile below T_N some, but not all, of the fluctuations, have stabilized and the splitting appears.

The above conceptual picture was quantitatively explored [3] by separating, and then scaling, the

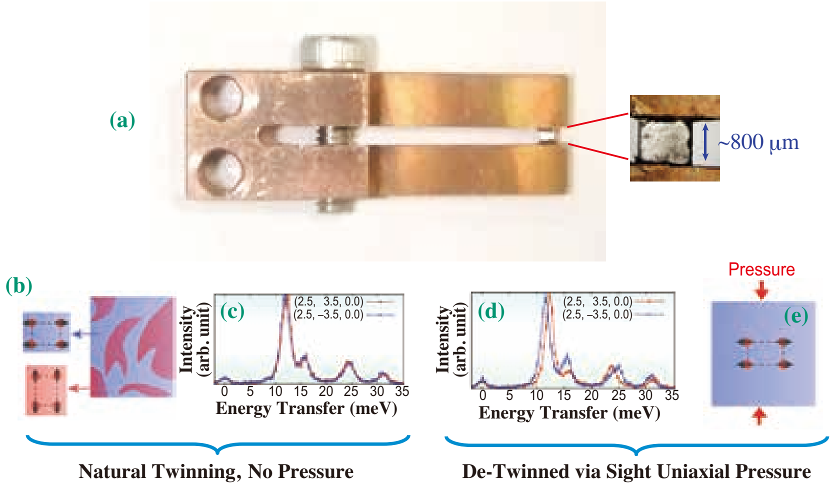

Fig. 1. Detwinning of a $SrFe_2As_2$ single crystal. The top panel, **(a)**, shows the sample glued in a holder used to exert slight pressure on the sample. The bottom panel shows the phonon response for a crystal without pressure **(c)** and detwinned **(d)**. Panels **(b)** and **(e)** schematically indicate the domain structure. For (c) and (d), the sample was held at 140K < T_N = 200 K.

anisotropic part of the force constant matrices derived from a magnetically ordered *ab initio* calculation. This led to greatly improved agreement between the calculations and measured results. In particular, below T_N, the anisotropic part of the force constant matrices had to be reduced by about a factor of 3 (see Fig. 3(a)), which, interestingly, is about the same factor as is needed to reduce the magnetic moment from the calculated to the observed value (see also discussion in [5]), and may be linked to fluctuations persisting below the onset of long-range order at T_N, in specific electronic orbitals [6]. Meanwhile, above T_N, where there is no magnetic order, selecting only the isotropic part of the force constants from the *magnetically ordered* calculation (e.g. setting the scale factor to zero) provides a much better model than the non-magnetic calculation (Fig. 3(b)).

This work solved several of the mysteries that had beset investigation of phonons in the iron pnictides. While we discuss only one material, $SrFe_2As_2$, in the "122" class of pnictides, similar disagreements between measurements and calculations exist also in other 122 materials, as well as the 1111 materials (such as PrFeAsO). Thus, it is probably reasonable to extend this picture, and calculational method, also to those materials. More generally, this is one example of how phonon response may be used to probe magneto-elastic coupling. Given better resolution (or different time scales) it may even be possible to directly probe the fluctuation time scale (e.g., the middle panels of Fig. 2) through phonon linewidth measurements. The investigation of magneto-elastic coupling is one of the goals of work at BL43LXU.

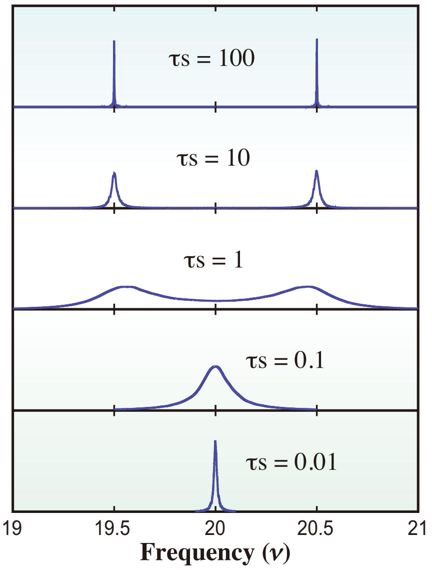

Fig. 2. Simple model for the effect of magnetic fluctuations on the phonon response. The calculations are for harmonic response of a mass m on a spring with a constant k that randomly fluctuates between two values, $k_1 < k_2$ where $s=(\sqrt{k_2}/\mathrm{m}-\sqrt{k_1}/m)/2\pi=1$. If the fluctuation occurs with a negative exponential distribution and has mean dwell time τ then the frequency response changes from two relatively well-defined lines for $\tau s \gg 1$ to a single line for $\tau s \ll 1$. The plot shows the frequency in units of splitting, s. (The average frequency of the phonon mode has no impact in this model [3]).

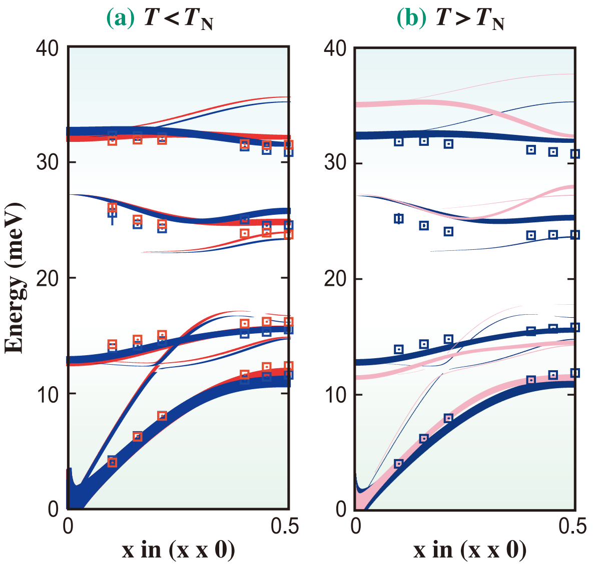

Fig. 3. Improved models incorporating reduced anisotropy to account for magnetic fluctuations. **(a)** shows the response below T_N with the anisotropy reduced by a factor of 3 while **(b)** shows the measurements above T_N compared to non-magnetic calculations (light pink) and the isotropic part of the magnetic response (light blue). The horizontal axis is the momentum transfer, the deviation from the (3 3 0) or (3 $\bar{3}$ 0) Bragg point in reciprocal lattice units (see also [3]). For the data points, the energy splitting below T_N (e.g., that in Fig. 1(d)) is visible as the slight separation between the red and blue data points in 3(a) which then merge in 3(b).

A. Q. R. Baron[a,*], N. Murai[a], T. Fukuda[b] and S. Tajima[c]

[a] RIKEN SPring-8 Center
[b] Quantum Beam Science Center, JAEA
[c] Department of Physics, Osaka University

*E-mail: baron@spring8.or.jp

References

[1] Y. Kamihara *et al*.: Am. Chem. Soc. **130** (2008) 3296.
[2] T. Fukuda *et al*.: Phys. Rev. B **84** (2011) 64504.
[3] *N. Murai, T. Fukuda, T. Kobayashi, M. Nakajima, H. Uchiyama, D. Ishikawa, S. Tsutsui, H. Nakamura, M. Machida, S. Miyasaka, S. Tajima and A.Q.R. Baron: Phys. Rev. B* ***93*** *(2016) 020301(R).*
[4] A.Q.R. Baron, in Synchrotron Light Sources Free. Lasers SE - 41-1, edited by E. Jaeschke *et al*. (Springer International Publishing, 2015), pp. 1-68 (see also: arXiv 1504.01098).
[5] I.I. Mazin and M.D. Johannes: Nat. Phys. **5** (2009) 141.
[6] Z.P. Yin *et al*.: Nat. Mater. **10** (2011) 932.

Discovery of suboxidic coordinate in high-T_C ferromagnetic semiconductor Co-doped TiO_2

High-Curie-temperature diluted ferromagnetic semiconductors (high-T_C DFSs) are strongly desired for the room-temperature operation of semiconductor spintronic devices. Among them, high-T_C DFS oxides have been intensively studied since the discovery of room-temperature ferromagnetism in Co-doped TiO_2 in 2001 [1]. The T_C of Co-doped TiO_2, ~600 K, is extraordinarily high considering the conventional carrier-mediated ferromagnetism seen in GaMnAs (~200 K). However, the microscopic origin of the high-T_C ferromagnetism has remained a mystery for a long time.

X-ray fluorescence holography (XFH) is a powerful tool for resolving a local structure, enabling a 3D atomic environment to be visualized around a selected element within a radius of nanometer orders without assuming any prior models [2]. To date, the advantageousness of XFH has been demonstrated for the evaluation of local lattice distortions around specified elements [3] and for the detection of nanocluster-like structures [4]. In this work, we experimentally determined local structures around the Co atoms in paramagnetic and ferromagnetic rutile Co-doped TiO_2 films by measuring XFH holograms. In addition, first-principles calculations based on density functional theory were carried out to evaluate the validity of the structure model obtained by XFH. In the ferromagnetic Co-doped TiO_2 film, suboxidic coordination around Co embedded in the rutile structure was observed. This suboxidic coordination may generate a ferromagnetic embryo leading to the strong exchange interaction realizing the high-T_C in Co-doped TiO_2 [5].

Two rutile $Ti_{1-x}Co_xO_2$ films with $x = 0.01$ and 0.05 were used, where the former and latter are paramagnetic and ferromagnetic, respectively. The XFH experiment was carried out at beamline **BL39XU**, and XAFS measurements were performed at beamline **BL22XU**. XFH data were recorded at incident X-ray energies of 8.0–12.0 keV in 0.5 keV steps by measuring Co Kα fluorescence (6.9 keV) intensity variation as a function of the incident beam direction. Figure 1(a) shows the hologram pattern of the $Ti_{0.95}Co_{0.05}O_2$ taken at 8.0 keV. The hologram data were symmetrized using the mirror symmetry of rutile TiO_2 (101) and then extended using the rotoreflection symmetry as shown in Fig. 1(b). Such data manipulation is important for providing accurate and high-resolution atomic images. The 3D atomic arrangements around the fluorescent element Co were reconstructed from multiple-energy holograms using Barton's algorithm [6].

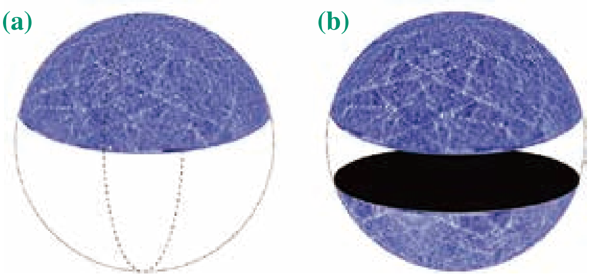

Fig. 1. Co holograms of $Ti_{0.95}Co_{0.05}O_2$ film. **(a)** Raw data and **(b)** symmetrized data. In (b), the data are mirror-symmetrized with respect to the dashed circle and then rotoreflection-symmetrized with respect to the (100) plane.

The 3D atomic images of $Ti_{0.99}Co_{0.01}O_2$ and $Ti_{0.95}Co_{0.05}O_2$ are shown in Figs. 2(a) and 2(b), respectively. In Fig. 2(a), the reconstructed 3D atomic images are superposed on the ideal Ti atomic positions of the rutile TiO_2, as marked by open circles, while the images of O atoms are hardly visible owing to their low scattering powers. Since the rutile structure, which shows in Fig. 2(c), is most stable form of TiO_2, the visible images are contributed to Ti atoms. Therefore, the Co atoms in the paramagnetic $Ti_{0.99}Co_{0.01}O_2$ substituted for Ti atoms without a large lattice distortion from the rutile structure. In contrast, the 3D atomic images in Fig. 2(b) are markedly different from the rutile structure. The surrounding atomic arrangement exhibits fourfold symmetry with respect to the normal to the rutile (101) plane (z-axis). Taking into account the very low visibility of O atoms, we can assume that the O atoms are located just above and below the Co atom along the z-axis, as denoted by dashed circles (Fig. 2(d)), corresponding to CoO_2Ti_4 coordination as discussed below.

To confirm the validity of our structure models in Figs. 2(c) and 2(d), we measured the Co K-edge XAFS spectra and calculated the XAFS spectra using the structure models and FEFF. The XAFS spectrum of the $Ti_{0.99}Co_{0.01}O_2$ agrees with that calculated using the rutile structure in Fig. 2(c). The spectrum of the $Ti_{0.95}Co_{0.05}O_2$ was calculated using the structure model in Fig. 2(d). The CoO_2Ti_4 and CoO_2Co_4 structure models were used for the calculation and their XAFS spectra were compared. The CoO_2Ti_4 structure model more closely reproduces the experimental spectrum of the $Ti_{0.95}Co_{0.05}O_2$ film.

To evaluate the stability of the suboxide cluster in the host rutile TiO_2, we carried out a series of first-principles calculations using the VASP code with the HSE06 hybrid functional for several possible atomic configurations. As the first step, to represent an isolated cluster model, the single CoO_2Ti_4+(Ti_8) cluster depicted in Fig. 2(d) was embedded in the rutile supercell structure while keeping the nearest Ti atoms trivalent. The cluster soon changed into an arrangement similar to that of the rutile crystal during the structure optimization process. This result indicates that an isolated CoO_2Ti_4 cluster is very unstable, also supporting the absence of the suboxide cluster in the low Co-doped film. Next, we aligned two CoO_2Ti_4 clusters in the rutile supercell structure ($Co_2O_{64}Ti_{34}$), as shown in Fig. 3(a), with an initial configuration where the O atoms are located above and below the Co atom orthogonal to the cluster alignment, and we obtained the structure in Fig. 3(b) by structure optimization. This structure preserves the original arrangement surrounding the CoO_2Ti_4 cluster, reproducing the XFH result in Fig. 2(b).

In conclusion, the presence of suboxide coordination in rutile $Ti_{0.95}Co_{0.05}O_2$ was revealed by the XFH and XAFS measurements. Possible atomic configurations of the suboxide network were investigated by first-principles calculation, which justified the reason why the clusters appear only at a high Co concentration. Furthermore, the suboxide network might be the source of the strong exchange interaction leading to the high T_C in Co-doped TiO_2.

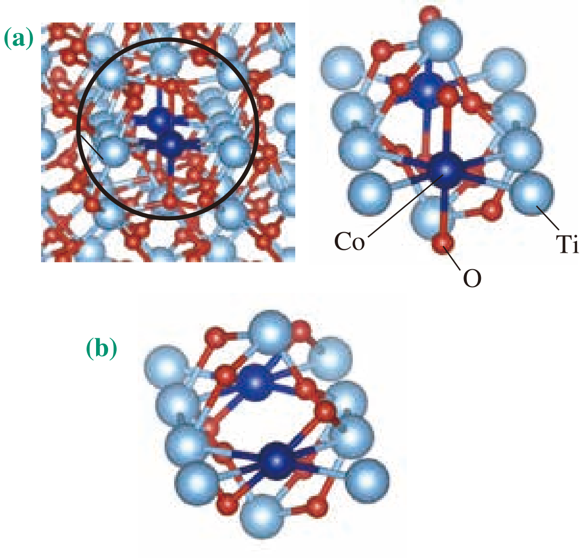

Fig. 3. Possible structures of the suboxide cluster embedded in rutile TiO_2. The structures were obtained by structure optimization based on a first-principles calculation. **(a)** Two aligned suboxide clusters embedded in rutile TiO_2. **(b)** Fully relaxed clusters.

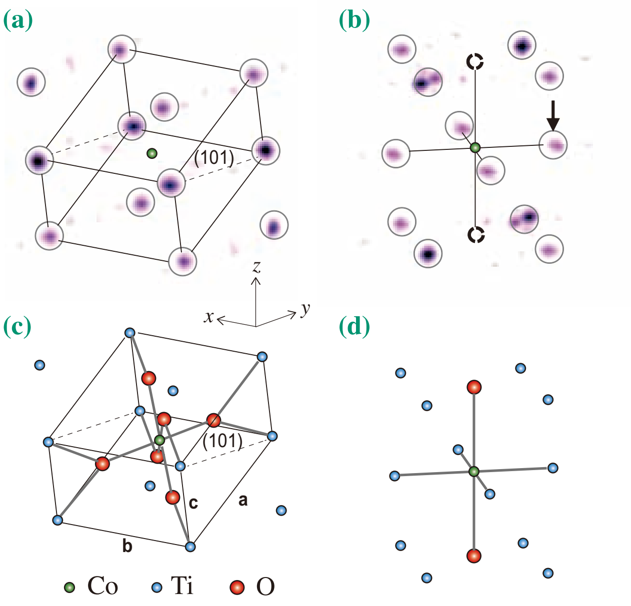

Fig. 2. Reconstructed real-space images around Co in **(a)** $Ti_{0.09}Co_{0.01}O_2$ and **(b)** $Ti_{0.95}Co_{0.05}O_2$ films. **(c)** and **(d)** Structure models obtained from the images in (a) and (b), respectively.

Wen Hu[a], Kouichi Hayashi[b,*] and Tomoteru Fukumura[c]

[a] National Synchrotron Light Source II,
Brookhaven National Laboratory, USA
[b] Department of Physical Science and Technology,
Nagoya Institute of Technology
[c] Department of Chemistry, Tohoku University

*E-mail: khayashi@nitech.ac.jp

References

[1] Y. Matsumoto *et al*.: Science **291** (2001) 854.
[2] K. Hayashi *et al*.: J. Phys.: Condens. Matter **24** (2012) 093201.
[3] W. Hu *et al*.: Phys. Rev. B **89** (2014) 140103(R).
[4] W. Hu *et al*.: Phys. Rev. B **80** (2009) 060202(R).
[5] *W. Hu, K. Hayashi, T. Fukumura, K. Akagi, M. Tsukada, N. Happo, S. Hosokawa, K. Ohwada, M. Takahasi, M. Suzuki and M. Kawasaki: App. Phys. Lett.* ***106*** *(2015) 222403.*
[6] J.J. Barton: Phys. Rev. Lett. **67** (1991) 3106.

Strongly correlated ground-state orbital symmetry of tetragonal and cubic Yb compounds probed by linear dichroism in *angle-resolved* core-level photoemission

Strongly correlated electron systems show a variety of intriguing phenomena such as unconventional superconductivity, nontrivial semiconducting behavior, and quantum criticality. Among them, the Yb-based single-crystalline $YbRh_2Si_2$, the Kondo semiconductor YbB_{12}, and the valence-fluctuating $YbCu_2Si_2$ have been synthesized and thus intensively studied over the past few decades. Since strong Coulomb repulsion (effective value of 5–10 eV order) acts between 4*f* electrons in Yb sites, an ionic picture is a good starting point for discussing and revealing their electronic structure as well as the origins of various phenomena. The majority of Yb ions in the above-mentioned materials are in Yb^{3+} ($4f^{13}$, one 4*f* hole in other words) configurations. Yb^{3+} 4*f* levels are split by spin-orbit coupling (~1.3 eV) and further split by a crystalline electric field (CEF, < 0.1 eV) in solids, as shown in Fig. 1.

Ground-state 4*f*-orbital symmetry determined by CEF splitting is very basic information on realistic strongly correlated electron systems. However, such ground-state symmetry is not straightforwardly revealed. Inelastic neutron scattering is useful, but other excitations such as phonon excitations often overlap with the 4*f*-4*f* excitation contributions [1]. Linear dichroism (LD) in 3*d*-4*f* X-ray absorption (XAS) is powerful for revealing the orbital symmetry owing to the dipole selection rules, as reported for heavy-fermion systems with nearly Ce^{3+} configurations [2,3]. However, LD in XAS is no longer available for compounds with cubic symmetry in which there is no anisotropic axis relative to the electric field of the incident light. Recently, we have discovered that the multiple-peak structure in *angle-resolved* core-level photoemission spectra relative to the crystal axis shows detectable LD reflecting the outer spatial distribution not only for tetragonal [4] but also for cubic [5] Yb compounds. This originates from the anisotropy in electron-electron Coulomb interactions and exchange interactions in the ionic 4*f* sites.

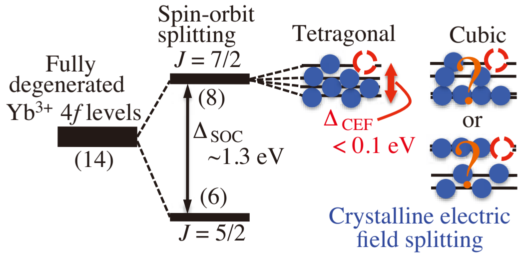

Fig. 1. Energy levels of Yb^{3+} ions in crystalline solids.

We have observed LD in hard X-ray photoemission spectroscopy (HAXPES) at beamline **BL19LXU**. In order to switch the linear polarization of the excitation light from the horizontal direction to the vertical direction, two single-crystalline (110) diamonds were used as a phase retarder. The experimental configuration for horizontally (vertically) polarized light excitation corresponds to *p*-polarization (*s*-polarization), in which the incident-light propagation and photoelectron detection directions are within the horizontal plane. Single crystals of the Yb compounds were cleaved or fractured *in situ*.

The polarization-dependent angle-resolved Yb^{3+} $3d_{5/2}$ core-level HAXPES spectra of $YbCu_2Si_2$ and $YbRh_2Si_2$ are shown in Fig. 2. There is a multiple-peak structure characteristic of ionic Yb^{3+} states yielding the $3d^94f^{13}$ multiplet-split peaks in the photoemission final states in all the spectra. Clear LD, defined by the difference in spectral weight between the *s*- and *p*-polarization configurations, is seen in the spectra depending on the material. For instance, in the spectra at $\theta = 0°$, the peak at 1527 eV is stronger in

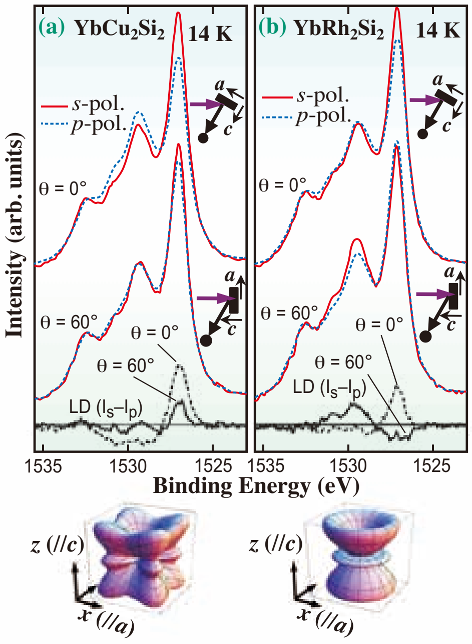

Fig. 2. (Upper) Polarization-dependent *angle-resolved* [$\theta = 0°$ and 60°, where θ denotes the angle between the photoelectron detection and the [001] direction] Yb^{3+} $3d_{5/2}$ core-level HAXPES spectra and their LD for tetragonal $YbCu_2Si_2$ **(a)** and $YbRh_2Si_2$ **(b)**. The inset illustrations denote the experimental configurations. (Lower) Yb^{3+} 4*f* charge spatial distributions corresponding to the ground-state wave functions (see text) for each compound obtained by our study.

the *s*-polarization configuration (*s*-pol.) than in the *p*-polarization configuration (*p*-pol.), whereas the structure with the 1529.5 eV peak and 1530.5 eV shoulder is stronger in the *p*-pol. for both compounds. On the other hand, the obtained LD is mutually different at θ = 60° (incident light along the *c*-axis); whereas the LD is reduced at θ = 60° while keeping the same sign as that at the same binding energy with θ = 0° for $YbCu_2Si_2$, the sign of the LD is flipped at θ = 60° relative to that at θ = 0° for $YbRh_2Si_2$. In the case of Yb^{3+} ions with tetragonal symmetry, the eightfold degenerate $J = 7/2$ state splits into four doublets as

$$|\Gamma_7^1\rangle = c|J_z = \pm 5/2\rangle + \sqrt{1-c^2}\,|J_z = \mp 3/2\rangle,$$

$$|\Gamma_7^2\rangle = -\sqrt{1-c^2}\,|\pm 5/2\rangle + c|\mp 3/2\rangle,$$

$$|\Gamma_6^1\rangle = b|\pm 1/2\rangle + \sqrt{1-b^2}\,|\mp 7/2\rangle,$$

$$|\Gamma_6^2\rangle = -\sqrt{1-b^2}\,|\pm 1/2\rangle - b|\mp 7/2\rangle,$$

where the coefficients $0 \le b \le 1$, $0 \le c \le 1$ define the actual 4*f* charge distributions and CEF splitting energies. In order to determine the ground-state symmetry on the basis of our experimental data, we have performed ionic calculations including the full multiplets and the local CEF splitting. We found that the polarization-dependent HAXPES data for $YbCu_2Si_2$ is best described by the ground state of $|\Gamma_7^2\rangle = -0.36|\pm 5/2\rangle + 0.93|\mp 3/2\rangle$. The LD and spectra of $YbRh_2Si_2$ are found to be best reproduced by the simulations for the pure $|J_z| = \pm 3/2$ state with the Γ_7 symmetry.

In the cubic symmetry, the $J = 7/2$ state splits into two doublets and one quartet as

$$|\Gamma_6\rangle = \sqrt{5/12}\,|\pm 7/2\rangle + \sqrt{7/12}\,|\mp 1/2\rangle,$$

$$|\Gamma_7\rangle = -\sqrt{3}/2\,|\pm 5/2\rangle + 1/2\,|\mp 3/2\rangle,$$

$$|\Gamma_8\rangle = \begin{cases} -\sqrt{7/12}\,|\pm 7/2\rangle + \sqrt{5/12}\,|\mp 1/2\rangle \\ 1/2\,|\pm 5/2\rangle + \sqrt{3}/2\,|\mp 3/2\rangle \end{cases}.$$

Since their 4*f* charge distributions deviate from spherical symmetry even in the cubic symmetry, it is natural to expect the observation of LD in core-level photoemission for cubic Yb compounds. Indeed, LD in core-level HAXPES has been successfully detected for cubic YbB_{12} as shown in Fig. 3. Slight but intrinsic LD can be seen in the Yb^{3+} $3d_{5/2}$ spectra, where the sign of the LD is flipped at the same binding energy between the data along the [100] and [111] directions. The observed LD and spectra for YbB_{12} are well reproduced by the simulations for the Γ_8 ground state.

The applicability of the LD in the core-level HAXPES even to the system with cubic symmetry, as demonstrated here, is promising for revealing the strongly correlated orbital symmetry of the ground state in a partially filled subshell.

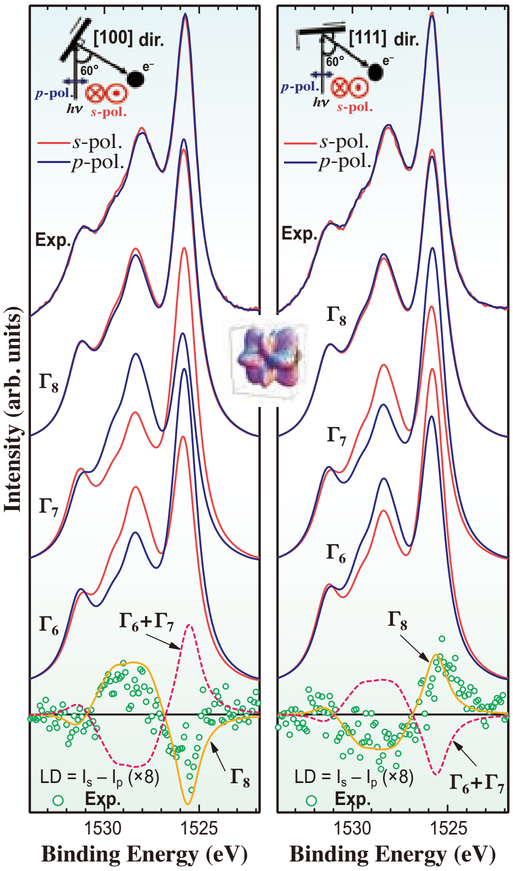

Fig. 3. Comparison of the polarization-dependent angle-resolved Yb^{3+} $3d_{5/2}$ core-level HAXPES spectra and their LD for cubic YbB_{12} with the theoretically simulated spectra for cubic symmetry. The Yb^{3+} 4*f* charge distribution corresponding to the ground-state wave function (see text) for the Yb^{3+} Γ_8 symmetry realized for YbB_{12} is also shown.

Akira Sekiyama[a,b,*], Yuina Kanai[a,b] and Shin Imada[b,c]

[a] Division of Materials Physics, Osaka University
[b] RIKEN SPring-8 Center
[c] Department of Physical Sciences, Ritsumeikan University

*E-mail: sekiyama@mp.es.osaka-u.ac.jp

References

[1] E. Holland-Moritz *et al.*: Phys. Rev. B **25** (1982) 7482.
[2] P. Hansmann *et al.*: Phys. Rev. Lett. **100** (2008) 066405.
[3] T. Willers *et al.*: Phys. Rev. B **80** (2009) 115106.
[4] *T. Mori, S. Kitayama, Y. Kanai, S. Naimen, H. Fujiwara, A. Higashiya, K. Tamasaku, A. Tanaka, K. Terashima, S. Imada, A. Yasui, Y. Saitoh, K. Yamagami, K. Yano, T. Matsumoto, T. Kiss, M. Yabashi, T. Ishikawa, S. Suga, Y. Onuki, T. Ebihara and A. Sekiyama: J. Phys. Soc. Jpn.* ***83*** *(2014) 123702.*
[5] *Y. Kanai, T. Mori, S. Naimen, K. Yamagami, H. Fujiwara, A. Higashiya, T. Kadono, S. Imada, T. Kiss, A. Tanaka, K. Tamasaku, M. Yabashi, T. Ishikawa, F. Iga and A. Sekiyama: J. Phys. Soc. Jpn.* ***84*** *(2015) 073705.*

Characterization of local strain in $Ge_{1\text{-}x}Sn_x$ / Ge fine structures by using microdiffraction

New technology, which enhances the carrier mobility in metal-oxide-semiconductor field-effect transistors, has attracted interest for improving the performance of future-generation ultra-large-scale integrated circuits (ULSIs) [1]. $Ge_{1\text{-}x}Sn_x$ as a source/drain stressor is one of the promising candidates for enhancing hole mobility while realizing uniaxial compressive strain in a Ge channel [2]. The precise estimation and control of local strain in a nanoscale region are required in order to design ULSIs and control the mobility. Microdiffraction using synchrotron radiation provides not only high reciprocal space resolution but also high real space resolution with up to sub-μm resolution [3,4]. In this study, we examined the formation of a Ge fine line structure sandwiched with epitaxially grown $Ge_{1-x}Sn_x$ as a source/drain stressor, and demonstrated microdiffraction analysis of the local strain structure in an individual Ge fine line whose width was as small as 25 nm [5].

We prepared Ge fine line structures with widths of 25, 35, and 60 nm by using SiO_2 hard mask layer and a lithography technique. After chemical and thermal cleaning, a 130-nm-thick $Ge_{1-x}Sn_x$ epitaxial layer with a Sn content of 2.9% or 6.5% was epitaxially grown on the recess region by molecular beam epitaxy at a substrate temperature of 150°C or 200°C, respectively. Microdiffraction measurement was performed at beamline **BL13XU** to analyze the local strain structure of Ge and $Ge_{1-x}Sn_x$. Synchrotron radiation light with an energy of 8 keV ($\lambda = 0.154980$ nm) was used, and an incident X-ray microbeam was focused on the sample using a Fresnel zone plate with a narrow slit. The exposed area of the incident microbeam was estimated to be 0.38×0.26 to 0.82×0.26 μm^2.

Figure 1(a) shows a bird's-eye view scanning electron microscope (SEM) image of a sample. Blue arrows in the figure schematically indicate an incident and diffraction X-ray microbeam. The typical size of the incident microbeam spot is also shown with a yellow ellipse in the figure. The incident microbeam position was moved with a 50 nm step at each reciprocal space mapping. Figure 1(b) shows a cross-sectional transmission electron microscope (TEM) image of a $Ge/Ge_{1-x}Sn_x$ fine line structure. The epitaxial growth of $Ge_{1-x}Sn_x$ layers sandwiching a Ge fine line was observed.

Figure 2(a) shows a typical microdiffraction reciprocal space map for 60-nm-wide Ge fine lines sandwiched with $Ge_{0.935}Sn_{0.065}$ stressors at the microbeam position on a Ge fine line structure. The Bragg reflection corresponding to not only $Ge_{1-x}Sn_x$ 004 but also strained Ge can be clearly observed in the reciprocal space map. Figure 2(b) shows a contour map of the intensity of Ge and $Ge_{1\text{-}x}Sn_x$ 004 Bragg reflections obtained by scanning the microbeam position. We can observe the Bragg reflection of strained Ge 004 from each individual Ge fine line.

Figure 3 shows contour maps of Ge and $Ge_{1-x}Sn_x$ 004 Bragg reflections obtained by scanning the microbeam position for Ge fine line samples with various-width. As the line width shrinks, the shift of the peak position related to the strained Ge Bragg reflection is clearly observed, which indicates increasing magnitude of the strain with decreasing width of the Ge fine line. The strain distribution in the fine structure was calculated by the finite element method (FEM), and the line width dependence of the strain observed in the microbeam diffraction experiment was in good agreement with the FEM calculation result. The maximum out-of-plane strain was estimated to be 0.8% for a 25-nm-width Ge fine line by using microdiffraction. Considering the FEM calculation, a uniaxial compressive strain of 1.4% is expected for the in-plane direction in this Ge line.

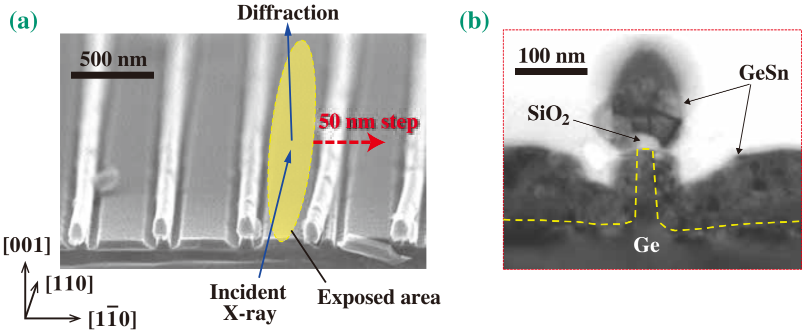

Fig. 1. **(a)** Bird's-eye view SEM image of a sample. A schematic of the incident and diffracted microbeam is superimposed. **(b)** Cross-sectional TEM image of a $Ge/Ge_{1-x}Sn_x$ fine line structure.

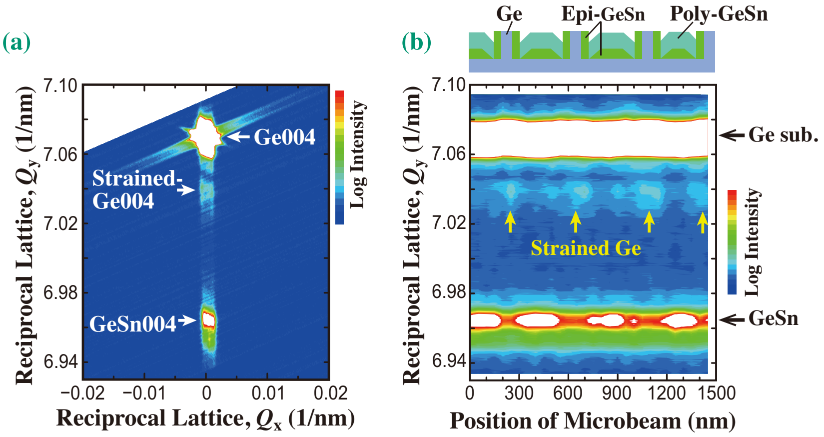

Fig. 2. **(a)** Typical microdiffraction reciprocal space map at the microbeam position on a Ge fine line structure. **(b)** Contour map of the intensity of Ge and $Ge_{1-x}Sn_x$ 004 Bragg reflections obtained by scanning the microbeam position for 60-nm-wide Ge fine lines sandwiched with $Ge_{0.935}Sn_{0.065}$ stressors. The diffraction signals from Ge substrate, strained Ge, and $Ge_{1-x}Sn_x$ layer are indicated with arrows.

In summary, we examined the formation of $Ge_{1-x}Sn_x$/Ge fine structures and investigated in detail the local strain with submicron resolution by microdiffraction measurement and the FEM. We successfully formed a locally strained Ge fin structure sandwiched with epitaxially grown $Ge_{1-x}Sn_x$. The microdiffraction revealed an anisotropic local strain in an individual Ge fine line structure with a width as small as 25 nm. Microdiffraction enables direct observation of the local strain structure with high spatial and strain resolution in submicron-scale semiconductor devices in future nanoelectronic applications.

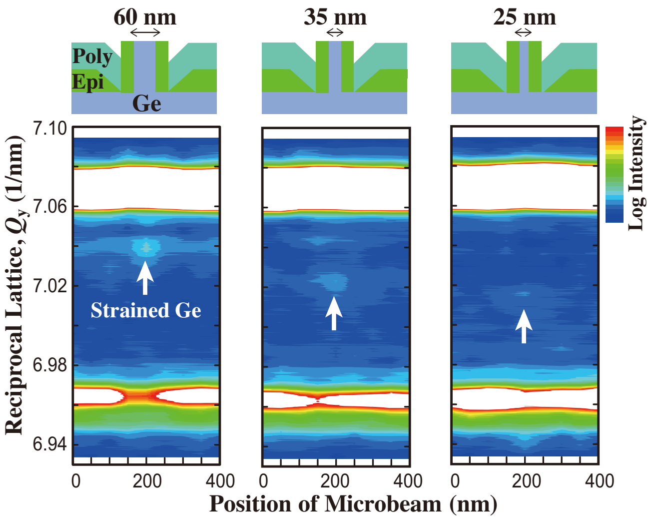

Fig. 3. Contour maps of Ge and $Ge_{1-x}Sn_x$ 004 Bragg reflections as a function of the microbeam position for Ge fine lines with various-widths. The diffraction signals from strained Ge are indicated with white arrows.

Osamu Nakatsuka[a,*], Shinichi Ike[a,b] and Shigeaki Zaima[a,c]

[a] Graduate School of Engineering, Nagoya University
[b] Japan Society for the Promotion of Science (JSPS), Research Fellowship
[c] Institute of Materials and Systems for Sustainability (IMaSS), Nagoya University

*E-mail: nakatuka@alice.xtal.nagoya-u.ac.jp

References

[1] S. Zaima: Jpn. J. Appl. Phys. **52** (2013) 030001.
[2] B. Vincent *et al.*: Microelectron. Eng. **88** (2011) 342.
[3] S. Mochizuki *et al.*: Thin Solid Films **508** (2006) 128.
[4] O. Nakatsuka *et al.*: Jpn. J. Appl. Phys. **50** (2011) 05ED03.
[5] *S. Ike, O. Nakatsuka, Y. Moriyama, M. Kurosawa, N. Taoka, Y. Imai, S. Kimura, T. Tezuka and S. Zaima: Appl. Phys. Lett.* ***106*** *(2015) 182104.*

Copper oxide without static Jahn-Teller distortion

The quantum spin liquid (QSL) state has been intensively studied since Anderson proposed the resonating valence bond model. For realizing a novel QSL state, orbital degrees of freedom have been considered a nuisance because orbital ordering usually appears at high temperatures accompanied by cooperative Jahn-Teller (JT) distortion and spin ordering. Therefore, the QSL candidates found so far have been mostly in spin-only systems without orbital degree of freedom: e.g., the two-dimensional kagome systems $SrCr_{9p}Ga_{12-9p}O_{19}$ ($S = 3/2$) and $ZnCu_3(OH)_6Cl_2$ ($S = 1/2$), the two-dimensional triangular lattice system $NiGa_2S_4$ ($S = 1$), the two-dimensional honeycomb lattice system $Bi_3Mn_4O_{12}(NO_3)$ ($S = 3/2$), and the three-dimensional hyperkagome lattice system $Na_4Ir_3O_8$ ($S = 1/2$).

Perovskite-type 6*H*-$Ba_3CuSb_2O_9$ is a novel candidate material for the spin-orbital liquid state, which we have reported recently [1,2]. In the material, spin-orbital short-range ordering occurs in the short-range honeycomb lattice of Cu^{2+} with e_g orbital degrees of freedom, as shown in Fig. 1(a). Powder X-ray diffraction performed at **BL02B2** indicates that even at low temperatures, hexagonal components remain along with some orthorhombically distorted components. In the hexagonal phase, a threefold symmetry exists for Cu^{2+} sites, which are surrounded by octahedrally coordinated oxygen atoms, indicating the absence of a cooperative JT distortion. To explain this unusual feature, we proposed two possible scenarios. (i) A non-cooperative static JT distortion (orbital glass state) appears. In this scenario, the local symmetry is lowered by a static JT distortion, as schematically shown in Fig. 1(b), but the overall hexagonal symmetry remains. (ii) The static JT distortion is absent and instead, a dynamic JT distortion appears, leading to a novel spin-orbital liquid state, as shown in Fig. 1(c). These two possible scenarios cannot be distinguished from experimental results obtained using powder specimens alone. A thorough structural study using a single crystal without orthorhombic components is required.

The progress in preparing single crystalline samples enabled us to obtain single crystalline samples without any orthorhombic components down to the lowest temperature. Figures 2(a) and 2(b) show single-crystal X-ray diffraction experimental data collected at **BL02B1** at 300 K and 20 K, respectively [3]. The peaks show no signs of splitting or broadening down to 20 K ("hexagonal sample"). The hexagonal sample can be well refined by using the centrosymmetric space group $P6_3/mmc$ at all temperatures. For $P6_3/mmc$, the threefold symmetry is retained for Cu^{2+} sites, indicating the absence of the cooperative JT distortion. These observations are in sharp contrast with our previous single-crystal X-ray diffraction study of 6*H*-$Ba_3CuSb_2O_9$. In that study, we found that the Bragg peak splits into several separate reflections with decreasing in temperature, as shown in Figs. 2(c) and 2(d). This result indicates that the hexagonal $P6_3/mmc$ symmetry is lowered to the orthorhombic *Cmcm* symmetry ("orthorhombic sample"). We attribute this effect to the cooperative JT distortion induced by the uniform orbital ordering of Cu^{2+} ions (Fig. 1(d)).

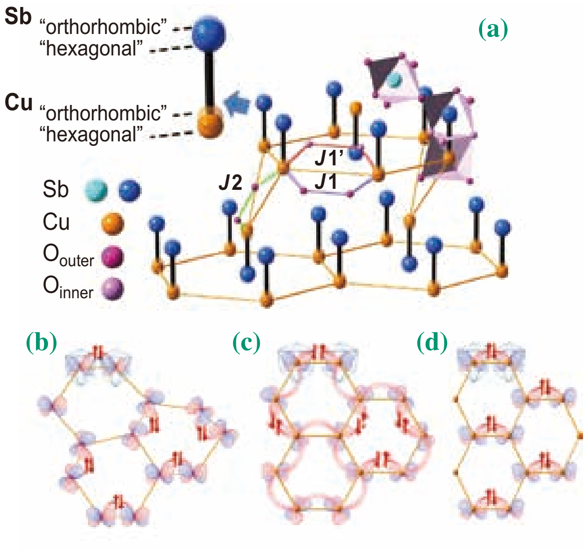

Fig. 1. **(a)** Schematic view of the local structure of hexagonal and orthorhombic samples. **(b)** Schematic image of a non-cooperative static JT distortion. **(c)** and **(d)** Schematic pictures of spin-singlet formation in short-range honeycomb lattices of Cu^{2+} for (c) hexagonal and (d) orthorhombic samples. For (c), a spin-orbital entangled short-range-order state is expected. A pair of upward and downward arrows indicates a singlet state of the dimer based on the neighboring Cu^{2+} spins. At each site, an unpaired electron of Cu^{2+} occupies the $d_{x^2-y^2}$, $d_{y^2-z^2}$ or $d_{z^2-x^2}$ orbital.

To clarify the factor that differentiates the hexagonal samples from the orthorhombic samples, we performed comprehensive studies using ICP-AES and powder X-ray diffraction experiments at beamline **BL02B2** [3]. Although their crystal structures are similar to that of the same space group of $P6_3/mmc$ at high temperatures, they can be differentiated on the basis of Sb/Cu ratio. As shown in Fig. 3(b), the hexagonal samples are located in the vicinity of the border of the orthorhombic phase, and the JT instability increases with increasing *a*-axis parameter at 400 K and when the Sb/Cu composition ratio slightly deviates from 2/1. When the Sb/Cu ratio is higher than 2/1, some Sb ions replace the Cu ions, which break locally the threefold symmetry of the short-ranged honeycomb lattice. This symmetry breaking inherent to off-stoichiometry induces the orthorhombic distortion at low temperatures. In comparison with the orthorhombic samples, strong geometrical frustration may exist in the hexagonal samples owing to the higher local symmetry. Although the Sb/Cu ratio was found to be always higher than 2/1 in the orthorhombic samples, as shown in Fig. 3(a), the orthorhombic distortion appears even when the Sb/Cu ratio became lower than 2/1.

Although the experimental details are not described here, electron spin resonance (ESR), which sensitively detects the local orbital configuration, has confirmed the isotropic *g* factors within the in-plane directions in the hexagonal samples down to 3.5 K, clearly indicating that the non-cooperative JT scenario is not realized and instead, a dynamic JT distortion appears [3]. Further studies using crystals will address the issues on the quantum spin-orbital liquid state, such as the orbital dynamics and the mechanism that stabilizes such an exotic liquid state.

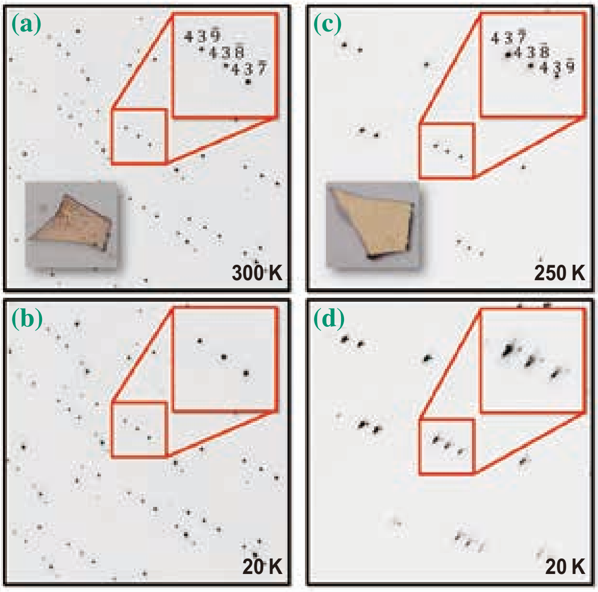

Fig. 2. Single-crystal X-ray diffraction profiles of **(a–b)** hexagonal and **(c–d)** orthorhombic samples. The insets in (a) and (c) are photographs of the transparent brown single crystals for the hexagonal and orthorhombic samples, respectively. The hexagonal samples are darker than the orthorhombic samples.

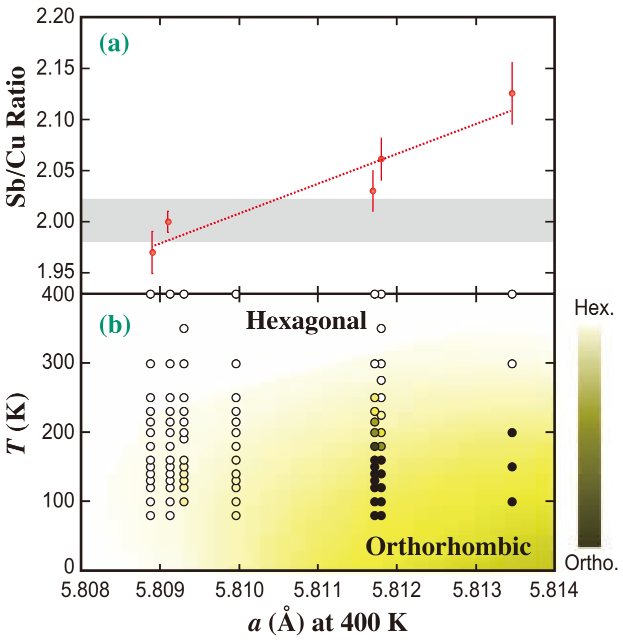

Fig. 3. **(a)** Sb/Cu ratio *vs* lattice parameters of several samples at 400 K. **(b)** Sample dependence on composition ratio between hexagonal and orthorhombic phases examined by decreasing temperature studied using several samples. The vertical axis is the *a*-axis lattice constant obtained at 400 K in the high-temperature hexagonal phase, with which samples are distinguished. Each circle represents a temperature point in powder X-ray diffraction measurements and its color indicates the volume fraction of the hexagonal (white) and orthorhombic (black) phases.

Naoyuki Katayama[a,*], Hiroshi Sawa[a] and Satoru Nakatsuji[b]

[a] Department of Applied Physics, Nagoya University
[b] Institute for Solid State Physics, University of Tokyo

*E-mail: katayama@mcr.nuap.nagoya-u.ac.jp

References

[1] S. Nakatsuji *et al.*: Science **336** (2012) 559.
[2] N. Katayama *et al.*: SPring-8 Information 17, No. 4303 (2012) 297. (in Japanese)
[3] *N. Katayama, K. Kimura, Y. Han, J. Nasu, N. Drichko, Y. Nakanishi, M. Halim, Y. Ishiguro, R. Satake, E. Nishibori, M. Yoshizawa, T. Nakano, Y. Nozue, Y. Wakabayashi, S. Ishihara, M. Hagiwara, H. Sawa and Satoru Nakatsuji: Proc. Natl. Acad. Sci. USA* ***112*** *(2015) 9305.*

Site-specific valence atomic orbital characterization by detection of angular-momentum-polarized Auger electrons

Copper is nonmagnetic, while nickel, which has one less electron than copper, is ferromagnetic. Gold is chemically inert, while platinum, which has one less electron than gold, is an essential element in catalyst chemistry. If we can generate a valence hole with an arbitrary atomic orbital character in a solid, an excited state with new electronic properties can be created, which cannot be achieved by simple thermal excitation of valence electrons in the vicinity of the Fermi level.

Based on core-level photoelectron diffraction, element-specific atomic structure information can be obtained. Forward focusing peaks (FFPs) appearing in a photoelectron intensity angular distribution (PIAD) indicate the directions of atoms surrounding a photoelectron emitter atom. Upon a core-level excitation by circularly polarized light (CPL), the angular momentum of light, i.e., helicity, is transferred to the emitted photoelectron. This phenomenon can be confirmed by the parallax shift measurement of the FFP direction in a stereograph of the atomic arrangement [1,2]. The core hole may decay via Auger electron emission, where in this two-electron process the angular momentum also has to be conserved. Here we report the observation of angular momentum transfer from excitation light to resonant Auger electrons [3,4]. Note that FFPs also appear in the Auger electron intensity angular distributions (AIADs) [5]. We succeeded in detecting angular-momentum-polarized Cu *LMM* Auger electrons at the *L* absorption threshold, where the excited core electron is trapped at the conduction band. The FFP covers a solid angle of about 10°. By setting an analyzer at the corresponding position in the FFP direction, a photoelectron or Auger electron with a specific angular momentum can be selectively detected. Correspondingly, an orbital-momentum-polarized hole state is created.

All the experiments were carried out using the two-dimensional display-type analyzer installed at the circularly polarized soft X-ray beamline **BL25SU**. We measured full hemisphere PIADs and AIADs from the Cu(001) surface [3,4]. Figure 1(a) shows a Cu valence PIAD at a kinetic energy of 914 eV. PIADs excited by both helicities I^+ and I^- were added and normalized. The incidence direction of CPL, i.e., the quantization axis, was aligned along the surface normal. Figure 1(b) shows a resonant Cu $L_3M_{45}M_{45}$ AIAD at the kinetic energy of 914 eV excited by CPL with a photon energy of 934.2 eV. The energy window width of the display-type analyzer was set to 5% of 914 eV and the whole valence band intensity or $L_3M_{45}M_{45}$ Auger electrons were integrated. The FFPs at the four ⟨101⟩ directions correspond to the scattering by the nearest-neighbor atoms, while the center [001] direction corresponds to scattering by the second-nearest-neighbor atoms along the surface normal. Note that at this kinetic energy, FFPs are also present even for a delocalized valence band due to the majority of the excitation coming from electron density existing in the vicinity of the nucleus.

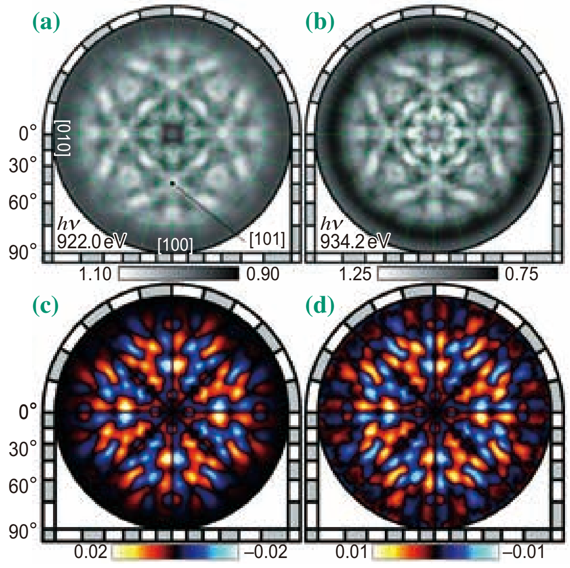

Fig. 1. **(a)** Cu valence PIAD at the kinetic energy of 914 eV. PIADs excited by both helicities (σ=±1) were added. **(b)** Resonant Cu $L_3M_{45}M_{45}$ AIAD at the kinetic energy of 914 eV excited by CPL with photon energy of 934.2 eV. **(c)** Difference between the two valence PIADs excited by both helicities and normalized by their sum. **(d)** Same as (c) but for the AIAD shown in (b).

Figure 1(c) shows the circular dichroism angular distribution (CDAD) of the valence band, i.e., the difference between the two PIADs excited by both helicities and normalized by their sum; $(I_1 - I_{-1})/(I_1 + I_{-1})$. The suffix denotes the helicity. Figure 1(d) shows the CDAD of the resonant AIAD. This result indicates that at the L_3 absorption threshold, where the excitation core electron is trapped in the conduction band, the angular momentum was partially transferred to the resonant $L_3M_{45}M_{45}$ Auger electrons instead of the photoelectron.

As shown in Fig. 2, the azimuthal intensity profiles of the [101] FFPs excited by CPL were individually fitted by Gaussians centered at the $\phi = 2.894° m_f$ directions corresponding to the different angular momenta of emitted electrons. Note that the photoelectrons from the 3*d* valence band gain angular momentum σ by CPL excitation ($m_f = 3, 2, \ldots, -1$), while the angular momenta of *LMM* Auger electrons are the same as those of 3*d* valence electrons ($m_i = \pm 2, \pm 1, 0$). Components of $m_f = \pm 3$ do not exist in the FFP of the AIAD as shown in Fig. 2. The origin of circular dichroism in the resonant AIAD at L_3 absorption threshold, where the excited core electron is trapped at conduction band, is attributed to the difference in transition to the final states $m_f = \pm 1$ and ± 2.

By combining Auger electron spectroscopy with the FFP shift measurements at the absorption threshold, element- and magnetic-quantum-number-specific hole states can be generated in the valence band. The Auger electron emission process that involves two valence electrons will allow, for example, the creation of a nickel-like $3d^8 4s^2$ atom in a copper matrix. As we show here, the polarization of this $3d^8 4s^2$ impurity may be controlled by the light incidence and polarization of the light used to create the core hole for the Auger decay process. The resonant Auger electron emission induced by CPL excitation is an excellent way to polarize a valence band with a specific orbital magnetic momentum and a specific atomic number in a controlled fashion localized in space and time. Furthermore, this phenomenon can be used for the atomic orbital characterization of the valence density of states at specific atomic sites in compound crystals and epitaxial thin films. For instance, we are now revealing the atomic orbital origin of the spin reorientation transition in a Ni perpendicular magnetized film [5] by applying this method.

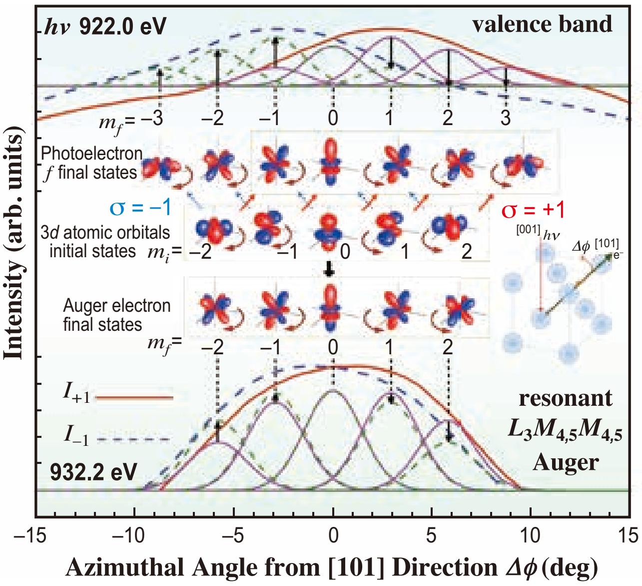

Fig. 2. Azimuthal profiles of the [101] FFP intensity for valence photoelectron and Auger electrons.

Fumihiko Matsui

Graduate School of Materials Science,
Nara Institute of Science and Technology

E-mail: matui@ms.naist.jp

References

[1] H. Daimon: Phys. Rev. Lett. **86** (2001) 2034.
[2] F. Matsui, *et al*.: J. Electron Spectrosc. Relat. Phenom. **195** (2014) 347.
[3] *F. Matsui, M. Fujita, T. Ohta, N. Maejima, H. Matsui, H. Nishikawa, T. Matsushita, H. Daimon: Phys. Rev. Lett.* ***114*** *(2015) 015501.*
[4] F. Matsui *et al*.: Z. Phys. Chem. **230** (2016) 519.
[5] F. Matsui *et al*.: Phys. Rev. Lett. **100** (2008) 207201.

Structure of an extremely fragile liquid

Glass formation from liquids is an important topic in glass science, and several theories of glass formation were established in the last century. Zachariasen [1] and Sun [2] proposed the basic concepts of glass formation by classifying constituents into glass formers, glass modifiers, and intermediates. Angell [3] introduced the concept of 'fragility' in glass-forming liquids (GFLs) on the basis of the relationship between glass transition temperature and viscosity: liquids can be classified as 'strong' and 'weak' according to their glass-forming ability. ZrO_2 is one representative of non-glass formers and is commonly used as a refractory material, suggesting that liquid (*l*)-ZrO_2 is indeed a non-GFL. As ZrO_2 has an extremely high melting point (T_m = 2,715°C), the difficulties in handling the liquid at high temperatures lead to problems in selecting suitable container materials that prevent contamination effects. We have developed a beamline aerodynamic levitation furnace that enables us to perform precise synchrotron X-ray diffraction measurements of containerless liquids at extremely high temperatures. Using the levitation furnace, we performed high-energy X-ray diffraction measurements on containerless levitated *l*-ZrO_2 [4] at beamlines **BL04B2** and **BL08W**. We also carried out large-scale density functional (DF)–MD simulations to clarify the liquid properties at the atomic and electronic levels. Furthermore, we compared *l*-ZrO_2 with a typical GFL, *l*-SiO_2 [5] to reveal the relationship between structure and glass-forming ability in liquids.

Figure 1(a) shows the Bhatia-Thornton [6] number-number partial structure factor $S_{NN}(Q)$ for *l*-ZrO_2 at 2,800°C compared with that for *l*-SiO_2 at 2,100°C. Only *l*-SiO_2 exhibits the first sharp diffraction peak (FSDP) at Qr_{AX} = 2.7 (r_{AX} is the atomic cation (A) – anion (X) distance in AX polyhedra). Since the Bhatia-Thornton $S_{NN}(Q)$ can eliminate the weighting factors for X-rays, the absence of an FSDP in $S_{NN}(Q)$ for *l*-ZrO_2 is a distinct signature of a non-GFL.

The coordination number distributions of *l*-SiO_2 and *l*-ZrO_2 calculated from the structural models are shown in Fig. 1(b). SiO_4 tetrahedra are predominant in *l*-SiO_2, whereas *l*-ZrO_2 comprises ZrO_5, ZrO_6, and ZrO_7. This comparison supports our view that the variety of oxygen coordination around cations in *l*-ZrO_2 is another characteristic feature of non-glass-forming behavior, because it can disturb the evolution of intermediate-range ordering.

To obtain structural features beyond the first coordination distance, polyhedral connection analysis was performed for *l*-SiO_2 and *l*-ZrO_2. Figure 1(c) shows the fractions of corner-sharing, edge-sharing, and face-sharing polyhedral units in the liquids. The corner sharing of oxygen is prevalent in *l*-SiO_2, which is a unique feature of GFLs according to Zachariasen [1]. However, *l*-ZrO_2 exhibits a considerable amount of oxygen edge sharing, implying that the variety of polyhedral connection is another characteristic feature of single-component non-GFLs.

Electronic structure analysis was carried out in terms of the electronic density of states (DOS) to obtain snapshots of the high-temperature phases of crystalline (*c*-) ZrO_2 and *l*-ZrO_2. The projections (P-DOS) reveal that the electronic spectrum is mainly associated with oxygen (O-2*p* orbitals) and the Zr semicore states, and the gap between the valence and the conduction bands in *l*-ZrO_2 is narrower than that in *c*-ZrO_2.

The difference between the electronegativities of Zr (1.3) and O (3.5) indicates that the chemical bonding between the two elements is mainly ionic. The effective charges calculated by the Bader method are +2.62*e* and –1.31*e* for Zr and O in *l*-ZrO_2, respectively, which reflect the ionic bonding.

The origin of the FSDP associated with the

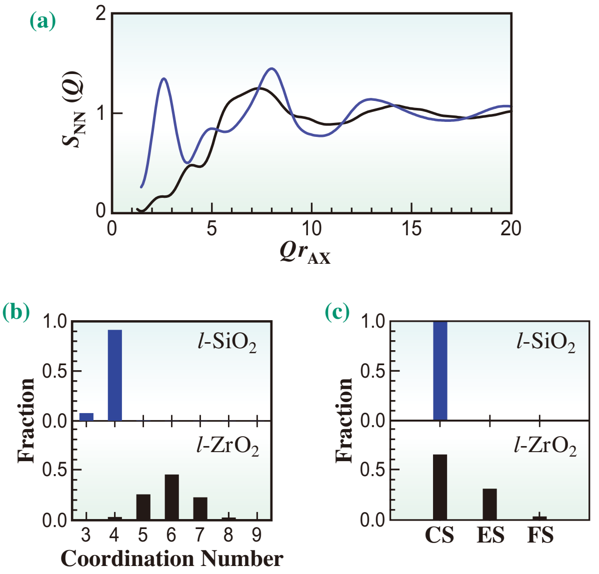

Fig. 1. **(a)** Bhatia-Thornton number-number partial structure factor $S_{NN}(Q)$ for *l*-ZrO_2 at 2,800°C derived from DF–MD simulation (black curve) [4] compared with that for *l*-SiO_2 at 2,100°C (blue curve) [5]. The momentum transfer Q was scaled by r_{AX}, which is the first coordination distance between A and X in the real-space function. **(b)** Coordination number distribution of oxygen atoms around the cations in *l*-ZrO_2 at 2,800°C [4] and *l*-SiO_2 at 2,100°C [5]. **(c)** Polyhedral connections in *l*-ZrO_2 at 2,800°C [4] and *l*-SiO_2 at 2,100°C [5]. CS, corner sharing of oxygen; ES, edge sharing of oxygen; FS, face sharing of oxygen.

formation of intermediate-range ordering in oxide glasses and liquids remains controversial [7], because the inherent disorder complicates the ability of AX polyhedral connections to form an A-X network. SiO$_2$ has exceptionally high glass-forming ability, and the origin of the FSDP in SiO$_2$ has often been studied. The random network model of Zachariasen [1], which was modified for an oxide glass, demonstrates that the intermediate-range ordering arises from the periodicity of boundaries between successive small cages in the network formed by connected, regular SiO$_4$ tetrahedra with shared oxygen atoms at the corners [7]. It has also been suggested that the small cages are topologically disordered, resulting in a broad distribution of ring sizes from threefold to twelvefold rings centered at sixfold rings [8]. This is reflected in $S_{NN}(Q)$ for *l*-SiO$_2$ (Fig. 1(a)), where the FSDP width is larger than that of the corresponding Bragg peak in the crystalline phase (β-cristobalite, *c*-SiO$_2$), where only a sixfold ring contributes. Figures 2(a) and 2(b) show the three-dimensional atomic configurations and schematic illustrations of *c*-SiO$_2$ and *l*-SiO$_2$, respectively. The crystalline phase exhibits only sixfold rings of six SiO$_4$ tetrahedra, resulting in long-range periodicity (dashed lines in Fig. 2(a)). However, some pseudo-Bragg planes (dashed lines in the left panel of Fig. 2(b)) can be recognized in *l*-SiO$_2$. Although the introduction of different ring sizes can easily modify the crystalline topological order (Fig. 2(b)), the interconnection of regular SiO$_4$ tetrahedra with shared oxygen atoms at corners only yields the broadened Bragg peak as the FSDP.

As can be seen in Fig. 1(a), an FSDP is absent in $S_{NN}(Q)$ for *l*-ZrO$_2$. This is because the variety of short-range structural units with large oxygen coordination, ZrO$_5$, ZrO$_6$, and ZrO$_7$, and the large contribution of oxygen edge sharing prevent the formation of intermediate-range ordering. Short-range structural disordering in *l*-ZrO$_2$ is further demonstrated in the three-dimensional atomic configuration and the schematic illustration of *l*-ZrO$_2$ (Fig. 2(c)). The periodicity of boundaries (dashed lines) is suppressed by the edge sharing of oxygen associated with the formation of ZrO$_5$, ZrO$_6$, and ZrO$_7$. Although ZrO$_2$ forms a network structure by interconnecting AX polyhedra in the liquid phase, we have shown that the various short-range structural units and their connectivity cause disorder in the intermediate range and prevent the evolution of an FSDP for the liquid. The absence of an FSDP in $S_{NN}(Q)$ of *l*-ZrO$_2$ suggests that *l*-ZrO$_2$ is an extremely fragile liquid. The fragility of *l*-ZrO$_2$ is confirmed by its very low viscosity (–2×10^{-3} Pa·s^{-1} at 2,800°C) and the short lifetime of the Zr-O bond (DF–MD simulation showed that 50% of the bonds break within 185 fs at 2,800°C).

In this study, we have succeeded in uncovering the relationship between structure and glass-forming ability in single-component oxide liquids. Finally, we stress that the containerless preparation and measurement techniques provide new tools for the study of unique features of extremely high temperature liquids, and we demonstrate the importance of combining experiment and theory for understanding the nature of liquids at the atomic (structure and dynamics) and electronic (chemical bonding) levels.

(a) ***c*-SiO$_2$**

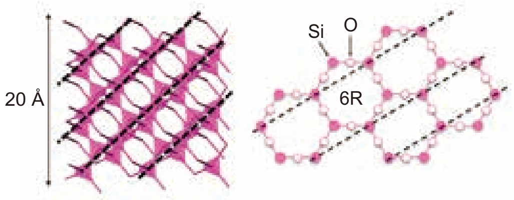

(b) ***l*-SiO$_2$ (2100°C)**

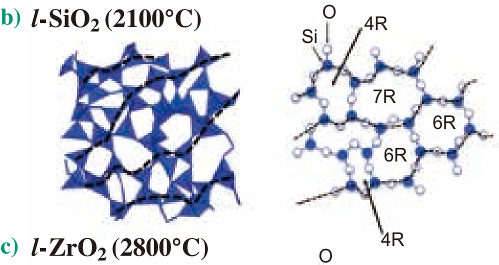

(c) ***l*-ZrO$_2$ (2800°C)**

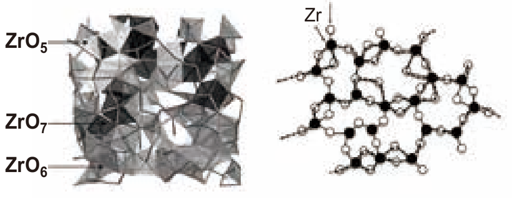

Fig. 2. Atomic configurations and schematic illustrations of **(a)** *c*-SiO$_2$, **(b)** *l*-SiO$_2$, and **(c)** *l*-ZrO$_2$. The periodicity of the cage boundaries is highlighted by dashed lines and curves.

Shinji Kohara[a,b,*] and Koji Ohara[b]

[a] Synchrotron X-ray Group,
National Institute for Materials Science (NIMS)
[b] Japan Synchrotron Radiation Research Institute (JASRI)

*E-mail: KOHARA.Shinji@nims.go.jp

References

[1] W.H. Zachariasen: J. Am. Chem. Soc. **54** (1932) 3841.
[2] K.-H. Sun: J. Am. Ceram. Soc. **30** (1947) 277.
[3] C.A. Angell: Science **267** (1995) 1924.
[4] *S. Kohara, J. Akola, L. Patrikeev, M. Ropo, K. Ohara, M. Itou, A. Fujiwara, J. Yahiro, J. T. Okada, T. Ishikawa, A. Mizuno, A. Masuno, Y. Watanabe and T. Usuki: Nat. Commun.* **5** *(2014) 5892.*
[5] A. Takada *et al.*: J. Non Cryst. Solids **345-346** (2004) 224.
[6] A.B. Bhatia & D.E. Thornton: Phys. Rev. B **4** (1971) 3004.
[7] Q. Mei *et al.*: Phys. Rev. B **78** (2008) 144204.
[8] S. Kohara *et al.*: Proc. Natl. Acad. Sci. USA **108** (2011) 14780.

Remarkable dispersion of the acoustic mode in liquid Bi linked to Peierls distortion

More than 50 years ago, Peierls [1] suggested that in a one-dimensional metal with a half-filled band, a regular chain structure (see Fig. 1(a)) is not stable, and a structural distortion (see Fig. 1(b)) allows the reduction of the system energy accompanied by a metal-to-insulator transition. This structural instability, the Peierls distortion, is realized in crystalline materials, including elemental As, Sb and Bi with the A7 structure (see Fig. 1(c)), where a distortion of a simple cubic structure divides the six equal-length nearest-neighbor bonds into three short ones and three long ones. It is then interesting to consider the possibility of an analogous distortion in a liquid, and indeed hints of anisotropic bonding has been observed in liquid As. The nearest-neighbor coordination number for liquid Bi is in fact about 10, different from that of liquid As, so the analogy is not perfect. However, the structure factor of liquid Bi exhibits a shoulder on the high momentum transfer side of the first maximum, which suggests that there might be anisotropic bonding similar to in liquid As.

Considering previous investigations of liquid Bi, it is noted that very recent *ab initio* molecular dynamics (AIMD) simulations suggested that for liquid Bi the acoustic mode excitation energy should be almost constant for $8 \leq Q \leq 17$ nm^{-1} [2]. This is very different from the sinusoidal dispersion observed in simple liquid metals. However, although the AIMD simulation [2] showed the acoustic mode excitation survived up to 17 nm^{-1}, inelastic neutron scattering (INS) results for liquid Bi suggested that the acoustic mode in liquid Bi disappeared for $Q > 6$ nm^{-1}. As classical molecular dynamics (CMD) simulations for liquid Bi also exhibited no distinct acoustic excitation for $Q > 6$ nm^{-1}, it was suggested that the disappearance of the inelastic excitation of the acoustic mode arises from an interatomic interaction unique to liquid Bi. However, other INS spectra measured in Japan suggested the excitation was visible for $Q \geq 6$ nm^{-1} [2]. In this context of unusual and possibly contradictory results from both experiments and calculations, it is then very interesting to make clear measurements of the dynamic structure factor, $S(Q, E)$, of liquid Bi, where Q and E are the momentum and energy transfers, respectively.

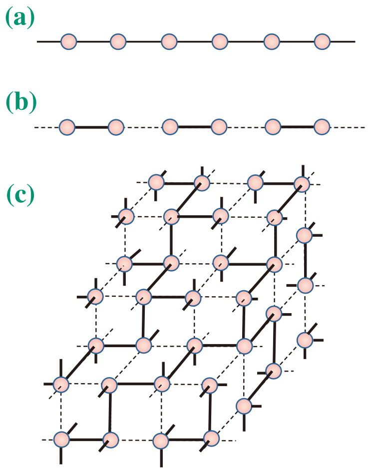

Fig. 1. (a) Regular chain. (b) Linear chain with a lattice distortion. Bold black lines denote shorter bonds. (c) Schematic structure of crystalline Bi on a simple cubic lattice. Bold black lines denote shorter bonds in the A7 structure.

Inui *et al*. investigated $S(Q, E)$ of liquid Bi using inelastic X-ray scattering (IXS) [3]. The IXS technique avoids the kinematic constraints, which limit INS studies, so good spectra are obtained up to large energy transfers. The very high photoelectric X-ray absorption of Bi makes IXS experiments challenging, but they are possible by taking advantage of new powerful beamlines and improved sample cell techniques. Inui *et al*. [3] were then able to obtain high-quality IXS spectra which, when complemented by new AIMD and CMD simulations and compared carefully against previous data sets, allowed them to resolve previous discrepancies.

The experiments were conducted at the high-resolution IXS beamline **BL35XU** [4]. Liquid Bi of 99.999% purity was mounted in a Tamura-type single-crystal sapphire cell [5] that was carefully machined to provide a 0.04 mm sample thickness. IXS spectra of liquid Bi were measured at 573 K and 1023 K. After scaling for sample transmission, the backgrounds were subtracted from the data and $S(Q, E)$ was obtained, as shown for liquid Bi at 573 K in Fig. 2. The profile at the lowest Q exhibits a central peak with the inelastic excitation of the acoustic mode clearly visible on each side. Notably, with the relatively good quality data, the inelastic excitation is preserved even at 14.6 nm^{-1}, much larger than 6 nm^{-1}.

$S(Q, E)$ of liquid Bi was analyzed with the memory function formalism to determine the excitation energy of the acoustic mode. The results are shown in Fig. 3 as a function of Q. The mode energy (black circles) disperses linearly for $Q \geq 7$ nm^{-1}, whereas for $8 \leq Q \leq 15$ nm^{-1} the dispersion flattens and the energy remains approximately constant at 8.5 meV. The IXS results are consistent with previous AIMD predictions [2], and more recent calculations [3]. Thus, the anomalous dispersion of liquid Bi is real, and it now remains to obtain some understanding of its origin.

A linear chain model provides some insight into the origin of the anomalous dispersion, as discussed in [3], Figure 3 shows the excitation energy of the acoustic mode of a regular chain (see Fig. 1(a)) as a function of Q. A sinusoidal dispersion curve exhibiting a maximum at 10 nm^{-1} is not consistent with the IXS results. On the other hand, a linear chain model with a lattice distortion (see Fig. 1(b)) reproduces the flat dispersion curve well, as denoted by the red line in Fig. 3. In effect, an additional Fourier component is needed to model the dispersion, which Inui *et al.* linked to different length/strength bonds. This suggests that the medium-range structure of liquid Bi takes an atomic configuration with the Peierls distortion, similarly to crystalline Bi shown in Fig. 1(c).

The present IXS research on collective dynamics reveals that liquid Bi preserves anisotropic bonding. It might be difficult to demonstrate the anisotropic bonding from the radial distribution function obtained by total scattering measurements. The present result suggests that the atomic configuration in the liquid state near the melting point is determined by the interatomic interaction on a nanometer length scale similarly to that in the solid state.

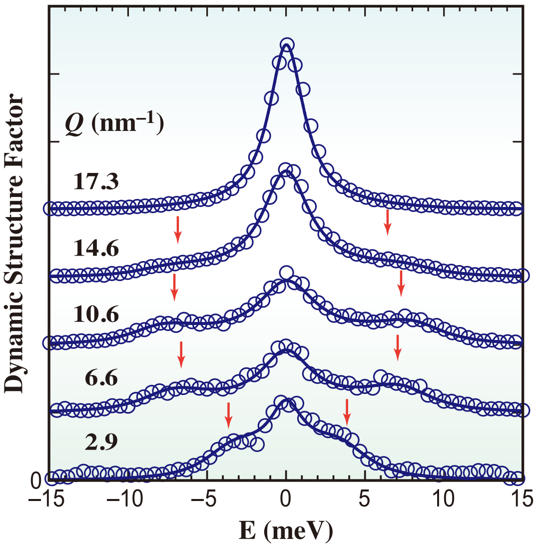

Fig. 2. Dynamic structure factor of liquid Bi at 573 K. Open circles and a bold line denote the IXS and the fitting results with the memory function, respectively. Red arrows indicate the inelastic excitations of the acoustic mode.

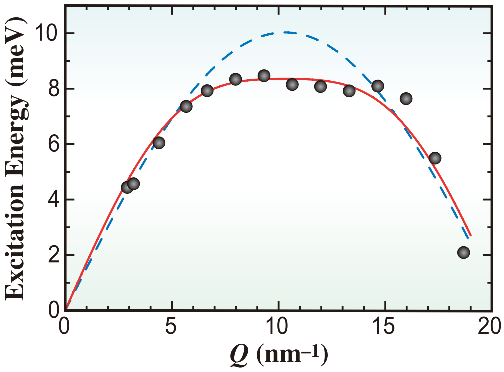

Fig. 3. Excitation energy of the acoustic mode in liquid Bi obtained by IXS (black circles). Also shown are the dispersion curve of the regular chain (blue broken line) and that of the distorted chain (red solid line) shown in Figs. 1(a) and 1(b), respectively.

M. Inui[a,*], Y. Kajihara[a], S. Munejiri[a] and A. Q. R. Baron[b]

[a] Graduate School of Integrated Arts and Sciences,
Hiroshima University
[b] RIKEN SPring-8 Center

*E-mail: masinui@hiroshima-u.ac.jp

References

[1] R. E. Peierls, "Quantum Theory of Solids" (Oxford University Press, 1955)
[2] J. Souto *et al.*: Phys. Rev. B **81** (2010) 134201 and references therein.
[3] *M. Inui, Y. Kajihara, S. Munejiri, S. Hosokawa, A. Chiba, K. Ohara, S. Tsutsui and A. Q. R. Baron: Phys. Rev. B* ***92*** *(2015) 054206.*
[4] A.Q.R. Baron *et al.*: J. Phys. Chem. Solids **61** (2000) 461.
[5] K. Tamura *et al.*: Rev. Sci. Instrum. **70** (1999) 144.

Proposal to generate an isolated monocycle X-ray pulse by counteracting the slippage effect in free-electron lasers

A monocycle pulse is an ultrashort light wave whose pulse length is reduced to the theoretical lower limit, namely, the wavelength of light. In the visible and infrared regions, the generation of monocycle pulse with a conventional laser has become a mature technology, and ultrashort pulses with a pulse length of several femtoseconds are already available that are used to probe ultrafast dynamics such as the chemical reaction and physical phenomenon. On the other hand, the generation of monocycle pulses in the X-ray region, i.e., the generation of monocycle X-ray free electron laser (XFEL) pulses, has not been realized and possible methods of producing them are yet to be proposed.

In XFELs, a high energy electron beam injected to an undulator generating a periodic magnetic field works as the laser medium. During the amplification process of XFEL, density modulation is performed in an electron beam with a period equal to the laser wavelength, which is called "microbunch," and the pulse length of the XFEL is roughly equal to that of the microbunch. Thus, it seems possible to generate a monocycle XFEL pulse if the microbunch is shortened to the scale of the laser wavelength (single microbunch) as shown in Fig. 1(a). In practice, however, the pulse length increases while the electron beam travels along a sinusoidal orbit in the undulator because the light wave overtakes the electron beam and shifts forward. As a result, the pulse length of XFEL generated by a single microbunch increases proportionally to the number of undulator periods.

The above phenomenon is generally called an optical slippage effect and has been the biggest obstacle to the realization of monocycle XFEL pulses. We have proposed a new scheme to suppress this effect using the interference of light waves to control the pulse length of XFEL, and we have numerically demonstrated its principle and feasibility [1].

In the proposed scheme, an electron beam with a microbunch having an irregular interval is injected to an undulator whose magnetic field amplitude is varied along its axis. What is important is that the n-th microbunch interval ($=\lambda_n$) is equal to the slippage length of the n-th undulator period. The simplest example that satisfies this requirement is shown in Fig. 1(b), where λ_n linearly changes with the period number n, and such a microbunch is referred to as a "chirped microbunch."

Now let us consider the radiation process of an electron beam with a chirped microbunch using Fig. 2. Figure 2(i) shows the outline of the current profile of the electron beam with a chirped microbunch, in which the electron beam current I is given as a function of the longitudinal position s. In this example, 11 microbunches are contained with the interval (λ_1–λ_{10}) that linearly decreases. The electron beam is then injected to an undulator with the n-th slippage length equal to λ_n. In order to satisfy this condition, a special undulator with the magnetic field amplitude decreasing linearly, which is called a tapered undulator, can be used. Figure 2(ii) shows schematically the waveform of light generated by the chirped microbunch after the

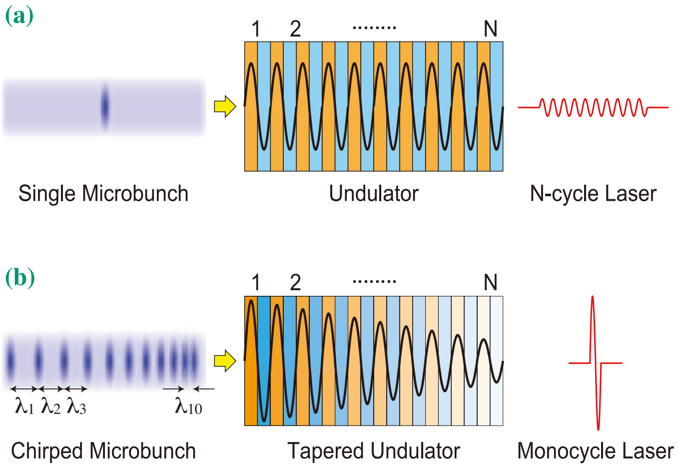

Fig. 1. Radiation process of an electron beam with **(a)** a single microbunch and **(b)** a chirped microbunch.

electron beam passes through the 1st period, where the electric field of radiation E is given as a function of s. Thus, the electron beam wiggling once emits light with the waveform similar to its current profile. It should be emphasized here that the light wave is shifted forward by the distance λ_1 because of the optical slippage effect. The peak indicated by an arrow denotes the position of the light pulse (hereinafter, resonant pulse) generated by the microbunch located at the tail position, which is shown by the dashed line and is defined as the origin of the coordinate. At this stage, the position of the resonant pulse is λ_1 ahead of the origin.

Figure 2(iii) shows the waveform of light after the 2nd period. The red solid line indicates the waveform generated at the 1st period, while the blue dotted line indicates that at the 2nd period. The slippage length at the 2nd period is λ_2 not λ_1, and thus the resonant pulse is located at $s = \lambda_1 + \lambda_2$. In Figs. 2(iv) and 2(v), the waveforms of light after the 3rd and 4th periods are shown in green dashed and cyan chain lines, respectively. The red solid lines shown in Fig. 2(vi) denote the waveforms created between the 1st and 10th periods, while the dashed line denotes the waveform created by summing all of them. It is easy to understand that the intensity of the resonant pulse is significantly enhanced by constructive interference, while those of other pulses are suppressed by destructive interference. The intensity contrast between the resonant and other pulses can be controlled by the change rate of the slippage length ($\lambda_1 - \lambda_{10}$), and a monocycle pulse can be ultimately generated.

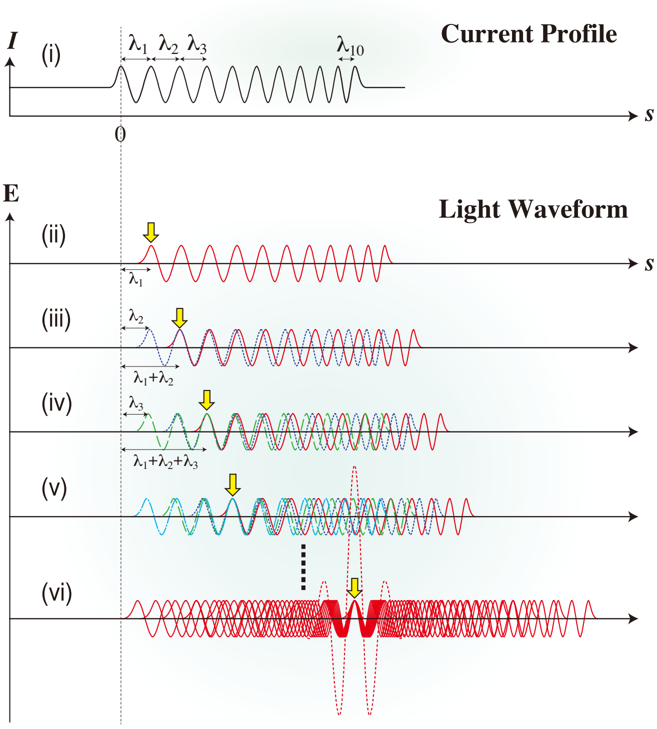

Fig. 2. Schematic illustration to explain the principle of operation of the proposed scheme. **(i)** Current profile of the electron beam with a chirped microbunch. **(ii)–(v)** Light waveforms emitted by the electron beam after the 1st–4th undulator periods. **(vi)** Light waveforms after the 10th period.

One idea for the practical implementation of the above principle in XFELs is in the so-called high gain harmonic generation (HGHG) FELs, in which a seed laser is upconverted through interaction with an electron beam moving in an undulator. This is referred to as monocycle harmonic generation (MCHG), and the most important advantage of MCHG over the normal HGHG is that the monocycle pulse can be upconverted without the pulse lengthening due to the optical slippage.

In order to demonstrate the feasibility and performance of MCHG, we carried out FEL simulations with the assumption that a monocycle pulse with a central wavelength of 60 nm and a pulse energy of 10 μJ is used as a seed laser to drive the MCHG scheme with an electron beam having an energy of 2 GeV and current of 2 kA. It has been found that a monocycle pulse with a peak power of 1.2 GW and pulse length of 46 as (attoseconds) is generated at the 7th harmonic, i.e., at the central wavelength of 8.6 nm.

The above example validates the feasibility of the proposed scheme in the soft X-ray region; however, it should be emphasized that no theoretical limit exists for the available wavelength. It is thus expected to open up a new field of research, so to speak, "zeptosecond science," by applying this scheme in the hard X-ray region, which will enable us to generate a monocycle X-ray pulse with a pulse length of several hundreds of zeptoseconds.

Takashi Tanaka

RIKEN SPring-8 Center

E-mail: ztanaka@spring8.or.jp

Reference

[1] *T. Tanaka: Phys. Rev. Lett.* ***114*** *(2015) 044801.*

Nanoplasma formation in rare-gas clusters ignited by intense X-ray free-electron laser pulses from SACLA

In early 2012, a new X-ray free-electron laser (XFEL) facility, the SPring-8 Angstrom Compact free electron LAser (SACLA) [1], started user operation. As one of the first experiments at SACLA, we performed an experiment to observe multiphoton multiple ionization of heavy Xe atoms [2]. We found that the ionization of heavy atoms irradiated by intense XFEL pulses rapidly progresses by repeated inner-shell photoionization and subsequent Auger/Coster-Kronig decay within the XFEL pulse duration. What will happen to heavy atomic clusters exposed to intense XFEL pulses? It is known that a nanoplasma is formed when clusters are irradiated by intense lasers with longer wavelengths. Rare-gas clusters exposed to an intense near infrared (NIR) laser field are probably the best-studied system. In the NIR laser field, field ionization takes place. A nanoplasma is formed when the electrons escaping from their mother atoms still remain within the Coulomb potential of the multiply charged cluster ion (i.e., inner ionization). The trapped electrons further acquire energy from the laser field via the inverse bremsstrahlung (IBS). When the electrons acquire sufficient energy, they escape from the cluster (i.e., outer ionization). When the laser field is turned off and the nanoplasma expands, electrons trapped in the nanoplasma are mostly recombined with the individual atomic ions. Rare-gas clusters exposed to intense extreme ultraviolet (EUV) laser pulses have also been studied extensively since the advent of EUVFELs. In the EUV regime, the main mechanism of the cluster ionization and heating is single-photon absorption of the individual atoms in the cluster. The outer ionization proceeds first if the photon energy is higher than the ionization potential of the individual atoms. With the increase in the charge of the cluster, the photoelectrons are decelerated and eventually trapped, although inner ionization still proceeds. As the number of trapped electrons increases, a nanoplasma is eventually formed. The following question now arises: is nanoplasma also formed by XFEL irradiation? We have investigated this question by electron spectroscopy using Ar and Xe clusters as target species [3,4].

The experiment was carried out at experimental hutch 3 (EH3) of beamline **BL3** of SACLA [5]. The XFEL beam is focused by a Kirkpatrick-Baez mirror system to a focal size of ~1 μm (FWHM) in diameter. Rare-gas (Ar or Xe) clusters were prepared by adiabatic expansion of the rare gases through a 25 μm nozzle at room temperature. The cluster beam was skimmed by two skimmers placed 20 and 400 mm from the nozzle. The inner diameters of the first and second skimmers were 0.5 and 2 mm, respectively. The distance between the second skimmer and the reaction point was 250 mm. The cluster beam at the reaction point was estimated to be ~2 mm (FWHM) in diameter. Thus, the source volume of the electrons was roughly cylindrical, ~1 μm in diameter and ~2 mm along the XFEL beam. The XFEL pulse energies were measured by a beam-position monitor located upstream of the beamline. The relative X-ray pulse energy passing through the interaction point was also measured shot-by-shot by a PIN photodiode.

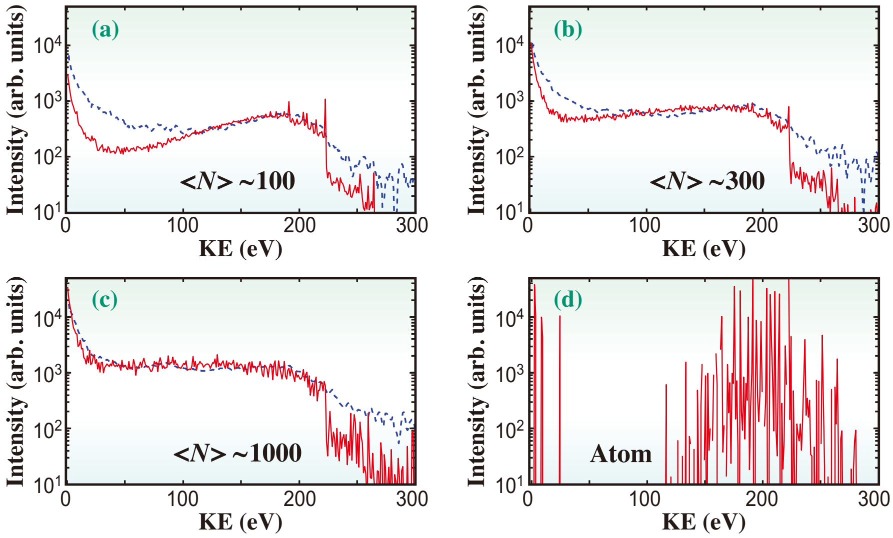

Fig. 1. Electron spectra of Ar clusters at a photon energy of 5 keV [3]. The peak fluence was ~50 μJ/μm^2. Dashed lines are the experimental results and solid lines are corresponding theoretical results.

Electrons produced in the source volume were extracted towards a velocity map imaging (VMI) spectrometer equipped with microchannel plates (MCPs) and a phosphor screen. Electron detection images on the phosphor screen were recorded using a CCD camera synchronized with the arrival of the FEL pulse in the interaction chamber. The measured two-dimensional projection allows us to obtain three-dimensional momentum distributions of the ejected electrons using the inverse Abel transformation.

Figure 1 depicts the electron spectra of Ar clusters with different average cluster sizes $\langle N \rangle$ at a photon energy of 5 keV [3]. The peak fluence of the XFEL pulse determined via the calibration using Ar atoms [2] was ~50 μJ/μm^2. In the spectrum for $\langle N \rangle$~100, we can identify a broad peak around 150–250 eV due to the LMM Auger electrons emitted after the KLL Auger process. The intensity of electron emission below 150 eV increases when the cluster size increases. This trend is interpreted as follows with the help of theoretical calculations that reproduce the experimental spectra as shown in Fig. 1 [3]. When the cluster is exposed to intense XFEL pulses, atoms in the cluster are ionized by photoionization and subsequent Auger decay(s). The charge state of the cluster increases when the number of ionized atoms increases. As a result, the LMM Auger electrons are decelerated by the positive potential from the highly charged cluster and form a plateau in the electron spectra. The decelerated electrons are eventually trapped by the cluster ions. The LLM Auger electrons and the secondary electrons produced by the low-energy electron impact are also trapped. As a result, we expect that a nanoplasma is formed. The peak at zero kinetic energy is due to thermal emission and is thus evidence of nanoplasma formation.

Figure 2(a) depicts the electron spectra of Xe clusters with different $\langle N \rangle$ exposed to XFEL pulses at a photon energy of 5.5 keV. The peak fluence was ~50 μJ/μm^2. In the spectrum for $\langle N \rangle$ ~80, there are peaks due to L_2 and L_3 photoemissions and MNN Auger emission at ~400 eV, ~700 eV, and ~500 eV, respectively. The valleys between the peaks become plateaus when $\langle N \rangle$ increases. This trend is also interpreted as the deceleration of the photoelectrons and Auger electrons by the Coulomb potentials from the charged cluster. A peak due to thermal emission from the nanoplasma at zero kinetic energy is also observed. Figure 2(b) depicts the peak fluence dependence of the electron spectrum of the Xe cluster with $\langle N \rangle$ ~10000. It is worth noting that the strong peak at zero kinetic energy is observed even at the peak fluence of the XFEL pulse of ~2.5 μJ/μm^2. In this case, only ~5% of the Xe atoms in the cluster are photoionized. This indicates that the nanoplasma is efficiently produced for the Xe clusters by Auger cascades and secondary ionization events.

In conclusion, we have investigated phenomena in rare-gas clusters exposed to intense XFEL pulses by electron spectroscopy and found that a nanoplasma is formed by trapping low-energy electrons. Note that nanoplasma formation can always occur whenever matter is exposed to intense XFEL pulses.

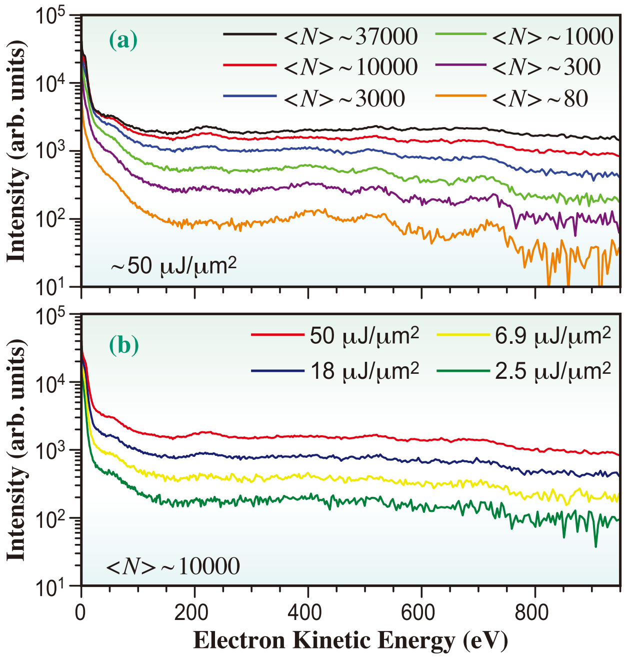

Fig. 2. Electron spectra of Xe clusters at a photon energy of 5.5 keV [4]. **(a)** Spectra for different $\langle N \rangle$ at peak fluence of ~50 μJ/μm^2. **(b)** Spectra for different peak fluences at $\langle N \rangle$ of ~10000.

Hironobu Fukuzawa[a,b], Tetsuya Tachibana[a,b]
and Kiyoshi Ueda[a,b,*]

[a] Institute of Multidisciplinary Research for Advanced Materials, Tohoku University
[b] RIKEN SPring-8 Center

*E-mail: ueda@tagen.tohoku.ac.jp

References

[1] T. Ishikawa *et al.*: Nat. Photonics **6** (2012) 540.
[2] H. Fukuzawa *et al.*: Phys. Rev. Lett. **110** (2013) 173005.
[3] *T. Tachibana, Z. Jurek, H. Fukuzawa, K. Motomura, K. Nagaya, S. Wada, P. Johnsson, M. Siano, S. Mondal, Y. Ito, M. Kimura, T. Sakai, K. Matsunami, H. Hayashita, J. Kajikawa, X.-J. Liu, E. Robert, C. Miron, R. Feifel, J. P. Marangos, K. Tono, Y. Inubushi, M. Yabashi, S.-K. Son, B. Ziaja, M. Yao, R. Santra, K. Ueda: Sci. Rep.* **5** *(2015) 10977.*
[4] *H. Fukuzawa et al.: J. Phys. B:* **49** *(2016) 034004. (Published 8 January 2016)*
[5] K. Tono *et al.*: New J. Phys. **15** (2013) 083035.

Surface-regulated nano-SnO_2/Pt_3Co/C cathode catalysts for polymer electrolyte fuel cells prepared by a new Sn deposition method

The development of next-generation polymer electrolyte fuel cells (PEFCs) with high performance and durable cathode catalysts under harsh PEFC operating conditions is indispensable for the widespread commercialization of PEFC vehicles. Various Pt-M alloy/C catalysts have been studied as promising cathode catalysts and considerable effort has been devoted to the fabrication of Pt-Co nanostructures with higher oxygen reduction reaction (ORR) activity and longer-term durability than Pt/C. On the other hand, Pt/C cathode catalysts have been modified by metal oxides to change the redox behavior and improve the ORR activity of Pt nanoparticles. We succeeded in preparing a SnO_2-modified Pt_3Sn/C cathode catalyst with better ORR performance than a Pt/C catalyst [1]. Recently, we have found a new way to fabricate surface-regulated SnO_2/Pt_3Co/C cathode catalysts with SnO_2 nanoislands on a Pt skeleton-skin surface with compressive strain and defects/dislocations on Pt_3Co nanoparticle cores. These catalysts were much more active than expected from the d-band center values [2]. The structural arrangement also created two different reaction sites (Site 1 at the Pt skin surface and the more active Site 2 at the nano-SnO_2 periphery) in a tunable mode with different Pt/Sn ratios. The SnO_2/Pt_3Co/C cathode catalysts were characterized by *in situ* XAFS, XPS, XRD, and TEM/STEM-EDS.

A series of SnO_2/Pt_3Co/C catalysts with Pt/Sn= 4/1, 9/1, 11/1, and 15/1 were prepared by a new selective Sn deposition method while regulating the electrochemical potential at –0.45 V *vs* AgCl in 0.1 M $HClO_4$. We found that at this potential, Sn deposition selectively occurs on the Pt surfaces and the Sn deposition on the carbon support can be neglected. The deposited Sn species were identified as SnO_2 nanoislands by XANES, XPS, and STEM-EDS [2].

Figures 1(a) and 1(c) are HR-TEM images of the Pt_3Co/C and SnO_2/Pt_3Co/C (Pt/Sn=9/1) catalysts, respectively [2]. The lattice contrast profiles of Fig. 1(b) along the red and blue arrows in Fig. 1(a) for a Pt_3Co/C particle revealed the regular Pt_3Co interplane distance for the Pt_3Co core and the Pt interplane distances for three Pt surface layers. The HR-TEM image for the SnO_2/Pt_3Co/C with Pt/Sn=9/1 after aging in Fig. 1(c) showed that the Pt-enriched surface possessed many atomic defects and dislocations, with typical ones indicated by yellow arrows. The lattice contrast profiles in Fig. 1(d) along the red, blue, and green arrows near the defects and dislocations (a-e) in Fig. 1(c) showed irregular intensities and intervals, which is evidence for a rough/skeleton surface morphology at the Pt surface layers. The atomic arrangements indicated compressive strain at the Pt surface layers due to the effect of the underlying Pt_3Co core structure. Figures 1(e) and 1(f) are a TEM image of the SnO_2/Pt_3Co/C catalyst (Pt/Sn=9/1) and EDS line profiles showing the Pt-enriched surface with SnO_2 nanoislands, respectively.

The ORR activities of the fabricated cathode catalysts were estimated by linear sweep voltammetry (LSV) at 0.9 V_{RHE}, and the mass activities (MAs) and surface specific activities (SAs) were estimated using Koutecky-Levich plots calculated from the LSV curves [2]. The MA of Pt_3Co/C was 2.2 times larger than that of Pt/C, and both values were within the MA values in the literature. Note that the MA of Pt_3Co/C was further increased by a factor 2.4 by the addition of SnO_2 (Pt/Sn=9/1). Thus,

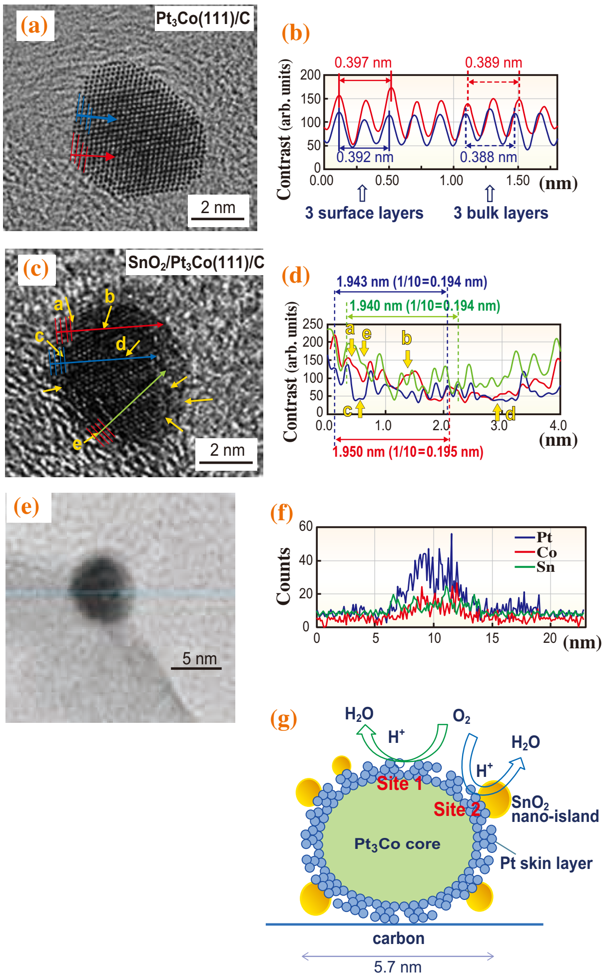

Fig. 1. **(a)** Atomic arrangement of $Pt_3Co(111)$ plane in a TEM image of Pt_3Co/C after aging. **(b)** Lattice contrast profiles for the interplane distances along the red and blue arrows in (a). **(c)** Atomic arrangement of $Pt_3Co(111)$ plane in a TEM image of SnO_2/Pt_3Co/C (Pt/Sn=9/1) after aging. Yellow arrows show typical defects and dislocations. **(d)** Lattice contrast profiles for the interplane distances along the red and blue arrows in (c). **(e)** TEM image of the SnO_2/Pt_3Co/C catalyst (Pt/Sn=9/1) and **(f)** EDS line profiles for Pt (blue), Co (red), and Sn (green) along the light blue line in the TEM image. **(g)** Model structure and proposed ORR sites for the nano-SnO_2-decorated Pt_3Co/C catalyst with a Pt skeleton surface with compressive strain and defects/dislocations. [2]

the MA of the $SnO_2/Pt_3Co/C$ catalyst (Pt/Sn=9/1) was 5.4 times larger than that of the Pt/C catalyst. This advantage of the $SnO_2/Pt_3Co/C$ catalyst (Pt/Sn=9/1) was also maintained after 5,000 load cycles, where the MA of $SnO_2/Pt_3Co/C$ was 7.8 times larger than that of Pt/C, showing the high durability of $SnO_2/Pt_3Co/C$. There was an optimum amount of SnO_2 for improving the ORR and durability. The SA of $SnO_2/Pt_3Co/C$ with Pt/Sn=11/1 after 5,000 load cycles was 5.0 times larger than that of Pt/C. However, the SA in the case of Pt/Sn=4/1 decreased almost linearly with increasing number of load cycles. Thus, the MA and SA of the $SnO_2/Pt_3Co/C$ catalysts are highest around Pt/Sn=9-11/1 [2].

The SAs of the catalysts were plotted against the CO stripping peak potential in Fig. 2(a) and changed as follows: Pt/C < Pt_3Co/C < $SnO_2/Pt_3Co/C$ (Pt/Sn=15/1) < $SnO_2/Pt_3Co/C$ (Pt/Sn=11/1) > $SnO_2/Pt_3Co/C$ (Pt/Sn=9/1) > $SnO_2/Pt_3Co/C$ (Pt/Sn=4/1), resulting in a volcano-shaped relationship between the CO stripping peak potential (relative d-band center) and the SA. The SAs of Pt-alloy catalysts have also been demonstrated to reveal a volcano-shaped relationship with the d-band center energy, as shown in the green dotted line in Fig. 2(a), where the two values reported in the literature for each of Pt/C (1), Pt_3Ni/C (2), Pt_3Co/C (3), Pt_3Fe/C (4), Pt_3V/C (5), and Pt_3Ti/C (6) were averaged and the values for Pt_3Co/C and Pt/C were normalized to the CO stripping peak potentials, respectively measured in this study [2]. Thus, the nano-SnO_2 in $SnO_2/Pt_3Co/C$ with compressive strain at the Pt skeleton surface layers electronically modified the 5d level to decrease the d-band center, which led to weaker oxygen adsorption and improvement of the ORR. However, the same d-band center value did not show the same ORR activity (Fig. 2(a)), which indicates the existence of another factor promoting the ORR in the case of $SnO_2/Pt_3Co/C$ catalysts in addition to the appropriate adjustment of the d-band center at the Pt surface sites (Site 1). Additional CO stripping peaks at much lower potentials (700-800 mV) appeared with the nano-SnO_2-decorated catalysts, which are regarded as being due to events at new surface sites (Site 2) [2]. We propose that the peripheral sites of the SnO_2 nanoislands with proton affinity at the Pt skeleton surface may provide these lower potential CO stripping sites and hence new ORR sites (Site 2 in Fig. 1(g)) for more weakly adsorbed O_2, facilitating the H^+-O_2 interaction [2].

To obtain electronic and structural information on the nano-$SnO_2/Pt_3Co/C$ catalysts, we conducted *in situ* XAFS measurements of RDE in 0.1 M $HClO_4$ by using a laboratory-built *in situ* XAFS cell at **BL36XU** [2]. Figure 2(b) shows the peak heights of the white lines ($2p \rightarrow 5d$) in the *in situ* Pt L_{III}-edge XANES spectra of Pt/C, Pt_3Co/C, and $SnO_2/Pt_3Co/C$ under stepwise changes in the potential at the RDE in 0.1 M $HClO_4$. In the potential gain process, the catalysts showed an increase in the white-line intensity above 0.8 V_{RHE}, indicating a positive charge of the Pt surfaces due to Pt-O bonding. During the decrease in potential from 1.0 V_{RHE} to 0.4 V_{RHE} the white-line responses for the Pt/C and Pt_3Co/C did not retrace those in the potential gain process, showing a clear hysteresis [3]. It is notable that the nano-$SnO_2/Pt_3Co/C$ exhibited no hysteresis in the potential operation between 0.4 and 1.0 V_{RHE}. Oxygen species adsorbed on the $SnO_2/Pt_3Co/C$ surface at 1.0 V_{RHE} are readily reduced below 1.0 V_{RHE}, resulting in higher ORR performance [2].

In conclusion, the significant improvements in the ORR activity and durability were achieved with new nano-$SnO_2/Pt_3Co/C$ catalysts, which were regulated by a strategic fabrication using a new selective electrochemical Sn deposition method and subsequent chemical treatments. The nano-$SnO_2/Pt_3Co/C$ catalysts possessed a Pt_3Co core/Pt skeleton-skin structure decorated with SnO_2 nanoislands at the surface. Their high performances originated from the unique reactive periphery of the SnO_2 nanoislands at the compressive Pt surface with defects and dislocations. The present results provide a new insight into the development of a new class of next-generation PEFC cathode catalysts [2].

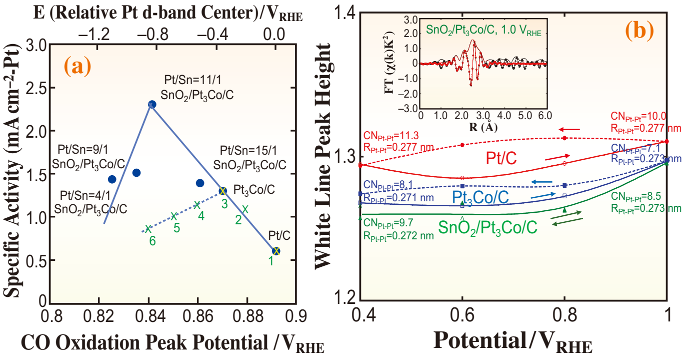

Fig. 2. **(a)** Relationship between the SAs and CO stripping peak potentials for $SnO_2/Pt_3Co/C$ (Pt/Sn=4/1, 9/1, 11/1, and 15/1), Pt_3Co/C, and Pt/C (see [2]). **(b)** White-line peak heights in the *in situ* XANES spectra for Pt/C (red), Pt_3Co/C (blue), and $SnO_2/Pt_3Co/C$ with Pt/Sn=11/1 (green) in the potential gain and decrease processes every 0.2 V between 0.4 and 1.0 V_{RHE}. Inset: results of EXAFS Fourier transform and curve fitting for $SnO_2/Pt_3Co/C$ (Pt/Sn=11/1) at 1.0 V_{RHE}. [2]

Kensaku Nagasawa*, Shinobu Takao and Yasuhiro Iwasawa

Innovation Research Center for Fuel Cells,
The University of Electro-Communications

*E-mail: k.nagasawa@pc.uec.ac.jp

References

[1] G. Samjeské *et al.*: Phys. Chem. Chem. Phys. **15** (2013) 17208.
[2] *K. Nagasawa, S. Takao, S. Nagamatsu, G. Samjeské, O. Sekizawa, T. Kaneko, K. Higashi, T. Yamamoto, T. Uruga and Y. Iwasawa: J. Am. Chem. Soc.* ***137*** *(2015) 12856.*
[3] K. Nagasawa *et al.*: Phys. Chem. Chem. Phys. **16** (2014) 10075.

Breakthrough in energy density of lithium ion batteries by spectroscopic X-ray diffraction

Global paradigm shift in energy supply and usage, which partially stems from the accident of nuclear power plant, calls for emergence of next-generation battery. Among various energy storage systems, lithium-ion batteries (LIBs) are the most promising candidates not only for portable electronics but also for large-scale energy storage at present. In practice, LIBs greatly contributed to the recent commercialization of eco-friendly electric vehicles. Although many studies on their performance have been made, there is still room for improvement of LIBs in terms of energy density per volume associated with how to strike a balance between the amount of active materials and pore volume for Li^+ diffusion in the composite electrode being composed of the active materials, binders and conductive agents. Such a manufacturing problem known as "packing-limitation" tends not to be spotlighted presumably because of analytical requirements totally different from those used in material synthesis.

Besides, recent progress on synchrotron optics using a compact channel-cut monochromator paved the way for the simultaneous use of *Spectroscopy* and *Diffraction*, resulting in successful understanding of electrochemical reactions for two-phase-coexistence-type-compound-electrode in LIBs [1]. This methodological approach motivated us to work out "spectroscopic X-ray diffraction (S-XRD)" in the true sense of the word. If, instead of using white X-rays as is often the case with energy-dispersive XRD, continuous irradiation with highly monochromatic X-rays in wide-ranging energy region was available, the diffraction spectrum as a function of the X-ray energy would be obtained [2]. This article covers a brief description as to the principle of S-XRD and introduces *operando* inspection for LIBs using high-energy-density electrodes as a demonstration analysis to break the ice for future industrial applications.

S-XRD is based on the rotation of the compact channel-cut crystal, indicating that a slight change in the height of the exited beam after the monochromator is inevitable (Fig. 1(a)). In the case of beamline **BL28XU**, the gap of the Si monochromator system is as small as 3 mm. The height change, less than 0.2 mm at the largest in our standard setup (5–30 keV), is smaller than the vertical width of the whole incoming beam. Thanks to two quadrant slits located at the downstream of the monochromator, the position, divergence and incident angle of the monochromatic X-ray on the sample are substantially unchanged with the energy change [2]. Note that the higher harmonics was eliminated by placing double Rh coated mirrors after the monochromator. Here, let us explain several important features of S-XRD. The spatial resolution, *h*, in the direction of the scattering vector under a symmetrical confocal condition using the incident- and receiving-slits is given in the following equation:

$$h = w/\cos(2\theta/2)$$

where *w* is the window size of the slit and 2θ is the angle determined by the incident X-ray and detector directions. The profile resolution, i.e., $\Delta d/d$, can be expressed as the contribution of the angular divergence ($\Delta\theta$) including the angle of view geometrically defined by the instrument and the energy resolution of monochromating device (ΔE) as follows:

$$|\Delta d/d| = |\Delta E/E| + |\cot\theta|\,\Delta\theta$$

where $\Delta E/E$ is the bandwidth of the Si_{111} channel-cut monochromator which typically offers the energy resolution on the order of 10^{-4} at BL28XU.

We compare powder XRD data for $Li_1Ni_{1/3}Co_{1/3}Mn_{1/3}O_2$ (NCM) film-type sample by the energy-scanning and angle-scanning XRD methods (see Fig. 1(b)). The vertical axis of the diffraction spectrum was normalized by the incident beam

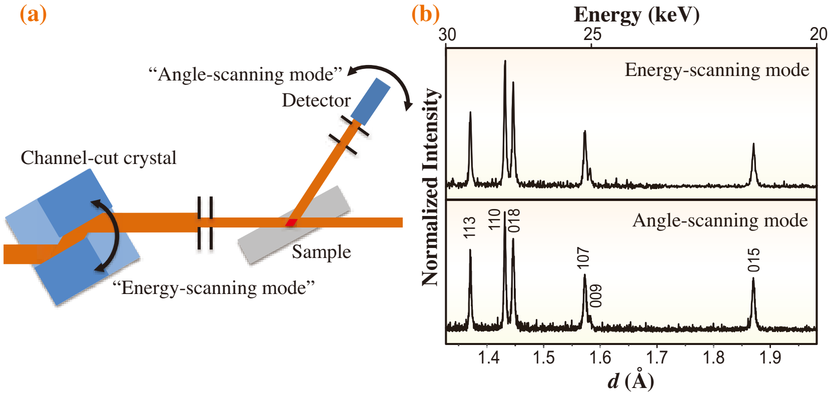

Fig. 1. **(a)** A schematic drawing of the energy-scanning confocal XRD analysis, **(b)** energy-scanning XRD spectrum (top) and angle-scanning XRD pattern (bottom) for the film-type electrode containing $Li_1Ni_{1/3}Co_{1/3}Mn_{1/3}O_2$.

intensity, the self-absorption, the detection efficiency, and the Lorentz's polarization factor. Importantly, the obtained *d*-values and peak intensities are fairly the same as those estimated from the angle-scanning XRD pattern. This result definitely demonstrates the great potential of S-XRD as a microscopic inspection of Li^+ concentration in the electrode of LIBs during the battery operation.

When the electrode density is increased, the specific capacity decreases and finally yields a poor value. This is the packing-limitation in LIBs. To tackle this issue, we focused on the decrease in free space (pore) governed by the amount of active materials in the electrode [3]. Judging from a way of the Li^+ transport in the composite electrode, the denser conformation should be disadvantageous to the Li^+ supply to the deepest part and evokes terrible rate-performance. The *operando* analysis aiming the reaction difference between the inner and outer parts of such a densely packed electrode may pick up the cause of the packing-limitation. Figure 2 shows the variation in Li^+ concentration of NCM at four different depths of the 18% porosity electrode at various discharge rates. Similar lithiation behavior was observed at the four divided positions of the electrode in the low-rate operation (0.1C), indicating that the electrode worked homogeneously. At higher-rate operation (0.5C), the Li^+ concentration differed between positions (i) and (iv). This difference suggests that the packing-limitation is essentially induced by the high-rate operation. Further high-rate operation, 1C, makes the discharge time shorter. The Li^+ concentration for the electrode surface, position (i), at the 1C operation definitely accounts for the cell potential identical to the cut-off potential. Thus, the deterioration of the discharge capacity observed in this study can be explained by the delay of Li^+ transport to the current collector side. Interestingly, the concentration differences among the positions after the discharge were relaxed in response to the potential difference exactly at the end of the discharge. These direct evidences indicate that rate-dependent packing-limitation originates from a bad accessibility of the Li^+ at the deepest part in the composite electrode. This study points out the essential advantage of thinner film-type electrodes in LIBs application and offers a concept to overcome this issue via installation of some shortcut for Li^+ diffusion to the composite electrode.

Lastly, we would like to emphasize again the importance of using S-XRD to understand what gives rise to the limitation of battery performances including the energy density. Further developments in the beamline optics and sources which allow us to brave a variety of scientific adventures, we believe, will boost the growth of battery industry.

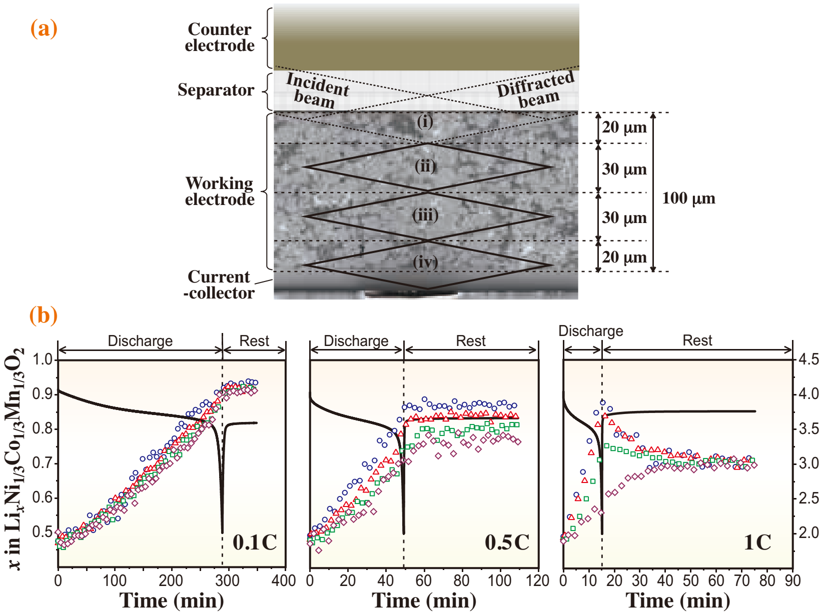

Fig. 2. **(a)** Illustration of the confocal points written on SEM image of the cross-section in the composite electrode. **(b)** Li^+ concentration of the active material (NCM) densely packed in the composite electrodes (~18% porosity). The open symbols (circle, triangle, square, and diamond) correspond to positions (i), (ii), (iii) and (iv), respectively, in the cross-section of the electrode in the top. The lines correspond to the change in cell potential depending on the time. The broken lines show the end of the cell discharge, indicating the specific capacity of the cell.

Katsutoshi Fukuda[a], Tomoya Kawaguchi[a]
and Eiichiro Matsubara[a,b,*]

[a] Office of Society-Academia Collaboration for Innovation, Kyoto University
[b] Dept. of Materials Science & Engineering, Kyoto University

*E-mail: matsubara.eiichiro.6z@kyoto-u.ac.jp

References

[1] K. Tokuda *et al*.: APL Mater. **2** (2014) 07071.
[2] H. Murayama *et al*.: J. Phys. Chem. C **118** (2014) 20750.
[3] *K. Kitada, H. Murayama, K. Fukuda, H. Arai, Y. Uchimoto, Z. Ogumi, E. Matsubara: J. Power Sources* ***301*** *(2016) 11.*

Understanding a battery with high-energy X-ray Compton scattering

Lithium-ion batteries have a high degree of hierarchical complexity, ranging from the quantum scale to the product scale. The respective hierarchies have their own scientific disciplines, such as physics, chemistry, materials science and engineering. As the hierarchies are interdependent on properties and functionality, a single multifunctional probe that can simultaneously provide multiple pieces of information used in different disciplines at different hierarchies is essential to develop economical and safe batteries. In this article, we present the capability of X-ray Compton scattering as a multifunctional probe of commercial batteries by demonstrating a quantum-scale characterization of redox orbitals in an electrode material and a product-scale mapping of the lithium distribution in a commercial battery.

An advantage of X-ray Compton scattering over other techniques is its high bulk-sensitivity, which enables us to measure disordered materials under various sample conditions. The electron momentum density observed by this technique is a ground-state property of an electron system, which allows us to interpret the experimental results straightforwardly with band structure calculations. Moreover, it can also probe materials inside a metal container, such as a commercial battery, which can be penetrated by high-energy X-rays. Therefore, high-energy X-ray Compton scattering is a unique tool for investigating a battery at the quantum and product levels under *in situ* and operando conditions.

The redox orbital is one of the essential concepts in electrochemistry and is defined as an electron orbital involved in the lithium insertion and extraction process. The redox process is mostly described by the change in the formal valency of cations, but its real nature is still controversial. Recently, the redox orbital in spinel $Li_xMn_2O_4$, a positive electrode material, has been studied by high-energy X-ray Compton scattering with highly accurate data measured at beamline **BL08W** [1]. In order to extract the redox orbital, the difference in Compton profiles between two samples with different lithium concentrations is considered (see Fig. 1). This difference enables us to zoom in on changes in electron occupancy near the Fermi level associated with the redox process by eliminating contributions of other irrelevant electrons. The Compton profile is a double integral of electron momentum density, which can be computed directly by modern band structure calculations. In general, each electron orbital has its own radial dependence on electron momentum density, depending on the orbital quantum number. Therefore, an oxygen 2*p* orbital contributes to the electron momentum density at low momenta, whereas the contribution of a manganese 3*d* orbital extends to high momenta. This means that the Compton profile of oxygen 2*p* states is narrow while that of manganese 3*d* states is broad. This tendency applies to the solid state, whose electron momentum density is correctly predicted by first-principles band structure calculations.

As shown in Fig. 1, the band structure calculation is in excellent agreement with the experimental result. The calculation also predicts that the number of electrons in the interstitial region, whose electron charges mostly originate from oxygen 2*p*, increases as the lithium concentration increases, whereas the number of manganese 3*d* electrons is almost constant. This shows

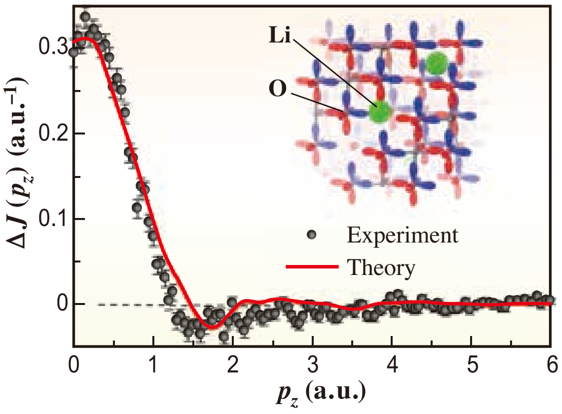

Fig. 1. Electron momentum density distributions (i.e., Compton profiles) of the redox orbitals in $Li_xMn_2O_4$. The experimental results are well reproduced by the theory, implying that electron charge is transferred to oxygen 2*p* states from inserted lithium.

that the active redox orbital possesses a strong oxygen 2*p* character, implying a strong anionic redox process in $Li_xMn_2O_4$. Interestingly, the manganese 3*d* states are inactive in terms of the number of electrons, but the negative excursion observed between 1 a.u. and 2 a.u. in the difference Compton profile reveals the behavior of manganese 3*d* states. The manganese 3*d* states become delocalized in real space by lithium insertion.

One of the current focuses in battery engineering is to understand and control the course of electrochemical reactions throughout the battery. *In situ* and operando observations of inhomogeneous lithium distributions are needed since electrochemical states in batteries are unstable. A new attempt has been made at BL08W using high-energy X-ray Compton scattering. Taking advantage of the intense, highly parallel X-ray beams, the behaviors of materials inside a commercial battery (CR2032) has been imaged (see Fig. 2) [2]. Scanning an incident X-ray beam with an energy of 115 keV, the intensity of Compton scattered X-rays from a local probing volume inside the battery has been measured under discharge as a function of position and discharging time. Here, the X-ray intensity is defined as the area under Compton-scattered X-ray lines, centered around 94 keV, between 84 keV and 104 keV. The scattered X-ray intensity is proportional to the average electron density over the probing volume, which depends on the lithium concentration in the electrode materials. The battery was discharged under a constant current of 5.5 mA for 15.75 h, which was much larger than the standard value of 0.2 mA. The blue area is the negative electrode of lithium metal, and the red and yellow areas are MnO_2 and Li_xMnO_2 in the positive electrode. The obtained intensity-time image captures the migration of lithium ions in the positive electrode and reveals the internal structural change due to the volume expansion of the positive electrode and the shrinkage of the negative electrode. The interplay between the electrochemical process and the internal structure under a working condition is critical to battery design.

Integration of the two methods mentioned above is straightforward and provides a link between quantum-level characteristics and product-level behaviors in batteries. For example, orbital occupation and electron configuration are closely related to phase transitions and volume changes, which lead to the fracture of the electrode and the degradation of battery performance with repeated cycle operations. This new methodology paves the way for an advanced characterization of commercial batteries and other electrochemical devices, such as fuel cells.

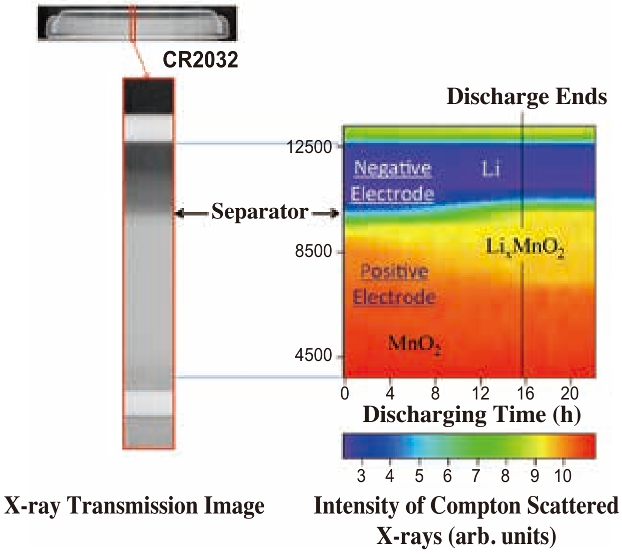

Fig. 2. Intensity map of Compton-scattered X-rays as a function of vertical position and discharge time of the battery (CR2032). Lithium migration and internal structure changes are clearly observed.

Yoshiharu Sakurai* and Masayoshi Itou

Japan Synchrotron Radiation Research Institute (JASRI)

*E-mail: sakurai@spring8.or.jp

References

[1] *K. Suzuki, B. Barbiellini, Y. Orikasa, H. Go, H. Sakurai, S. Kaprzyk, M. Itou, K. Yamamoto, Y. Uchimoto, Y. J. Wang, H. Hafiz, A. Bansil and Y. Sakurai: Phys. Rev. Lett.* ***114*** *(2015) 087401.*
[2] *M. Itou, Y. Orikasa, Y. Gogyo, K. Suzuki, H. Sakurai, Y. Uchimoto and Y. Sakurai: J. Synchrotron Rad.* ***22*** *(2015) 161.*

Ultrathin inorganic molecular nanowires based on transition metal oxide

Nanowires are one-dimensional (1D) materials, whose diameters are on the order of nanometers or smaller and whose length can be increased without limitation. Different compounds, such as metallic compounds, semiconducting compounds, metal oxides, and organic polymers, can be grown to form nanowires, which have been attracting much attention owing to their large surface area, quantum mechanical effects, and other unique properties.

Molecular wires, as a type of nanowire, are grown in length by repeating a single molecular unit. The common types of molecular wires are organic, organometallic, and biological polymers, which have been widely applied to nanotechnology, semiconductors, electrochemistry, and cell biology. In the inorganic field, all-inorganic molecular wires are very rare, leaving a field full of challenges. The most common example of inorganic molecular wire is $[Mo_6S_{9-x}I_x]_n$ [1,2]. The material is assembled by growing the molecule unit $Mo_6S_{9-x}I_x$ along the *c*-axis to form a nanowire. The material shows excellent magnetic, electronic transport, biological, mechanical, and optical properties and has been applied to field emitters, composites, nonlinear optical limiters, chemisensors, biosensors, lubricants, Li batteries, and molecular-scale connectors for molecular electronics.

Transition metal oxide molecular wires have various advantages over organic molecular wires including their stable structure, tunable chemical composition, and tunable property. Metal oxides with a nano-architecture can be formed by the assembly of metal oxygen octahedra. 0D nanomolecular clusters and 2D nanomolecular sheets are obtained by this approach. However, no molecular nanowire assembled using transition metal oxide octahedra has been reported so far.

Herein, we report the first crystalline transition metal oxides based on molecular wires, which were formed by repeating the hexagonal molecular unit $[X^{IV}Mo^{VI}_6O_{21}]^{2-}$ (X = Te or Se) along the length, denoted as Mo-Te oxide and Mo-Se oxide, respectively [3]. The molecular wires assemble in a hexagonal manner with water and ammonium cations between them to form crystals. Breakage of a crystal forms small nanowires, even single molecular wires, which can be observed by TEM and AFM.

The materials were synthesized by a hydrothermal method. $(NH_4)_6Mo_7O_{24}\cdot4H_2O$ was used as a Mo source, and Se^{IV} (SeO_2) and Te^{IV} (formed by reduction of the $Te(OH)_6$ with $VOSO_4$) were used as the Se and Te sources, respectively. After the reaction mixture was heated at 448 K for 24 h, the resulting solid was recovered from the solution by filtration.

Mo-Te oxide can grow into a large crystal that is suitable for single-crystal X-ray analysis. Single-crystal X-ray structural analysis performed at beamline **BL40XU** combined with elemental analysis and valence analysis showed that six Mo-O octahedra surrounded one Te or Se ion in the a-b plane, forming the molecular unit $[X^{IV}Mo^{VI}_6O_{21}]^{2-}$ (X = Se or Te) (Fig. 1(a,b)). Hexagonal $[X^{IV}Mo^{VI}_6O_{21}]^{2-}$ units were stacked along the *c*-axis to form prismatic clusters

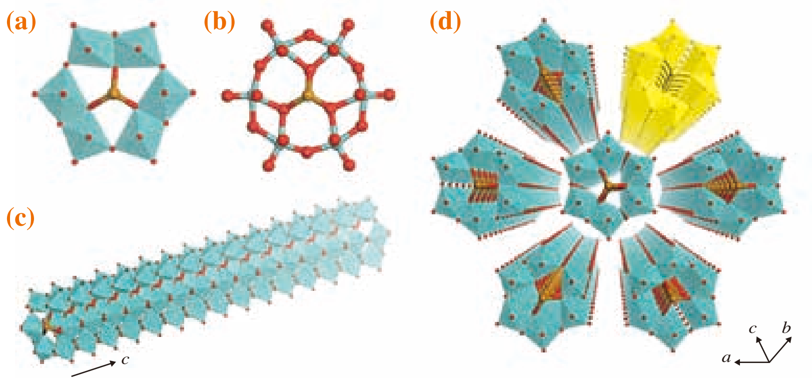

Fig. 1. Structural representations: **(a)** polyhedral representation of hexagonal unit $[Te^{IV}Mo^{VI}_6O_{21}]^{2-}$ or $[Se^{IV}Mo^{VI}_6O_{21}]^{2-}$, **(b)** ball-and-stick representation of hexagonal unit $[Te^{IV}Mo^{VI}_6O_{21}]^{2-}$ or $[Se^{IV}Mo^{VI}_6O_{21}]^{2-}$, **(c)** single molecular wire, and **(d)** assembly of single molecular wires into crystalline Mo-Te oxide (or Mo-Se oxide). A single molecular wire is highlighted in yellow; Mo, blue; Te (Se), yellow; O, red.

(Fig. 1(c)) as molecular wires. The anionic molecular wires were further packed parallel to each other in a hexagonal manner to form the material (Fig. 1(d)), and ammonium cations and water were between the molecular wires. The nanowires were *ca*. 1.2 nm in width and micrometer scale in length.

Single molecular wires can be isolated from the crystalline Mo-Te oxide based on molecular wires using a simple process (Fig. 2(a)). Proton exchange cracked the crystal of Mo-Te oxide. Breakage of crystals after proton exchange was more clearly shown by SEM. Mo-Te oxide maintained its rod shape after proton exchange, and some gaps could be observed on the crystal surface (Fig. 2(b)).

Mo-Te oxide after proton-exchange could be disassembled into smaller particles by dispersion in ethanol using ultrasound. Thin particles and even single molecular wires can be observed. High-resolution TEM (HRTEM) revealed that the molecular wires were <5 nm in width and ~100 nm in length, and some isolated molecular wires were 1.5 nm in width (Fig. 2(c)). The isolated nanowires were further characterized by AFM, and the diameter of the nanowires was determined by line profile analysis. AFM images of Mo-Te oxide after isolation experiments show tubular particles. Figure 2(d) shows typical particles with diameters of *ca*. 1.2 nm (particle i), and the diameter of particle (i) was identical to that of a single molecular wire (Fig. 2(e)). The diameter of particle (ii) was *ca*. 4.8 nm, which is ascribed to a structure with four layers of molecular wires (Fig. 2(f)).

The separated nanowire shows acid catalytic activity for ester formation from alcohol, which indicated similarity in activity to homogeneous heteropoly acids.

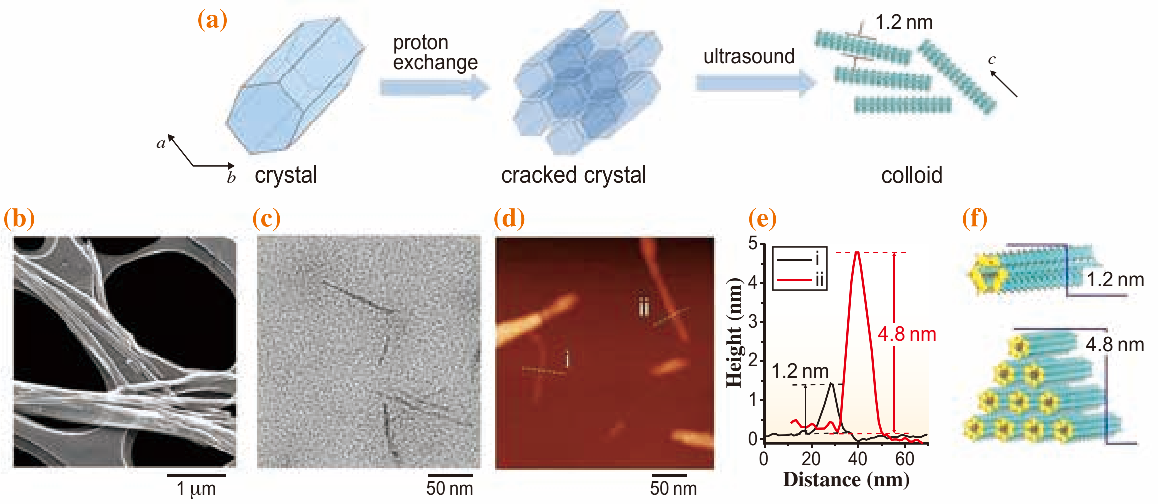

Fig. 2. Mo-Te oxide molecular wire: **(a)** isolation process for crystalline Mo-Te oxide to obtain nanowires, **(b)** SEM images of Mo-Te oxide after proton exchange, **(c)** HR-TEM images of Mo-Te oxide after ultrasound irradiation, **(d)** AFM images of Mo-Te oxide after ultrasound irradiation, **(e)** line profiles from AFM images, and **(f)** proposed structures from line profile analysis, with yellow highlighting the a-b plane of the materials.

Z. Zhang[a], T. Murayama[b], N. Yasuda[c] and W. Ueda[a,*]

[a] Faculty of Engineering, Kanagawa University
[b] Graduate School of Urban Environmental Sciences,
Tokyo Metropolitan University
[c] Japan Synchrotron Radiation Research Institute (JASRI)

*E-mail: uedaw@kanagawa-u.ac.jp

References

[1] M. Remskar *et al*.: Science **292** (2001) 479.
[2] D. Mihailovic: Prog. Mater. Sci. **54** (2009) 309.
[3] *Z. Zhang, T. Murayama, M. Sadakane, H. Ariga, N. Yasuda, N. Sakaguchi, K. Asakura, W. Ueda: Nat. Commun.* ***6*** *(2015) 7731.*

Role of liquid indium in the structural purity of wurtzite InAs nanowires that grow on Si(111)

The epitaxial growth of vertical InAs nanowires (NWs) on Si(111) substrates offers the possibility to integrate monolithically the two semiconductor classes maintaining a high quality interface despite of the large mismatch between their lattice constants and thermal expansion coefficients. However, the general susceptibility of III–V NWs to structural polytypism when they are grown along the [111] crystallographic orientation can affect basic properties of any device application. Extensive experimental investigations, also supported by classical nucleation theory models, have shown that it is possible to control the polytypism when the NWs are grown in the Au-assisted, and to a lesser extent in the self-assisted, vapor–liquid–solid (VLS) mode by tuning the supersaturation or the contact angle of the catalyst particle (via the growth conditions). In contrast, the freedom to tune the polytype of choice is limited in the vapor–solid (VS) growth mode, where the (111)B top facet of the NWs is directly exposed to the vapors.

Executing an *in situ* growth experiment at SPring-8, we developed a procedure to monitor the temporal evolution of the zincblende (ZB) and wurtzite (WZ) polytypes as well as the presence of liquid indium during the growth by molecular beam epitaxy (MBE), based on time-resolved X-ray scattering and diffraction measurements [1]. Assisted by Masamitsu Takahashi and his team the experiment has been performed at beamline **BL11XU**, using the MBE system integrated with a surface X-ray diffractometer [2]. The geometrical configuration of the X-ray experiment is shown in Fig. 1. The glancing angle of the primary X-ray beam ($\lambda = 0.620$ Å, size: 0.3×0.3 mm^2) was fixed smaller than the critical angle of the silicon (111) substrate in order to reduce the diffuse scattering from the substrate, whereas the large footprint of the X-ray beam on the surface ensures that a large number of nanowires is illuminated. The X-rays diffracted from the WZ $(10\bar{1}1)$ and the ZB (101) InAs Bragg peaks were collected by a 2D-CMOS detector. Also we detected a characteristic powder-like scattering signal of liquid Indium formed at any stage of the growth by placing the detector close to angle of its maximum scattering (see inset Fig. 1). The scanning electron microscopy (SEM) inset in Fig. 1 illustrates that the substrate surface is mostly covered by InAs NWs, 300 nm in length and 250 nm in diameter, whereas a few InAs structures of larger diameter and multiple facets (henceforth referred to as parasitic islands) are also present.

Figure 2 shows the temporal evolution during the growth of InAs NWs of (a) the scattering signal from liquid Indium and (b) the diffraction signals from the two polytypes of InAs. The growth started at $t = 0$ s by initiating the supply of Indium, whereas the supply of As$_4$ had been initiated several minutes in advance. Despite the As-rich conditions, we detected the formation of liquid Indium phase during the first 1000 s

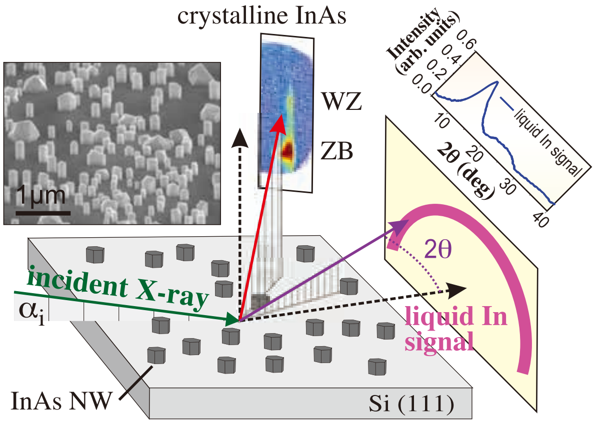

Fig. 1. Diffraction geometry within the MBE chamber. The incident X-ray beam illuminates the sample surface under a shallow angle of $\alpha_i = 0.07°$. Liquid indium causes a powder-like scattering signal at small scattering angles. The diffraction from crystalline InAs can be observed using a two-dimensional detector. The inset shows an SEM image of the grown NWs and parasitic crystallites after 1800 s of growth.

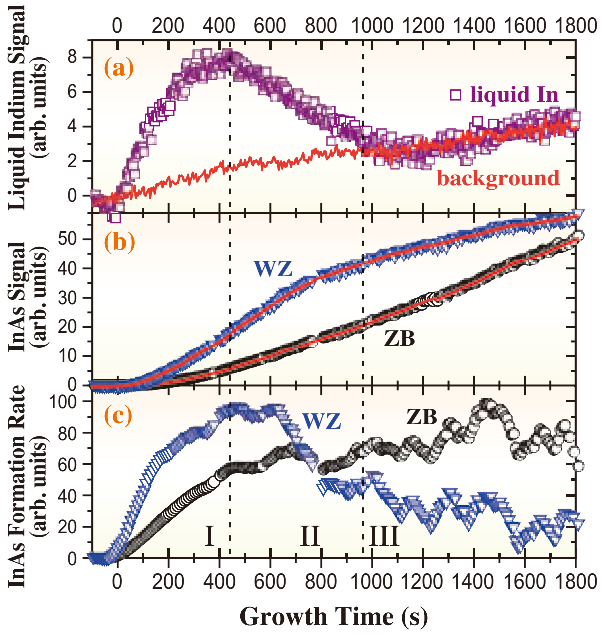

Fig. 2. **(a)** Evolution of the liquid indium signal (open squares) during NW growth, showing a maximum ~440 s after opening the In shutter at t=0 s. **(b)** Evolution of the crystalline WZ (triangles) as well as the respective ZB signals (open spheres) as function of growth time. Solid lines represent a running average of the data. **(c)** Growth rates of ZB and WZ materials, obtained as derivative of the solid lines in (a), showing a good correlation with the liquid In signal.

of the growth. Based on the signal behavior with time, we define three regimes. Regime I is characterized by the monotonic increase of the signal of liquid Indium, which reaches its maximum at t ≈ 440 s. Then, the signal drops continuously and eventually diminishes within regime II, following the background-noise level for the rest of the growth duration (regime III). The continuous increase of the background-noise level with time is attributed to the additional material deposited on the substrate.

The actual role of liquid Indium in the nucleation of InAs NWs emerges from the study of the structural dynamics of the two InAs polytypes. The diffraction intensity from the WZ polytype increases during the first 440 s, followed by a tendency to stabilize for the remaining of the growth (Fig. 2(c)). Because the diffraction intensity is proportional to the amount of material growing in the respective phase, the formation rate of the polytype can be calculated from the time derivative of the intensity. From the result shown in Fig. 2(c), we see that the behavior of the WZ formation rate correlates well with the three time regimes that were defined previously for the presence of liquid Indium. In regime I, the WZ formation rate increases continuously, reflecting the increase of the number of InAs NWs that nucleate on the substrate. The formation rate slows down to half of the peak value in regime II, manifesting not only the completion of the nucleation stage, but also the fast degradation of the WZ purity of the growing NWs that were nucleated within regime I. Thus, we conclude that the locally Indium-rich conditions that formed spontaneously on the substrate in the beginning of the growth promoted the nucleation of InAs in the WZ phase (regime I), whereas the subsequent transition to As-rich conditions defined the end of the nucleation stage (regime II) and accounted for the decrease of the WZ purity in the growing NWs (regimes II and III). All these findings are fully consistent with the model that we already suggested in Ref. 3, which was based though only on indirect observations. The diffraction signal and the respective formation rate from the ZB polytype in Figs. 2(b,c) exhibited a different behavior than the WZ ones. The formation rate increased monotonically throughout the growth duration, with a faster increase in regime I and a significantly slower one in regimes II and III. Unfortunately, safe conclusions about the temporal evolution of the ZB polytype inside the NWs cannot be drawn because the InAs NWs and parasitic islands grow simultaneously on the substrate surface, and they both contain ZB segments. The smooth transition of the ZB formation rate between regimes I and II, unlike the WZ peak at 440 s, suggests that the ZB signal in regime I reflects mostly the InAs islands, which nucleate and grow solely in VS mode. The ZB formation rate practically stabilized outside regime I, suggesting that the nucleation phase of the parasitic islands completed at the end of regime I, in coincidence with the nucleation phase of the NWs.

Andreas Biermanns-Föth[a], Emmanouil Dimakis[b]
and Ullrich Pietsch[a,*]

[a] Solid State Physics, University of Siegen, Germany
[b] Paul Drude Institute für Festkörperelektronik, Germany

*E-mail: pietsch@physik.uni-siegen.de

References

[1] *A. Biermanns, E. Dimakis, A. Davydok, T. Sasaki, L. Geelhaar, M. Takahasi and U. Pietsch: Nano Lett.* ***14*** *(2014) 6878.*
[2] M. Takahasi *et al.*: Jpn J. Appl. Phys. **41** (2002) 6247.
[3] E. Dimakis *et al.*: Cryst. Growth Des. **11** (2011) 4001.

Bonding and electronic states of boron in silicon nanowires characterized by infrared synchrotron radiation beam

Considerable research has been carried out on one-dimensional semiconducting nanowires (NWs). Silicon (Si) NWs have attracted particular attention due to their compatibility with current Si complementary metal-oxide-semiconductor (Si CMOS) integrated circuit technology and their better scalability. These NWs have potential for use in the channel, source and drain regions of MOS field-effect transistors (FETs). Impurity doping will be of increasing importance in realizing high-speed transistor channels using SiNWs. However, to be able to realize them, it is important to clarify the states of impurity atoms, such as their chemical bonding states and electrical activity. First, we applied Raman scattering and electron spin resonance (ESR) [1]. Local vibrational modes of ^{11}B and ^{10}B in SiNWs were observed by Raman scattering measurements, indicating B doping into the crystalline Si core of SiNWs. Asymmetric broadening due to Fano resonance was also observed in the Si optical phonon peak, showing the electrical activity of B atoms in SiNWs. These techniques also clarified the segregation behaviors of B and P atoms in SiNWs [2]. Fourier transform infrared (FT-IR) techniques also allow the vibrational characterization of impurity atoms in bulk Si. However, it is very difficult to apply FT-IR techniques to characterize impurity atoms in nanostructures due to the difficulty of preparing sufficiently large samples. The use of IR synchrotron radiation (IR-SR) as an IR light source in **BL43IR** has the advantage of a greater brilliance than conventional IR light sources using thermal radiation. The brilliance of IR-SR is 10^2 times higher than that of general black-body light. This allows the optical spectrum, in even microscopic regions, to be measured down to lower frequencies. IR-SR in BL43IR also has a wide range of wavenumbers from the visible to far IR regions, making it possible to characterize nanostructure materials such as SiNWs.

SiNWs were synthesized by laser ablation of a Si target with nickel (Ni) as the metal catalyst. The growth mechanism of SiNWs is VLS (vapor-liquid-solid) growth [3]. Figure 1(a) is a schematic illustration of our laser ablation system for the synthesis of SiNWs. A special collector made of quartz was installed in the quartz tube to effectively collect SiNWs grown in an Ar gas atmosphere. Laser ablation was continued for 3 h to deposit thick layers of SiNWs with the aim of increasing the optical absorption by B atoms. The thickness of the layer of SiNWs reached 10 μm order (Fig. 1(c)). Typical STEM and high-resolution TEM images of SiNWs synthesized using $Si_{98}Ni_1B_1$ targets (Fig. 1(b)) are respectively shown in Figs. 1(d) and 1(e). The SiNWs are composed of a crystalline Si core and surface oxide layer. The average core diameter is about 20 nm and the thickness of the surface oxide layer is about 10 nm.

The whole range of the IR-SR absorption spectra observed for B-doped and undoped SiNWs is shown in Fig. 2. Four peaks were observed at 468, 806, 1085, and 1200 cm^{-1} for both samples, which were assigned to different oxygen-related modes in the surface oxide layer of the SiNWs by comparison with the results for bulk silicon. The first peak at 468 cm^{-1} is due to the rocking mode of the O atom about the axis through the two Si atoms. The second peak at 806 cm^{-1} is due to symmetrical stretching of the O atom along the line bisecting the axis formed by the two Si atoms. The third and fourth peaks at 1085 and 1200 cm^{-1} are due to the asymmetrical stretching motion of the O atoms. In this stretching motion, the O atoms move back and forth along a line parallel to the axis through the two Si atoms. These results show that our IR-SR technique is applicable even for the characterization of Si nanostructures. In addition to these oxygen-related

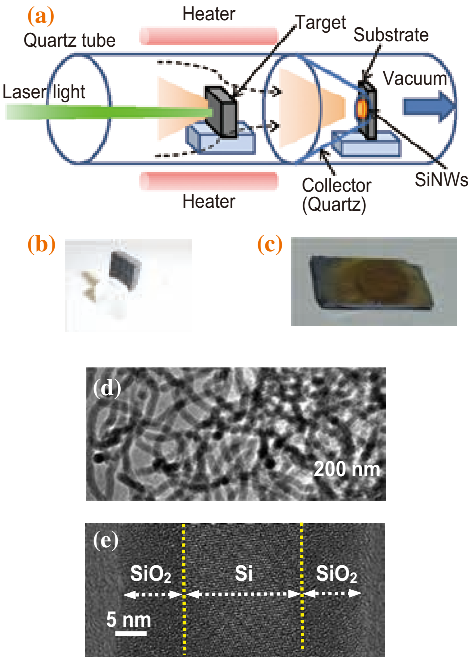

Fig. 1. **(a)** Schematic illustration of synthesis of SiNWs by a laser ablation system. Photographs of **(b)** a target and **(c)** a sample for IR synchrotron radiation measurements. Typical **(d)** STEM and **(e)** high-resolution TEM images of SiNWs synthesized using the $Si_{89}Ni_1B_{10}$ target.

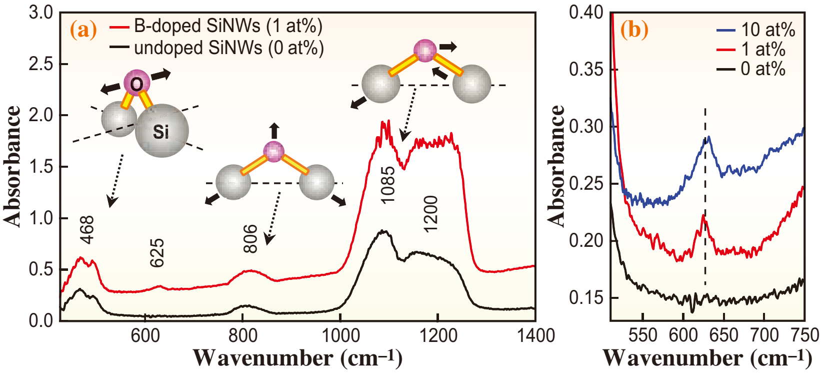

Fig. 2. **(a)** IR-SR absorption spectra observed for B-doped and undoped SiNWs. **(b)** IR-SR absorption spectra observed for B-doped and undoped SiNWs.

peaks, a new peak was observed at about 625 cm^{-1} in B-doped SiNWs [4]. The peak position is similar to those of the ^{11}B (618 cm^{-1}) and ^{10}B (643 cm^{-1}) local vibrational peaks observed by Raman measurements. The intensity of the IR-SR peak at 625 cm^{-1} shows a good correlation with that of the Raman result. Based on the peak position and its dependence on the B doping level, the newly observed IR-SR peak at 625 cm^{-1} is assigned to the B vibrational peak in SiNWs. The positions of the IR-SR absorption peaks are at higher frequencies than those of the Raman peaks. The Raman measurements were performed at room temperature, while the IR-SR measurements were performed at 4.2 K. Hence, the higher frequency shift at lower temperatures can be mainly explained by the temperature effect. The reason why we performed IR-SR measurements at 4.2 K is that the electronic transition peaks explained below become narrow and easily observed.

The electronic transition of B in Si can be observed in the far-infrared region. Two peaks were newly observed at about 278 and 319 cm^{-1} (Fig. 3) [4]. The high noise in the low-frequency region is due to the sensitivity of our IR-SR measurements. Burstein *et al.*, while performing low-temperature IR measurements of B-doped bulk silicon, were the first to note discrete electronic transitions of bound holes from the ground state of neutral B acceptor atoms to a series of hydrogen-like excited levels lying below the band edge [5]. The most characteristic peaks are observed at about 278 and 320 cm^{-1} and are respectively assigned to the 1*s*-2*p* and 1*s*-3*p* transitions of B in Si. The newly observed peak positions for B-doped SiNWs correspond very closely to the 1*s* - 2*p* and 1*s* - 3*p* transitions. These peaks were not observed for undoped SiNWs, showing that they are related to electronic transitions from the ground state of a neutral B acceptor atom to excited levels. The full width at half maximum data of the 1*s* - 3*p* transition of B in SiNWs is plotted in Fig. 3(b) in addition to the previously reported data. The broadening of the absorption peaks is likely to be due to the effect of higher B doping in the SiNWs.

These results clearly demonstrate the potential usefulness of the IR-SR method as a new tool for characterizing nanomaterials.

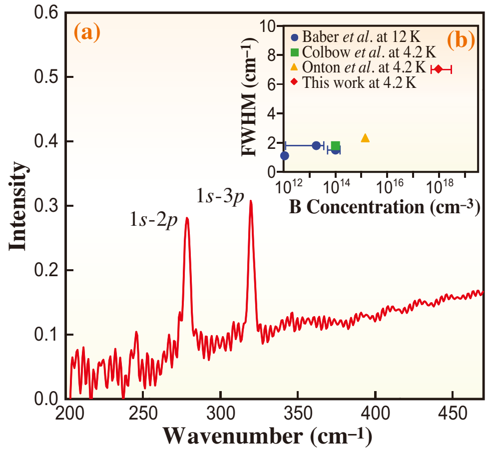

Fig. 3. **(a)** IR-SR absorption spectra related to electronic transition of B in SiNWs synthesized using Si$_{98}$Ni$_1$B$_1$ targets. **(b)** Dependence of FWHM on B concentration.

Naoki Fukata[a,*], Yuka Ikemoto[b] and Taro Moriwaki[b]

[a] International Center for Materials Nanoarchitectonics, NIMS
[b] Japan Synchrotron Radiation Research Institute (JASRI)

*E-mail: FUKATA.Naoki@nims.go.jp

References

[1] N. Fukata: Adv. Mater **21** (2009) 2829.
[2] R.S. Wagnerand, W.C. Ellis: Appl. Phys. Lett. **4** (1964) 89.
[3] N. Fukata *et al.*: Nano Lett. **11** (2011) 651.
[4] *N. Fukata, W. Jevasuwan, Y. Ikemoto and T. Moriwaki: Nanoscale 7 (2015) 7246.*
[5] E. Burstein *et al.*: J. Phys. Chem. Solids. **4** (1958) 148.

Direct observation of bond formation in solution with femtosecond X-ray scattering

The making and breaking of atomic bonds in molecules are essential processes in chemical reactions. The ultrafast bond-breaking processes in various molecular systems have been intensively investigated using time-resolved techniques for several decades [1]. In contrast, the ultrafast bond-making process, especially in solution, has been generally acknowledged that it is more difficult to be investigated due to its bimolecular nature. In a bond-making process, two reactant parties should meet first by slow diffusion through solvent, as a result, it is difficult to synchronize the bond formations in all reactant pairs with laser excitation. In this regard, a gold trimer complex, $[Au(CN)_2^-]_3$, offers a good model system for investigating the ultrafast dynamics of the bond-making process in solution. In the ground state of the complex, gold atoms are weakly bound to each other by a non-covalent interatomic interaction known as aurophilicity [2]. Formation of covalent bonds between adjacent Au atoms can be triggered by laser excitation without the limitation of slow diffusion [3].

We performed the X-ray solution scattering experiments at **BL3** beamline of SACLA and NW14A beamline of KEK to capture the moment of the bond formation in the gold trimer complex as well as revealing the detailed structural dynamics. Experimental scheme for the experiment is illustrated in Fig. 1. We obtained experimental difference scattering curves, $\Delta S(q)$, measured at various time delays from –800 fs to 300 ns by subtracting scattering curves measured before the laser excitation. The time-resolved difference scattering curves are shown in Fig. 2(a). Then, time-resolved radial distribution functions (RDFs), $r^2S(r)$, shown in Fig. 2(b) were calculated by performing Fourier sine transformation on $q\Delta S(q)$. Considering that the contributions from C and N atoms on total scattering intensities are essentially negligible, the RDFs actually represent the interatomic distances among the Au atoms of $[Au(CN)_2^-]_3$ in real space. The distances of the Au_1-Au_2 pair (R_{12}) and the Au_2-Au_3 pair (R_{23}) are encoded by the position of a p_1 peak, and the Au_1-Au_3 (R_{13}) distance is represented by a p_2 peak. Considering positions of the two peaks at a time delay of –800 fs (~3.6 Å and ~5.56 Å for p_1 and p_2, respectively), Au atoms in the ground state, S_0, are weakly bound to each other compared to a typical Au-Au covalent bond (~2.7 Å), and the S_0 state has a bent structure. Compared to the S_0 state, at a time delay of 200 fs, R_{12} and R_{23} both decrease

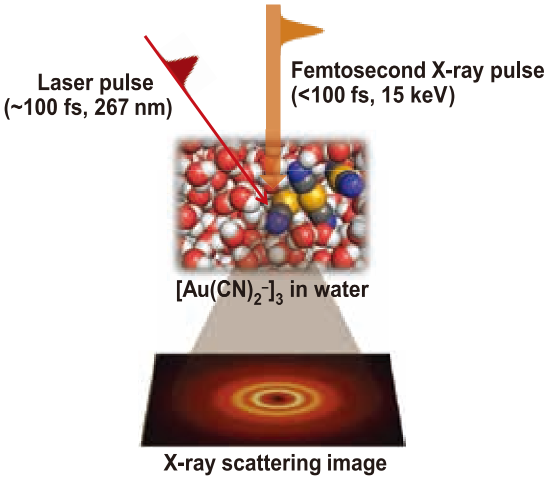

Fig. 1. Schematic of femtosecond X-ray solution scattering experiment. In the gold trimer sample in an aqueous solution, bond formations between adjacent gold atoms are triggered by a laser excitation at 267-nm wavelength. Then, the structural evolution is identified by scattering information arising from a subsequent femtosecond X-ray pulse. Scattered light is detected by a fast two-dimensional charge-coupled device (CCD) detector.

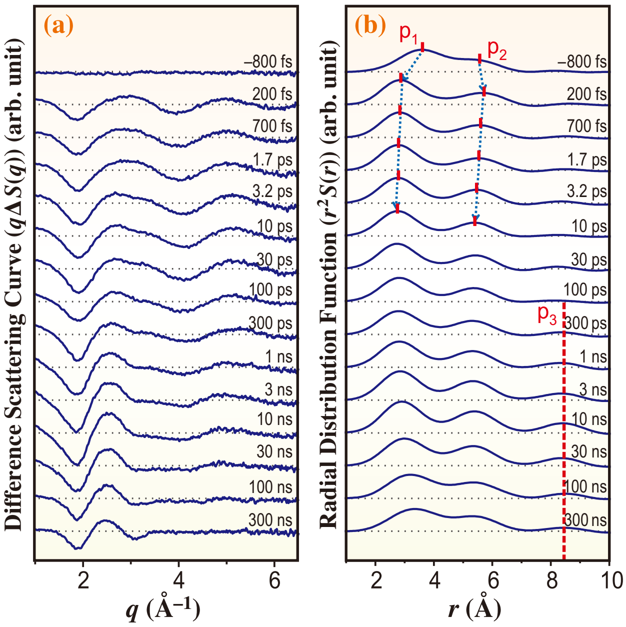

Fig. 2. **(a)** Experimental difference scattering curves, $q\Delta S(q)$, measured at time delays from –800 fs to 300 ns. **(b)** RDFs, $r^2S(r)$, obtained by the Fourier sine transformation of $q\Delta S(q)$. The blue dashed arrows represent the evolution of the positions of the p_1 and p_2 peaks. The red dashed line indicates the position of the p_3 peak.

significantly (~2.8 Å), indicating the formation of an Au-Au covalent bond at this moment. In contrast, R_{13} increases slightly (~5.63 Å), which is similar to the sum of R_{12} and R_{23}, indicating that a conformational transition occurs from the bent to the linear geometry.

By performing subsequent kinetic analysis on the time-resolved RDFs, we identified four structurally distinct states, the ground (S_0) state, an excited (S_1) state, a triplet (T_1) state and a tetramer, and obtained species-associated RDFs (Fig. 3(a)) as well as their kinetics (Fig. 3(b)). The detailed three-dimensional structures of the four states were reconstructed through a structural fitting analysis with sub-angstrom spatial resolution. The resulting structural parameters (R_{12}, R_{23} and R_{13}) are presented in Fig. 3(a). The S_0 state has weakly bounded Au atoms in a bent geometry, as can be inferred from Fig. 2(b), and it is converted to the S_1 state within our experimental time resolution, ~500 fs. In the S_1 state, Au atoms are bound to each other by covalent bonds and aligned in a linear geometry. The time scale of the bent-to-linear structural transition determined from our experiment is in good agreement with that predicted from a previous theoretical study [4]. The S_1 state is further converted to the T_1 state with a time constant of 1.6 ps, accompanying a contraction of the two Au-Au bonds induced by the formation of stronger Au-Au bonds. The T_1 state retains a linear structure similar to that in the S_1 state. Finally, we observed the formation of tetramer species at ~3 ns, which can be also recognized due to the appearance of the p_3 peak shown in Fig. 2(b) corresponding to the Au_1-Au_4 pair distance (R_{14}). The tetramer ultimately recovers to the S_0 state with a time constant of 100 ns.

In summary, we have demonstrated the capability of XFEL-based femtosecond TRXSS by scrutinizing the reaction mechanism of the formation of covalent Au-Au bonds in the $[Au(CN)_2^-]_3$ complex [5]. Femtosecond TRXSS can be used as a fundamental tool to study the structural dynamics of chemical and biological systems in solution by visualizing the structural evolution with high spatial and temporal resolutions.

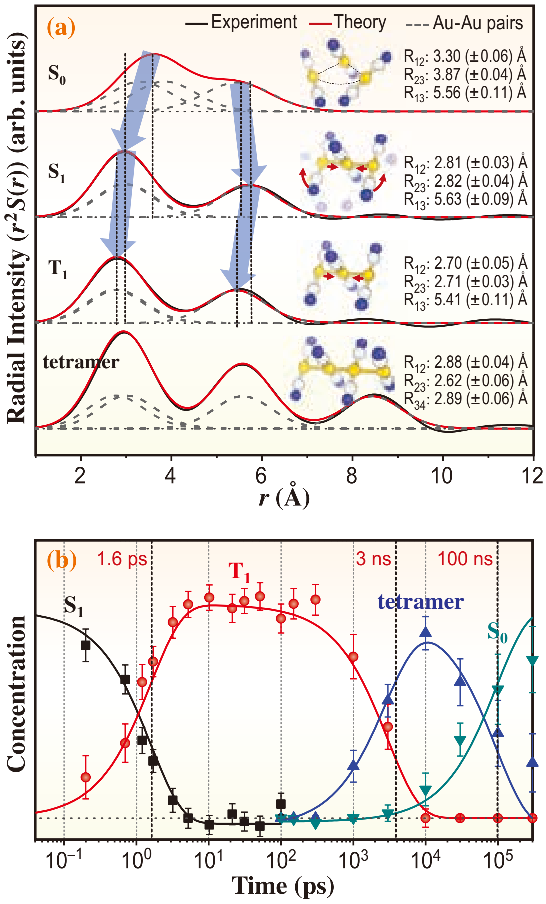

Fig. 3. **(a)** Species-associated RDFs for the four states obtained by the singular value decomposition and principal-component analyses (black) and their fits (red) obtained by structural fitting analyses. For each state, the structural parameters obtained from structural fittings are shown with their standard errors determined from 50 independent measurements. **(b)** Concentration changes of the four states. The notations for the four states and the time constants of their transitions are shown.

Jong Goo Kim[a,b], Hyotcherl Ihee[a,b,*] and Shin-ichi Adachi[c,d]

[a] Center for Nanomaterials and Chemical Reactions,
Institute for Basic Science, South Korea
[b] Dept. of Chemistry, KAIST, South Korea
[c] Institute of Materials Structure Science, KEK
[d] Dept. of Materials Structure Science,
The Graduate University for Advanced Studies

*E-mail: hyotcherl.ihee@kaist.ac.kr

References

[1] H. Ihee *et al.*: Science **309** (2005) 1223.
[2] S.G. Wang *et al.*: J. Am. Chem. Soc. **126** (2004) 1266.
[3] M.A. Rawashdeh-Omary *et al.*: J. Am. Chem. Soc. **123** (2001) 11237.
[4] G. Cui *et al.*: Angew. Chem. Int. Ed. **52** (2013) 10281.
[5] *K.H. Kim, J.G. Kim, S. Nozawa, T. Sato, K.Y. Oang, T.W. Kim, H. Ki, J. Jo, S. Park, C. Song, T. Sato, K. Ogawa, T. Togashi, K. Tono, M. Yabashi, T. Ishikawa, J. Kim, R. Ryoo, J. Kim, H. Ihee and S. Adachi: Nature* ***518*** *(2015) 385.*

Fast ortho-para conversion of H_2 observed in a coordination nanospace

The hydrogen molecule H_2 has two different nuclear-spin isomers, para (p) and ortho (o), owing to the requirement of symmetry of the wavefunction. Since interconversion between these isomers is a forbidden process in an isolated molecule, it has a long time constant, 100 hours. The o-p conversion accompanied by heat generation causes a boil-off problem in cryogenic H_2 storage. Recently, fast o-p conversions on the order of one or a few minutes have been observed on the H_2 physisorbed porous coordination polymer (PCP) [1] and amorphous solid water (ASW) [2]. Several theoretical mechanisms, Spin-Orbit-Electric Dipole-Hyperfine Contact (SOPY) [3], ion-molecule electron exchanges (XY), and charge transfer [3], have also been proposed for these fast o-p conversions of non-magnetic insulating catalysts. We found an o-p conversion of less than 10 minutes for H_2 adsorbed in a Hofmann-type PCP, $\{Fe(pz)[Pd(CN)_4]\}$ (pz = pyrazine), on the basis of the temperature dependence of Raman spectra. The charge density study using synchrotron radiation X-ray powder diffraction (SR-XRPD) reveals the electric field generated in coordination nanospace. The present results corroborate similar findings observed on different systems and confirm that o-p conversions can occur on non-magnetic solids and that an electric field can induce the catalytic hydrogen o-p conversion [4].

The Hofmann-type PCP $\{Fe(pz)[Pd(CN)_4]\cdot 2H_2O\}$ was synthesized as microcrystals suitable for X-ray diffraction. The guest-free PCP $\{Fe(pz)[Pd(CN)_4]\}$ was prepared by heating under vacuum at 423 K for 3 h. Figure 1 shows a crystal structure of $\{Fe(pz)[Pd(CN)_4]\}$. Hydrogen gas adsorption isotherms were measured at 77, 65, 35 and 20 K, in which the framework was diamagnetic. The amounts of adsorbed H_2 at 77, 65, 35 and 20 K under 80 kPa are 2.5, 2.7, 3.3 and 3.5 per pore, respectively. It was found that approximately one extra H_2 was adsorbed per pore by lowering the temperature.

In situ microscopic Raman spectroscopy of H_2 gas adsorption was carried out in the temperature range of 20 to 77 K. Three new Raman-active bands assigned to the adsorbed H_2 were observed at 307 (peak A), 328 (peak B) and 609 cm^{-1} (peak C) in comparison with the guest-free form at the same temperature of 77 K. The rotational quanta of H_2 is given by $S_0(J) = E_{0,J+2} - E_{0,J}$ where $E_{0,J}$ is the rotational energy in the vibrational ground state ($v = 0$; v is the vibrational quantum number). Two peaks, A and B, at around 300 cm^{-1} corresponded to the $S_0(0)$ spectra of p-H_2 and a peak C at around 600 cm^{-1} corresponded to the $S_0(1)$ spectra of o-H_2. We found some changes in the intensity and peak position for the Raman bands upon cooling from 77 to 20 K. The intensities of peaks A and C decreased with cooling and peak B shifted and increased in intensity at 35 K, indicating an o-p conversion.

An *in situ* SR-XRPD experiment of H_2 adsorption was performed at beamline **BL44B2** to determine the structures in the conversion. The powder sample was loaded into a glass capillary with 0.4 mm internal diameter and the capillary was mounted on the goniometer head connected to the gas pressure control system. The temperature of the sample was controlled with a He open-flow cooling device. We measured the data with high counting statistics and a wide d-spacing range, $d > 0.45$ Å, at 35 and 65 K in the H_2-adsorbed and -desorbed states. We determined accurate charge densities, $\rho(\boldsymbol{r})$, and electrostatic potentials, $\phi(\boldsymbol{r})$, with the Maximum Entropy Method (MEM) as shown in Fig. 2.

We found three H_2 sites that we call site-I, -II, and -III from the MEM charge densities. Site-I is the center of the pore, site-II is between the pz rings, and site-III is at 1/4, 1/4, 0. The schematic structures of H_2 sites are shown in Fig. 2 as red (site-III), blue (site-II), and green (site-I) spheres. The charge densities of H_2 at 65 K correspond to the mixture of site-I and -II. The H_2 densities at 35 K are interpreted to be a mixture of site-I and -III.

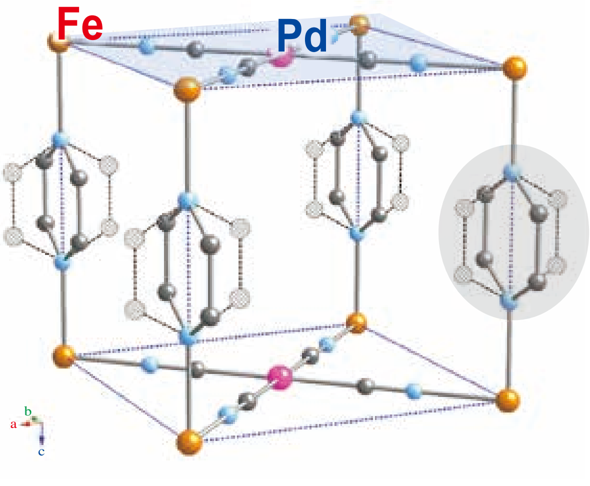

Fig. 1. Crystal structure of $\{Fe(pz)[Pd(CN)_4]\}$.

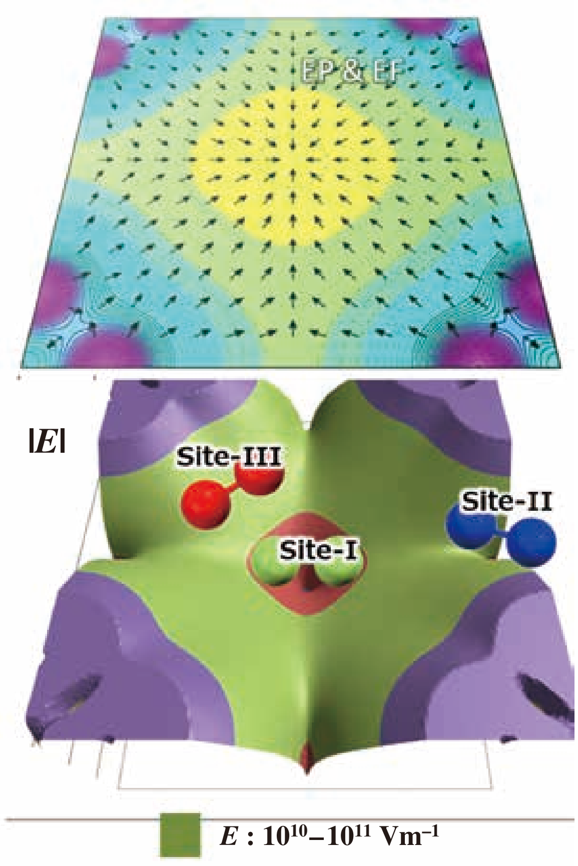

Fig. 2. (top) Electrostatic Potential (*EP*) and Electric Fields (*EF*) of the pole of {Fe(pz)[Pd(CN)$_4$]} as a 2D contour map. *EF* is shown as a vector field. (bottom) Bird's-eye view of |*EF*| and H_2 sites. The H_2 sites are schematically shown as green, blue, and red balls.

Three Raman peaks, A, B, and C, were successfully assigned to site-I, II and III. Peak A was assigned to p-H_2 at site-I and peak C was also assigned to o-H_2 at site-I. Peak B at 35 K was easily assigned to site-III on the basis of Raman spectra and the structure. Therefore, peak B at 77 and 65 K can be assigned to p-H_2 at site-II. We propose two principal processes to induce the conversion from o-H_2 to p-H_2 in the present PCP: (1) trapping of H_2 at site-II and -III; (2) site exchange from site-I and -II to site-III upon cooling. Because of the time of SR-XRPD and Raman spectrum measurements, an upper limit of 10 min for the o–p conversion time in the present PCP is proposed.

We investigated structural differences between site-I, -II and -III using the charge densities and electrostatic potentials experimentally determined. The received electric fields of H_2 from the {Fe(pz)[Pd(CN)$_4$]} framework can be estimated from electrostatic potential in the desorbed state. We calculated the electric fields, $\boldsymbol{E}(\boldsymbol{r})$, of site-I, -II, and -III using the gradient of the electrostatic potential, $\nabla\phi(\boldsymbol{r}) = -\boldsymbol{E}(\boldsymbol{r})$. $\boldsymbol{E}(\boldsymbol{r})$ is shown in Fig. 2. $\boldsymbol{E}(\boldsymbol{r})$ for site-I is 0.0 Vm^{-1} because of the inversion symmetry. $\boldsymbol{E}(\boldsymbol{r})$ for site-II and -III is 7.38×10^{10} Vm^{-1} and 7.62×10^{10} Vm^{-1}, respectively. There is a huge difference in $\boldsymbol{E}(\boldsymbol{r})$ between site-I and sites-II, -III. Recently, several theoretical mechanisms have been proposed [2,3] for these fast o-p conversions of non-magnetic insulating catalysts under huge electric field. The evidence of electric fields has been observed in the present study.

In the present study, we observed the correlation between the structure and the nuclear-spin state of H_2 in the three-dimensional Hofmann-type PCP, {Fe(pz)[Pd(CN)$_4$]}, providing regular coordination nanospace by combining the SR X-ray charge density study and Raman spectrum. The nanospace constructed by PCPs would offer the possibility of designing of the desirable electric filed. Electric-field-induced processes for such catalytic hydrogen o-p conversion were proposed using the electric field obtained from X-ray diffraction data.

Eiji Nishibori[a,b,*], Takashi Kosone[b,c] and Masaaki Ohba[b,d]

[a] CiRfSE & TIMS, University of Tsukuba
[b] RIKEN SPring-8 Center
[c] FREA, AIST
[d] Dept. of Chemistry, Kyushu University

*E-mail: nishibori.eiji.ga@u.tsukuba.ac.jp

References

[1] S.A. FitzGerald *et al.*: Phys. Rev. B **81** (2010) 104305.
[2] T. Sugimoto and K. Fukutani: Nat. Phys. **7** (2011) 307.
[3] E. Ilisca, F. Ghiglieno: Eur. Phys. J. B **87** (2014) 235.
[4] *T. Kosone, A. Hori, E. Nishibori, Y. Kubota, A. Mishima, M. Ohba, H. Tanaka, K. Kato, J. Kim, J.A. Real, S. Kitagawa and M. Takata: R. Soc. Open Sci.* **2** *(2015) 150006.*

Visualizing photoinduced intramolecular electron transfer

Photosynthesis designates the intricate chain of chemical reactions by which plants capture and store solar energy into chemical bonds [1]. Understanding this process would enable scientists to devise artificial supramolecular assemblies capable of mimicking splitting water to produce clean fuels [2]. Among the various key steps which have been delineated so far, the intramolecular conversion of an incident photon into an activated electron has remained one of the most challenging to date [3]. This work shows how novel analytical methods that utilize intense femtosecond X-ray pulses can provide unique information about this process [4].

The large molecule shown in Fig. 1 consists of a bimetallic ruthenium (Ru) antenna linked to a cobalt (Co) center. The photoinduced electron transfer from the photoexcited Ru to the optically-dark Co was studied at beamline **BL3** of SACLA XFEL using the combined techniques of X-ray emission spectroscopy (XES) and X-ray diffuse scattering (XDS). The Ru center was selectively excited using 400 nm optical laser pulses (60 fs pulse length), and the induced dynamics were probed using 8 keV X-ray laser pulses (10 fs pulse length, 0.3% bw, 10^{10} photons per pulse) generated by SACLA. The fluorescent X-ray photons of a specific energy (Co Ka) were selected using a bent crystal in the Johan geometry and detected using a MultiPort Charged Coupled Device (MPCCD) area detector. The XDS signal was detected directly behind the sample using a secondary MPCCD area detector.

Figure 2(a) shows the transient X-ray emission signal detected at 6.93 keV, which probes the valency and spin state of the Co center. The analysis of the time trace indicates that the electron crosses the bridge in less than half a picosecond (i.e. half a trillionth of a second), and that a second electronic relaxation step in the form of a spin state transition, occurs at the Co center with a 1.9 picosecond time constant, following the electron transfer.

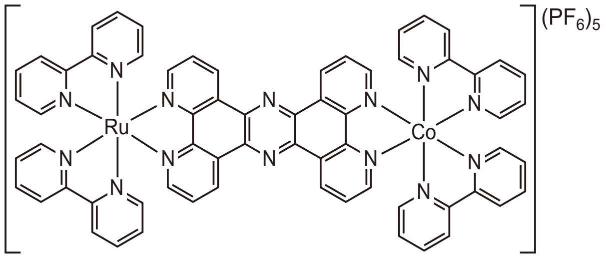

Fig. 1. The bimetallic photoactive molecule investigated, consisting of a ruthenium (Ru) antenna linked to a cobalt (Co) center.

Figure 2(b) shows the transient X-ray diffuse scattering signal, which is sensitive to global structural changes of the solute and the solvent. The analysis of this pattern allows not only to retrieve the internal changes of the molecular structure as the electron localizes at the Co center, but also the amount of energy dissipated into the surrounding solvent as heat. The internal structural dynamics are dominated

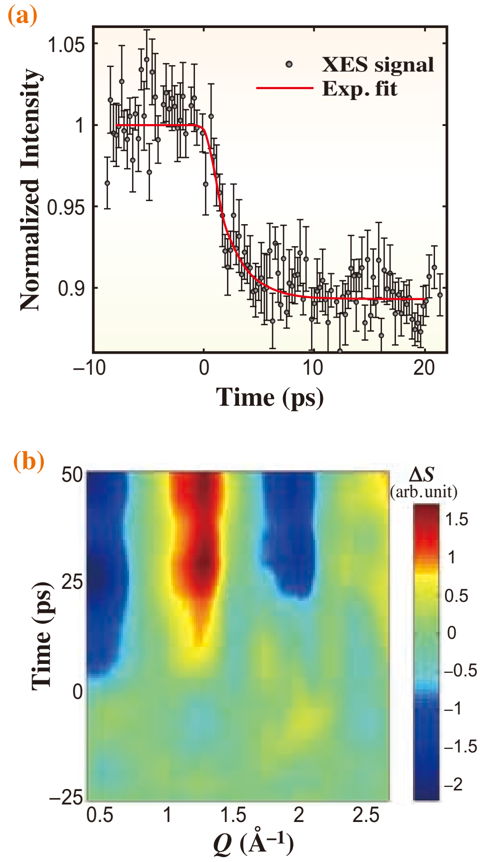

Fig. 2. **(a)** The transient X-ray emission signal detected at 6.93 keV (black circles), with standard error (black lines) and the description of the data resulting from the proposed electronic transfer pathways. **(b)** The transient X-ray diffuse scattering signal measured simultaneously with the X-ray emission signal.

by a 0.2 Å expansion of the Co-N bonds, induced by the electron transfer and spin state transition at the Co center.

Figure 3 summarizes the fundamental timescales and processes, as obtained from these combined X-ray measurements delivering the complete picture of the photoinduced electron transfer process.

In conclusion, this experiment shows that it is now possible to track all the stages of electron transfer through a large photoactive molecule. This will contribute to elucidate at the atomic level the various factors that govern the efficiency of functional systems, such as photocatalysts or photovoltaic solar cells.

Another important finding of this study is that molecules, where photoconversion and electron transduction are so fast that they proceed with minimal energy loss as heat, can indeed be constructed under the fumehood of the chemistry lab. Such photochemical molecular devices are of great potential for future sustainable production of fuel or electricity.

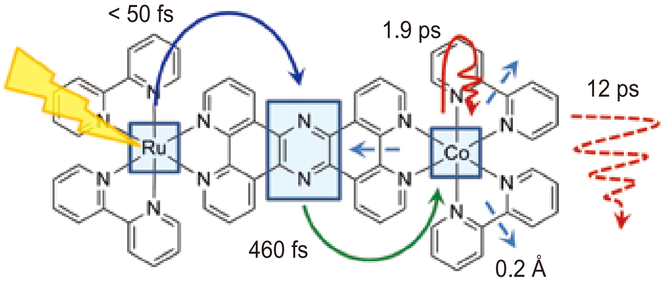

Fig. 3. Summary of the fundamental timescales and processes following photoexcitation, obtained from the combined X-ray measurements described here. Full arrows show electronic dynamics, dashed arrows show structural dynamics. Dark blue arrow shows the initial electron transfer from the photoexcited Ru center to the bridge, and green arrow shows electron transfer from the bridge to the Co center. The red arrow shows the spin state transition at the Co center induced by the electron transfer. Dashed lines show the structural dynamics, consisting of a 0.2 Å bond length expansion of the Co-N bonds (blue), and a reorganization of the solvent as it is heated by the transfer of excess excitation energy from the excited molecule (red).

Sophie E. Canton[a], Kasper S. Kjær[b] and
Martin M. Nielsen[c,*]

[a] Deutsches Elecktronen Synchrotron (DESY), Germany
[b] PULSE Institute, Stanford University, USA
[c] Department of Physics, Technical University of Denmark, Denmark

*E-mail: mmee@fysik.dtu.dk

References

[1] E. Rabinowitch and Govindjee: Photosynthesis, John Wiley & Sons, (1969).
[2] A. Magnuson *et al*.: Accounts Chem. Res. **42** (2009) 1899.
[3] D. Gust *et al*.: Accounts Chem. Res. **34** (2001) 40.
[4] *S.E. Canton, K.S. Kjær, G. Vankó, T.B. van Driel, S. Adachi, A. Bordage, C. Bressler, P. Chabera, M. Christensen, A.O. Dohn, A. Galler, W. Gawelda, D. Gosztola, K. Haldrup, T. Harlang, Y. Liu, K.B Møller, Z. Németh, S. Nozawa, M. Pápai, T. Sato, T. Sato, K. Suarez-Alcantara, T. Togashi, K. Tono, J. Uhlig, D.A. Vithanage, K. Wärnmark, M. Yabashi, J. Zhang, V. Sundström, M.M. Nielsen: Nat. Commun.* ***6*** *(2015) 6359.*

Melting of Pb charge glass and simultaneous Pb-Cr charge transfer in $PbCrO_3$ as the origin of volume collapse

Charge degrees of freedom of transition metal ions gives rise to various fascinating properties of transition-metal compounds, such as superconductivity or magnetoresistance. The ordering or disproportionation of charges in systems with integer or half-integer charge number per atom, such as $Pr_{0.5}Ca_{0.5}MnO_3$ or $CaFeO_3$, causes metal-insulator transitions. These can be regarded as the crystallization of charges. The insulating state tends to have a glassy nature when randomly located dopants are introduced. A charge cluster glass state owing to geometric frustration arising from a triangular arrangement without randomness was recently observed in an organic, compound θ-(BEDT-TTF)$_2$RbZn(SCN)$_4$, and is attracting significant attention.

Bi and Pb are the main group elements, but they have a charge degree of freedom depending on $6s^0$ and $6s^2$ electronic configurations. These are so-called valence skippers because the $6s^1$ state is prohibited and charge disproportionation of Bi is found in perovskites $Ba^{2+}Bi^{3+}_{0.5}Bi^{5+}_{0.5}O_3$ and $Bi^{3+}_{0.5}Bi^{5+}_{0.5}Ni^{2+}O_3$. $PbCrO_3$ has long been regarded as a perovskite compound with a $Pb^{2+}Cr^{4+}O_3$ oxidation state, like metallic $SrCrO_3$ [1]. However, despite the fact that Sr^{2+} and Pb^{2+} have similar ionic radii and that $PbCrO_3$ and $SrCrO_3$ have the same cubic structure with *Pm-3m* symmetry, $PbCrO_3$ is an antiferromagnetic insulator with an enhanced lattice constant of 4.01 Å, which is 4.8% larger than that of $SrCrO_3$. Using synchrotron X-ray scattering and electronic microscopes, we have unraveled a mystery that has eluded researchers for 50 years. $PbCrO_3$ was found to be $Pb^{2+}_{0.5}Pb^{4+}_{0.5}Cr^{3+}O_3$ where Pb^{2+} and Pb^{4+} ions forms a distorted "charge glass" state [2].

The Pb-4*f* hard X-ray photoemission (HAXPES) spectrum for $PbCrO_3$ collected at beamline **BL47XU** is shown in Fig. 1. Both the $4f_{5/2}$ and $4f_{7/2}$ peaks, which are split by the spin-orbit interaction, are doubles and asymmetric with shoulders at higher binding energies, indicating the coexistence of two valence states, namely, Pb^{2+} and Pb^{4+}. The valence state of $PbCrO_3$ is thus determined to be $Pb^{2+}_{0.5}Pb^{4+}_{0.5}Cr^{3+}O_3$. Cr^{3+} with the t_{2g}^3 electronic configuration, which accounts for explaining the large lattice constant and insulating nature of $PbCrO_3$.

Next the local structure of $PbCrO_3$ was investigated. We performed the pair distribution function (PDF) analysis of synchrotron X-ray total scattering data collected at **BL22XU**, as shown in Fig. 2(a), assuming an ordered model with the $3a_0 \times 3a_0 \times 3a_0$ superstructure suggested by the diffuse scattering in electron diffraction and synchrotron X-ray powder diffraction data collected at **BL02B2**. The 27 Pb sites are divided into 2 groups, A and B with the rock-salt-type arrangement, as shown in Fig. 2(b), corresponding to Pb^{2+} and Pb^{4+} or vice versa, as clarified by HAXPES. Then, longitudinal wave-type shift of the Pb positions was applied to both sublattices. The Pb positions were constrained so that these form sine waves in *a*, *b*, and *c* directions. Large shifts of the Pb positions were indeed observed in the high-angle annular dark-field (HAADF) STEM image (Fig. 2(c)). The distribution of the Pb-Pb lengths, 3.4 – 4.2 Å, agrees quite well with each other. It should be noted that the numbers of Pb^{2+} and Pb^{4+} are different in this model, 14:13 or vice versa. Furthermore, there are A-A or B-B arrangements at the interface between $3a_0 \times 3a_0 \times 3a_0$ cells. The long-range ordering of Pb^{2+} and Pb^{4+} is therefore prohibited. Taking into account the above results, one can conclude that Pb^{2+} and Pb^{4+} form a glassy structure, namely, charge glass.

Finally, we investigated the pressure effect on the structure and resistivity of $PbCrO_3$. The unit cell volume calculated from the peak positions of energy-dispersive SXRD (collected at **BL14B1**) is plotted in Fig. 3 as a function of pressure. It decreases by 2.7%, corresponding to a volume collapse of 7.8% at 2.5 GPa, as reported earlier [3]. The electrical resistivity suddenly drops at the corresponding pressure.

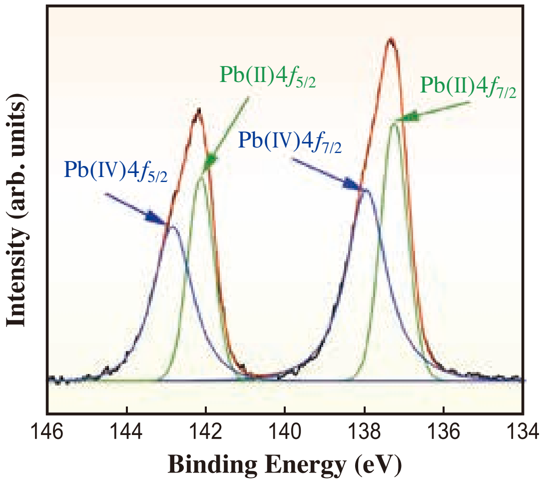

Fig. 1. Pb-4*f* core-level XPS spectrum of $PbCrO_3$ with the fitted results. The black and red lines are observed spectra and total fitted spectrum, respectively.

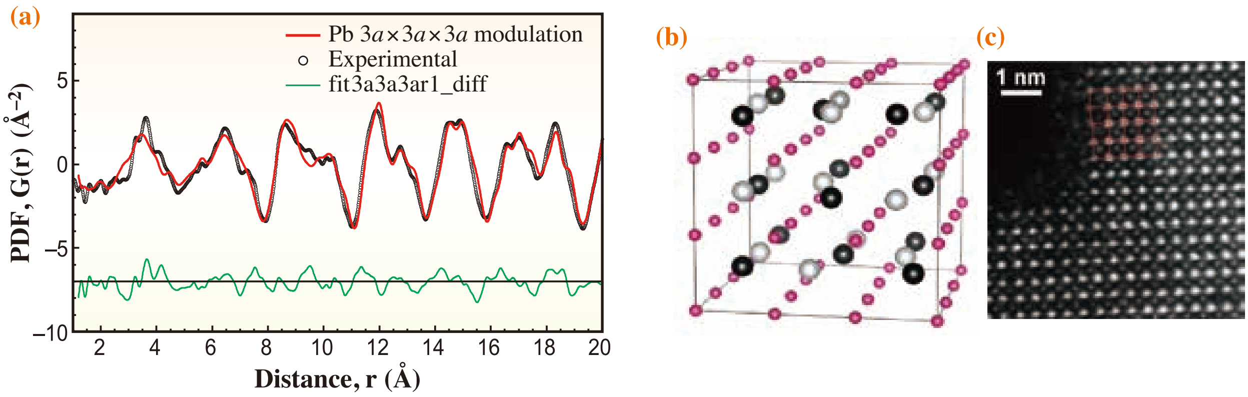

Fig. 2. **(a)** Observed and calculated PDF of an ordered model with $3a_0 \times 3a_0 \times 3a_0$ superstructure. **(b)** The refined crystal structure of the ordered model with $3a_0 \times 3a_0 \times 3a_0$ superstructure. The pink atoms are Cr and the other atoms are Pb. **(c)** HAADF STEM image viewed along the perovskite [001] zone axis. The lateral shift of Pb positions is evident.

The observed volume collapse and simultaneous insulator-to-metal transition can be explained by assuming a pressure-induced intermetallic charge transfer between Pb^{4+} and Cr^{3+} ions and a $Pb^{2+}Cr^{4+}O_3$ valence state for the high-pressure phase (see insets of Fig. 3).

In conclusion, we showed that $PbCrO_3$ has a $Pb^{2+}_{0.5}Pb^{4+}_{0.5}Cr^{3+}O_3$ valence state with a glassy distribution of Pb^{2+} and Pb^{4+} ions and that intermetallic charge transfer between Pb^{4+} and Cr^{3+} induced by the application of pressure leads to the volume collapse and the insulator-to-metal transition.

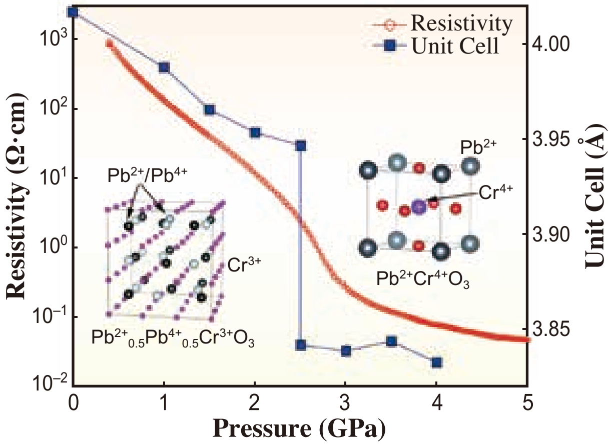

Fig. 3. Pressure evolutions of crystal structure, electrical resistivity and lattice constant of $PbCrO_3$. Abrupt decreases in the lattice constant and resistivity owing to the transition from $Pb^{2+}_{0.5}Pb^{4+}_{0.5}Cr^{3+}O_3$ to $Pb^{2+}Cr^{4+}O_3$ are evident.

Runze Yu* and Masaki Azuma

Materials and Structures Laboratory,
Tokyo Institute of Technology

*E-mail: physyu@hotmail.com

References

[1] W.L. Roth *et al.*: J. Appl. Phys. **38** (1967) 951.
[2] *R. Yu, H. Hojo, T. Watanuki, M. Mizumaki, T. Mizokawa, K. Oka, H.J. Kim, A. Machida, K. Sakaki, Y. Nakamura, A. Agui, D. Mori, Y. Inaguma, M. Schlipf, K. Rushchanskii, M. Ležaić, M. Matsuda, J. Ma, S. Calder, M. Isobe, Y. Ikuhara and M. Azuma: J. Am. Chem. Soc.* ***137*** *(2015) 12719.*
[3] W.S. Xiao *et al.*: Proc. Natl. Acad. Sci. **107** (2010) 14026.

Successful formation of uniform organic thin films of macroscopic size by rational space-filling design

Thin film is an important form of materials for many practical applications. The perfect control of the orientation and alignment of constituent molecules in organic films would realize maximal utility of the intrinsic nature of the molecules, thus leading to the development of high-performance organic materials and devices [1-3]. However, it is extremely difficult to fabricate organic films that have a uniform structure over large areas. One of the general reasons is that when molecules assemble on a substrate, the nucleation and growth of assemblies take place at various locations, resulting in the formation of many nanometer-size domains, which are usually oriented randomly on the substrate. The domain boundaries severely degrade the properties of films in terms of, for example, mechanical strength and electrical conduction. To solve this problem in the fabrication of organic films, we recently devised a rational strategy and successfully constructed large-area thin films devoid of domain boundaries using a newly designed molecular building block [4].

Our strategy for achieving large-area uniform thin films is based on a space-filling design of a "2D + 1D" assembly (Fig. 1(a)), which is inspired by the structure of graphite consisting of atomic 2D hexagonal arrays of carbon. We conceived that a three-bladed propeller-shaped molecular building block could form a one-dimensional (1D) stacking structure of two-dimensional (2D) hexagonal arrays (Fig. 1(a)). Such propeller-shaped molecules mesh like gears to form nested hexagonal packing, which is an ideal motif for the tessellation of the 2D plane. Furthermore, translational and rotational motions, which are possible factors behind the formation of domain boundaries, would be limited in the nested packing of the propeller units. The construction of this kind of two-dimensional sheet may facilitate regular packing in a three-dimensional (3D) space by vertical stacking (Fig. 1(a)). We expected that this space-filling design would be realized using a particular type of triptycene, which is a propeller-shaped rigid molecule comprising three phenylene rings. On the basis of the above idea, we synthesized a series of tripodal triptycenes such as **Trip** (Fig. 1(b)), to which three paraffinic side chains are regiospecifically introduced.

To elucidate the assembly structure of **Trip**, we performed powder X-ray diffraction (XRD) analysis of a bulk sample of **Trip** using synchrotron X-ray radiation at **BL44B2** and **BL45XU**, in collaboration with Dr. Takaaki Hikima and Dr. Masaki Takata (RIKEN). The obtained XRD pattern showed that **Trip** indeed formed a 2D sheet structure by nested packing, which aligns one-dimensionally to form a 1D lamellar structure (Fig. 2(a)). We successfully fabricated a uniform film simply by sandwiching a powder sample of **Trip** between sapphire substrates, heating it to its isotropic hot melt (215°C), and slowly cooling (0.5°C/min) it to 25°C (Fig. 2(b)). The resulting crystalline film showed an entirely dark image in the polarized optical microscopy observation, indicating the formation of a highly oriented assembly. Interestingly, the through-view XRD image of this crystalline film clearly showed hexagonally arranged diffraction spots originating from the 2D hexagonal lattice (Fig. 2(c)), while diffractions arising from the 1D lamellar structure were not detected. These observations indicate that a 2D layer structure uniformly develops parallel to the substrate. Importantly, the domain size of the assembly is larger than the X-ray beam size ($350 \times 150\ \mu\text{m}^2$). To our surprise, the through-view XRD patterns, obtained at more than 30 different points of the crystalline film, showed hexagonally

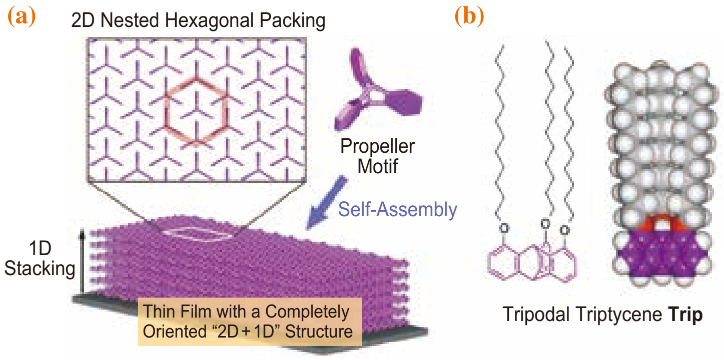

Fig. 1. **(a)** Schematic representation of a space-filling model with a three-bladed, propeller-shaped motif that forms a 2D hexagonal array by nested packing. 1D stacking of the 2D hexagonal leads to a layered structure with high structural order. **(b)** Molecular structure of tripodal paraffinic triptycene **Trip** that embodies the space-filling design.

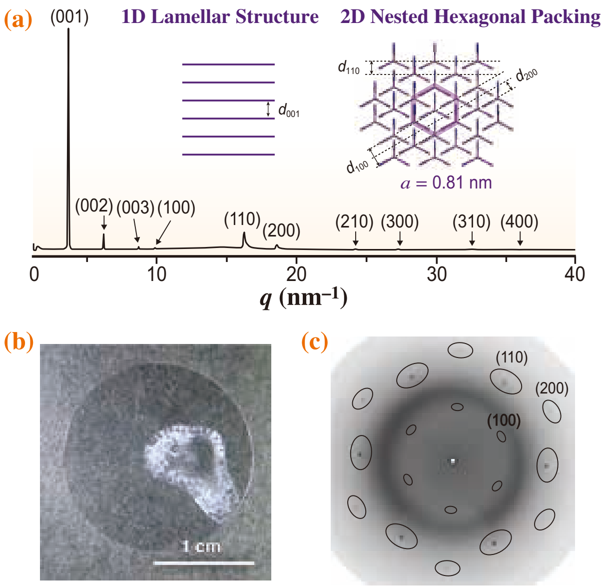

Fig. 2. **(a)** 1D powder XRD profile and schematic representation of the assembly structure (inset) of a bulk sample of **Trip** at 30°C upon cooling from its isotropic hot melt in a glass capillary. **(b)** Photograph of a large-area crystalline **Trip** film sandwiched by sapphire substrates. **(c)** Through-view XRD image of the large-area crystalline **Trip** film. Values in parentheses are Miller indices.

arranged diffraction spots with identical orientation to one another, thus demonstrating that this **Trip** film is devoid of domain boundaries at the centimeter length scale. The fabrication of domain-boundary-free film at this scale is the equivalent of regularly paving the entire surface of the *Eurasia* continent with 1.8 m^2 tiles.

Trip can be vacuum-deposited onto various substrates, affording uniform thin films. Grazing-incidence X-ray diffraction (GI-XRD) analysis at BL45XU clearly showed that the evaporated 50-nm-thick film of **Trip** on a silicon substrate has a completely oriented “2D + 1D” structure (Fig. 3(a)). Furthermore, the through-view XRD pattern of the evaporated film on a sapphire substrate (Fig. 3(b)) displayed hexagonally arranged short arcs (Fig. 3(c)), indicating that the 2D nested hexagonal triptycene arrays in the film are aligned to some extent. By measuring the XRD images at different points of the film at least one centimeter apart, this evaporated film was found to have no detectable domain boundaries. The GI-XRD images observed for the evaporated 50-nm-thick films of **Trip**, fabricated on polyimide (PI), polyethylene terephthalate (PET), quartz, and mica, are essentially identical to one another. Therefore, even in assembly from the vapor phase, **Trip** can exhibit its extraordinary 2D structuring capability.

In summary, the space-filling design using a simple tripodal triptycene building block allows the formation of 2D arrays with extraordinary long-range structural integrity. The 2D arrays pile up next to one another to give a “2D + 1D” structure, resulting in the formation of completely oriented, domain-boundary-free molecular thin films with a size beyond the centimeter length scale. The tripodal triptycenes may serve as useful building blocks for the development of functional thin-film materials [5].

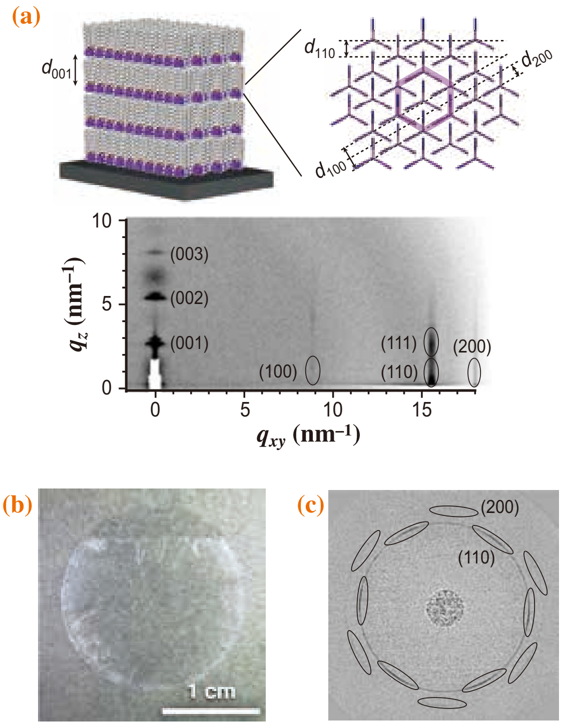

Fig. 3. **(a)** Schematic representation of the assembly structure of **Trip** (top) and a 2D GI-XRD image of a 50-nm-thick evaporated film of **Trip** on a silicon wafer. **(b)** Photograph of a 50-nm-thick evaporated film of **Trip** on a sapphire substrate. **(c)** Through-view XRD image of the evaporated **Trip** film on a sapphire substrate. Values in parentheses are Miller indices.

Yoshiaki Shoji, Takashi Kajitani and Takanori Fukushima*

Chemical Resources Laboratory,
Tokyo Institute of Technology

*E-mail: fukushima@res.titech.ac.jp

References

[1] G.M. Whitesides & B. Grzybowski: Science **295** (2002) 2418.
[2] N. Hosono *et al*.: Science **330** (2010) 808.
[3] J. Soeda *et al*.: Appl. Phys. Express **6** (2013) 076503.
[4] *N. Seiki, Y. Shoji, T. Kajitani, F. Ishiwari, A. Kosaka, T. Hikima, M. Takata, T. Someya and T. Fukushima: Science* ***348*** *(2015) 1122.*
[5] H. Shioya *et al*.: Appl. Phys. Express **8** (2015) 121101.

Quantitative design of fiber strength by structural development analysis of PET

The improvement of mechanical properties has always been a major research theme for synthetic fibers because they are their most important characteristics. In particular, the strength of synthetic fibers is far lower than their theoretical values. For example, the 1.1 GPa strength of industrial-grade poly-(ethylene terephthalate) (PET) fiber corresponds to only 4% of the theoretical value. The causes were explained to be the molecular weight limitations, incomplete molecular orientation and crystallinity, and, in particular, the inhomogeneity in the molecular orientation. The external force is mainly born by the micro-fibril, which consists of highly oriented molecule chains. For ductile materials such as a PET fiber, the strength is decided mainly by the “taut tie-chains” in the amorphous phase, that connect the crystallites in the micro-fibril. Therefore, to produce high-strength synthetic fibers, one should generally aim for a high molecular weight and a high molecular orientation. However, because a high molecular weight causes poor spinnability and drawability, it is difficult to form fibers with highly oriented molecular chains. Thus, the concept of “melt structure control” was proposed to obtain high-strength fibers, whereby a homogeneous chain network structure is formed by melt spinning, followed by the-high-draw ratio drawing of the network [1,2]. Conjugated melt spinning, in which two types of polymers are simultaneously extruded from a spinneret, has been investigated as one technique of melt structure control. For example, as shown in Fig. 1, by the conjugated spinning of PET with a thermotropic liquid-crystalline polymer (TLCP), PET fibers that have obviously higher strength than the single-component-spun and drawn fibers were obtained by high-draw-ratio drawing [2]. The polystyrene (PS) selected as the coupling polymer with PET in this study, identically to the TLCP shown above, has a higher activation energy of extensional viscosity and a higher glass transition temperature (Tg) than PET, so the stress applied in the spin-line was mostly loaded onto the PS component and the PET component was relaxed after the solidification of the PS component. Therefore, the PET fiber could be drawn to a higher draw ratio, resulting in a high strength PET fiber. In addition, it is noteworthy in Fig. 1 that the molecular orientation was almost saturated at about 0.8 for both conjugated and single-component spun fibers, although the fiber strength largely differed. This indicates that the information on the fiber structure, such as molecular orientation, crystallinity, and crystallite size, is insufficient for estimating fiber strength quantitatively. Therefore, we attempted to establish a new category of structural information for estimating the strength of resulting fiber, that is, the process of fiber structure development.

A schematic diagram of the *in situ* measurement system is shown in Fig. 2. By laser irradiation, the running fiber can be heated almost instantaneously as well as homogeneously [3]. It has the merit of accurate on-line measurement of fiber structure development, because the necking location during the continuous fiber drawing process is almost stationary. By taking the WAXD and SAXS images at a certain distance *D*, one can analyze the fiber structure at a certain elapsed time after necking. The ultrahigh-intensity X-ray beam of **BL03XU** used in this study yielded high-precision measurements not only with an improved S/N ratio but also with a 0.1 ms time resolution. The high time resolution permits us to analyze the effects of process conditions on fiber structure development. More concretely, the effects of conjugated spinning with a PS component, the molecular weight of the PET, and the draw ratio were analyzed in this study [4].

A part of the results is shown in Fig. 3: the normalized integrated intensities of both smectic (001') and crystal equatorial diffractions. The smectic

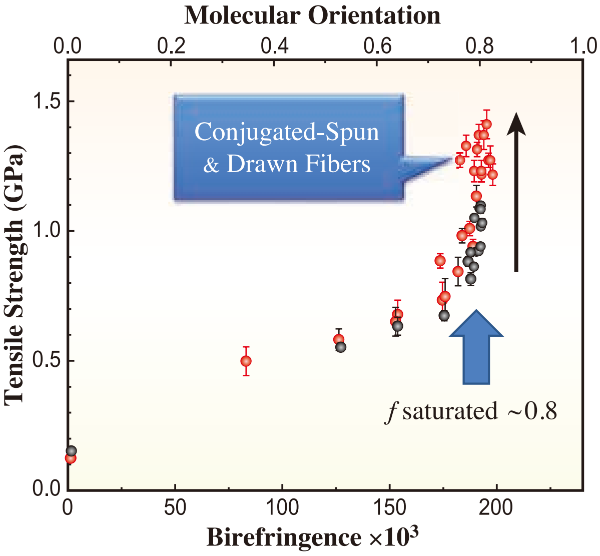

Fig. 1. Strength of drawn PET fibers plotted against their birefringence. Although the molecular orientation was almost saturated for the maximally drawn fibers, the strength of conjugated-spun and drawn was clearly higher than that of single-component spun and drawn fibers.

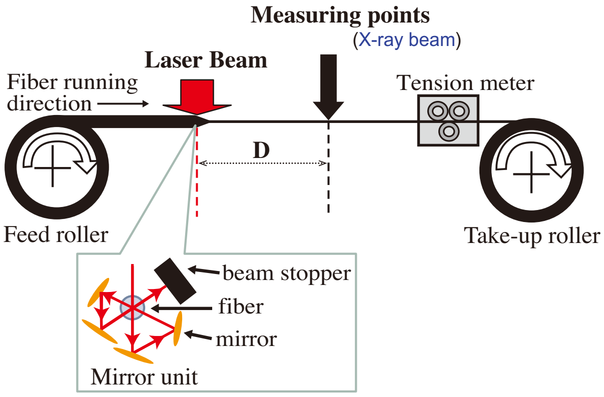

Fig. 2. Schematic diagram of *in situ* measurement system.

phase is the fibrillar-shaped mesophase regarded as the embryo of the microfibril that bears most of the external force [5]. By drawing the higher molecular weight PET to a higher draw ratio, a larger amount of the fibrillar smectic mesophase was formed after necking, and a more highly oriented crystal was formed after the extinction of the smectic mesophase. Accordingly, fibers with higher strength and higher thermal shrinkage stress were obtained. On the other hand, by conjugated spinning with a PS component, the amount of the smectic mesophase formed by the conjugated spinning process was drastically decreased. No crystallization induction time was observed, and the crystallization, particularly the growth of a lamellar crystal, was promoted by the conjugated spinning. Therefore, it was revealed that the fibrillar smectic mesophase seems to inhibit the development of the lamellar crystal at the initial stage of fiber structure development, and the resultant fibrillar structure tends to result in a higher strength, but a relatively lower modulus and yield strength of the fiber.

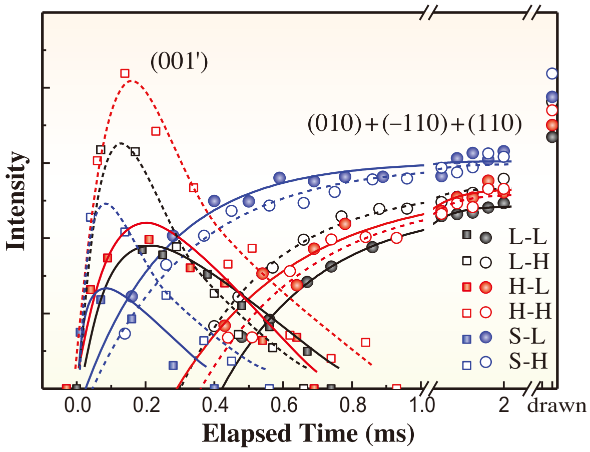

Fig. 3. Integrated intensity of (010), (−110), and (100) diffractions of PET crystal, along with the intensity of smectic (001') diffraction are plotted against the elapsed time after necking. The first and second letters of the sample name indicate the materials and draw ratios. L: low IV PET, H: high IV PET, S: low IV PET conjugated spun with PS, and almost the minimum (L), and maximum (H) draw ratios for stable drawing.

Yutaka Ohkoshi

Faculty of Textile Science and Technology,
Shinshu University

E-mail: yokoshi@shinshu-u.ac.jp

References

[1] T. Kikutani: "Fundamental and Practical Technologies for Nano-structured Polymeric Materials", CMC Press, (2008) 56.
[2] K. Nakata *et al*.: Int. Polym. Proc. **27** (2012) 386.
[3] W. Okumura *et al*.: Int. Polym. Proc. **17** (2002) 24.
[4] *K. Sugawara, T. Ikaga, K. H. Kim, Y. Ohkoshi, K. Okada, H. Masunaga, T. Kanaya, M. Masuda and Y. Maeda: Polym.* ***79*** *(2015) 37.*
[5] T. Yamaguchi *et al*.: J. Polym. Sci.: Part B: Polym. Phys. **46** (2008) 2126.

Oxygen storage capability of $BaYMn_2O_{5+\delta}$ studied by high-temperature X-ray diffraction under precisely controlled oxygen pressures

The so-called "oxygen storage materials (OSMs)" have attracted increased attention in the materials research community. OSMs are categorized as oxides with fast and reversible oxygen intake/release capability. Such materials may be applicable to various oxygen-related technologies owing to their potential ability for a precise control of redox reaction, and hence contribute to solutions of energy and environmental issues. Developments of novel OSMs are highly desirable to open up the possibility of various future applications.

We recently reported the remarkable oxygen storage capability of $BaYMn_2O_{5+\delta}$ [1]. This oxide crystallizes in a double-perovskite type structure, which contains a layered arrangement of smaller yttrium and larger barium ions at the perovskite A-site. The oxygen site within the yttrium plane is readily filled/unfilled in response to variations in temperature and the surrounding atmosphere, resulting in large oxygen nonstoichiometry ranging $0 \leq \delta \leq 1$, see a schematic illustration in Fig. 1. The oxygen intake/release behaviors of $BaYMn_2O_{5+\delta}$ are clearly beyond those of conventional perovskite oxides in terms of the magnitude and sharpness of the processes. This emphasizes the importance of the characteristic crystal structure involving the layered cationic order of Ba^{2+} and Y^{3+}. Understanding of key structural factors of the remarkable oxygen intake/release is particularly important to develop novel/better OSMs. Motivated by such a research background, we examined *in situ* high-temperature X-ray diffraction (XRD) experiments on $BaYMn_2O_{5+\delta}$ [2].

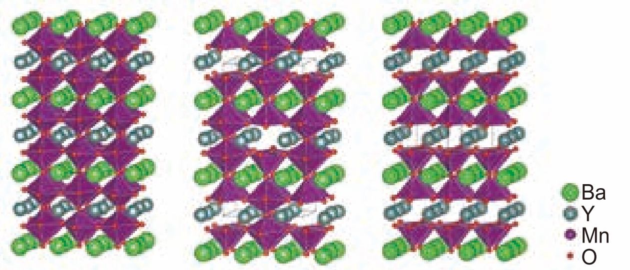

$\delta = 1$
"O_6" phase

$\delta = 0.5$
"$O_{5.5}$" phase

$\delta = 0$
"O_5" phase

Fig. 1. Schematic illustration of the crystal structures of $BaYMn_2O_{5+\delta}$ with oxygen contents $\delta = 1, 0.5$, and 0 ("O_6", "$O_{5.5}$", and "O_5" phases, respectively). The illustration was drawn with VESTA software [5] on the basis of the room-temperature structural models reported in the literature.

Our preliminary investigations revealed that $BaYMn_2O_{5+\delta}$ crystallizes in either the oxygenated "O_6" (Fig. 1(a)) or the intermediate "$O_{5.5}$" form (Fig. 1(b)) at 750°C depending on oxygen pressures $P(O_2)$, enabling us to study these distinct forms selectively upon varying $P(O_2)$ at a constant temperature. *In situ* powder XRD measurements were performed at **BL02B2** beamline. A large Debye-Scherrer camera equipped with a gas/vapor pressure control system [3] was used for the data acquisition at 750°C under precisely controlled oxygen pressures of $P(O_2) = 10^3$ and 10 Pa.

Figures 2(a) and 2(b) present XRD patterns for $BaYMn_2O_{5+\delta}$ taken at 750°C under $P(O_2) = 10^3$ and 10 Pa, respectively. The data clearly indicate that this oxide indeed undergoes a distinct structural change upon lowering oxygen pressure, from a slightly oxygen-deficient "O_6" phase ($BaYMn_2O_{5.89}$; $P(O_2) = 10^3$ Pa) to an oxygen-vacancy ordered "$O_{5.5}$" phase ($BaYMn_2O_{5.51}$; $P(O_2) = 10$ Pa). The $BaYMn_2O_{5.89}$ structure was reasonably refined assuming an orthorhombic *Cmmm* unit cell with lattice constants a, b, $c \approx 2a_p$, where a_p denotes the lattice constant of the cubic perovskite structure. The refined $BaYMn_2O_{5.89}$ structure is depicted in the inset of Fig. 2(a). Our careful refinement suggests that yttrium resides in a split site at a less symmetrical position with 50% occupancy, see the [001] projection shown in Fig. 2(c). The site splitting for yttrium leads to its random displacements within the yttrium plane. Since the oxygen sites within the yttrium plane are slightly unfilled, nonequivalent distances of shorter Y-O and longer Y-V_O (V_O denotes an oxygen vacancy) may be more favorable. We thus interpret the large yttrium displacement as a consequence of oxygen vacancy formation at the surrounding oxygen sites.

Meanwhile, the pattern for $BaYMn_2O_{5.51}$ was fitted well with the orthorhombic *Icma* model (Fig. 2(b); a, $b \approx 2a_p$, $c \approx 4a_p$) that is proposed for a room-temperature "$O_{5.5}$" structure [4]. The $BaYMn_2O_{5.51}$ structure contains alternate ordering of oxygen and vacancy arrays within the yttrium plane (Fig. 2(d)), giving rise to two distinct manganese sites: one with square pyramidal coordination and the other with octahedral coordination. It is thus evident that the "O_6"-to-"$O_{5.5}$" transformation involves drastic modifications in the Mn polyhedra. Moreover, a closer look at the coordination geometry around manganese has revealed important structural features underlying the remarkable oxygen intake/release. As demonstrated in Fig. 3, both the MnO_5/MnO_6 polyhedra in the $BaYMn_2O_{5.51}$ structure are significantly distorted: the Mn-O bond parallel to the *c*-axis is much longer than those within the *ab* plane, while octahedral MnO_6 is largely elongated along the *a*-axis. This feature is in contrast to the $BaYMn_2O_{5.89}$ structure, in which the Mn octahedra are much more isotropic having similar Mn-O bond lengths for all directions.

The peculiar atomic arrangement in $BaYMn_2O_{5.51}$ can be understood as a consequence of alternate orbital ordering for the Jahn-Teller active Mn^{3+} ions consisting of dz^2-type orbital along the *c*-axis at the pyramidal site and that along the *a*-axis at the octahedral site. It should be noted that this high-temperature structure is essentially identical to the room-temperature structure, indicating the robustness of the orbital-ordered "$O_{5.5}$" structure in a wide temperature range. As demonstrated by the comparison of Figs. 2(c) and 2(d), the abrupt "O_6"-to-"$O_{5.5}$" transformation can also be viewed as discontinuous structural reconstruction within the yttrium plane, involving oxygen/vacancy redistribution and yttrium displacement organization, being triggered by the relative stabilization of the two phases. That is to say, the abrupt jump in the oxygen content and thereby the remarkable oxygen intake/release behaviors are attributed to the exceptional stability of the "$O_{5.5}$" structure consisting of particular Mn^{3+} orbital ordering, and the instability of the "O_6" structure disrupted by the increased number of oxygen vacancies and associated random displacements of yttrium.

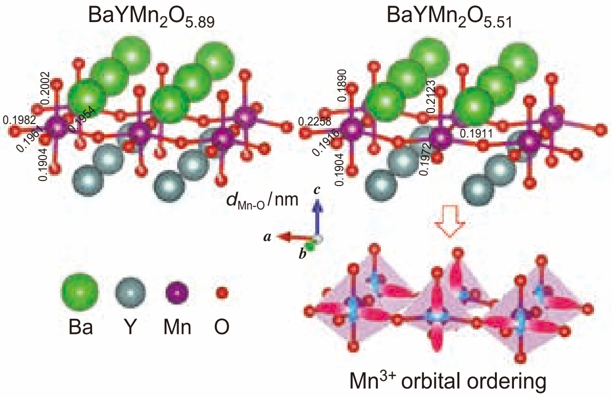

Fig. 3. Atomic arrangements of $BaYMn_2O_{5.89}$ (upper left) and $BaYMn_2O_{5.51}$ (upper right) at 750°C. The schematic illustration of the Mn^{3+} orbital ordering is also given (bottom right).

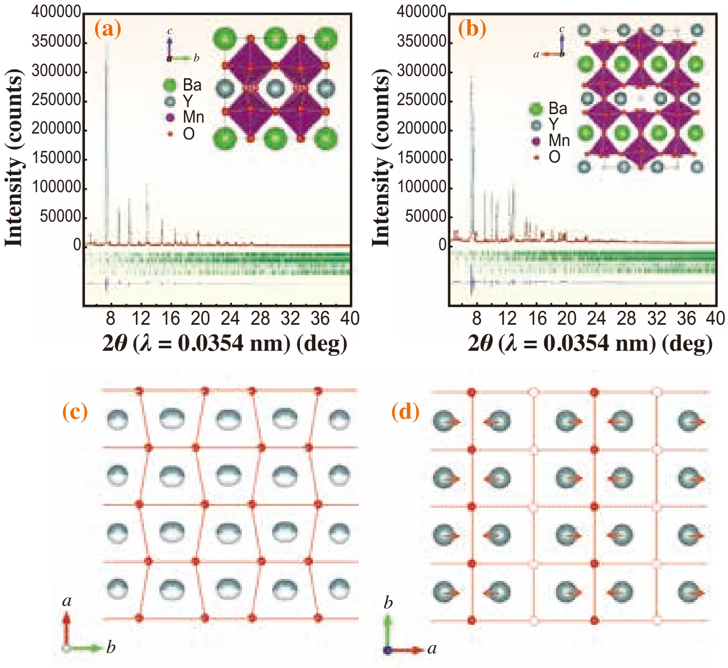

Fig. 2. High-temperature X-ray diffraction patterns for **(a)** $BaYMn_2O_{5.89}$ and **(b)** $BaYMn_2O_{5.51}$ measured at 750°C under $P(O_2) = 10^3$ and 10 Pa, respectively. The crystal structures were refined by the Rietveld method using the RIETAN-FP program [6]. The resultant crystal structure is visualized in the inset of each figure. The [001] projections of the two structures, showing local atomic arrangements within the yttrium plane are presented in **(c)** and **(d)**.

Teruki Motohashi[a,*], Yoshiki Kubota[b]
and Hiroshi Kageyama[c]

[a] Department of Materials and Life Chemistry,
Kanagawa University
[b] Department of Physical Science,
Osaka Prefecture University
[c] Department of Hydrocarbon Chemistry,
Kyoto University

*E-mail: t-mot@kanagawa-u.ac.jp

References

[1] T. Motohashi *et al.*: Chem. Mater. **22** (2010) 3192.
[2] *T. Motohashi, T. Takahashi, M. Kimura, Y. Masubuchi, S. Kikkawa, Y. Kubota, Y. Kobayashi, H. Kageyama, M. Takata, S. Kitagawa, and R. Matsuda: J. Phys. Chem. C* ***119*** *(2015) 2356.*
[3] K. Kato *et al.*: AIP Conf. Proc. **1234** (2010) 875.
[4] C. Perca *et al.*: Chem. Mater. **17** (2005) 1835.
[5] K. Momma and F. Izumi: J. Appl. Crystallogr. **44** (2011) 1272.
[6] F. Izumi and K. Momma: Solid State Phenom. **130** (2007) 15.

Fe^{4+}-based quadruple perovskite catalyst for oxygen evolution reaction

The oxygen evolution reaction (OER) is an essential electrochemical reaction for energy conversion in various applications such as rechargeable metal-air batteries and water electrolysis for hydrogen production. Highly active and durable OER catalysts are required to reduce high overpotential, which causes a huge loss of energy. Precious-metal-based oxides such as RuO_2 and IrO_2 are widely used as OER catalysts, but alternative OER catalysts consisting of earth-abundant elements are desired. Transition metal oxide catalysts with the perovskite structure are extensively investigated because of their flexible chemical compositions and electronic states. Cobalt-based perovskite oxides such as $Ba_{0.5}Sr_{0.5}Co_{0.8}Fe_{0.2}O_{3-\delta}$ (BSCF) and $R_{0.5}Ba_{0.5}CoO_3$ (R = rare-earth metals) are considered promising candidates for OER catalysis materials. Suntivich *et al*. proposed that the occupancy of e_g orbitals of B-site metal ions for ABO_3 perovskite is related to catalytic activity for OER [1], in which B-site ions with $e_g^{\sim 1}$ configuration show the highest catalytic activity. Furthermore, the energy level of the oxygen 2*p* band center was proposed as another descriptor of OER catalytic activity [2]. However, the design principle for highly active and durable catalysts has not been established.

Fe^{4+}-based oxides with the nominal electron configuration of $t_{2g}^3 e_g^1$ are also expected to be good candidates for highly active OER catalysts, but their catalytic properties have not been carefully investigated yet probably because of their severe synthesis conditions such as high pressures (several GPa) and high temperatures. Recently, we have reported that the quadruple perovskite oxide $CaCu_3Fe_4O_{12}$ (CCFO) containing Fe^{4+} ions demonstrate very high OER catalytic activity [3]. We also found that CCFO has higher stability under OER conditions than the simple perovskites $AFe^{4+}O_3$ (A = Ca, Sr). The electron density distribution analysis based on synchrotron X-ray powder diffraction indicates that the increased stability of CCFO under OER conditions is derived from the covalent bonding network incorporating multiple transition metal ions such us Cu^{2+} and Fe^{4+}, and we propose a new guideline to achieve both catalytic activity and durability.

Figures 1(a) and 1(c) show the crystal structures of $SrFeO_3$ and CCFO. $SrFeO_3$ crystallizes in a simple cubic perovskite structure, whereas CCFO crystallizes in an $AA'_3B_4O_{12}$-type quadruple cubic perovskite structure, in which A-site Ca^{2+} and A'-site Cu^{2+} ions are spatially ordered because of the differences in ionic size and coordination preference. Both CCFO

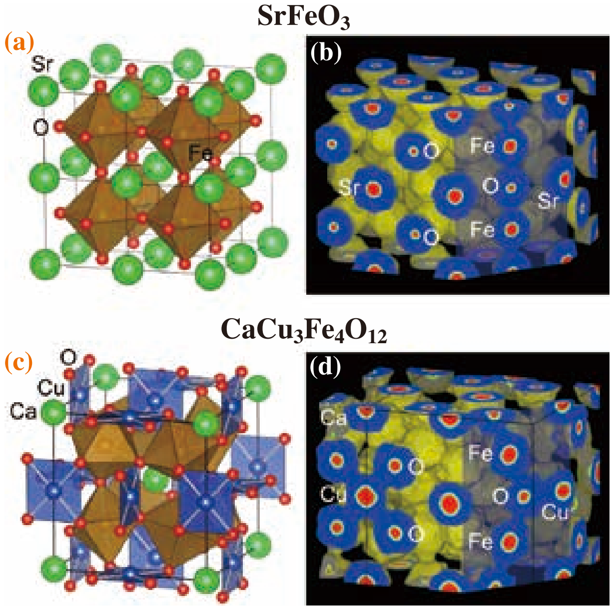

Fig. 1. Crystal structures of Fe^{4+}-perovskites **(a)** $SrFeO_3$ and **(c)** $CaCu_3Fe_4O_{12}$. Electron density mapping obtained by the maximum entropy analysis of synchrotron X-ray powder diffraction data for **(b)** $SrFeO_3$ (equidensity level: 0.4 $Å^{-1}$) and **(d)** $CaCu_3Fe_4O_{12}$ (equidensity level: 0.5 $Å^{-1}$).

and $SrFeO_3$ can be synthesized under high-pressure and high-temperature conditions of above several GPa and approximately 1000°C.

Figure 2(a) shows the linear sweep voltammograms of various transition metal oxides under OER conditions. CCFO shows the lowest onset potential (lowest overpotential) and a rapid increase in current density, indicating a high catalytic activity, which exceeds those of the state-of-the-art catalysts BSCF and RuO_2. It should also be noted that $CaFeO_3$ has a higher catalytic activity than $LaMnO_3$ with Mn^{3+} in the electron configuration of $t_{2g}^3 e_g^1$, nominally identical to Fe^{4+}. The superiority of Fe^{4+} in OER catalysis is attributed to its unique electronic state. It is considered that ligand holes in oxygen 2*p* orbitals are predominant in unusual high-valence Fe^{4+} ions because of the deeply lying Fe 3*d* orbitals; thus, electron configuration of Fe^{4+} is close to $t_{2g}^3 e_g^2 \underline{L}^1$ ($\underline{L}$ ligand hole), not to conventional $t_{2g}^3 e_g^1$. The above finding indicates that the oxygen 2*p* band is lifted up close to the Fermi level in Fe^{4+}-oxides, satisfying the descriptor suggested by Grimaud *et al.* [2].

It is also notable that CCFO has relatively higher stability than simple Fe^{4+}-perovskites. Figure 2(b) shows cyclic voltammograms of $CaFeO_3$ and CCFO in 100 cycles. $CaFeO_3$ shows serious degradation in the 100th sweep and its current density markedly decreases during the cycles. On the other hand, CCFO shows no degradation after 100 cycles, retaining a high current density and a low overpotential. The high stability of CCFO under OER conditions was investigated in terms of chemical bonding. Synchrotron X-ray powder diffraction data were collected at **BL02B2** beamline. Figures 1(b) and 1(d) show the electron density distributions of $SrFeO_3$ and CCFO. A certain electron density is observed between Fe and O ions for $SrFeO_3$, which is attributed to the high covalency of the Fe–O bond. In contrast, Sr ions are separated from neighboring O ions because of its ionic characteristic. This probably leads to the dissolution of Sr ions. Together with Fe–O bonds, substantial electron densities are also confirmed between neighboring Cu and O ions for CCFO (Fig. 1(d)), resulting in a widespread covalent bonding network which inhibits the degradation in a number of OER cycles.

In summary, we demonstrate that Fe^{4+}-based perovskite oxides synthesized under high-pressure and high-temperature conditions have high catalytic activities for OER. The stability under OER conditions of CCFO is much higher than those of simple Fe^{4+}-perovskites. A widespread covalent bonding network consisting of Cu, Fe, and O ions is determined by the electron density distribution analysis of synchrotron X-ray powder diffraction, which is a key to realizing robust and highly active OER catalysts.

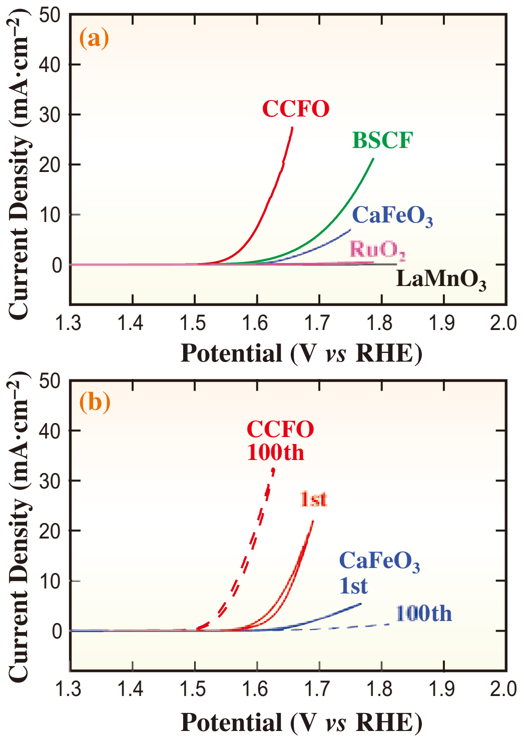

Fig. 2. **(a)** Linear sweep voltammograms of various transition metal oxides for OER. **(b)** Cyclic voltammograms of $CaFeO_3$ and $CaCu_3Fe_4O_{12}$ during continuous 100 cycle OER measurements.

Ikuya Yamada* and Shunsuke Yagi

Nanoscience and Nanotechnology Research Center,
Osaka Prefecture University

*E-mail: i-yamada@21c.osakafu-u.ac.jp

References

[1] J. Suntivich *et al.*: Science **334** (2011) 1383.
[2] A. Grimaud *et al.*: Nat. Commun. **4** (2013) 2439.
[3] *S. Yagi, I. Yamada, H. Tsukasaki, A. Seno, M. Murakami, H. Fujii, H. Chen, N. Umezawa, H. Abe, N. Nishiyama, S. Mori: Nat. Commun.* ***6*** *(2015) 8249.*

Reaction of CO_2 on stepped Cu(997) surface revealed by ambient-pressure X-ray photoelectron spectroscopy

Today, society presents a strong demand towards developing novel catalysts that will solve energy and environmental problems. In catalysis research, the importance of *Operando* spectroscopy has recently begun to be realized. Gaps in pressure and temperature exist between ideal surface science studies (ultrahigh vacuum (UHV) and low/moderate temperature) and real catalytic conditions (above atmospheric pressure and high temperature). Such differences in pressure and temperature may result in distinct reactivity under ambient conditions compared with the case of UHV conditions, reflecting thermodynamic and kinetic effects. Ambient-pressure X-ray photoelectron spectroscopy (AP-XPS) [1] is a powerful *Operando* spectroscopy that allows us to investigate electronic and chemical states of the adsorbate and substrate under gas atmosphere.

The activation of CO_2 is an important topic in the efficient use of CO_2 as a chemical feedstock. Methanol synthesis from CO_2 and H_2 on Cu/ZnO catalysts has been widely studied and is already developed industrially. CO_2 is chemically inert, and thus the interaction of the molecule with metallic Cu surfaces plays an essential role in molecular activation. The previous studies in UHV revealed that stepped Cu surfaces are active in the dissociation of CO_2 [2,3]. However, the reaction mechanism of CO_2 at defect sites such as steps and kinks on the Cu surface, which are abundant on real catalysts, is not yet fully understood. In this study [4], therefore, we investigated the reaction process of CO_2 on the stepped Cu(997) surface at a CO_2 pressure of 0.8 mbar and a temperature of 340 K by AP-XPS.

We developed a new AP-XPS system (Fig. 1) at the soft X-ray undulator beamline **BL07LSU** [5]. AP-XPS measurements were carried out using a differentially pumped electron analyzer (SPECS, PHOIBOS 150 NAP) with an ambient-pressure gas cell. A one-dimensional delay-line detector (DLD) is adopted as the detector in the electron analyzer. The ambient-pressure gas cell is equipped with an Si_3N_4 window for X-ray transmission and a small aperture (300 μm in diameter), which is the entrance to the differentially pumped electron analyzer. The whole gas cell is mounted on a manipulator of the load-lock chamber, and is docked to the front of the electron analyzer. In the ambient-pressure gas cell, a sample is placed close (~300 μm) to the entrance aperture in order to minimize the scattering of photoelectrons by gas-phase molecules. The high performance of our AP-XPS instrument was confirmed by successful measurements of the Au 4*f* core level of polycrystalline Au foil in the presence of 20 mbar N_2 gas.

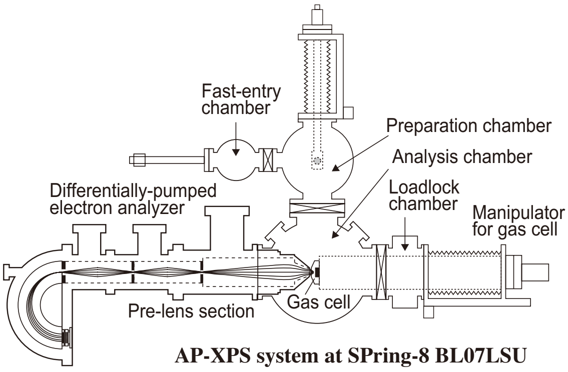

Fig. 1. Schematic of the AP-XPS system.

Figures 2(a) and 2(b) show a series of O 1*s* and C 1*s* AP-XPS spectra of Cu(997) at 340 K under a CO_2 pressure of 0.8 mbar as a function of elapsed time. Gas-phase CO_2 peaks in O 1*s* and C 1*s* spectra were observed at 536.6–536.4 eV and at 292.8–292.6 eV, respectively. A peak of the adsorbate was observed at 531.3 eV in the O 1*s* XPS (t = 376 s), whereas three peaks were observed in the C 1*s* XPS (t = 507 s): at 288.4 eV with a broader shoulder peak at higher binding energy (289.0 eV), and at 284.4 eV. The intensities of XPS peaks at 531.3, 289.0, and 288.4 eV were saturated at $t \sim$ 2000 s, and then a new peak at 529.5 eV appeared in O 1*s* XPS spectra. Temporal evolutions of each O 1*s* and C 1*s* XPS peak are shown in Fig. 3.

The XPS peaks at 531.3, 289.0, and 288.4 eV are assigned to carbonate (CO_3) species, on the basis of the binding energies and the atomic O/C ratio of 3.1±0.1 estimated from the area intensities of O 1*s* and C 1*s* XPS peaks. Two different C 1*s* peak positions of CO_3 may originate from different adsorption sites of CO_3 on Cu(997), such as steps. The O 1*s* XPS peak at 529.5 eV, which appeared after the saturation of CO_3, is attributed to atomic oxygen. The C 1*s* XPS peak at 284.4 eV is assigned to neutral carbon species (C_0) such as graphitic carbons and hydrocarbons.

Next we discuss the reaction mechanism of CO_2 on the Cu(997) surface under near-ambient conditions. Previous experimental studies in UHV revealed the dissociation of CO_2 on the stepped Cu surfaces [2,3]. The CO_2 dissociation should also proceed on the Cu(997) surface under near-ambient conditions to form atomic oxygen and CO. The formed CO is readily desorbed from the Cu surface at 340 K [3],

$$CO_2 \rightarrow CO\ (gas) + O \tag{1}$$

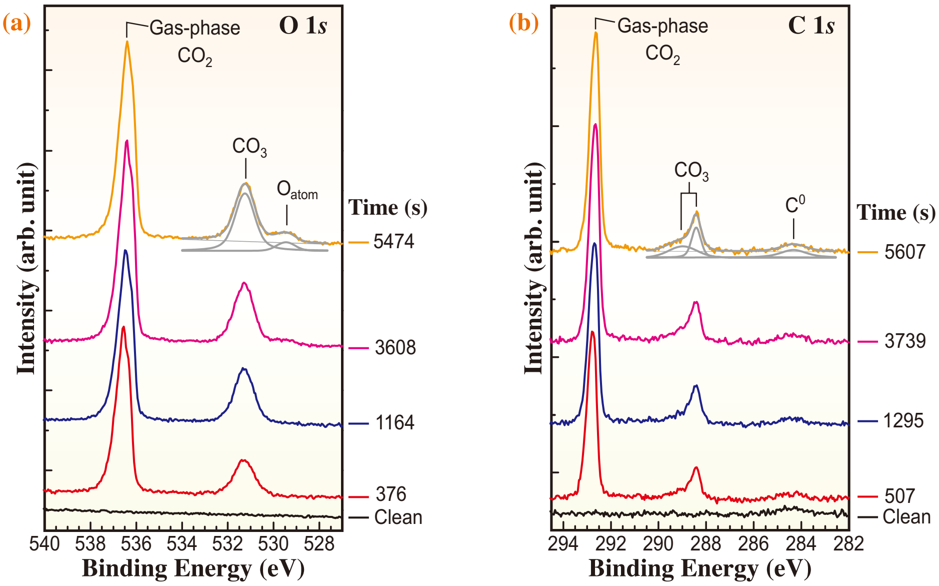

Fig. 2. A series of **(a)** O 1s and **(b)** C 1*s* AP-XPS spectra of Cu(997) at 340 K under CO_2 pressure of 0.8 mbar as a function of elapsed time. Only selected spectra from the whole series are shown in the figure. The photon energy was 630 eV. The CO_2 gas was introduced to the gas cell at $t = 0$ s. The fitting results for the spectra at $t = 5474$ s (O 1*s*) and $t = 5607$ s (C 1*s*) are also shown in the figures.

Then, the produced atomic oxygen reacts with CO_2 to form CO_3,

$$O + CO_2 \rightarrow CO_3 \qquad (2)$$

The produced CO_3 is stable on the Cu surface at 340 K, as seen in Fig. 2.

It should be noted that the estimated saturation coverage of CO_3 is rather small (0.05 molecules per surface Cu atom). This indicates that the formed CO_3 species stay at some specific sites, and probably block further CO_3 formation. After the saturation of CO_3 coverage, the atomic O gradually appears on the surface. It may be because minor reaction sites for the CO_2 dissociation remain on the surface while most of the active sites are covered by CO_3.

The present study clearly shows the formation of CO_3 on the stepped Cu(997) surface, and suggests that CO_3 is a candidate for a reaction intermediate in the CO_2 chemistry on Cu surfaces.

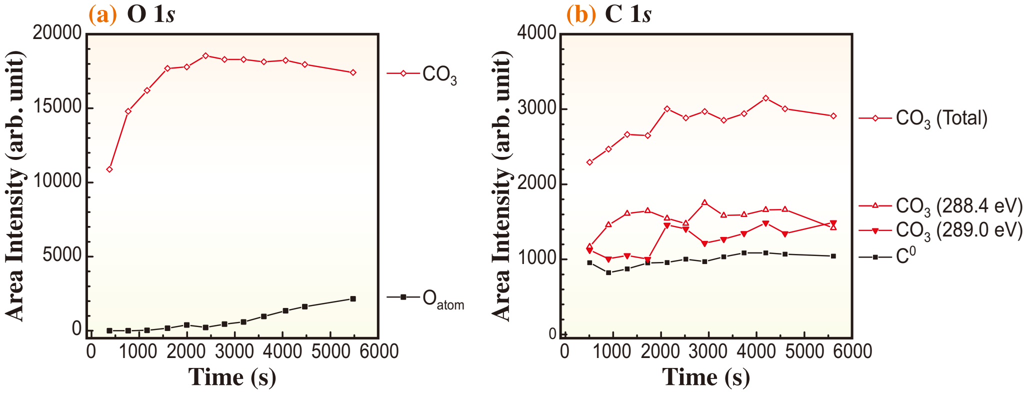

Fig. 3. Area intensities of each component in **(a)** O 1*s* and **(b)** C 1*s* spectra in Figs. 2(a) and 2(b) as a function of elapsed time ($p(CO_2) = 0.8$ mbar, $T = 340$ K).

Susumu Yamamoto*, Takanori Koitaya and Jun Yoshinobu

The Institute for Solid State Physics,
The University of Tokyo

*E-mail: susumu@issp.u-tokyo.ac.jp

References

[1] M. Salmeron, R. Schlögl: Surf. Sci. Rep. **63** (2008) 169.
[2] S.S. Fu, G.A. Somorjai: Surf. Sci. **262** (1992) 68.
[3] I.A. Bönicke *et al.*: Surf. Sci. **307-309** (1994) 177.
[4] *T. Koitaya, S. Yamamoto, Y. Shiozawa, K. Takeuchi, R.-Y. Liu, K. Mukai, S. Yoshimoto, K. Akikubo, I. Matsuda, J. Yoshinobu: Topics in Catalysis* ***59*** *(2016) 526.*
[5] S. Yamamoto *et al.*: J. Synchrotron Rad. **21** (2014) 352.

Mechanistic investigation of iron-catalyzed Kumada-Tamao-Corriu-type cross-coupling reactions based on solution-phase XAFS

A renaissance of iron-catalyzed cross-coupling reactions in the last decade has been triggered in the standpoint of element strategy, the aim of which is the discovery of unprecedented reactivity and selectivity of common and ubiquitous metals apart from those of conventional precious metals. Despite the significant progress in cross-coupling technology through the use of 3*d*-transition metal catalysts including iron catalysts, the large paramagnetic shifts and the related loss of spin-spin coupling information in NMR spectra often hampers solution-phase structural study of catalytic intermediates in the reaction mixture. Conventional ESR spectroscopy also suffers difficulty in measuring typical Fe^{+2} and Fe^{+3} species with $S > 1/2$, as they are often invisible. In addition, the inherent chemical instabilities of 3*d*-metal–carbon bonds toward H_2O and O_2 complicate the conventional mechanistic study based on X-ray crystallography of isolated intermediates. We therefore attempted to apply synchrotron X-ray absorption spectroscopy (XAFS) for the structural and mechanistic investigation of paramagnetic organometallic intermediates in homogeneous iron-catalyzed reactions. Despite the widespread application and significant contribution of synchrotron XAFS in the research field of heterogeneous catalysts, its application to homogeneous catalysts is still underdeveloped and rare for *in situ* structural determination of unstable and highly reactive organometallic intermediates, especially in organic reaction mixtures.

Recently, we reported the solution-phase XAFS-based identification and structural determination of the organoiron intermediates of iron-catalyzed Kumada-Tamao-Corriu (KTC)-type cross-coupling reactions [1]. We have developed an iron bisphosphine complex, FeX_2(SciOPP) [2], that has proven to be highly effective toward various types of coupling reaction. For the FeX_2(SciOPP)-catalyzed KTC-type reaction, we proposed a formal non-redox Fe^{+2}–Fe^{+2} mechanism, as shown in Fig. 1. However, a variety of mechanisms including Fe^{+1}–Fe^{+3}, Fe^{0}–Fe^{+2}, and Fe^{-2}–Fe^{0} redox pathways have been proposed, and complicating the issue of the mechanism of iron-catalyzed cross-coupling reactions. Therefore, we carried out a solution-phase XAFS study at beamlines **BL14B2** and **BL27SU** to elucidate the oxidation state and structures of the corresponding intermediates that are engaged in the FeX_2(SciOPP)-catalyzed KTC-type coupling. Firstly, the formation of the described organoiron intermediates of FeBrMes(SciOPP) **2** and $FeMes_2$(SciOPP) **3** was examined by solution-phase XANES. The reaction of $FeBr_2$(SciOPP) **1** and MesMgBr was conducted in THF with 1:1 and 1:2 ratios at –30°C. In a glovebox, the warmed reaction mixture was transferred into a gastight cell for solution-phase XAFS, as shown in Fig. 2. The Fe *K*-edge XANES spectra of the THF solution of **1**, and the reaction mixtures obtained from

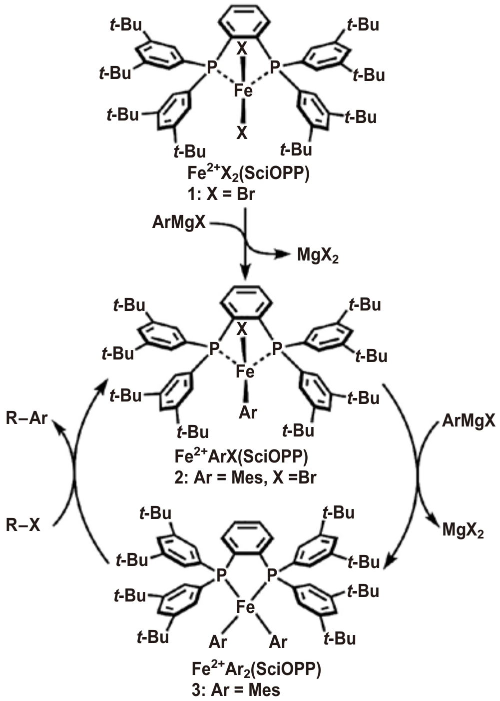

Fig. 1. Proposed mechanism of FeX_2(SciOPP)-catalyzed KTC-type coupling of arylmagnesiumhalide with haloalkanes.

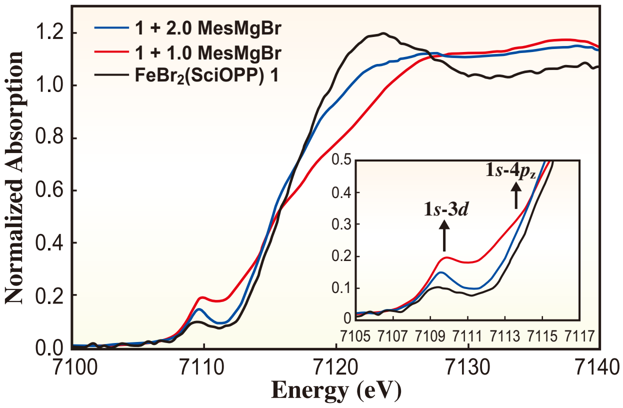

Fig. 2. A series of Fe *K*-edge XANES spectra of THF solution of **1** (black line) and reaction mixtures of **1** with 1.0 equiv (blue line) and 2.0 equiv (red line) MesMgBr.

1.0 and 2.0 equiv additions of MesMgBr to **1** revealed the formation of the expected divalent organoiron species of monomesityliron FeBrMes(SciOPP) **2** and dimesityliron $FeMes_2$(SciOPP) **3**. The observed pre-edge peak at around 7109.5 eV and the shoulder peak at 7112.3 eV can be assigned to a characteristic $1s$–$3d$ electron transition of tetrahedral iron(II) complexes and the $1s$–$4p_z$ transition of square planar iron(II) complexes, respectively.

The observed organoiron intermediates were successfully isolated under strictly water- and oxygen-removed conditions and the resulting micron-size single crystals were used in low-temperature rapid single-crystal X-ray diffraction analysis at beamlines **BL40XU** and **BL02B1** to elucidate the molecular structures of **2** and **3**. As shown in Fig. 3, the tetrahedral geometry of **2** and square planar geometry of **3** are in close agreement with the geometries predicted by XAFS.

Solution-phase structure determination based on Fe *K*-edge XAFS was successfully performed in THF solutions of **2** and **3** and high-quality EXAFS spectra were obtained (Fig. 4). The FEFF fitting calculation using crystal-structure-based fitting models revealed that the Fe–C, Fe–Br, and Fe–P bond lengths, as well as the solution phase geometries of **2** and **3**, agree well with those of the crystal states.

Finally, the cross-coupling activity of isolated mesityliron species **2** and **3** were adequately confirmed by their reactions with 1-bromodecane under both stoichiometric and catalytic conditions. The formation of the corresponding **1** was also confirmed by *in situ* EXAFS analysis of the reaction mixture.

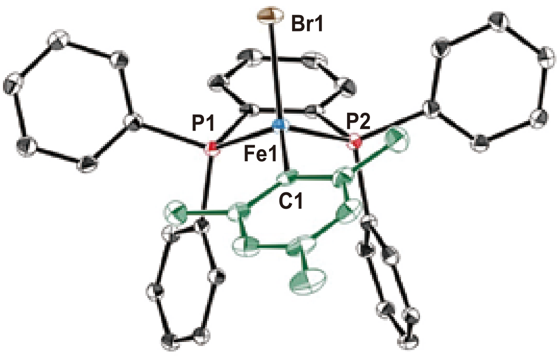

Selected bond lengths and angles

Fe1–Br1	2.4182(5) Å	P1–Fe1–C1	124.86(8)°	P1–Fe1–P2	78.33(2)°
Fe1–P1	2.4575(8) Å	P2–Fe1–C1	119.72(8)°	C2–Fe1–Br1	125.38(8)°
Fe1–P2	2.4430(7) Å	P1–Fe1–Br1	96.97(2)°		
Fe1–C1	2.046(3) Å	P2–Fe1–Br1	100.19(2)°		

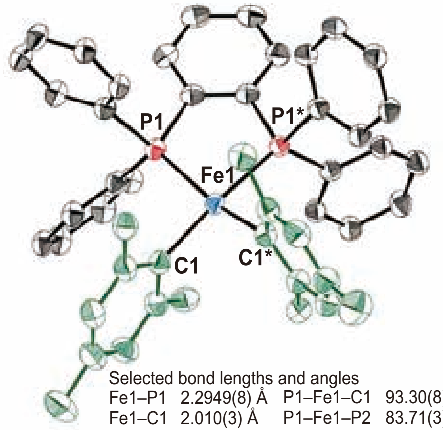

Selected bond lengths and angles

Fe1–P1	2.2949(8) Å	P1–Fe1–C1	93.30(8)°
Fe1–C1	2.010(3) Å	P1–Fe1–P2	83.71(3)°
		C1–Fe1–C2	93.3(1)°

Fig. 3. Molecular structures of **2** and **3** with selected bond lengths and angles. Hydrogen atoms and *t*-Bu groups have been omitted for clarity.

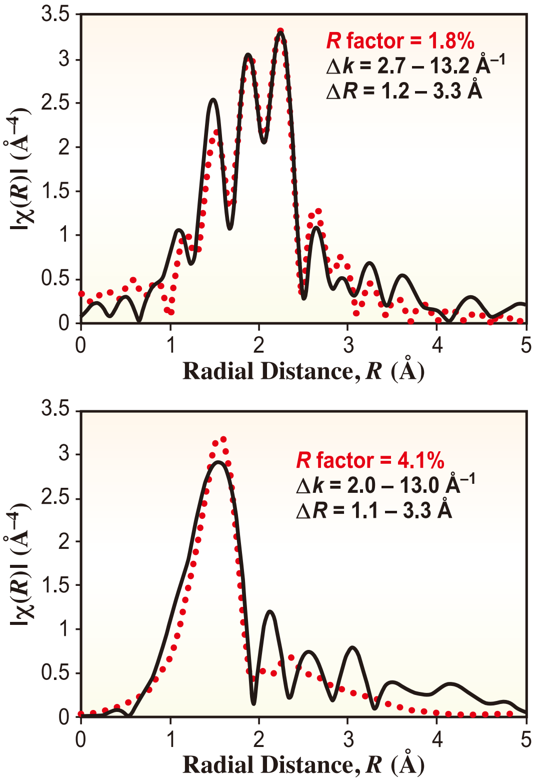

Fig. 4. EXAFS spectra of the THF solutions of **2** and **3** with fitted results.

Hikaru Takaya[a,b,*], Sho Nakajima[a,b]
and Masaharu Nakamura[a,b]

[a] International Research Center for Elements Science, Kyoto University
[b] Department of Energy and Hydrocarbon Chemistry, Kyoto University

*E-mail: takaya@scl.kyoto-u.ac.jp

References

[1] *H. Takaya, S. Nakajima, N. Nakagawa, K. Isozaki, T. Iwamoto, R. Imayoshi, N.J. Gower, L. Adak, T. Hatakeyama, T. Honma, M. Takagaki, Y. Sunada, H. Nagashima, D. Hashizume, O. Takahashi, M. Nakamura: Bull. Chem. Soc. Jpn.* ***88*** *(2015) 410.*
[2] T. Hatakeyama *et al.*: Chem. Lett. **40** (2011) 1030.

Accumulation and distribution of cesium in *Egeria densa*, a submerged plant

Radionuclides were discharged into the environment in the northeast region of Japan after the destruction of the Fukushima Daiichi Nuclear Power Station, located approximately 250 km north of Tokyo, in March 2011. The radionuclides fell on the land and were dispersed by rainwater and mountain streams to rivers, lakes, and ponds. Radioactive cesium (^{134}Cs and ^{137}Cs) is a major fission product and plays a crucial role in both external and internal doses, because of the emission of beta and gamma radiation, the long half-lives (^{134}Cs: 2.06 years, ^{137}Cs: 30.2 years), and its rapid incorporation into biological systems [1]. The development of techniques for the removal of radioactive Cs requires knowledge of the mobility of Cs in the environment. Several reports have shown that the fate of ^{134}Cs and ^{137}Cs derived from the nuclear accident fallout and associated radiological hazards are strongly dependent on their mobility in the surface soils.

Plant uptake is a major pathway for the migration of radiocesium from the soil to the human diet. To predict the movement of radionuclides and to remove them from the northeastern area of Japan, the radioactivities of terrestrial plants have been monitored and reported in several articles. The released radionuclides have also probably been incorporated into aquatic ecosystems; however, there is little information about the contamination of freshwater ecosystems.

In this work, we focused on the bioaccumulation of Cs in a freshly submerged vascular plant, *Egeria densa* (Brazilian waterweed, Hydrocharitaceae), to investigate the behavior of Cs in fresh aquatic ecosystem. We collected *E. densa* plants, waters, and sediments that are contaminated by radioactive fallout in Fukushima Prefecture in September 2012 (Fig. 1(a)). The activities of ^{134}Cs, ^{137}Cs, and ^{40}K were measured using a germanium semiconductor detector (Fig. 1(b)).

Environmental radioactive Cs concentration varied among the sampling points. The highest total radiocesium (^{134}Cs and ^{137}Cs) activity was 123 Bq·kg^{-1} from fresh plants sampled in Minamisoma. ^{40}K is a natural isotope whose percentage of the total potassium content found in nature has been estimated to be 0.0117%, and whose concentration in farming soils ranges from 150 to 500 Bq·kg^{-1} in Japan. Radiocesium was accumulated mainly in sediments and had concentrations of 1800 (Koori), 124 (Nishiyama), 1300 (Nakamura), and 20 900 (Minamisoma) Bq·kg^{-1}, which partially correlated with the air dose rates.

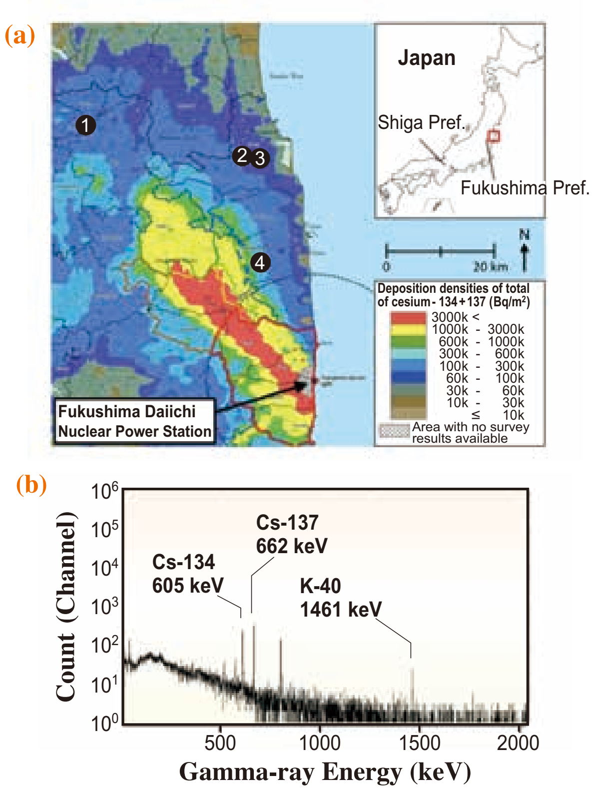

Fig. 1. Sampling sites in Fukushima Prefecture. **(a)** *E. densa* plant, sediment, and water samples were collected from Koori (1) in Date-gun, Nishiyama (2) and Nakamura (3) in Soma-shi, and in Minamisoma (4), and the sampling sites are shown on the distribution map of the total dose rate of ^{134}Cs and ^{137}Cs obtained by airborne monitoring in June 2012 (Extension Site of the Distribution Map of Radiation Dose, Digital Japan, *http://ramap.jmc.or.jp/map/eng/*). **(b)** Spectra for *E. densa* shoots sampled in Minamisoma. The counting time was 20000 s and ^{134}Cs, ^{137}Cs, and ^{40}K were detected.

To discuss the uptake mechanism of Cs, stable ^{133}Cs was applied separately to shoots and roots in a two-compartment bath (Fig. 2(a), [2]). Leaves around the stem-root joint were removed. The joint was wrapped with a plastic paraffin film and inserted into a slit between the two chambers. The slit was carefully sealed with a silicone sealant to avoid leaking of the media. The contents of Cs were determined by furnace atomic absorption spectrometry. The results showed that the environmental Cs transferred to both the shoots and roots of plants (Figs. 2(b-d)).

To analyze the detailed localization of Cs in plants, synchrotron radiation-based micro X-ray fluorescence (SR-μ-XRF) analysis was performed for plants cultivated in a hydroponic medium containing ^{133}Cs [3]. The newly developed small plants were excised from the node of a mother plant and rinsed with water

(Fig. 3(a)). Then the small plants were pretreated in a plastic bucket containing 3 L of medium for 24 h and transferred to plastic containers containing 500 mL of Gaudet's medium and 20 μM CsCl for 72 h. Because the plants' leaves contain a single longitudinal vascular bundle and the blades consist of only two layers of cells, the elemental distribution of a leaf segment was shown without preparation of sections of the tissue. High-resolution imaging was then performed at **BL37XU** to observe the subcellular distribution of Cs. Strong Cs signals were detected in the cell wall and in the apoplastic regions (Fig. 3(b)). The distribution mobility of Cs appears to be similar to that of K as well as divalent metals, such as Ca, Mn, Fe, and Zn, indicating the nonspecific absorption of metals by the cell wall or apoplastic regions. The apoplastic detoxification of Cd was previously observed in the pith of the young stems of a willow [4]. We consider that *E. densa* plays an important role in the deposition of radioactive Cs in fresh water and that it will be useful for the removal of radiocesium from water columns.

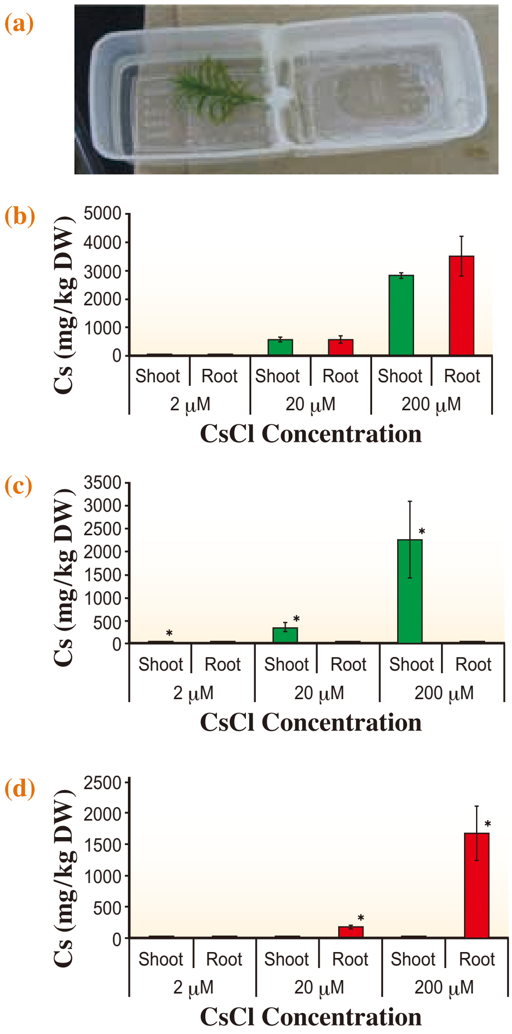

Fig. 2. Endogenous Cs concentrations (mg·kg^{-1} DW) in the shoots and roots of *E. densa*. **(a)** The plants were incubated in a small two-compartment bath. **(b)** Both shoots and roots, **(c)** shoots, and **(d)** roots were treated with 2, 20, and 200 μM CsCl for 24 h. Values are means ±SD (n = 3). Asterisks indicate a statistically significant difference: *P < 0.01. Statistical analysis was performed by an unpaired Student's t-test.

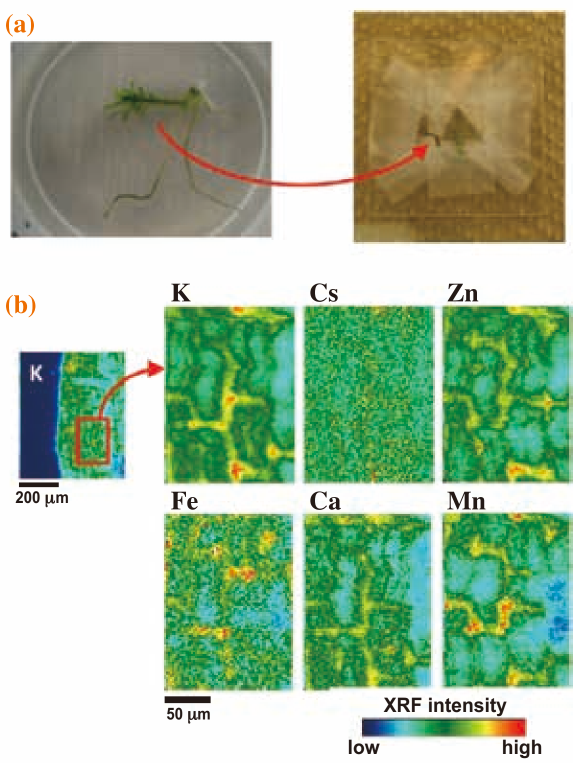

Fig .3. μ-XRF imaging of the leaf of *E. densa* treated with CsCl. **(a)** The leaf was set over a 4 × 4 cm^2 acrylic plate with a 1.0-cm-diameter hole and covered with a Mylar film. **(b)** High-resolution images of the area of the leaf in the red square. Two-dimensional distributions of K, Cs, Zn, Fe, Ca, and Mn are shown. The XRF signal intensity is shown as a color scale. Beam energy: 10 keV. Step size: 2.0 μm. Exposure time: 0.5 s per point.

Emiko Harada[a,*], Yoshiyasu Nagakawa[b] and Akiko Hokura[c]

[a] School of Environmental Science,
The University of Shiga Prefecture
[b] Tokyo Metropolitan Industrial Technology Research Institute
[c] School of Engineering, Tokyo Denki University

*E-mail: harada.e@ses.usp.ac.jp

References

[1] N. Yamaguchi *et al.*: Bull. Natl. Inst. Agro-Environ. Sci. **31** (2012) 75.
[2] S. Takayanagi *et al.*: J. Plant Res. **125** (2012) 669.
[3] *H. Kowata, Y. Nagakawa, N. Sakurai, A. Hokura, Y. Terada, H. Hasegawa, E. Harada: J. Anal. At. Spectrom. 29 (2014) 868.*
[4] E. Harada *et al.*: Metallomics **3** (2011) 1340.

Chemical forms of cesium in ashes generated from municipal solid waste incineration

The Fukushima Daiichi Nuclear Power Plant was damaged by a huge earthquake and tsunami in March 2011, resulting in the release of radioactive nuclides, primarily ^{134}Cs and ^{137}Cs, to the atmosphere. These radioactive nuclides contaminated the disaster waste, municipal solid waste (MSW), and sewage sludge from the surrounding area. According to the IAEA guidelines, incineration is the most commonly used thermal process for reducing the volume of such waste [1]. In Japan, waste that contains ^{134}Cs and ^{137}Cs exceeding 8,000 Bq/kg activity is referred to as "specified radioactive waste." Although approximately 80% of the specified radioactive waste consisted of incinerated ash and inorganic soils, the other 20% was combustible waste, i.e., sewage sludge, agricultural waste, and MSW to be treated [2].

Radioactive nuclides in waste can concentrate in the resulting ash (fly ash and bottom ash) formed by incineration and may be in different chemical forms in either ash. The chemical forms of Cs in ash are important for the determination of appropriate treatment and stabilization of the ash, but there is little information about the forms.

Our study attempts to clarify the chemical forms of cesium in ash generated from waste incineration. Specifically, refuse-derived fuel (RDF) with added ^{133}Cs (a stable nuclide) was combusted using a pilot-scale incinerator, and the chemical forms of ^{133}Cs in the bottom ash and fly ash were investigated in relation to the equivalence air ratio (EAR) by X-ray absorption fine structure (XAFS) analysis.

The RDF pellets used in this study were manufactured from MSW from a plant located in west Japan. An aqueous solution containing nuclides was added to the RDF, and the sample was adjusted to 30% moisture content. The nuclide concentration in the RDF was 5,100 mg/kg for ^{133}Cs added as Cs_2CO_3. A rotary kiln-stoker furnace (processing capacity ~1,000 kg/h, NGK Insulators Ltd.) was used in this study (Fig. 1). The bottom ash was collected from the rotary kiln and stoker. Flue gas was recombusted in the secondary combustor at 900°C. After recombustion, the gas was cooled in the cooling tower, and the fly ash was collected in the ceramic filter. The RDF was incinerated in the rotary kiln at 700°C at a rate of 30 kg/h while being stirred. The EAR was controlled to 2.2, 1.7, and 1.4 by varying the amount of combustion air. MSW ash generally has a high titanium (Ti) content. The energy of the Ti *K*-edge (4,964 eV) is close to that of the Cs L_3-edge (5,011 eV). Therefore, the Cs *K*-edge XAFS spectra of bottom ash and fly ash at beamline **BL01B1** were measured [3].

The differential X-ray absorption near edge structure (XANES) spectra of standard Cs substances ($CsSO_4$, pollucite: the $(Cs,Na)(AlSi_2)O_6{\cdot}nH_2O$, Cs_2CO_3, and CsCl), bottom ash, and fly ash samples are shown in Fig. 2. These spectra of the bottom ash and fly ash were different despite the small effect of the EAR, indicating that the EAR has a minimal effect on the Cs in each ash. While the differential XANES spectrum of the bottom ash had a positive peak within the range of 36,032 eV to 36,033 eV and appeared similar to the spectrum for Cs_2CO_3, the spectrum of Cs_2CO_3 in fly ash had a peak in the range of 36,034 eV to 36,035 eV, which was more similar to the spectrum of CsCl.

Fig. 1. Rotary kiln and stoker incineration plant: **(a)** rotary kiln, **(b)** secondary combustor, and **(c)** chamber of ceramic filter.

Most of the potassium (K) in ash exists in the form of KCl gas and $K_2Si_4O_9$ liquid above 780°C, as determined by a theoretical calculation that assumed the thermodynamic equilibrium in a Danish straw incinerator [4]. The same theoretical calculation was performed for ash in a modified MSW incinerator and it was reported that most of the K existed in the form of KCl gas and solid $KAlSi_2O_6$ above 940°C and 850°C, respectively [5,6]. NIES (2012) investigated ash with K replaced by Cs, and reported $CsAlSi_2O_6$ and CsCl to be the main forms of Cs in bottom ash and fly ash, respectively [6].

In our XAFS analysis, the main chemical form of Cs in fly ash was CsCl. This finding matched the above results of theoretical calculations. On the other hand, the chemical form of Cs in the bottom ash, Cs_2CO_3, was different from the calculated results, which indicated aluminosilicate or silicate, because the combustion temperature in this experiment was approximately 700°C, which is higher than the melting point of Cs_2CO_3 and lower than the temperature of the theoretical calculation. Most of the Cs_2CO_3 remained in the bottom ash without conversion to another chemical form. A part of the Cs_2CO_3 was transferred to the secondary combustor by flue gas, recombusted at 900°C, converted to CsCl, and condensed in fly ash at the ceramic filter. The combustion of MSW contaminated with radioactive Cs in a stoker-type incinerator at higher temperatures of 850°C–900°C, should result in the conversion of Cs to CsCl and aluminosilicate or silicate in the combustion chamber. CsCl should then vaporize and transfer to the fly ash. Therefore, MSW can be separated into a small amount of fly ash with a high concentration of radioactive Cs and bottom ash with a low concentration of radioactive Cs by incinerating at a high temperature.

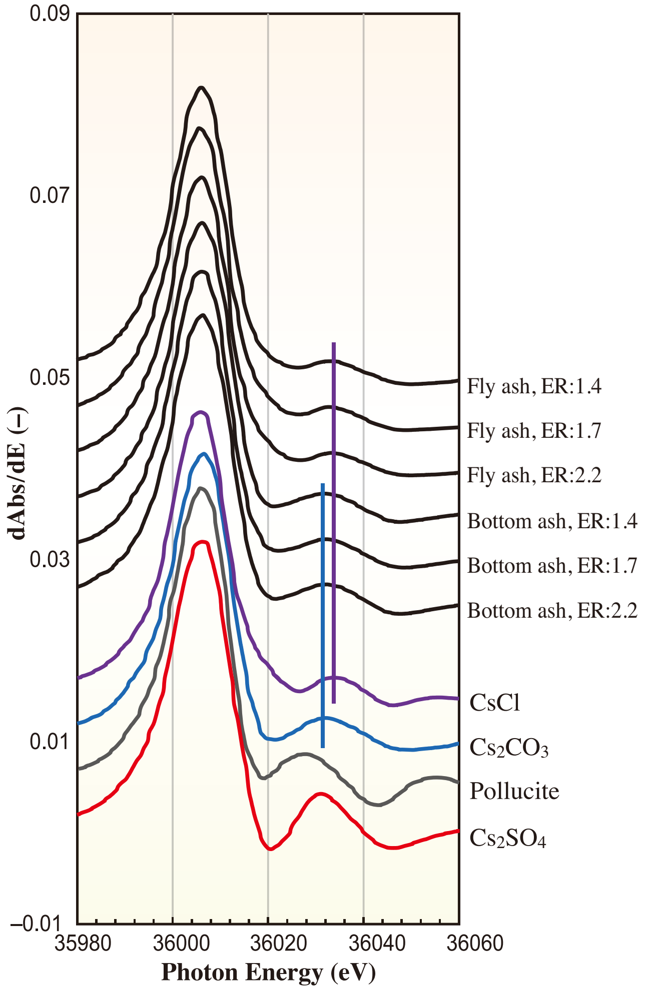

Fig. 2. Differential XANES spectra of Cs compounds and types of ash.

Kazuyuki Oshita[a,b,*], Kenji Shiota[b]
and Masaki Takaoka[a,b]

[a] Dept. Global Ecology, Graduate School of Global Environmental Studies, Kyoto University
[b] Dept. Environmental Engineering, Graduate School of Engineering, Kyoto University

*E-mail: oshita@epsehost.env.kyoto-u.ac.jp

References

[1] IAEA: Application of Thermal Technologies for Processing of Radioactive Waste. TECDOC 1527, (2006) 20.
[2] Ministry of Environment, Government of Japan: The Amount of Specified Waste (26th, Sep, 2014).
[3] *K. Oshita, H. Aoki, S. Fukutani, K. Shiota, T. Fujimori, M. Takaoka: J. Environ. Radioactiv.* ***143*** *(2015) 1.*
[4] X. Wei *et al.*: Fuel **84** (2005) 841.
[5] D. Poole *et al.*: Fuel **87** (2008) 1318.
[6] National Institute for Environmental Studies (NIES), Center for Material Cycles and Waste Management Research (CMW): Proper Treatment of Wastes Contaminated by Radioactive Substances (Overview of Technical Document), **5** (2012).

Arsenic distribution and speciation around rice roots

Health risks associated with the long-term, low-dose uptake of arsenic (As) have been of great concern in Southeast Asia, where rice is a staple crop. Among the agricultural crops, rice cultivated in flooded soil is the greatest contributor to inorganic As uptake through food. This is because As is present as As(III), which is mobile under the anaerobic condition in flooded soil [1]. When a soil is aerobic, As is less mobile because As(V) is strongly sorbed to mineral soil components such as Fe(III) hydroxide minerals (Fig. 1(a)). When anaerobic conditions develop in flooded soils, Fe(III) in Fe minerals is reduced to Fe(II), which is soluble. Consequently, the arsenic associated with Fe minerals is released into the solution as the adsorption phase is lost (Fig. 1(b)). However, soil in the vicinity of rice roots is aerobic because oxygen is supplied from above the ground to the root surface through the root aerenchyma (Figs. 1(b-d)). Therefore, dissolved Fe(II) is oxidized and deposited as Fe(III) hydroxide in the vicinity of the root surface (Figs. 1(b,c)). The Fe(III) hydroxide deposited around rice roots is referred to as Fe-plaque (Fig. 1(c)).

The significant correlation between the spatial distributions of As and Fe near rice roots indicates that As sequestration in Fe-plaque occurs [2]. Because Fe-plaque on rice roots has a greater affinity to As(V) than As(III), the oxidation of As(III) in the rhizosphere promotes the sequestration of As in Fe-plaque. Arsenic uptake from roots is partly restricted by Fe-plaque, but the degree of restriction strongly depends on the speciation of As. We observed the microscale distribution and speciation of As in the vicinity of rice roots in paddy soil by X-ray fluorescence mapping and X-ray absorption spectroscopy.

In a typical cultivation cycle of paddy rice in Japan, the soil is flooded for 5 months. The floodwater is drained approximately 10 days before harvesting and thereafter the soil redox condition gradually shifts from anaerobic to aerobic. Soil blocks containing rice roots were collected from a flooded paddy field and under an aerobic condition 1 month after harvesting. Soil blocks were freeze-dried, embedded in epoxy resin, and cut into thin sections with a thickness of 80 μm. The microscale As and Fe distributions in the thin sections were determined by synchrotron microbeam X-ray fluorescence (μXRF) with an excitation energy of 12.5 keV at BL4A of PF KEK. Arsenic *K*-edge μ-X-ray absorption near edge structure (μXANE) spectra were collected from various locations on the Fe-plaque and soil particles. The proportions of As(III) and As(V) were calculated by linear combination fitting using the standard XANES spectra of $NaAsO_2$ (As(III)) and Na_2HAsO_4 (As(V)). In addition, roots from rice seedlings that were grown under flooded conditions were removed from soil and frozen in liquid nitrogen. Transverse sections (50 μm in thickness) of the roots were prepared with a cryomicrotome (CM1850, Leica, Wetzlar, Germany) and were frozen until analysis. μXRF maps of the frozen root sections and As *K*-edge μXANES spectra were obtained by maintaining a frozen thin section under a stream of cryogenic N_2 gas (Cryojet XL, Oxford Instruments, UK) at **BL37XU** in SPring-8.

Optical microscope observation showed that Fe-plaque (shown as a dark-red stain around roots) coated the roots (Fig. 2(a)) but it did not noticeably cover the root apex when the roots were taken from flooded

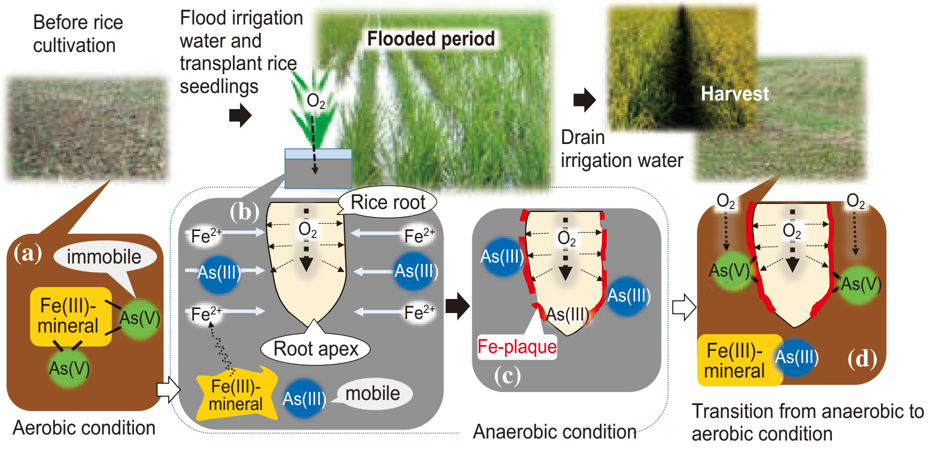

Fig. 1. Behavior of arsenic during rice cultivation in paddy field.

soil (Fig. 2(e)). The root apex is responsible for active solute uptake. The arsenic distribution map provided the evidence that As and Fe were absorbed by the root apex (Figs. 2(e,f)). The μXANES analysis indicated that the proportions of As(III) in the root interior and on the Fe-plaque did not differ significantly. Approximately 80% of the total As was in the form of As(III). This result suggested that As(III) was present near the root despite the occurrence of aerobic conditions in its vicinity. The presence of Fe-plaque can act as a barrier to As(V) absorption by roots but enhance As(III) absorption. Therefore, Fe-plaque may not reduce the absorption of As(III) by rice roots that are grown in flooded soil [3]. The absence of Fe-plaque around the root apex also allowed As absorption.

In the thin sections of soil prepared from the soil collected after rice harvesting, Fe minerals accumulated approximately 100 μm from the root (Fig. 3(a)). The fluorescence intensities of Fe Kβ did not differ between the Fe minerals in the soil matrix and those in the Fe-plaque around the roots (Fig. 3(b)). The fluorescence intensities of As Kα were greater on the Fe-plaque around the roots than on the Fe aggregates in the soil matrix (Fig. 3(c)). The relationships between the As Kα and Fe Kβ intensities clearly indicated the existence of two areas with different the As to Fe ratios. The areas with the greater As to Fe ratio corresponded to areas of Fe-plaque around the roots (Fig. 3(d)). The μXANES analysis indicated that 33% of the As that was associated with Fe minerals at a distance of 100 μm from the root surface was in the form of As(III). In contrast, As(V) was the dominant As species on the Fe-plaque that was attached to the root (Fig. 3(c)). The larger proportion of As(V) on the Fe-plaque after harvesting suggested that the shift to aerobic conditions was faster around the root than in the soil matrix [3].

In summary, Fe-plaque on rice roots did not effectively block As absorption from the roots under a flooded condition because As on the Fe-plaque was present in the form of As(III). After draining the floodwater, As on the Fe-plaque is oxidized faster than that in the soil matrix, thereby Fe-plaque sequestrates As(V).

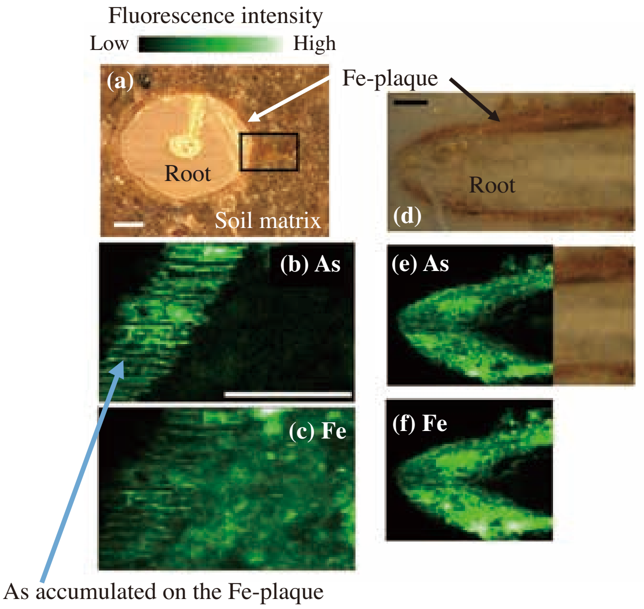

Fig. 2. Light microscope and micro-X-ray fluorescence (μXRF) images taken around rice roots grown under anaerobic condition. Light microscope images **(a, d)**, As images **(b, e)**, and Fe images **(c, f)** of freeze-dried resin embedded cross sections **(a-c)** and the transverse section of a frozen root **(d-f)** are presented. The black boxes in (a) show where μXRF maps were obtained. Black and white bars indicate 500 and 200 μm, respectively.

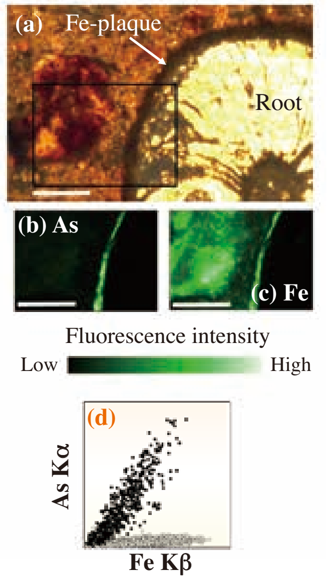

Fig. 3. Light microscope and μXRF images of rice roots collected 1 month after harvesting. Light microscope images **(a)**, As images **(b)**, Fe images **(c)**, and the relationships between the fluorescence intensities of As Kα (b) and Fe Kβ (c) around the roots **(d)** are presented. The black and white circles correspond to location on the Fe-plaque and Fe minerals, respectively (d). The black boxes in (a) show where the μXRF maps were obtained and the white bars indicate 200 μm.

Noriko Yamaguchi

Institute for Agro-environmental Sciences,
National Agriculture and Food Research Organization

E-mail: nyamag@affrc.go.jp

References

[1] N. Yamaguchi *et al.*: Chemosphere **83** (2011) 925.
[2] N.K. Blute *et al.*: Environ. Sci. Technol. **38** (2004) 6074.
[3] *N. Yamaguchi, T. Ohkura, Y. Takahashi, Y. Maejima and T. Arao: Environ. Sci. Technol.* ***48*** *(2014) 1549.*

Mercury sulfide formation process under mechanochemical reaction using a planetary ball mill

The Minamata Convention on Mercury is a legally binding multilateral environmental agreement that was adopted by governments in 2013. When the Convention is enacted in the near future, Japan will prohibit the export of elemental mercury, except for mercury for essential use, following the lead of the EU and USA [1,2]. Once the export of elemental mercury is prohibited, approximately 70–80 tons of excess mercury, having no commodity value, will accumulate in Japan each year as hazardous waste [3]. It is thus important to prepare for the safe and long-term storage or permanent disposal of such mercury waste. Metal mercury is liquid at room temperature and has high volatility, allowing it to move easily in the environment. It is preferable that elemental mercury be recovered by a distillation method that converts it to mercury sulfide (HgS), which is the most stable chemical form of mercury, for long-term storage or permanent disposal. In this study, we used a planetary ball mill (Pulverisette-6; Fritsch Co., Ltd.) for the stabilization of metal mercury (99.5% purity; Wako Pure Chemical Industries, Ltd.) by mixing it with powdered sulfur (98% purity; Nacalai Tesque, Inc.) under a variety of conditions to gain a better understanding of the stabilization process. The planetary ball mill can produce high-energy conditions and enable samples to react within a short period of time by providing mill pot rotation and revolution movement simultaneously. We were able to observe the process of mercury sulfide formation within a reaction time of 5 to 90 min [4]. This process is shown in Fig. 1. From 5 to 15 min, the first stage of the reaction, a silver-gray and labile material adhered to the periphery of the mill pot bottom. This material was sufficiently soft to be scraped away with a medicine spoon, and was similar to a dental amalgam. It appears that physical contact between metal mercury and sulfur powder is facilitated, and they then form a solid solution (hereinafter called an intermediate). During the second stage, after 15 min, this labile material gradually hardened and became pulverized by the balls, which resulted in the production of cinnabar (α-HgS) and metacinnabar powder (β-HgS). This process was completed at 50°C after 90 min. Oji *et al.* developed a high-shear blending technique for converting elemental mercury into mercury sulfide. Cinnabar is formed when the temperature of the inner vessel is over 270°C [5]; however, cinnabar could be formed at a lower temperature in our method. This suggests that the mechanochemical effect influences the formation of mercury sulfide, which enables the sulfurization of metal mercury without the use of a heating process.

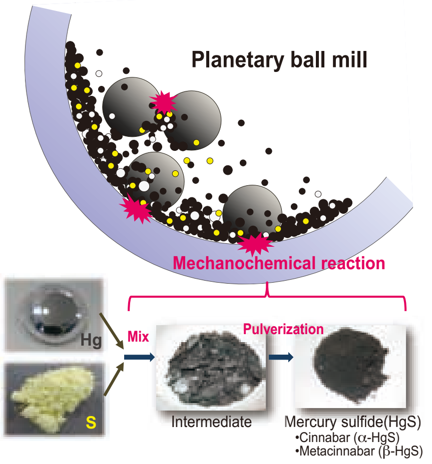

Fig. 1. Stabilization process by which elemental mercury and powder sulfur are converted to mercury sulfide by a planetary ball mill.

In order to determine the chemical form of the products, we measured the Hg L_{III}-edge XANES spectra at beamline **BL01B1**. The change in the pattern with the reaction time from 5 to 90 min can be easily seem in the differential XANES spectra shown in Fig. 2(a). The differential XANES spectra of metal mercury, metacinnabar, and cinnabar as standard substances are shown for comparison. At the first stage of the reaction, between 5 and 15 min, during the intermediate remained, the differential XANES spectra were very similar to that of metal mercury. Second, an inflection point appeared at photon energy of around 12,300 eV and the pattern became similar to that of metacinnabar after a reaction time of 20 min when all of the intermediate had been pulverized to powder. Third, another peak appeared at 12,288 eV after 30 min, and the spectrum gradually became that of cinnabar. We conducted pattern fitting of these spectra using the spectra for two standard materials, metacinnabar and cinnabar, to quantitatively determine their ratio. The results are shown in Fig. 2(b). The fitting value after reaction times of 5 to 15 min is not shown because the R value was too large and the spectrum could not be fitted. It appears that the spectrum of the intermediate cannot be represented by a linear combination of those for standard materials. After 20 min, the proportion of cinnabar increased with the reaction time and reached approximately 80 mol% at 90 min. This indicates a continuous change from metacinnabar to cinnabar.

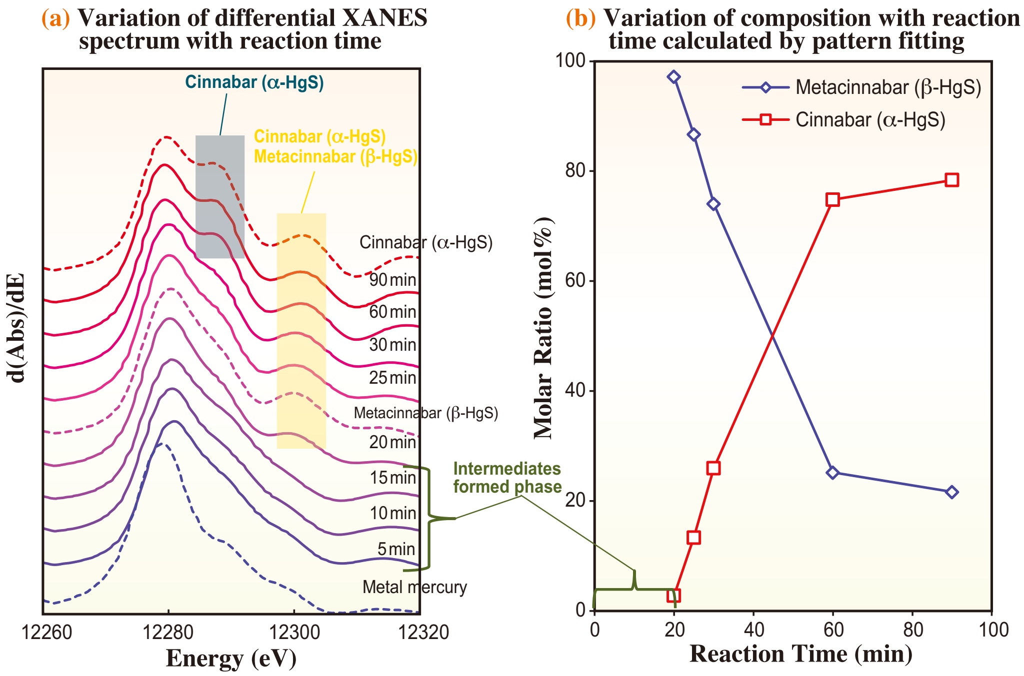

(a) Variation of differential XANES spectrum with reaction time

(b) Variation of composition with reaction time calculated by pattern fitting

Fig. 2. Variation of **(a)** differential Hg L_{III}-edge XANES spectrum and **(b)** composition, calculated by pattern fitting, of metacinnabar (β-HgS) and cinnabar (α-HgS) measured at BL01B1.

We measured the mercury leaching concentration by the Japanese leaching test (JLT-46) at each reaction time to evaluate the stability of the products. The results are shown in Fig. 3. The total mercury leaching concentration is regulated in Japan to be below 0.5 μg/L. The intermediate has a high mercury leaching concentration between reaction time of 5 and 15 min, indicating the incomplete formation of mercury sulfide. The mercury leaching concentration decreases rapidly from 15 to 20 min with the complete formation of metacinnabar. After that, it gradually decreases with the transformation from metacinnabar to cinnabar. The environmental criterion is satisfied after 30 min.

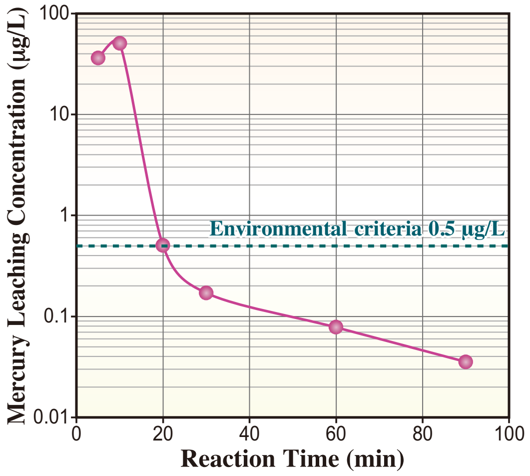

Fig. 3. Variation in mercury leaching concentration of products with reaction time obtained by Japanese leaching test (JLT-46).

In conclusion, we succeeded in mercury stabilization that satisfied the environmental criterion for the mercury leaching concentration without heating using a planetary ball mill. In this process, labile intermediate mercury sulfide was observed in the early stages of milling, and then the intermediate was pulverized into stable metacinnabar. After that, the crystal structure gradually changed from metacinnabar to cinnabar.

Naomichi Fukuda[a] and Masaki Takaoka[a,b,*]

[a] Department of Environmental Engineering,
Kyoto University
[b] Department of Global Ecology, Kyoto University

*E-mail: takaoka.masaki.4w@kyoto-u.ac.jp

References

[1] The European parliament and the council of the European Union
REGULATION(EC) No 1102/2008 OF THE EUROPEAN PARLIAMENT AND OF THE COUNCIL of 22 October 2008 on the banning of exports of metallic mercury and certain mercury compounds and mixtures and the safe storage of metallic mercury (2008) http://eur-lex.europa.eu/LexUriServ/LexUriServ.do?uri=OJ:L:2008:304:0075:0079:EN:PDF (2013/8/31)
[2] U.S. EPA Homepage: Questions and Answers about the Mercury Export Ban Act of 2008 http://www.epa.gov/hg/exportban-ques.htm (2013/8/31)
[3] M. Takaoka: J. Mater. Cycles Waste **17** (2015) 665.
[4] *N. Fukuda, M. Takaoka, K. Oshita, T. Mizuno: J. Hazard. Mater.* ***276*** *(2014) 433.*
[5] L.N. Oji: J. Environ. Eng. **124** (1998) 945.

Speed of sound in liquid Fe-C alloy under high pressures using inelastic X-ray scattering

The structure of the Earth is divided into three layers, the uppermost hydrosphere, the silicate crust and mantle, and a metallic core (Fig. 1). This layered structure was primarily the result of geological processes occurring just after the Earth was formed. Today, structural information in Earth's interior is provided by seismological measurements that accurately give the sound velocities of pressure (P-) and shear (S-) waves and density (Fig. 1). In the past decades, the understanding of the mantle has significantly progressed, thanks to developments in laboratory measurements and theoretical calculations for possible silicate and oxide minerals. However, the composition of the metallic core is still controversial. This is because there are no available rock samples originally from the core, and it remains very challenging to perform laboratory measurements of the physical properties of possible core materials under the relevant extremely high-pressure and high-temperature conditions.

Geochemical and geophysical arguments show that the core consists mainly of iron. However shock compression experiments showed that the sound velocity and density of pure liquid iron are ~3% faster and ~10% lower than those of the liquid core (e.g., [1]), which indicates that some lighter elements are present. The nature of the lighter elements is fundamental to understanding a number of geological questions such as the core dynamo, the core temperature, and indeed the core formation process. Carbon is one of the candidate lighter components in the outer core. In order to constrain the amount of carbon in the outer core, we determined the sound wave velocity of liquid Fe-C alloy up to 70 GPa using inelastic X-ray scattering (IXS) at beamline **BL35XU** [2].

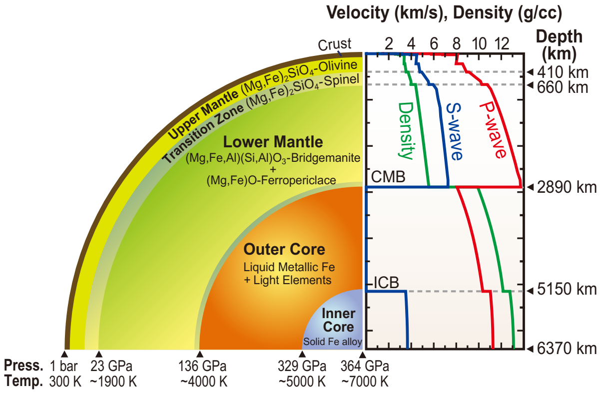

Fig. 1. Schematic of internal structure and seismological parameters of the Earth.

Samples of $Fe_{84}C_{16}$ alloy (4 wt% carbon) were melted at high pressure and temperature in an external-resistance-heated (EH) or a laser-heated (LH) diamond-anvil cell (DAC). The sample was loaded into the DAC with single-crystal sapphire discs that served as thermal and chemical insulators. Pressure was determined from the Raman shift of diamond or using the equation of state for Fe_3C observed before melting. Temperatures were monitored using a type-R thermocouple in the EH-DAC or by a spectroradiometric method in LH-DAC experiments, where uncertainties were less than 20 K or ±10%, respectively. The melting experiments were performed at 7.6–70 GPa and 1500–2800 K. The DACs were placed into vacuum chambers in order to minimize background scattering by air. The molten state of the specimen was confirmed by X-ray diffraction by the absence of diffraction peaks and/or the presence of diffuse signals from the sample. IXS with ~2.8 meV energy resolution, using Si (999) backscattering geometry at 17.79 keV, was used to determine the longitudinal acoustic, P-wave sound velocity. The scattered photons were collected by an array of twelve spherical Si analyzers leading to twelve independent spectra at momentum transfers (Q) between 3.2–6.6 nm^{-1} with a resolution $\Delta Q \sim 0.45$ nm^{-1} (full width). The energy transfer range of ±30 (or –10 to +30) meV was scanned for 1 to 3 h.

The IXS spectra (Fig. 2(a)) included three peaks: the Stokes and anti-Stokes components of the longitudinal acoustic (LA) phonon mode from the Fe-C sample, and a quasi-elastic contribution near zero energy. The excitation energies (E) for the LA phonon mode of the liquid sample obtained in a pressure range of 7.6–70 GPa are plotted as a function of momentum transfer (Q) in Fig. 2(b). The P-wave velocity (V_P) corresponds to the long-wavelength LA velocity at $Q \to 0$ limits. We made a linear fit to the data obtained at low Q below 3.5 nm^{-1} to determine the P-wave velocity, because positive dispersion may appear at higher $Q >> 3$ nm^{-1}. The resulting sound velocity of liquid $Fe_{84}C_{16}$ is plotted in Fig. 3(a).

We constructed an equation of state (EoS) for liquid $Fe_{84}C_{16}$ to extrapolate the present V_P data and to calculate its density ρ in the core pressure range. The adiabatic Murnaghan EoS can be described as a function of pressure P:

$$\rho = \rho_0 \left(1 + \frac{K'_S}{K_{S0}} P\right)^{\frac{1}{K'_S}} \qquad (1)$$

where ρ_0 is the density, K_{S0} is the adiabatic bulk modulus and K'_S is its pressure derivative at zero pressure. With the relationship $V_P = (K_S/\rho)^{0.5}$, the above EoS can become

$$V_P = \sqrt{\frac{K_{S0}}{\rho_0}}\left(1+\frac{K'_S}{K_{S0}}P\right)^{\frac{1}{2}-\frac{1}{2K'_S}} \qquad (2)$$

The zero pressure density was obtained from literature data [3]. We fitted Eq. (2) to the present P-V_P data set, and then extrapolated to core pressures (Fig. 3). In this fitting, the temperature effect on V_P was ignored as in previous studies (e.g., [1]). Using the fitted parameters of K_{S0} and K'_S, the density profiles (Fig. 3(b)) for liquid $Fe_{84}C_{16}$ were also calculated along two adiabatic temperatures (Fig. 3(c)). The temperature profiles were calculated with a Grüneisen parameter for liquid pure Fe [1] to give possible core temperatures.

The P-wave velocity of liquid $Fe_{84}C_{16}$ is much faster than that of pure Fe at core pressures (Fig. 3(a)). Therefore, under the assumption of a linear relation between V_P and the carbon content of liquid Fe, only 5.2–4.0 atom% carbon in liquid Fe is required to match the seismological velocity [4] of the liquid outer core. However, much more carbon of 15.4–12.0 atom% is required to account for the core density (Fig. 3(b)). Therefore, carbon alone cannot explain the seismological observations and its maximum content will be less than 5.2 atom%, which corresponds to 1.2 wt%.

This result is also consistent with other geochemical considerations. The $^{13}C/^{12}C$ isotopic ratio of the present silicate mantle suggests that ~1 wt% carbon could have been incorporated into the core [5]. In addition, the mantle abundances of molybdenum and tungsten could be explained simply by the partitioning between the silicate magma ocean and the core-forming metal during the core formation process if the core-forming metal contained ~0.6 wt% carbon [5]. The present constraint on the carbon content of the liquid outer core is in agreement with those geochemical arguments.

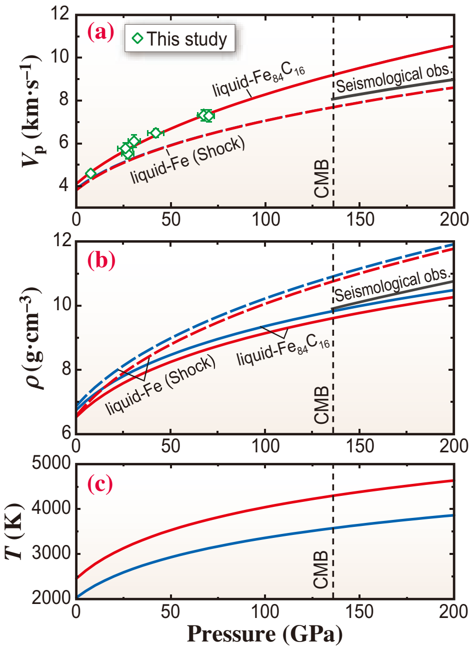

Fig. 3. Velocity and density of liquid $Fe_{84}C_{16}$. The P-wave velocity **(a)** and density **(b)** profiles of liquid $Fe_{84}C_{16}$ are calculated along two adiabatic temperature curves **(c)** of 3600 K (blue) and 4300 K (red) at the CMB, and are compared with that of liquid pure Fe (broken lines) [1] and seismological observations [4] for the liquid outer core. The open symbols are the present experimental data.

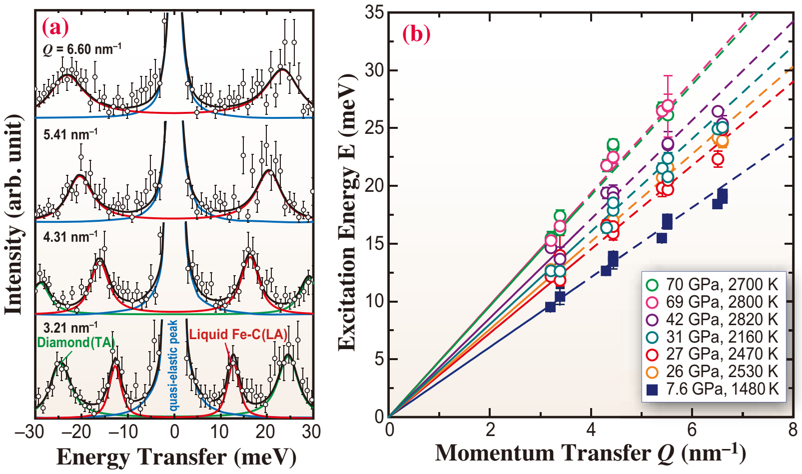

Fig. 2. Typical inelastic X-ray scattering spectra and phonon dispersion of liquid $Fe_{84}C_{16}$. **(a)** IXS spectra were collected at 26 GPa and 2530 K. Three components can be seen; quasi-elastic peak, longitudinal acoustic (LA) phonon mode of liquid sample, and transverse acoustic (TA) phonon mode of diamond from a diamond anvil cell. **(b)** Longitudinal acoustic phonon dispersions were obtained up to 70 GPa. Open and solid symbols exhibit laser-heated and external-resistance-heated DAC experiments, respectively.

Y. Nakajima[a,*], S. Imada[b], K. Hirose[c]
and A. Q. R. Baron[a]

[a] RIKEN SPring-8 Center
[b] Japan Synchrotron Radiation Research
Institute (JASRI)
[c] Earth-Life Science Institute,
Tokyo Institute of Technology

*E-mail: yoichi.nakajima@spring8.or.jp

References

[1] W.W. Anderson & T.J. Ahrens: J. Geophys. Res. **99** (1994) 4273.
[2] *Y. Nakajima, S. Imada, K. Hirose, T. Komabayashi, H. Ozawa, S. Tateno, S. Tsutsui, Y. Kuwayama, A.Q.R. Baron: Nat. Commun.* **6** *(2015) 8942.*
[3] K. Ogino *et al.*: J. Jpn. Inst. Met. **48** (1984) 1004.
[4] A.M. Dziewonski and D.L. Anderson: Phys. Earth Planet. Inter. **25** (1981) 297.
[5] B.J. Wood *et al.*: Rev. Miner. Geochem. **75** (2013) 231.

Magma fracturing and friction: Implications for volcanic eruptions

A volcanic eruption is a dynamic phenomenon that releases magma from Earth's interior to the surface. Magma is molten rock, which ascends as a viscous fluid in a volcanic conduit that connects the magma reservoir to the surface. A central issue in volcanology is to understand how magma ascends in the conduit because the process of magma ascent is thought to control the explosivity and variety of eruption style. For instance, magma vesiculates during magma ascent and subsequent decompression because it contains volatiles such as water and carbon dioxide. This vesiculation strongly reduces magma density, which becomes a driving force of magma ascent and eruption.

In the last two decades, volcanologists have discovered an important process that may have a large impact on magma ascent dynamics: "magma fracturing and friction" [1]. Magma is viscous fluid, but it has viscoelasticity and shows brittle deformation under high shear flow. If magma shows the transition between viscous and brittle deformation during ascent, the magma ascent dynamics are affected, which may explain the observations at the surface that have been a mystery for many years, such as the cause of volcanic seismicity [2]. Recently, magma fracturing under high temperature and pressure conditions was directly observed using synchrotron radiation X-ray radiography and computed tomography [3]. The direct observation showed that magma fracturing is a common process for silicic magma, and the fracturing results in shear localization. A fractured and shear-localized zone becomes a magmatic fault, and the deformation mode changes from viscous flow to friction. This transition also changes the explosivity of magma ascending in the conduit because viscous deformation causes bubble coalescence and enhances outgassing [3]. To investigate the transition between viscous flow and frictional sliding, we performed friction tests for magmatic gouge at high temperatures [4].

The friction tests were performed using a rotational deformation apparatus set on an X-ray imaging beamline **BL20B2**. The magmatic gouge zone was simulated by sandwiching rhyolitic glass powder with rhyolitic glass discs (Fig. 1). The sample was set in a graphite cylinder and heated to temperatures of 800 and 900°C in the furnace. Normal stresses on the discs were controlled to be 1–10 MPa, and a disc was rotated at rates of 0.1 to 10 rpm. Sample deformation at high temperature was observed using X-ray radiography (Fig. 1). We were able to directly observe the sample using this experimental system because the furnace has a small hole for the X-ray path, hence only the graphite and sample are on the path.

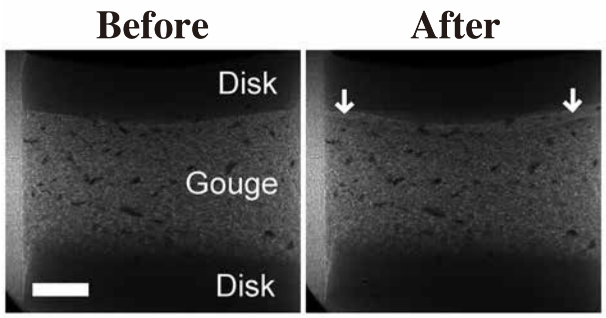

Fig. 1. *In situ* X-ray radiographic image of deforming samples. The images were taken just before and after the deformation at 800°C under a normal stress of 1 MPa. Gray and light-gray parts are disk and granular melts (gouge), respectively. In this experiment, frictional sliding was observed, and a sharp fault in the fractured zone (indicated by white arrows in After) was also found. Small iron particles (black particles), used as a strain maker, are found in granular melts. The white bar indicates a 1 mm scale.

We identified the flow type based on X-ray radiography and the relationship between the rotational rate and torque necessary to twist the sample. For viscous flow, the torque is proportional to the rotational rate, while the torque is almost constant under the rotational rate used in this study when frictional sliding is dominant. We observed both viscous flow and frictional sliding depending on temperature, normal stress, and rotational rate. At a temperature of 800°C, the magmatic fault showed frictional sliding along the boundary between the granular melt and the upper disk at normal stresses of 1 and 5 MPa. On the other hand, viscous deformation without a clear localization and frictional sliding dominated at a temperature of 900°C under normal stresses of 5 and 10 MPa and rotation rates of 0.1 to 1 rpm. The flow regime was well determined by using the ratio of viscous shear stress to normal stress ($T = \eta\dot{\gamma}/\sigma$, where η, $\dot{\gamma}$, and σ represent melt viscosity, shear strain rate, and normal stress, respectively) (Fig. 2(a)). The boundary between viscous flow and frictional sliding is 0.45–0.79. This result also indicates that the friction coefficient of magmatic faults is 0.45–0.79.

To investigate the flow regime (viscous flow vs. frictional sliding) during magma ascent, we calculated the T value of magmatic faults and compare it with the regime map (Fig. 2(b)). The T value increases with magma ascent because normal stress decreases and magma viscosity increases because of melt dehydration. The rate of magma deformation during its ascent is a parameter that is not well constrained. The strain rate yielding in magma can be directly observed from the shapes of the bubbles in pyroclasts and lava, which is on the order of ~10^{-2} and 10^{-7} s^{-1}, respectively [5]. On the other hand, numerical simulation of magma flow dynamics in the conduit shows a strain rate of 1 s^{-1} for explosive eruption and lava effusion rates provide a bulk deformation rate of $10^{-3.5}$ s^{-1} (see the details in [4]). Here, we simply assume a rate of 1 and 10^{-3} s^{-1} to discuss the cases of explosive and effusive eruption, respectively. When we assume strain rate yielding in magma to be 1 s^{-1}, magma shows frictional sliding at depths shallower than 200–600 m. This means that flow type changes from viscous flow to frictional sliding at depth, and the transition can reduce apparent magma viscosity. This may cause rapid ascent of the magma column along a magmatic fault and finally explosive volcanism (Fig. 3). In contrast, when the strain rate is 10^{-3} s^{-1}, magma shows frictional sliding only at very shallow depths (<~50 m). This means that magma experiences viscous deformation, which enhances magma outgassing (Fig. 3) [3]. In this case, the potential for magma explosion is reduced and lava effusion is expected, and the lava plug would show friction only near at the surface, as observed at Mt. Unzen in Japan and Mt. St. Helens in the U.S.A. As shown here, the coupled effect of magma rheology, i.e., the transition between viscous flow and frictional sliding, and magma outgassing, may be a controlling factor of magma ascent rate and eruption style.

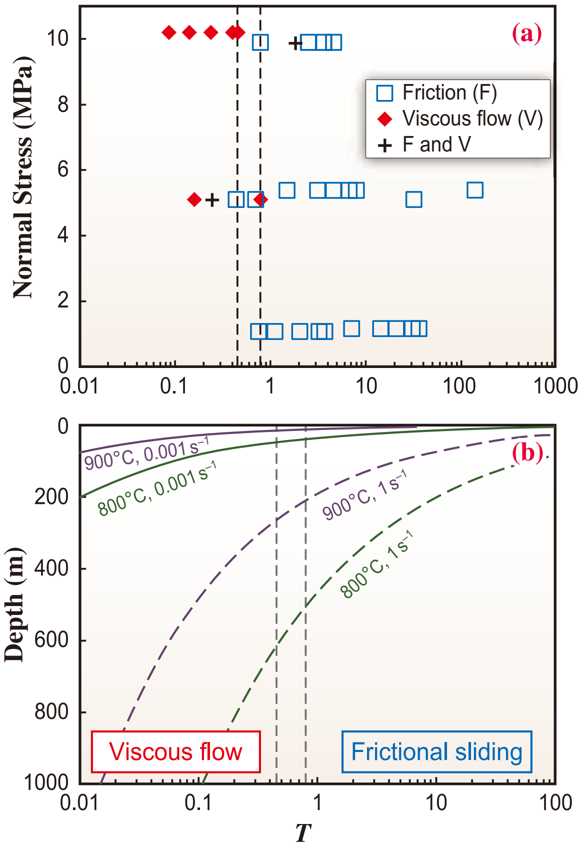

Fig. 2. **(a)** Flow type represented in the *T*-normal stress diagram. Blue squares and red diamonds represent frictional sliding (friction, F) and viscous flow (V), respectively. Crosses represent the transition from viscous flow to frictional sliding during a constant rotation rate. Two vertical dashed lines (T = 0.45 and 0.79) represent the transition zone between viscous flow and frictional sliding. **(b)** Evolution of the *T* value during the ascent of silicic magmas at 800 and 900°C. [4]

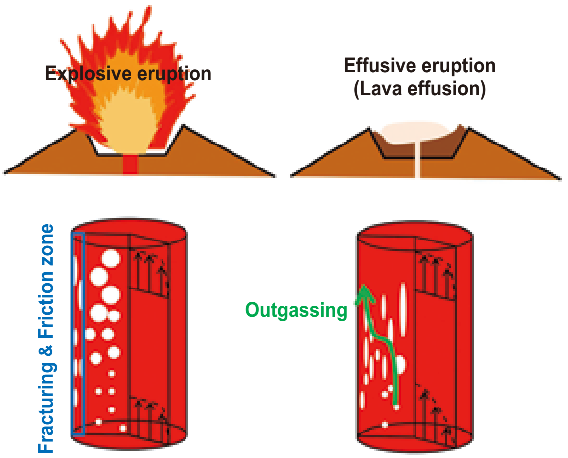

Fig. 3. Schematic model of magma ascent during explosive (left panel) and effusive (right panel) eruptions. During explosive eruption, magma experiences shear localization and results in the formation of a fractured and friction zone along the conduit. Magma can ascend rapidly along this zone. During effusive eruption, magma shows viscous flow, and the outgassing is enhanced by viscous deformation. Only at very shallow parts in the conduit, magma ascent is dominated by friction, resulting in lava effusion.

Satoshi Okumura

Division of Earth and Planetary Materials Science,
Tohoku University

E-mail: sokumura@m.tohoku.ac.jp

References

[1] D.B. Dingwell: Science **273** (1996) 1054.
[2] H. Tuffen *et al*.: Nature **453** (2008) 511.
[3] S. Okumura *et al*.: Earth Planet. Sci. Lett. **362** (2013) 163.
[4] *S. Okumura, K. Uesugi, M. Nakamura, O. Sasaki: J. Geophys. Res.* ***120*** *(2015) 2974.*
[5] A. Rust *et al*.: J. Volcanol. Geotherm. Res. **122** (2003) 111.

Grain boundary sliding as the major flow mechanism of Earth's upper mantle

Earth's surface plates (thickness, ~60 km), on which we live, move and are subducted along with the flow of the upper mantle (depths 60–410 km), which is composed mainly of olivine. Natural phenomena, such as earthquakes and volcanic eruptions, occur as a result of the subduction of plates. For over 45 years since 1970, the generally accepted theoretical model has explained that the flow of the upper mantle is controlled by the motion of dislocations in olivine (i.e., dislocation creep: [1]). However, the dislocation creep model cannot explain the geophysical viscosity profiles because a strong depth dependence of mantle viscosity is expected in the case of the dislocation creep of olivine. Here, we report that dislocation-accommodated grain boundary sliding (DisGBS), rather than dislocation creep, dominates the deformation of olivine under middle and deep upper mantle conditions [2]. The estimated viscosity of olivine controlled by DisGBS is independent of depth and ranges from $10^{19.6}$–$10^{20.7}$ Pa·s throughout the asthenospheric upper mantle with a representative water content (50–1000 ppm H/Si), which is consistent with geophysical viscosity profiles.

We have conducted uniaxial deformation experiments on olivine aggregates combined with synchrotron *in situ* X-ray observations at pressures of 1.5–6.7 GPa, temperatures of 1273–1473 K, and strain rates of 0.3–7.2 × 10^{-5} s^{-1} using a deformation-DIA apparatus at beamline **BL04B1**. The temperature and pressure ranges are equivalent to the conditions in the shallow to middle region of the upper mantle. Plastic flow of minerals at high temperatures is commonly described by the power-law equation. Using the steady-state creep strength of olivine obtained under experimental conditions, we determined the flow-law parameters for olivine aggregates as follows:

$$\dot{\varepsilon} = 10^{-4.89\pm0.24}\frac{\sigma^{3.0\pm0.3}}{G}f_{\mathrm{H2O}}^{1.25}$$
$$\exp\left(-\frac{423\pm56\,\mathrm{kJ/mol}+P\times17.6\pm0.8\times10^{-6}\ \mathrm{m^3/mol}}{RT}\right) \quad (1)$$

where $\dot{\varepsilon}$ is the strain rate (in s^{-1}), G is the grain size (in m), σ, f_{H2O} and P are the differential stress, water fugacity and pressure, respectively (in MPa), R is the gas constant, and T is the temperature. The obtained values of the stress exponent and the grain-size exponent in Eq. (1) show that the deformation of olivine is controlled by DisGBS. The obtained value of the activation energy is close to that for DisGBS of dry olivine (445 ± 20 kJ/mol) [3] and is between the activation energies for dislocation creep (530 ± 4 kJ/mol) and diffusion creep (375 ± 50 kJ/mol) of dry olivine [4].

Steady-state creep strength, which is normalized at a fixed temperature and strain rate, is plotted against pressure in Fig. 1. The pressure dependence of the creep strength of olivine aggregates controlled by DisGBS is apparently weak owing to a combination of a relatively small activation volume and a strong water-weakening effect. In contrast, the pressure dependence of the creep strength of olivine controlled by dislocation creep is much

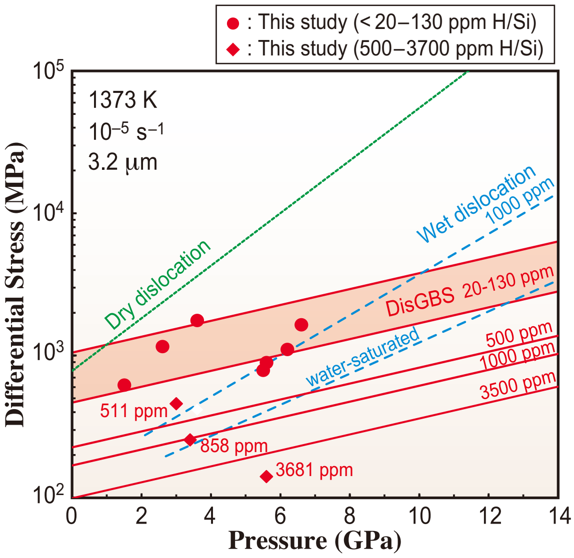

Fig. 1. Pressure dependence of creep strength of olivine aggregates. All data are normalized to an axial strain rate of 10^{-5} s^{-1}, a temperature of 1373 K, and a grain size of 3.2 μm (i.e., a typical experimental condition). Solid circles and diamonds represent the strength of dry olivine aggregates (< 20–130 ppm H/Si) and wet olivine aggregates (500–3700 ppm H/Si; water content is shown near the symbols), respectively. Red lines represent the strength of olivine aggregate controlled by DisGBS obtained using Eq. (1) (thick lines with hatched area: < 20–130 ppm H/Si; thin lines: 500–3500 ppm H/Si of water in olivine). The green dotted line represents the strength of dry olivine aggregates controlled by dislocation creep. Blue dashed lines represent the strength of wet olivine aggregates controlled by wet dislocation creep (1000 ppm H/Si and water-saturated cases are considered). See Ohuchi *et al*. [2] for the references.

stronger than that in the case of DisGBS. In order to determine which creep mechanism controls the upper mantle flow, we calculated deformation mechanism maps as a function of stress and grain size under representative upper mantle conditions (Fig. 2). Figure 2 shows that the viscosity of the dry upper mantle is controlled by DisGBS of olivine at high pressures (≥ 7 GPa), while the contributions of dislocation and diffusion creep to mantle flow are limited to only the shallow upper mantle [2].

Figure 3 shows the viscosity-depth profiles in the upper mantle based on the present results. Figure 3 shows a strong depth dependence of viscosity controlled by dislocation creep. In contrast, the upper mantle is estimated to have relatively constant viscosities in a limited range of $10^{20.1}$–$10^{20.7}$ Pa·s (in the case of 50 ppm H/Si of water) or $10^{19.6}$–$10^{20.1}$ Pa·s (in the case of 1000 ppm H/Si of water) at depths greater than ~100 km when the constant-stress flow is controlled by DisGBS (Fig. 3). The viscosity-depth profiles derived from geophysical observations of post-glacial rebound (e.g., [5]) are well explained by DisGBS with 50 ppm H/Si of water (the 1000 ppm H/Si case is marginally consistent with the observations). Therefore, we conclude that water content in the upper mantle is between 50–1000 ppm H/Si. Assuming dislocation creep of dry olivine significantly overestimates the deep upper mantle viscosity by ~10–10^2 times. Such an estimate of upper mantle viscosity leads to the highly unlikely conclusion that the deep upper mantle may have a viscosity of ~10^{23} Pa·s, which corresponds to the upper bound of the lower mantle viscosity (10^{21}–10^{23} Pa·s). The dynamics of the upper mantle should be re-evaluated using our new flow law for DisGBS of olivine (Eq. 1).

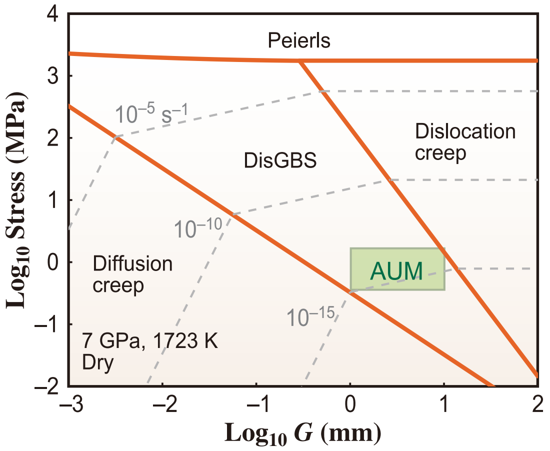

Fig. 2. Example of deformation mechanism maps for dry olivine on the axes of differential stress *versus* grain size (G) at a pressure of 7 GPa and temperature of 1723 K. The thick orange lines represent the boundaries between two deformation mechanisms (i.e., dislocation creep, diffusion creep, the Peierls mechanism, and DisGBS). See Ohuchi *et al*. [2] for the references). The green-hatched area represents typical conditions of the asthenospheric upper mantle (AUM). The gray dashed lines represents the contours of strain rates.

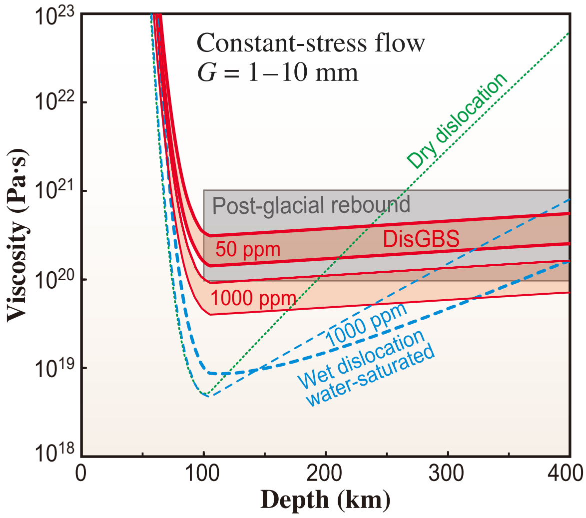

Fig. 3. Depth dependence of the viscosity of olivine. The dominant deformation mechanism is assumed to be DisGBS (red solid curves with red-hatched areas, thick: 50 ppm H/Si of water; thin: 1000 ppm H/Si) or dislocation creep (green dotted curve: dry; blue dashed curves, thin: 1000 ppm H/Si; thick: water-saturated). The constant stress and geotherms below the oceans of 50 m.y. old and mantle adiabat are used for the calculation. The gray-hatched area represents the range of upper mantle viscosity estimated from geophysical observations of post-glacial rebound (e.g., [5]).

Tomohiro Ohuchi[a,*], Tetsuo Irifune[a,b] and Yuji Higo[c]

[a] Geodynamics Research Center, Ehime University
[b] Earth and Life Science Institute,
Tokyo Institute of Technology
[c] Japan Synchrotron Radiation Research Institute (JASRI)

*E-mail: ohuchi@sci.ehime-u.ac.jp

References

[1] J. Weertman: Rev. Geophys. Space Phys. **8** (1970) 145.
[2] *T. Ohuchi, T. Kawazoe, Y. Higo, K. Funakoshi, A. Suzuki, T. Kikegawa, T. Irifune: Sci. Adv.* ***1*** *(2015) e1500360.*
[3] L.N. Hansen *et al*.: J. Geophys. Res. **116** (2011) B08201.
[4] G. Hirth, D.L. Kohlstedt: Inside the Subduction Factory (2003) Geophysical Monograph Series, AGU.
[5] J.X. Mitrovica, A.M. Forte: Earth Planet. Sci. Lett. **225** (2004) 177.

Curious kinetic behavior in silica polymorphs solves seifertite puzzle in shocked meteorite

The evolution of asteroids by collision was the main process of planetary formation in the early solar system. Physical conditions of the collisional process have been recorded in shocked meteorites. Recent findings of various high-pressure silica polymorphs including seifertite, a high-pressure polymorph of silica with the α-PbO_2-type structure, in Martian [1], lunar [2] and other achondritic meteorites are important clues to understanding the shock conditions. However, previous studies faced the problem of the presence of seifertite because this phase is thermodynamically stable at more than 100 GPa [3], which is an unrealistically high pressure condition for shocked meteorites.

In order to solve the seifertite problem, we newly investigated the kinetic aspects of high-pressure transformations of silica by time-resolved X-ray diffraction measurements using a Kawai-type high-pressure apparatus (SPEED-1500) installed at beamline **BL04B1** [4]. The starting materials of synthetic SiO_2 α-cristobalite and reagent-grade SiO_2 quartz powders were first compressed up to ~30 GPa at room temperature, and then heated in 100 K steps up to ~1450 K at a constant load. We kept temperature constant for ~10–50 min at each step and collected diffraction patterns of the sample every 30 to 200 s by the white X-ray energy dispersive method.

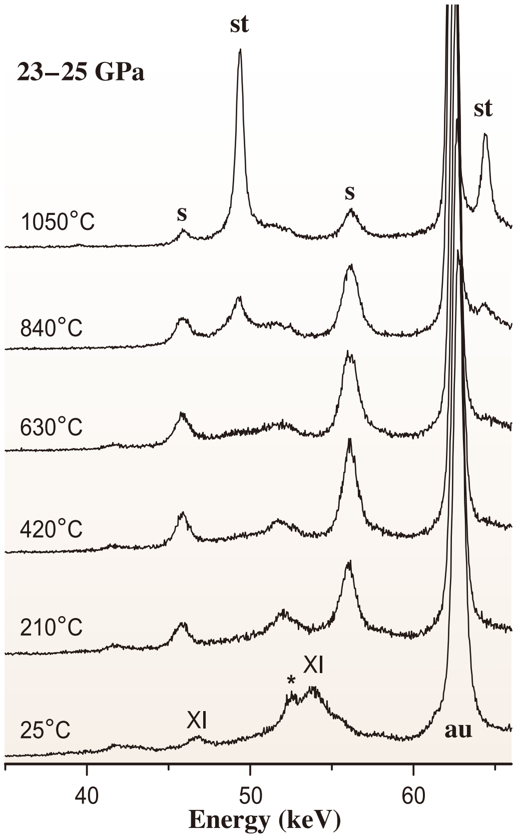

Fig. 1. Changes in X-ray diffraction patterns in cristobalite showing formation of seifertite (s) and stishovite (st) upon heating at 23–25 GPa. Other abbreviations: XI, cristobalite X-I; au, gold pressure marker; *, graphite sample capsule.

Figure 1 shows changes in the diffraction peaks during heating after cold compression in an experiment using α-cristobalite as the starting material. The cold compression of α-cristobalite to around 30 GPa causes high-pressure transitions to cristobalite-II and X-I. When heating the sample at high pressures, we observed the formation of metastable seifertite. Further heating leads to the transformation from seifertite to the stable phase of stishovite. Our experiments suggest that seifertite metastably appears down to ~11 GPa, which is far from its stability field. When using quartz powder as a starting material, we did not observe seifertite formation up to ~25 GPa and 900 K. Stishovite is formed from quartz at much lower temperatures than those in the case of cristobalite.

We quantitatively observed the kinetics of the formation of metastable seifertite and stable stishovite by time-resolved X-ray diffraction measurements. Analysis of the kinetic data (the time dependence of the transformed fraction data) using the Avrami rate equation indicated clear differences in kinetics between seifertite and stishovite formations (Fig. 2). In the case of seifertite formation, the activation energy is very low (~10 kJ/mol) and there is no detectable pressure dependence, implying fast kinetics even at low temperatures because of the diffusionless transformation mechanism from cristobalite to seifertite. On the contrary, the formation of stishovite from seifertite has a relatively high activation energy (~110 kJ/mol) and large activation volume, which is thought to have originated from a diffusion-controlled mechanism.

On the basis of the kinetic parameters obtained in our experiments, we constructed the time-temperature-transformation (TTT) curves for seifertite and stishovite formation (Fig. 3) to discuss the progress of the reaction on short time scales of the shock event in the range from ~0.01 s to ~1 s estimated for Martian and lunar meteorites. Seifertite formation has temperature-insensitive but time-sensitive kinetics, which requires shock durations of at least ~0.01 s to start, even at temperatures of ~2000 K and higher. Completion is difficult within the time scale of shock events. In contrast, stishovite formation is temperature-sensitive, requiring temperatures higher than ~1200–1500 K to start, and can be completed at less than ~2000 K. When considering impact velocities of ~5–10 km/sec and shock durations of ~0.01 sec, the critical size of an impactor that might produce seifertite is estimated to be ~50–100 m. Our finding of the clear difference in kinetics between the metastable seifertite and stable stishovite formations not only solves the seifertite puzzle, but also is potentially capable of being a simple index for the impactor size.

We previously proposed an indicator of shock conditions based on the plagioclase amorphization and crystallization kinetics of high-pressure minerals [5]. When used in combination with the present study, the shock metamorphism observed in achondritic meteorites can be consistently discussed. Thus, the curious kinetic behaviors of silica and plagioclase observed in shocked meteorites can be used as a unique hybrid shock indicator of the collisional history of differentiated parental bodies in the early solar system.

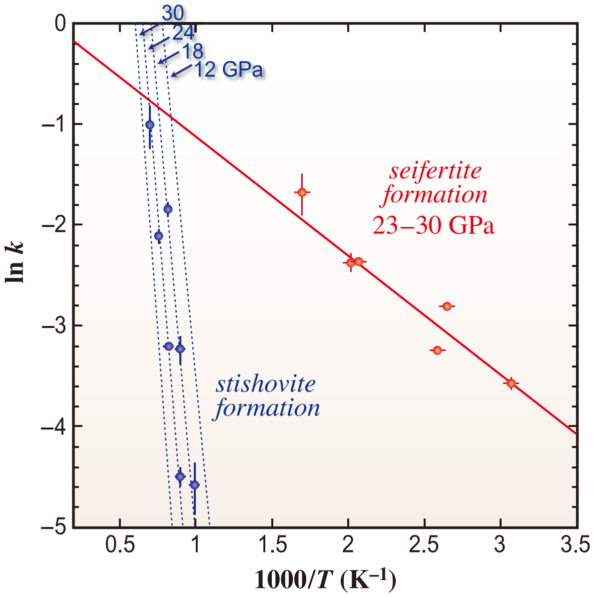

Fig. 2. Temperature dependence of rate constant k. In stishovite formation, the pressure dependence was also observed.

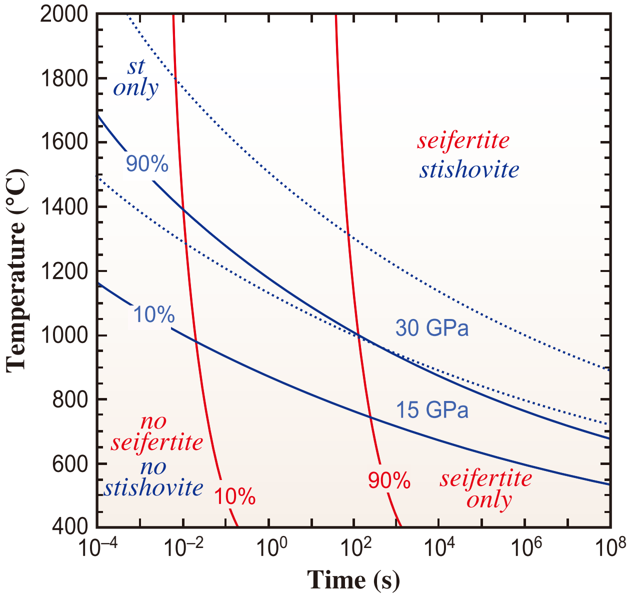

Fig. 3. Time-Temperature-Transformation (TTT) curves constructed on the basis of kinetic parameters determined from Fig. 2.

Tomoaki Kubo* and Takumi Kato

Department of Earth and Planetary Sciences,
Kyushu University

*E-mail: kubotomo@geo.kyushu-u.ac.jp

References

[1] T.G. Sharp *et al*.: Science **284** (1999) 1511
[2] M. Miyahara *et al*.: Proc. Natl. Acad. Sci. USA **111** (2014) 10939.
[3] M. Murakami *et al*.: Geophys. Res. Lett. **30** (2003) 1207.
[4] *T. Kubo, T. Kato, Y. Higo and K. Funakoshi: Sci. Adv.* ***1*** *(2015) e1500075.*
[5] T. Kubo *et al*.: Nat. Geosci. **3** (2010) 41.

Analyzing reaction mechanism of Li-ion secondary battery by element-specific *in situ* X-ray absorption spectroscopy and theoretical spectral simulations

Rechargeable Li-ion batteries (LiBs) were first commercialized as a power source for mobile electronic devices. They are now about to be applied to large-scale applications such as electric or plug-in hybrid vehicles and stationary power sources for smart energy grids. The development of better electrode materials is strongly desired to fulfill the requirements for the higher capacity and higher stability LiBs used for such large-scale applications. Primary targets in developing high-capacity positive electrode materials include multi-element or multi-component transition-metal oxides with complex structures, as represented by a Li-rich solid-solution layered system. In such complex materials, however, it is not easy to understand the roles played by each element (in each crystallographic site) in the redox reaction. Thus, it is becoming important to develop electronic structure analysis methods with elemental and crystallographic site selectivity to obtain clues to designing better materials.

To date, *in situ* X-ray absorption spectroscopy (XAS) at transition-metal *K*-edges has been most widely used to analyze the reaction mechanism during battery operations by monitoring the "valence change," which is determined by the absorption edge shift. However, conventional analysis of the X-ray absorption near-edge structure (XANES) simply involves comparing the absorption edge position with those of references. As long as we use such a simple method, we cannot always evaluate the true valence changes of materials. Although basically XANES reflects valence states, it is also affected by the distribution of wave functions and the electron configurations of absorbing atoms. XANES exhibits very complicated behaviors when the electronic structure and lattice structure of absorbing atoms simultaneously change. To overcome such issues, we have developed a new method taking these effects into account by first-principle XANES simulations. We demonstrated the effectiveness of this method via reinvestigation of the electrochemical process for a typical positive electrode material $Li(Ni_{1/3}Co_{1/3}Mn_{1/3})O_2$ – one basic component of a Li-rich layered solid solution.

The sample electrode was formed by mixing $LiNi_{1/3}Co_{1/3}Mn_{1/3}O_2$ powder with acetylene black and polyvinylidene fluoride (PVdf) in n-methyl pyrrolidone (NMP) solution. The electrolyte used was 1 M $LiPF_6$ in an ethylene carbonate/diethyl carbonate (EC/DEC)

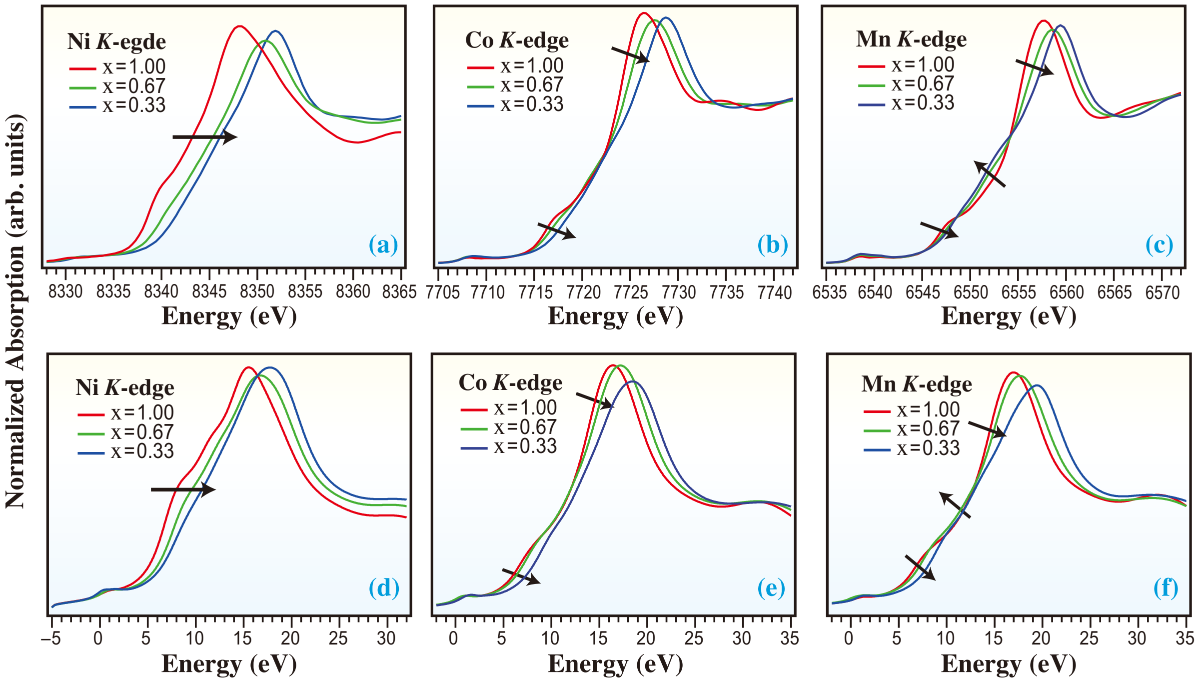

Fig. 1. Experimental *K*-edge XANES spectra of **(a)** Ni, **(b)** Co, and **(c)** Mn. Calculated *K*-edge XANES spectra of **(d)** Ni, **(e)** Co, and **(f)** Mn.

solution. Then, a laminate-type cell was assembled. *In situ* XAS measurements at the transition-metal *K*-edge were performed at beamline **BL16B2**. The XAS data were collected at the Ni, Co, and Mn *K*-edges. Simulations of *K*-edge XANES spectra were carried out by using the full-potential augmented plane wave plus local orbitals (APW+lo) package and WIEN2k [1] within the generalized gradient approximation (GGA) for the exchange-correlation functional.

Figures 1(a) to 1(c) show the results of *in situ* XAS measurements of the transition-metal *K*-edges (Ni, Co, and Mn) in the charge processes. An obvious shift in the entire XANES region was observed for the Ni *K*-edge XANES spectra, indicative of a valence change of Ni due to a redox reaction. On the other hand, it was more difficult to interpret the behaviors of the Co and Mn XANES spectra. Although the shape of the XANES spectra changed and the peak position shifted to a higher energy in the charging process, the absorption edges remained at the same position. One part of the shoulder shifted to the low-energy side and the other part shifted to the high-energy side, as shown by the arrows. In such cases, the theoretical XANES simulation demonstrates its capability.

Figures 1(d) to 1(f) show the calculated XANES spectra for the Ni, Co, and Mn *K*-edges, respectively. Fundamental features observed in experiments were well reproduced by the simulation. The entire calculated Ni-*K* XANES spectra shifted to a higher energy, which was consistent with the experimental results. Regarding the Co *K*-edge XANES, the peak shifted to a higher energy in both the experimental data and the simulated spectra, while the absorption edge remained at the same position. The complex behaviors observed in the experimental spectra (arrows) were also mostly reproduced. These results indicate that the electronic structure and local structures of absorbing atoms determined by first-principles calculation are sufficiently good to describe X-ray absorption phenomena. The degrees of the valence change for each element in battery operation are summarized in Fig. 2.

As shown above, we successfully demonstrated that the combination of XAS methods and theoretical calculations is an effective way to analyze in details the redox behaviors of positive electrode materials.

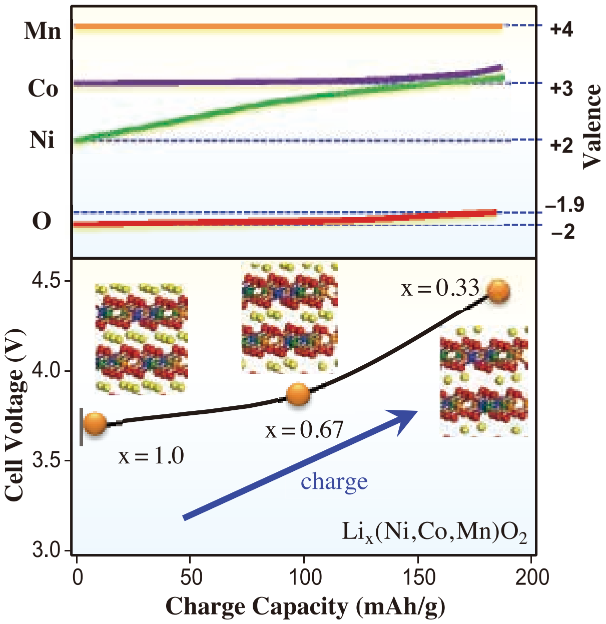

Fig. 2. Summary of valence changes of Ni, Co, Mn, and O in $Li(Ni_{1/3}Co_{1/3}Mn_{1/3})O_2$ in the charging process.

Hideto Imai*, Masato Mogi and Kei Kubobuchi

Device-functional Analysis Department
NISSAN ARC Ltd.

*E-mail: imai@nissan-arc.co.jp

Reference

[1] P. Blaha *et al*.: WIEN2k, An Augmented Plane Wave+Local Orbitals Program for Calculating Crystal Properties, Karlheinz Schwarz, Techn. Universität Wien, Austria (2001).

Scanning three-dimensional X-ray diffraction microscopy for non-destructive observation of plastic deformation in metallic materials

Metals and alloys are formed into functional shapes using a wide variety of plastic-forming operations in automobile industry. The development of advanced metallic materials with high plastic formability and high strength has led to the reduced weight of automobile parts. Because conventional experimental methodologies for the development of such materials are too expensive and time consuming, researchers have attempted to construct models to predict the plastic behaviors of materials. Although many models are now available, there is no adequate way to judge which model is useful owing to a lack of experimental methods to validate such models.

The plastic deformation of metals and alloys is microscopically caused by crystallographic slips or twinning, which are well understood in great detail through observations by transmission electron microscopy. The slips and twinning caused by mechanical loads give rise to macroscopic changes in crystallographic orientations. The macroscopic behaviors of slips or twinning in polycrystals have been investigated using orientation-imaging microscopy (OIM) by the electron backscatter diffraction (EBSD) technique. However, OIM information obtained by the EBSD technique is limited to close to the surface. Although successive serial sectioning of samples allows us to obtain three-dimensional information, changes in orientations cannot be tracked because the observed volumes are destroyed. Recently, a synchrotron radiation (SR) X-ray diffraction technique has enabled new experimental methods. High-energy X-ray diffraction approaches based on 3D X-ray diffraction (3DXRD) microscopy [1] enable the non-destructive 3D mapping of orientations.

In 3DXRD microscopy, an SR beam illuminates a polycrystalline sample and X-ray diffracted beams from multiple grains are detected by near- and far-field area detectors. Orientations of individual grains are analyzed from the positions of diffraction spots on the far-field detector using a polycrystal indexing technique [1]. The grain positions and shapes are analyzed from the positions and shapes of diffraction spots on the near-field detector. The main problem with 3DXRD-type experiments is the overlap of diffraction spots from multiple grains. This implies that there is a limit to the number of grains that can be illuminated by an incoming SR beam. Industrial metallic materials such as steel tend to cause this overlap of polycrystalline diffraction spots due to a large number of grains, mosaicity, strains, and textures. In the case of such samples, the wide sheet-like SR beam illumination often used in 3DXRD-type experiments is applicable to those with relatively small diameters. However, it is often not possible to investigate the mechanical characteristics of bulk materials using narrow samples rather than bulky samples.

In this study, we have proposed a modified 3DXRD technique, named scanning 3DXRD, as a solution to the main problem [2]. The scanning 3DXRD approach is considerably different from 3DXRD. First, the overlap of polycrystalline diffraction spots is reduced as much as possible by SR microbeam illumination. Second, only the far-field detector is employed to provide sufficient space around the specimen for an *in situ* stress rig. The diffraction spots are collected through scans of the sample rotation, ω, and the sample translation, X, as shown in Fig. 1. How is a 2D orientation map reconstructed from the ω-X scan data? The answer is as follows, (1) Only the diffraction spots obtained when the microbeam illuminates an arbitrary point inside the sample are extracted. (2) The diffraction spots are divided into groups in which the same crystal is the origin of the diffraction spots by using the polycrystalline indexing technique [1]. (3) The selection of the crystal corresponding to a point is performed on the basis of the number of diffractions for each group. The probability of microbeam illumination through a point is the largest among the groups for extracted diffraction sets because it is the imaginal rotation center. The crystal with the largest number of diffraction spots is selected as that corresponding to the given point. A 2D orientation

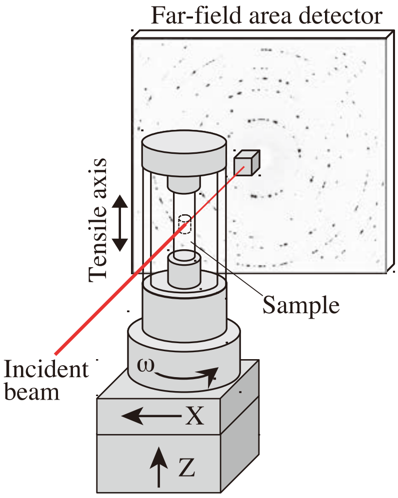

Fig. 1. Schematic of scanning 3DXRD microscopy setup.

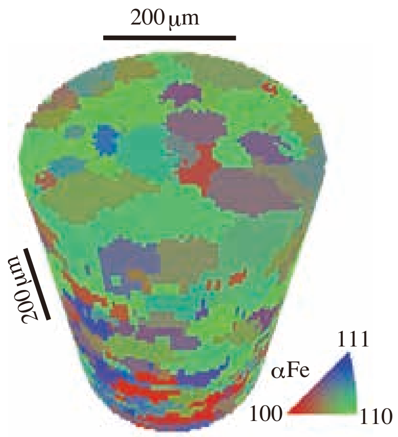

Fig. 2. 3D orientation map of coarse-grained polycrystalline iron. The colors correspond to the inverse pole figure in the tensile direction.

map is thus reconstructed by sweeping the given point. The stack of 2D orientation maps results in a 3D orientation map as shown in Fig. 2, where orientations are represented by colors, and single domains with the same color correspond to single grains.

As a first demonstration, a scanning 3DXRD experiment was performed at the Toyota beamline **BL33XU** using an SR beam through 20 μm slits and a coarse-grained pure iron sample with an average grain size of 60 μm. Actually, the result is the 3D orientation map in Fig. 2. Then, using an *in situ* stress rig, the 3D orientation map in a deformed state is obtained in the same way. Thus, the changes in orientations, i.e., crystal lattice rotations, are observed [3].

By adopting the observed 3D orientation map before deformation as the initial orientation map in the model, crystal lattice rotations caused by plastic deformation can be simulated. Figure 3 shows the observed and simulated orientations for some typical coarse grains at macroscopic tensile strains of ε = 0.2%, 4.0%, 8.0%, and 10.7% [4]. The simulation reproduced significant observed rotation behaviors: (i) mean rotations toward the preferential <110> orientation of the body-centered-cubic tensile texture, (ii) an increase in intragranular misorientation, which is seen as the spread of orientations in single grains, and (iii) intragranular multidirectional rotations of grains near the <100> corner toward orientations between <110> and <111>.

Thus, the scanning 3DXRD microscopy method was demonstrated using a coarse-grained pure iron sample. The next step is the observation of industrial materials such as steel with a grain size of 10–20 μm. Toward this challenge, a scanning 3DXRD microscope apparatus using a high-energy microbeam with a beam size of 1–2 μm has been installed at the Toyota beamline BL33XU. In terms of the reconstruction algorithm, improvements are needed because the above observed spread of orientations (ii) in single grains is smaller than the simulated spread, which implies that the experimental reconstruction method underestimates intragranular misorientations. Finally, we are planning to apply the improved scanning 3DXRD microscopy method to the validation of a crystal plasticity finite element model that predicts slip deformation in carbon steel [5]. Then, we will work on a current hot topic of 3DXRD, the investigation of twin deformations in magnesium alloy, toward improving the formability of next-generation light alloys in automobile industry.

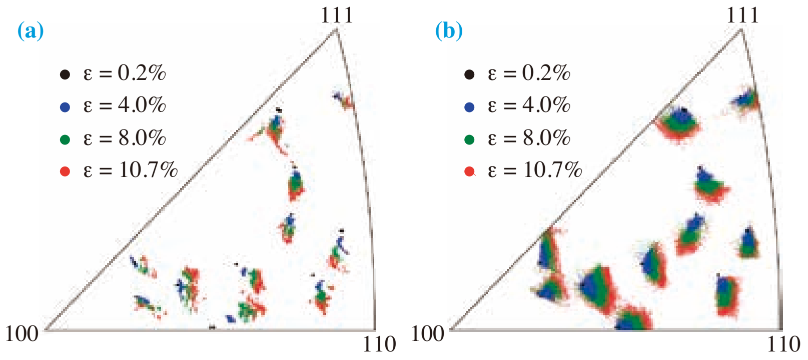

Fig. 3. **(a)** Observed and **(b)** simulated grain rotations represented by the inverse pole figures in the tensile direction for some coarse grains at ε = 0.2%, 4.0%, 8.0%, and 10.7%.

Yujiro Hayashi*, Yoshiki Seno and Daigo Setoyama

Toyota Central R&D Labs., Inc.

*E-mail: y-hayashi@mosk.tytlabs.co.jp

References

[1] H. F. Poulsen: J. Appl. Cryst. **45** (2012) 1084.
[2] *Y. Hayashi, Y. Hirose and Y. Seno: J. Appl. Cryst. **48** (2015) 1094.*
[3] Y. Hayashi *et al.*: Mater. Sci. Forum **777** (2014) 118.
[4] D. Setoyama *et al.*: Mater. Sci. Forum **777** (2014) 142.
[5] N. Iwata *et al.*: R&D Rev. Toyota CRDL **45** (2014) 1.

Enhancement of out-of-plane mobility in P3HT film: Face-on orientation produced by rubbing

The orientation of a conjugated polymer in a thin film affects the optical and electrical properties of the film. The control of the orientation is important to investigate the optoelectronic properties of conjugated polymers and produce functional polymer films. The increase in the use of conjugated polymers in a wide range of applications such as sensors, solar cells, and LEDs has motivated a number of attempts to investigate oriented polymer films. Poly(3-hexylthiophene) (P3HT) is a prototypical conjugated polymer associated with organic solar cells fabricated via solution processes. The anisotropic features of light absorption, light emission, and carrier transport have been reported for oriented P3HT films. The rubbing technique is a method employed to align molecules and has been applied to the preparation of oriented P3HT films [1]. The carrier mobilities in a P3HT film before and after rubbing have been reported as the in-plane mobility, i.e., carrier transport occurs parallel to the substrate [1].

Out-of-plane mobility is crucial for the performance of solar cells and LEDs, because the carriers migrate along the direction normal to the substrate of solar cells and LEDs. An increase in the power conversion efficiency of a solar cell employing rubbed P3HT film has been reported [2]. To further improve the performance of solar cells, it is important to investigate the carrier transport and film structure after rubbing. We have investigated the out-of-plane mobility and structure of thin films of P3HT [3], Si-nanocrystal/P3HT [4], and MEH-PPV [5]. In these studies, the out-of-plane mobility was measured using the time-of-flight (TOF) method, while the structure was examined using two-dimensional grazing-incidence X-ray diffraction (2D-GIXD). Here, we introduce recent results for the out-of-plane mobility and structure of a P3HT film after rubbing [3]. The orientation, molecular structure, and morphology after rubbing were investigated using polarized absorption, Raman spectroscopy, and microscopy. The structure change in the out-of-plane direction was investigated using 2D-GIXD.

2D-GIXD measurements of P3HT films before and after rubbing were conducted at beamline **BL19B2** with an X-ray energy of 12.39 keV (λ = 1 Å). The X-ray was irradiated at an incident angle of 0.12° in the direction parallel to the rubbing direction. The scattered X-ray was recorded using a 2D image detector (Dectris, Pilatus 300K).

Figure 1 shows the typically obtained 2D-GIXD patterns of P3HT films before and after rubbing. The (010) peak emerges in the out-of-plane (q_z) direction after rubbing, whereas it is in the in-plane direction (q_{xy}) before rubbing. Since the (010) peak corresponds to the π-π stacking of P3HT, the GIXD result indicates an increase in the out-of-plane π-π stacking, i.e., the face-on orientation. The increase in the face-on orientation can contribute to increasing the out-of-plane mobility because the carriers migrate in the film along the π-π stacking direction.

Figure 2(a) shows the time profile of the TOF signal for holes migrating along the out-of-plane direction in the P3HT film after rubbing. The out-of-plane hole mobility is obtained by analyzing the TOF profile and is enhanced up to eightfold after rubbing. Thus, the rubbing produces a film in which holes efficiently migrate in the out-of-plane direction. After rubbing, the face-on orientation is formed in the out-of-plane direction, as shown in Fig. 2(b). In addition, the in-plane anisotropy of the surface morphology is produced by rubbing, as shown in Fig. 2(c). Figure 2(d) shows the electronic absorption spectra of the π-π^* transition of P3HT in the film after rubbing. The anisotropic absorbance indicates the orientation of P3HT molecules in the direction parallel to the rubbing

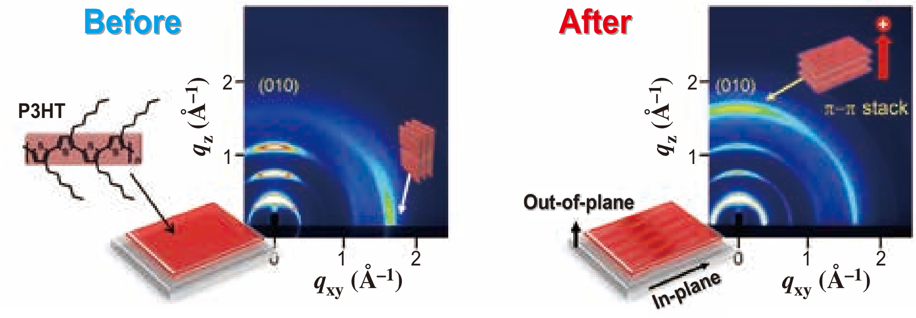

Fig. 1. 2D-GIXD patterns for P3HT films before and after rubbing.

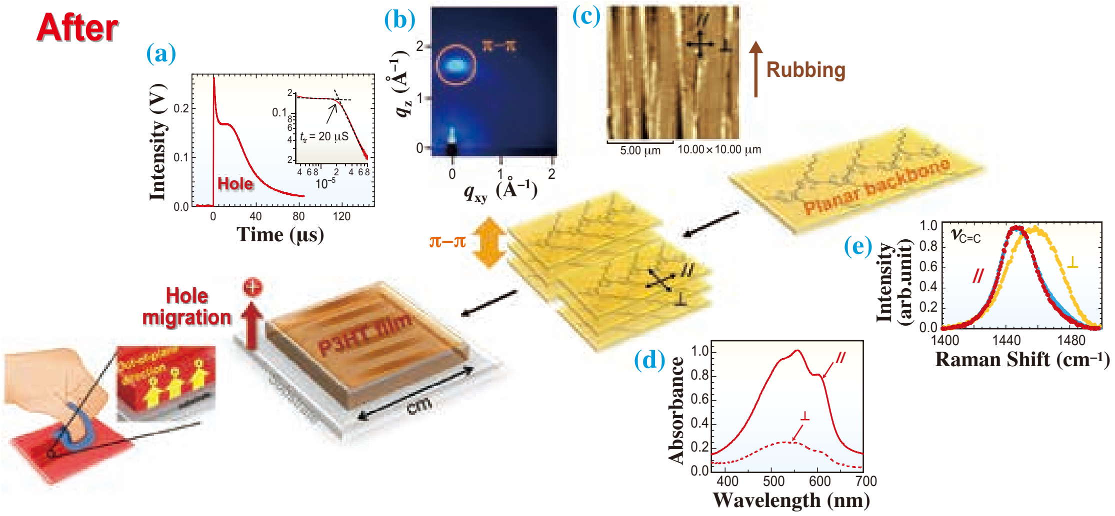

Fig. 2. Hole transport and structure of P3HT film after rubbing. **(a)** TOF, **(b)** GIXD, **(c)** AFM, **(d)** absorption spectra, and **(e)** Raman spectra results. [3]

direction. The degree of aggregation is obtained by analyzing the spectral profile and is enhanced after rubbing. Figure 2(e) shows the Raman spectra of the P3HT film after rubbing. The Raman result reveals an increase in the degree of planarity of the P3HT backbone structure. Thus, the rubbing enhances the out-of-plane mobility, face-on orientation, aggregation, and molecular planarity.

Figure 3 shows the enhancement factors (EFs) of mobility and aggregation resulting from rubbing. The EFs were obtained by using P3HTs different regioregularity (RR). All of the EF values are greater than 1, indicating the enhanced mobility and aggregation in all films with different RR values. These EFs reveal that slight aggregation (EF_{agg} = 1.2) results in a significant mobility enhancement (EF_{μ} = 8). A lower-RR film produces a larger EF. In particular, the hole mobility of the film with a low RR (91%) became almost equal to that of the film with a high RR (98%).

In summary, the eightfold enhancement of the out-of-plane hole mobility was achieved by rubbing. After the rubbing, the π-π stacking of P3HT was formed in the out-of-plane direction, whereas the P3HT backbone was oriented in the in-plane direction. Aggregation and planarity were enhanced by rubbing and facilitated carrier migration in a P3HT thin film [3]. These results are useful for further developing polymer-based devices.

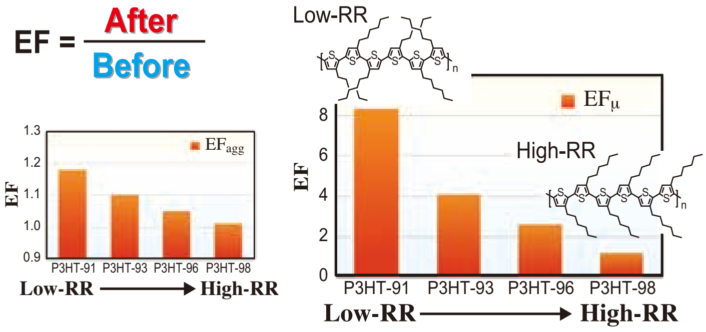

Fig. 3. EF of aggregation (EF_{agg}) and EF of mobility (EF_{μ}) as a function of RR. [3]

Daisuke Kajiya[a], Tomoyuki Koganezawa[b]
and Ken-ichi Saitow[a,c,*]

[a] Natural Science Center for Basic Research and Development (N-BARD), Hiroshima University
[b] Japan Synchrotron Radiation Research Institute (JASRI)
[c] Graduate School of Science, Hiroshima University

*E-mail: saitow@hiroshima-u.ac.jp

References

[1] L. Hartmann *et al*.: Adv. Funct. Mater. **21** (2011) 4047.
[2] V. Vohra *et al*.: J. Phys. Chem. Lett. **3** (2012) 1820.
[3] *D. Kajiya, S. Ozawa, T. Koganezawa and K. Saitow: J. Phys. Chem. C* ***119*** *(2015) 7987.*
[4] D. Kajiya, K. Saitow: Nanoscale **7** (2015) 15780.
[5] D. Kajiya *et al*.: AIP Adv. **5** (2015) 127130.

Formation of stable self-assembled multilayer palladium nanoparticles for ligand-free coupling reactions

Cross-coupling reactions with an organometallic catalyst, especially a palladium-based catalyst, are a key to the synthesis of functional molecules such as those used in pharmaceuticals, agricultural chemicals, solar cells, and organic electroluminescent displays. For the synthesis of functional molecules, carbon-nitrogen bond-forming reactions are frequently used, as well as carbon-carbon bond-forming reactions [1].

Metal cross-coupling reactions generally require the use of an excellent ligand [1]. Cross-coupling reactions of metals, including Pd-coupling reactions, have evolved with ligand development. The ligand has several important roles in cross-coupling reactions. For example, in the Buchwald-Hartwig reaction, the ligand inhibits metal aggregation, accelerates oxidative addition, and/or reduces elimination steps. The use of ligands is, however, associated with a problem of product purification. Separation of the product from the ligand is a costly and time-consuming process. Moreover, sophisticated ligands are generally expensive. Furthermore, inert reaction conditions are generally required as phosphorus ligands are oxidized easily.

To emancipate cross-coupling reactions from the restrictions imposed by ligands, the use of metal nanoparticles as catalysts has emerged as one of the most promising solutions. Transition-metal nanoparticles are usually 1–10 nm in diameter and have a narrow size dispersion, and their synthesis is reproducible with well-defined compositions and clean surfaces. To achieve a useful nanoparticle catalysis, the key technique in metal nanoparticle preparation is the stabilization of particles by a protective agent to avoid the formation of bulk metal. Two types of stabilization can be achieved depending on the nature of the protecting agents: (a) electrostatic stabilization using ionic compounds as protecting agents and (b) steric stabilization using neutral molecules such as polymers or other bulky molecules [2]. On the other hand, the immobilization of nanoparticles on supports can increase the stability of metal dispersions to achieve catalytic systems with novel properties. In other words, combination of the advantages of heterogeneous and homogeneous catalysis is desirable. The development of systems of organometallic catalysts involving metallic nanoparticles is an active research field.

With this background, we recently developed a novel Pd nanoparticle catalyst, named sulfur-modified gold-supported palladium (SAPd, Fig. 1) [3]. SAPd can be easily prepared by the treatment of gold with Piranha solution, a mixture of sulfuric acid and hydrogen peroxide, and subsequent palladium absorption. In earlier investigations, SAPd was applied to a ligand-free Buchwald-Hartwig reaction [4], Suzuki-Miyaura couplings [3], and a carbon (sp^3 and sp^2)-hydrogen bond activation reaction, and exhibited superior performance to conventional Pd catalysis. SAPd is an environmentally sustainable ideal catalyst since SAPd can usually be used repeatedly and the amount of leached Pd in the whole reaction mixture is less than 1 ppm. SAPd is now commercially available and widely used for ligand-free Pd cross-coupling including liquid-phase combinatorial synthesis, medicinal library synthesis, and flow-reaction systems.

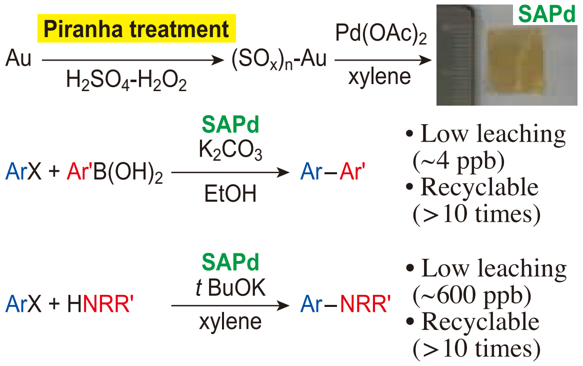

Fig. 1. Preparation of SAPd and its use in ligand-free Pd coupling.

We have also characterized the structural and chemical properties of SAPd by spectroscopic analytical techniques [5]. Extended X-ray absorption fine structure (EXAFS) experiments (Fig. 2) at beamlines **BL14B2** and **BL27SU** and transmission electron microscopy (TEM) analyses were performed to clarify the geometrical properties of Pd catalysis in SAPd. X-ray absorption near-edge structure (XANES) analysis at the sulfur and carbon *K*-edges was used to determine the chemical states of sulfur and carbon in SAPd. As a result, we found that SAPd was constructed with about 10 layers of Pd(0) nanoparticles with a diameter of less than 5 nm (Fig. 3).

In summary, we discovered by performing XAFS and TEM analyses that SAPd, which catalyzes Pd cross-coupling in the absence of any ligand, has approximately 10 layers of self-assembled Pd(0) nanoparticles of less than 5 nm in diameter on a sulfur-modified gold surface. It is noteworthy that the Pd nanoparticles in SAPd are embedded in the high-density layers without condensation. The matrix of SAPd, which comprises organic matter formed by the complexes of sulfate and xylene embedding the Pd nanoparticles in SAPd, prevents the aggregation of nanoparticles. These findings also clarify the ease and usefulness of the SAPd preparation method for constructing multilayers of highly reactive Pd nanoparticles on metal substrates and opens a new route for preparing other metal nanoparticles for organic synthesis. On the basis of these structural findings for SAPd, we very recently succeeded in making nickel, ruthenium, and iron nanoparticle catalysts for functional molecular syntheses.

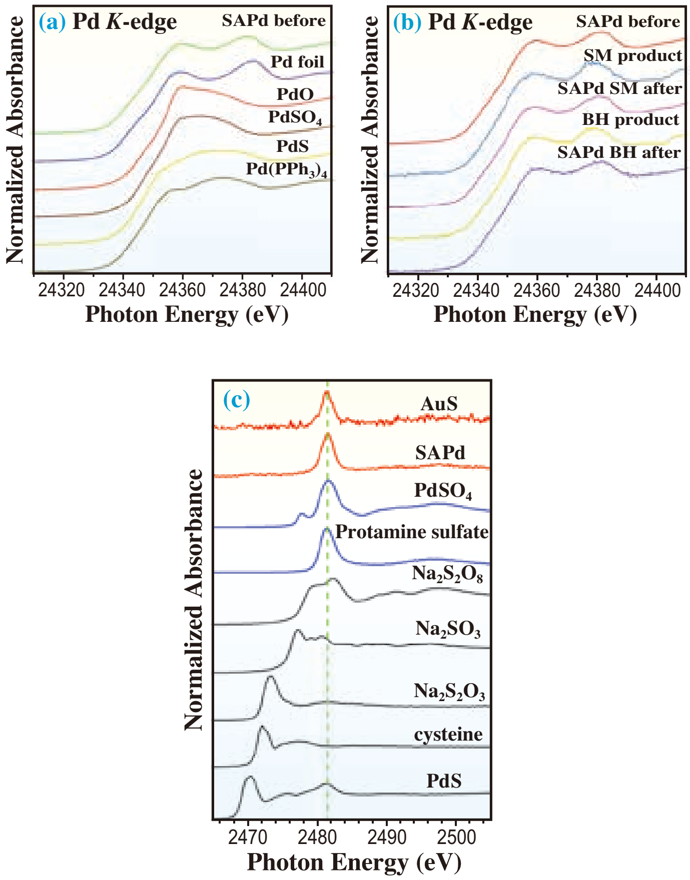

Fig. 2. Pd *K*-edge XANES spectra of **(a)** SAPd before: before cross-coupling reaction and standard materials, **(b)** SAPds. **(c)** S *K*-edge XANES spectra of SAPd before and standard materials.

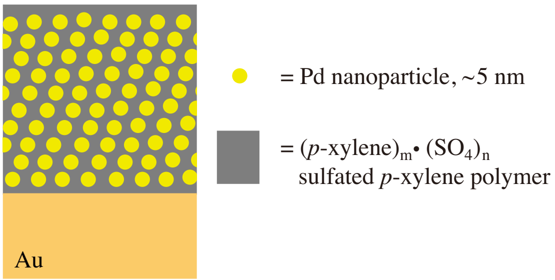

Fig. 3. Drawing of the SAPd structure.

Naoyuki Hoshiya[a,b], Satoshi Shuto[a]
and Mitsuhiro Arisawa[a,c,*]

[a] Faculty of Pharmaceutical Sciences,
Hokkaido University
[b] Kyoto Pharmaceutical University
[c] Graduate School of Pharmaceutical Sciences,
Osaka University

*E-mail: arisaw@phs.osaka-u.ac.jp

References

[1] J.F. Hartwig: Organotransition Metal Chemistry, University Science Books, 2010.
[2] C. Deraedt, D. Astruc: Acc. Chem. Res. **47** (2014) 494.
[3] N. Hoshiya *et al.*: J. Am. Chem. Soc. **132** (2010) 7270.
[4] M. Al-Amin *et al.*: Adv. Synth. Catal. **354** (2012) 1061.
[5] *M. Arisawa, M. Al-Amin, T. Honma, Y. Tamenori, S. Arai, N. Hoshiya, T. Sato, M. Yokoyama, A. Ishii, M. Takeguchi, T. Miyazaki, M. Takeuchi, T. Maruko, S. Shuto: RSC Adv.* **5** *(2015) 676.*

ACCELERATORS & BEAMLINES FRONTIERS

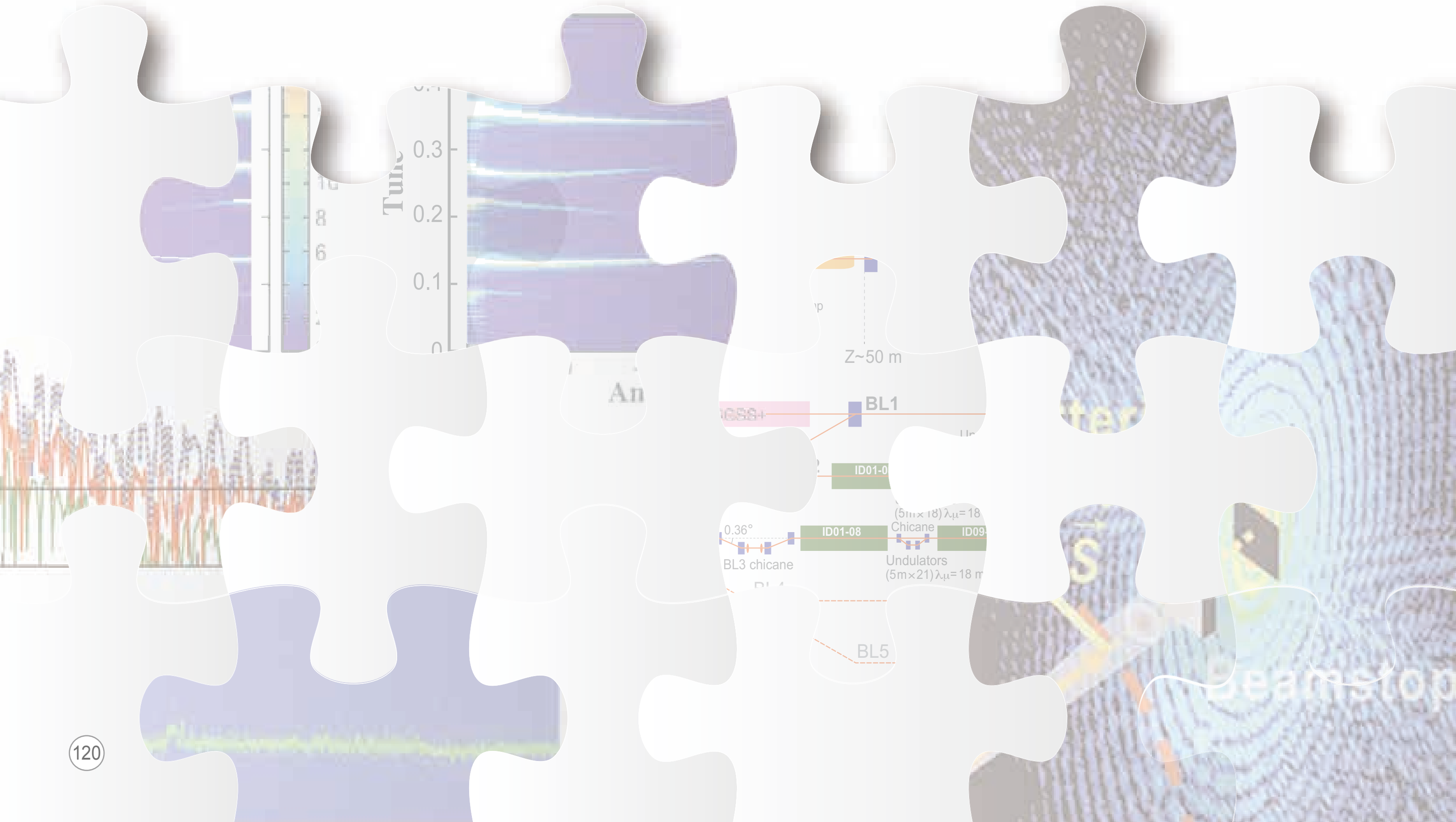

SPring-8 Beam Performance

Optimization of Nonlinear Optics of the Storage Ring

While the top-up injection has already been indispensable for user experiments at the SPring-8 storage ring, the insertion devices (IDs) have perturbed the stability of the top-up injection. When users change the gaps of the IDs, the betatron tunes are shifted from the initial values. For some IDs, this tune shift is large and when the working point moves closer to a nearby nonlinear resonance, the injection efficiency is largely affected. Here, sextupole magnets are usually utilized to correct the linear chromaticity to ensure stable electron motion, but these nonlinear fields also cause various dynamic phenomena such as the nonlinear resonances mentioned above and the dependence of the betatron tune on the oscillation amplitude. In order to optimize the sextupole magnetic fields to improve the top-up injection efficiency and beam lifetime, we newly built a correction scheme and applied it to the SPring-8 storage ring. In Fig. 1 and Fig. 2, the dependences of the vertical tune on the horizontal amplitude before and after the optimization are respectively shown. The experimentally observed tune shift is in good agreement with the theoretical shift, and it became almost flat against the horizontal amplitude after the optimization. The dependence of the horizontal tune on the horizontal amplitude was also corrected in the same way. By optimizing the sextupole magnetic fields, the injection beam loss observed within 100 turns was suppressed, and the top-up injection efficiency was improved from about 80% to 90%. The momentum acceptance was slightly decreased from 3.3% to 3.1%, but this change is negligible for beam lifetime. The new set of sextupole magnetic fields have been applied in user operation since October 2015.

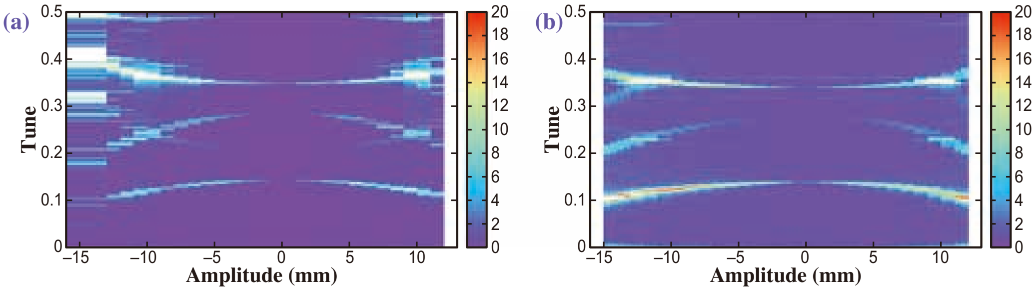

Fig. 1. Dependence of the vertical tune on the horizontal amplitude before optimizing the sextupole magnetic fields. Simulation results **(a)** are compared with experimental data **(b)**.

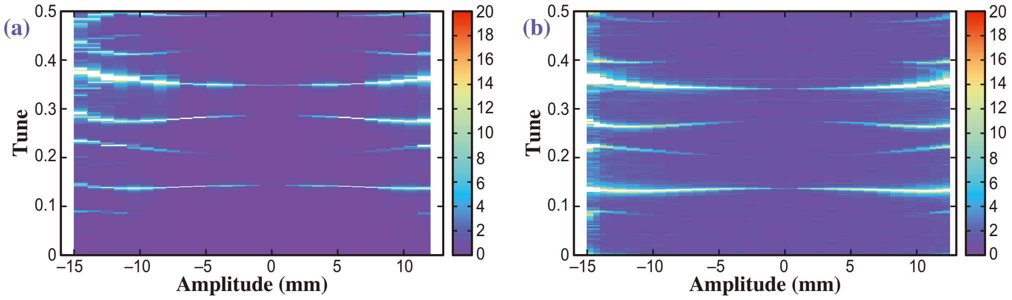

Fig. 2. Same as Fig. 1 but after optimizing the sextupole magnetic fields.

S. Goto*, M. Takao and T. Watanabe

Japan Synchrotron Radiation Research Institute (JASRI)

*E-mail: sgoto@spring8.or.jp

CONTROLS & COMPUTING

Development, implementation and operation of MADOCAII middleware for accelerator and beamline control

1. Introduction

1.1. What is MADOCA SPring8 Control Middleware?

The control group of SPring-8 developed MADOCA (Message and Database Oriented Control Architecture) middleware for the SPring-8 storage ring control system in 1997. The SPring-8 control system consists of workstations in the central control room and embedded computers placed close to accelerator components such as the magnet power supplies, vacuum pumps, beam monitors and radio frequency generators. These computers are connected by a network, and the operators send commands from the workstations to the embedded computers. Over 500 embedded computers distributed around SPring-8 control with more than 30,000 control points.

1.2. Communication management

The MADOCA middleware transports control commands issued by graphical user interface (GUI) applications, which run on operator workstations, to the equipment control applications (Equipment Manager, EM), which run on embedded computers placed close to the accelerator components. The operator sends a command such as 'set b-magnet power supply to 12.34A'. We build a command such as set/sr_mag_ps_b/12.34A and send this string as a message. In this command, the operator does not care which embedded computer controls the b-magnet power supply and how the embedded computer controls a power supply to give 12.34A. MADOCA takes care of these issues. We refer to this scheme as *device abstraction*. When MADOCA middleware running on the operator workstation receives this message from a GUI, it delivers this message to another MADOCA middleware running on an embedded computer. The relationships between the embedded computers and components are registered in the parameter database. An application running on the embedded computer receives a message from the MADOCA middleware, interprets the command and converts it to the machine language for the components. This device abstraction makes GUI development easy because detailed information is not required to control components. The messages between the GUI and EM must be delivered in an accurate, fast, reliable and simple way by the middleware. The MADOCA middleware was designed to satisfy these requirements.

1.3. Database

1.3.1. Parameter management

The other aspect of MADOCA is its database-oriented architecture. MADOCA manages almost every parameter required for the accelerator and beamline operations using a single relational database management system (RDBMS). It manages accelerator parameters including magnet positions, components, embedded computer relations, alarm thresholds and setting parameters for the components of the accelerator.

1.3.2. Logging

The RDBMS not only manages parameters but also logs data collected from almost every component around SPring-8. SPring-8 has over 30,000 control points. If one piece of equipment malfunctions, one may be notified by the electron beam stopping, but how do we figure out which equipment is broken? MADOCA answers this question by monitoring every piece of equipment continuously. Monitored data are stored in the logging database implemented on the same RDBMS server. The logging database makes troubleshooting easy. The MADOCA logging database has stored all data since SPring-8 was commissioned. Storing the logging data in the RDBMS provides a consistent and simple means of data access. One can access logged data from GUI using C-library or browser using web interfaces.

2. MADOCAII, the next-generation MADOCA

The first MADOCA system was developed to control the storage ring. It now covers beamlines, injector synchrotron, injector linac, New SUBARU and SACLA. Since its development about 17 years ago, we have experienced many shortcomings of the MADOCA system. We have thus developed a new next-generation control system (MADOCAII) based on new technologies. We have experienced several limitations of MADOCA that were serious obstacles in developing the next-generation control system. We will discuss the limitations of MADOCA regarding both messaging and the logging database in the following section.

2.1. Messaging in MADOCAII

2.1.1. Messaging in MADOCA

The messaging in MADOCA was based on an ONC-RPC (open network computing remote procedure call) system. Although ONC-RPC can handle data structures of any length, we limited exchanges to fixed-length strings. This works well for exchanging short or scalar messages such as ‘switch on’ or ‘set 12.3A’; however, it cannot handle large amount of data, such as images, or complex data structures. These data were exchanged using a network file system (NFS). This system is slow and lacks real-time capability. Moreover, MADOCA messaging was limited to only Unix-like systems and a C-language environment. Although Windows OS, which is not a Unix-like system, is embedded in many commercial instruments, it cannot handle MADOCA messaging. We had to set Unix gateways to use Windows OS in the SPring-8 control system. It was also difficult to use ONC-RPC with other computer languages such as LabView or Python, which have recently become commonly used in the SPring-8 accelerator and beamline control system. When one issues an ONC-RPC command to an application, it is necessary to wait for the callback. This means applications must be written in a “send command, wait for answer” which is called synchronous programming. This slows down the control application because while waiting for the callback, the application cannot perform other tasks. In the next-generation control system, asynchronous programming is used to solve this problem. In asynchronous programming, the application works in a “send, send, send, send commands, do something while waiting and receive callbacks” manner, which reduces the waiting time compared with that in synchronous programming. In the MADOCA system, the roles of the client (GUI) and server (embedded computer) were fixed and it was difficult to change the roles, for example, to send commands from an embedded computer to an operator console or to communicate between GUIs.

2.1.2. Messaging in MADOCAII

The messaging in MADOCAII overcomes the problems in the old MADOCA messaging system. The most important point is that we use the ZeroMQ asynchronous messaging library instead of ONC-RPC. ZeroMQ can exchange variable-length messages asynchronously on multiple platforms and in multiple computer languages. The ZeroMQ library can transport variable-length strings. We can use not only scalar values like voltage, current and vacuum measurement but also complex data structures and images by packing them into strings by using the MessagePack object serialization library. Because the ZeroMQ and MessagePack libraries run on various platforms including Windows OS and support major languages, MADOCAII can run on a wide range of platforms and languages. Because ZeroMQ provides flexible connections, it is possible to communicate not only from operator workstations to embedded computers but also from workstations to workstations and between embedded computers. This enables many opportunities for control in the future. Although MADOCAII has dramatically changed internal communication, we designed MADOCAII without rewriting the applications written in the MADOCA environment. Other than a very small number of applications, old applications now work with MADOCAII without any modifications.

2.2. Data logging in MADOCAII

2.2.1. Data logging in MADOCA

Data logging in MADOCA also had many problems. The RDBMS has low performance for data logging to maintain critical consistency, which is essential in parameter management. We inserted a group of values into the RDBMS in each transaction to compensate for its low performance. While *one value by one insertion* is ideal for data management, it requires too many transactions for the RDBMS. Moreover, for consistency, the RDBMS requires one unified memory space in the system, which means that to obtain better performance by upgrading hardware, the computer hardware has to be an expensive shared-memory type multicore CPU.

2.2.2. Data logging in MADOCAII

2.2.2.1. *NoSQL database*

In the logging database management of MADOCAII we use the NoSQL (not only SQL) database instead of the RDBMS. We use the Cassandra database for perpetual data storage and the Redis database for the newest data cache. Both databases are NoSQL databases. Cassandra runs on a homogeneous inexpensive multi-node computer cluster, which means there is no master or slave. We found that the performance of Cassandra is linearly proportional to the number of nodes. Therefore, if it is necessary to improve performance of the Cassandra cluster, we will simply add computers.

In the Cassandra database, each data record is copied into three replicas and distributed to different computer nodes. Thus, if one or two computers in the cluster are broken, data are kept safely and clusters will still run. Redis is an ultrafast in-memory database with which one can obtain the newest values one order of magnitude faster than the RDBMS. Both Redis and Cassandra pack data into string format using the MessagePack library. Thus, we build only one data table format to reduce the workload in database management.

2.2.2.2. *Data acquisition*

When we introduced the NoSQL database, we drastically changed our data acquisition processes. MADOCA data acquisition process running on a workstation periodically requests data to the embedded computers, packs received data into a RDBMS command and sends it to the RDBMS. The newly developed MADOCAII data acquisition system reverses this process. MADOCAII performs processes on the embedded computers, which send data to a relay server at their own timing. The relay server then writes the data into NoSQL servers. We installed two identical relay servers for fault tolerance and load balancing. If one server is broken, the other relay server will work, and, if necessary, performance can be improved by adding another relay server. Similarly to the messaging in MADOCAII, the MADOCAII database library has backward compatibility to the MADOCA database system so that no modifications were needed to the source code.

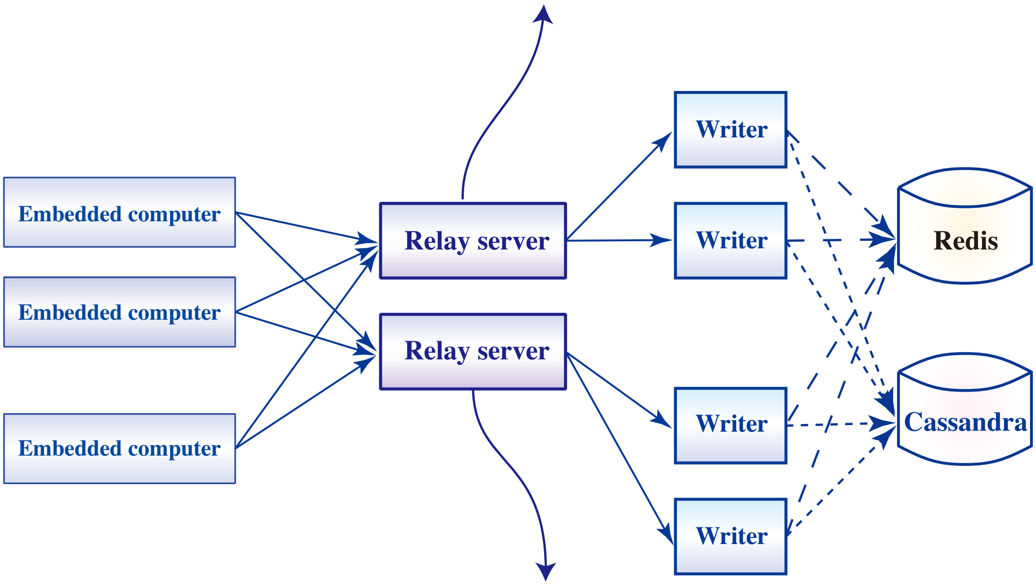

MADOCA II data acquisition system schematics. Data from embedded computers are packed in ZeroMQ messages and sent to the relay servers (solid line). Two relay servers are in operation for redundancy. The relay servers pass the messages to the writer processes. The writer processes write data into the NoSQL database servers. The dashed lines mean the data path to the Redis servers and the Cassandra API is expressed in the dotted line. The relay servers also publish messages with pub/sub mechanism (curly lines).

3. Performance and Operation

3.1. Performance

We measured the performance of MADOCAII. For the messaging, the round-trip messaging between processes running in the same computer takes 0.4ms. It takes 1.8 ms for the round-trip between operator workstations and embedded computers. The data insertion performance of Cassandra exceeds about half a million per second in the case of six computer nodes. This is about 50 times higher than that for the previous MADOCA RDBMS system. The performance will also linearly increase with the number of nodes.

3.2. Operation

MADOCAII messaging has been in operation since September 2012 and the database has been working since January 2015 in the SPring-8 accelerator and beamlines after prolonged testing. Both have been working with few major problems.

4. Conclusion

We have developed and implemented the new MADOCAII system. Although it has an almost identical interface to the old MADOCA system, the internal processes are radically changed by using new information technology such as asynchronous messaging and NoSQL databases. The main aim of the development has been achieved and we expect MADOCAII to serve as the future SPring-8 control system.

Akihiro Yamashita* and Tomohiro Matsushita

Japan Synchrotron Radiation Research Institute (JASRI)

*E-mail: aki@spring8.or.jp

SACLA
BEAM PERFORMANCE

In April 2015, SACLA launched routine user operations for two XFEL beamlines, BL2 and BL3. Later that year during the two-month summer shutdown, the large-scale transformation of BL1 from a short-pulsed spontaneous X-ray source to a new soft X-ray FEL source was completed and beam commissioning of BL1 is now underway. Figure 1 shows schematic drawings of the current SACLA facility. Substantial improvements to the tuning and preparation procedures have increased the total public user time available to about 4000 hours, corresponding to 60% of the total operations time. Further improvements are expected to increase availability to 70%. Machine enhancements enabled the generation of a laser peak intensity of 0.6 mJ/pulse at 10 keV and an average trip interval of 1 hour with a regular repetition rate of 30 Hz.

1) New BL2 beamline open for user experiments

The construction of BL2 was completed during the 2014 summer shutdown, with the first lasing obtained in October 2014. Subsequent beam tuning activities improved the efficiency, enabling an XFEL intensity greater than 100 μJ/pulse and the availability of BL2 for user experiments. User operations at BL2 began in April 2015 in a DC mode without pulse-by-pulse XFEL switching, where users can select either BL2 or BL3 according to the needs of their experiments.

In January 2015, testing began for multi-beamline operations combining pulse-by-pulse switching with time-interleaved multi-energy acceleration [1,2] in order to more fully utilize the capabilities of SACLA. In July 2015, stable lasing was successfully achieved using multi-beamline operations with pulse energies around 100–200 μJ, providing broad tunability of the laser wavelengths between the beamlines. This multi-beamline operation capability has been available for user experiments since autumn 2015. Figure 2 shows the stability of the laser pulse energies achieved at the two beamlines during multi-beamline operations.

Note that the peak current is currently limited to about 2 kA due to the CSR effects at the doglegged beam transport to BL2. Modifications of the beam transport, including the pulse-switching system, are under investigation, with a goal of achieving multi-beamline operations that provide a regular peak current greater than 10 kA.

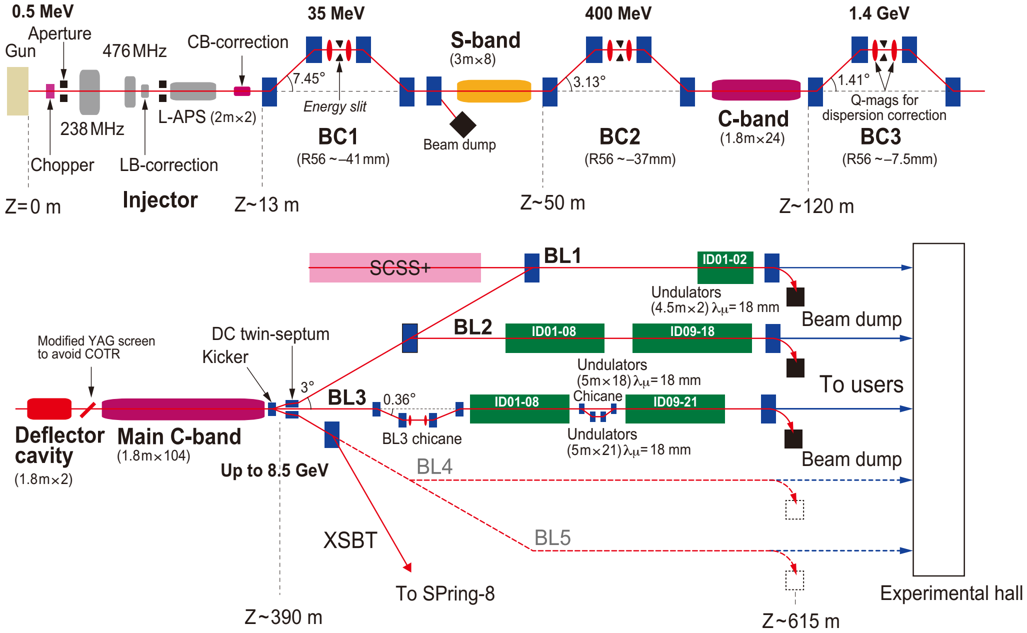

Fig. 1. Schematic drawings of the current SACLA facility. Two beamlines, BL2 and BL3, are now available for user experiments; a third beamline, BL1, that will provide a soft X-ray FEL is currently under commissioning.

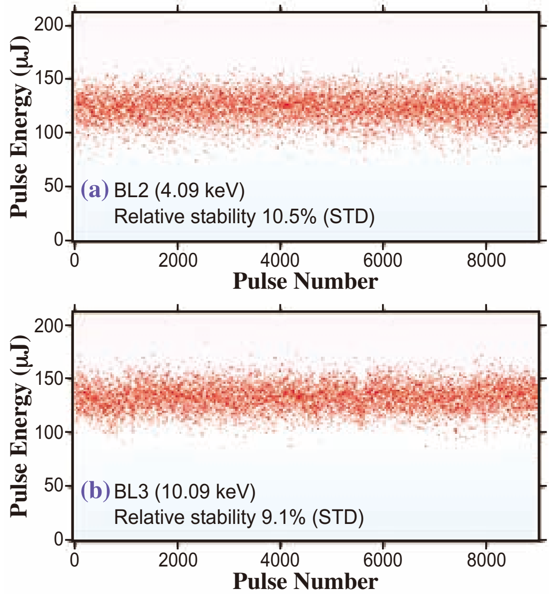

Fig. 2. Stability of the laser pulse energy for **(a)** BL2 and **(b)** BL3 during the multi-beamline operation. Each red dot represents the result for a single shot. The electron beam energies were 6.3 GeV for BL2 and 7.8 GeV for BL3. The undulator K-values were 2.85 for BL2 and 2.1 for BL3.

2) Successful upgrading of the existing beamline, BL1

Substantial renovation of BL1 was completed during the summer shutdown of 2015. Figure 3 shows the linear accelerator system dedicated to the BL1 beamline. This dedicated accelerator was constructed mainly by relocating the SCSS test accelerator [3] and adding two C-band acceleration units to the accelerator. Three in-vacuum undulators, each of which has a period of 18 mm, were installed in the BL1 beamline. The X-ray beamline components, including equipment at the frond-end and optical components in the optics hutch, were also greatly enhanced to accommodate a soft X-ray FEL.

The two electron drivers, i.e., the dedicated accelerator and the SACLA linear accelerator, are switchable. The operation of BL1 is independent of that of SACLA when the dedicated accelerator is selected. Enabling this flexibility required modification to the beam transport channels and the safety and machine interlock systems.

Beam commissioning began on September 14, 2015, and the first lasing was obtained at a wavelength of 30 nm a few weeks later on October 7 [4]. The upgraded BL1 beamline passed its radiation inspection the following November. Beam tuning progressed well and the SASE pulse energy reached a few μJ by the end of 2015. Figure 4 shows the laser profile measured in the optics hutch. After additional beam tuning, user experiments at BL1 will commence in 2016.

Fig. 3. Linear accelerator system dedicated to the BL1 beamline. This picture was taken from the electron gun side (i.e., the uppermost-stream side of BL1).

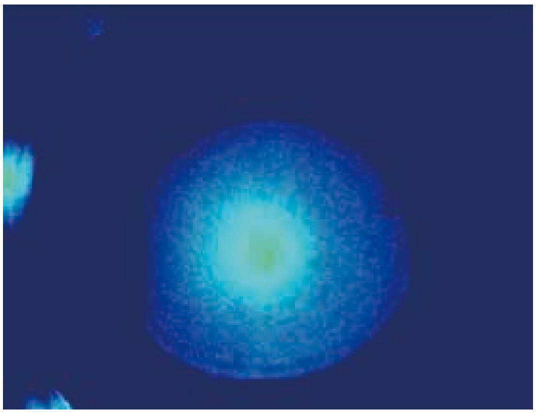

Fig. 4. Laser profile measured by the MCP (microchannel plate) in the BL1 optics hutch.

Hitoshi Tanaka

RIKEN SPring-8 Center

E-mail: tanaka@spring8.or.jp

References

[1] T. Hara *et al*.: PRSTAB **16** (2013) 080701.
[2] T. Hara *et al*.: Proc. FEL2015, Daejeon Korea (2015) 293.
[3] T. Shintake *et al*.: Nature Photonics **2** (2008) 555.
[4] T. Sakurai *et al*.: Proc. 12th Annual Meeting of Particle Accelerator Society of Japan, Tsuruga, Japan (2015) 256.

Highly efficient arrival time diagnostics for SACLA

A pump and probe technique combining XFELs and ultrafast optical lasers is a powerful approach for investigating the dynamics of phase transitions, shock compression, and charge transfer with ultrahigh spatio-temporal resolution.

The time resolution in pump and probe experiments is determined by the pulse widths of the pump and probe beams and the accuracy of the timing difference between the pump and probe pulses (Fig. 1). SACLA is able to generate X-ray pulses with a pulse width of less than 10 femtoseconds, which fixes the ultimate temporal resolution. However, the time resolution in pump and probe experiments can be degraded by timing instabilities, including short-term jitters and long-term drifts, between the pump and probe pulses, which may originate from the phase jitter of an electron bunch at the accelerator radio frequency (RF), a change in the SASE lasing part in an electron bunch, imperfect synchronization between the optical laser and the RF signal, and vibration of the optical transport channel. Typical values of the timing jitter are on the order of 100 fs, which is much larger than the pulse duration of SACLA.

To improve the time resolution in pump and probe experiments, a scheme based on a post-process analysis combined with arrival time diagnostics has been proposed. Several methods, such as a THz streak and a change in optical reflectivity/transmission, have recently been developed at XFEL facilities. In the hard X-ray region, changes in the optical transmittance of materials excited with XFEL pulses have been utilized for timing diagnostics at LCLS [1]. In this case, large pulse energy of X-rays on the order of millijoule has been employed due to the weak interaction between matter and hard X-rays. SACLA generates a moderate pulse energy with shorter wavelengths that has weaker interactions. We thus needed to develop a technique with higher efficiency .

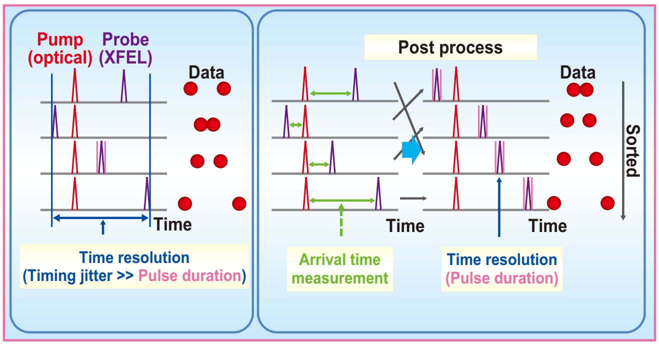

Fig. 1. Schematic images of the time resolution in a pump and probe experiment. **(a)** Time resolution including timing jitter. **(b)** Time resolution improved by post process technique with arrival time diagnostics.

For this purpose, we developed arrival time diagnostics combining a spatial decoding technique and a one-dimensional focusing mirror, which was utilized to increase the intensity of an X-ray [2]. The spatial decoding technique was applied to convert the arrival time of an X-ray pulse into spatial distribution. Since the spatial decoding technique is affected by the spatial intensity modulation of the X-ray profile, we utilized a high-quality mirror developed by an elastic emission machining (EEM) technique.

We performed an experiment at beamline **BL3** of SACLA (photon energy of 12 keV, pulse energy of 12 ± 2 μJ). We used a GaAs wafer as a target. When intense X-rays are irradiated to the GaAs, a number of electron-hole pairs are generated. This, which causes modulation of the band structure and changes of the absorption coefficient of an optical laser with a photon energy larger than the band gap (1.43 eV). We are able to retrieve the timing information from a spatially modulated transmission profile of the optical laser.

Figures 2(a), 2(b), and (2c) show the typical single-shot spatial profiles of the transmitted laser pulse under an intense XFEL pulse, which originate from the changes in optical transmission. The temporal overlap information is projected in the horizontal direction. The lower axis corresponds to the horizontal pixel number while the upper axis represents the time Δt determined from the geometry. A larger Δt indicates the earlier arrival of an X-ray pulse relative to the optical laser pulse. Figure 2(a) shows the profile measured without the temporal overlap, where the timing of the optical laser was 2 ps in advance of that of the XFEL pulse. In this case, the optical laser pulse is mostly absorbed by the GaAs. Figure 2(b) shows the profile with temporal overlap, which causes a change in the optical transmission. The right edge of the bright spot corresponds to the onset of the temporal overlap between these pulses. Figure 2(c) shows the profile without temporal overlap, where the timing of the optical laser was 2 ps after XFEL irradiation. Both edges of the profile originating from a slit show the timing window of this arrival time monitor.

In order to evaluate the temporal jitter between XFEL pulse from SACLA and the optical laser pulse, we performed a measurement with this system. Figure 3(a) shows the arrival timings of each pulse , plotted over 1000 shots. The positional change of the

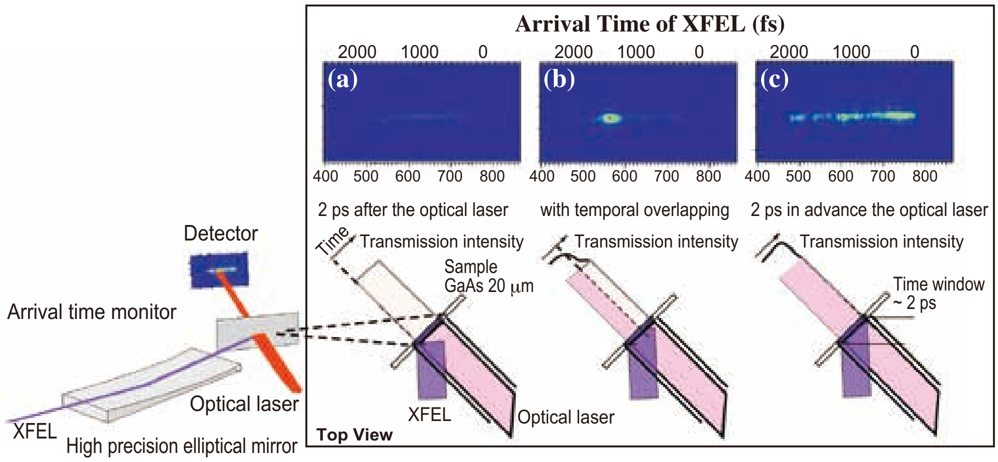

Fig. 2. Schematic image of the spatial decoding technique and typical profiles of optical laser pulses with X-ray pulse irradiation. **(a)** 2 ps after the optical laser. **(b)** With temporal overlapping. **(c)** 2 ps in advance of the optical laser.

right edge corresponds to the timing jitter. From these results, we obtained a distribution of the arrival time (Fig. 3(b)) and determined the temporal jitter in this period (100 s) to be 110 fs in RMS.

The timing diagnostics should be performed in parallel with user experiments to compensate for timing jitter using a post-process technique. The pulse energy to be required for our scheme is only around 10 μJ at 10 keV, which is less than 3% of total pulse energy of SACLA. Although the present method is in a destructive scheme, our highly efficient method allows simultaneous measurements to be performed, if we extract a small fraction of the X-ray pulse energy to a dedicated branch for the timing diagnostics. For this purpose, we are developing an X-ray diagnostic branch with an X-ray transmission grating [3], which will provide information on the arrival time at each shot.

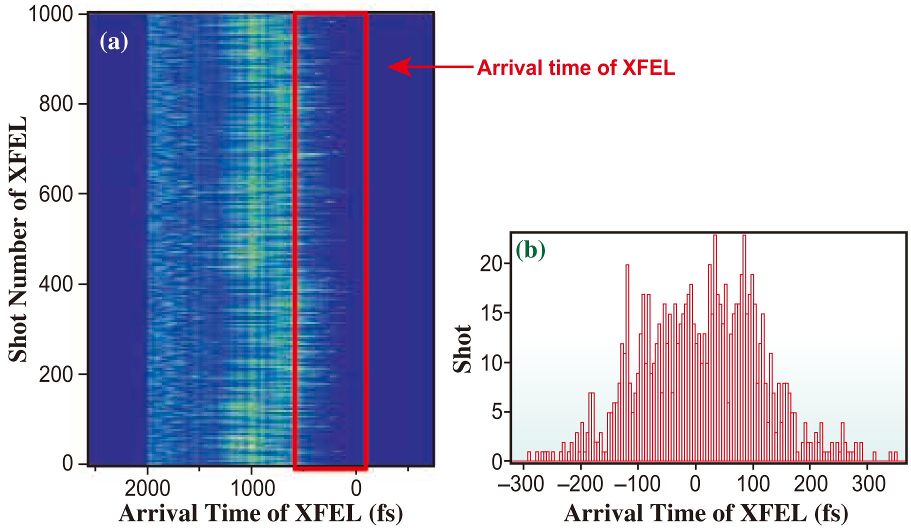

Fig. 3. **(a)** Change in transmission intensity profile for 1000 shots. The vertical axis indicates the shot number of the XFEL while the horizontal axis shows the relative arrival time. **(b)** Histogram of the measured arrival time obtained from (a). [2]

Takahiro Sato[a,*] and Makina Yabashi[a,b]

[a] RIKEN SPring-8 Center
[b] Japan Synchrotron Radiation Research Institute (JASRI)

*E-mail: tsato@chem.s.u-tokyo.ac.jp

References

[1] M. Harmand *et al*.: Nat. Photonics **7** (2013) 215.
[2] *T. Sato, T. Togashi, K. Ogawa, T. Katayama, Y. Inubushi, K. Tono and M. Yabashi: Appl. Phys. Exp.* ***8*** *(2015) 012702.*
[3] T. Katayama *et al*.: Appl. Phys. Lett. **103** (2013) 131105.

Experimental platform for serial femtosecond crystallography at SACLA

Serial femtosecond crystallography (SFX) with an X-ray free electron laser (XFEL) provides damage-free diffraction patterns from tiny crystals with micrometer sizes [1]. In this method, a stream of crystals interacts with an XFEL pulse, a duration of which is on the order of femtoseconds. Radiation damage to the sample can be circumvented because diffraction events can be terminated within a timescale much shorter than those of damage processes. Typically 10^4 or more diffraction patterns are collected from randomly oriented crystals to provide the statistical reliability required for building a structure model.

A key process in SFX experiments is the delivery of crystals. Micrometer-size crystals are dispersed in a fluid carrier and delivered to the interaction point using a fluid injector. Various types of injectors have been developed so far [2]. A liquid-jet injector with a gas dynamic virtual nozzle (GDVN) produces a micrometer-size stream of a crystal suspension. The electro spinning technique is also employed to deliver crystal suspensions at low flow rates on the order of 10^{-1} μl·min^{-1}. To reduce sample consumption, viscous-fluid injectors have been developed to produce a slow flow of crystals dispersed in a highly viscous carrier such as an LCP matrix or a grease-matrix carrier.

In the early SFX experiments, the interaction point was in a vacuum environment, which is advantageous for reducing background signals. One technical issue in the case of crystal delivery into vacuum is that the carrier fluid can freeze easily. A frozen carrier would inhibit an injector from stable operation, and more seriously, it would produce strong X-ray signals that may cause damage to a detector.

At SACLA, we have developed an ambient-pressure system for SFX experiments, Diverse Application Platform for Hard X-ray Diffraction in SACLA (DAPHNIS) [3]. The freezing issue can be avoided under the ambient-pressure operation, which also helps to maintain an appropriate temperature and humidity around the sample. Because of these advantages, DAPHNIS is applicable to a variety of samples beyond protein crystals, including live organisms, solutions, and powders dispersed in liquids.

Figure 1 shows a photograph of DAPHNIS, which basically consists of a sample chamber, injectors, and a multiport charge-coupled-device (MPCCD) detector with eight sensor modules [4]. This system is connected to a micrometer focusing system on a hard X-ray beamline of SACLA. Samples are delivered to the X-ray focal point using an injector, which is mounted on a motorized manipulator. The X-ray beam is blocked by a beam stopper in front of the detector. The distance between the detector sensor and sample is adjustable in the range between 50 and 100 mm. The highest nominal resolution is 1.5 Å (2.5 Å) at a distance of 50 mm (100 mm) and an X-ray wavelength of 1.24 Å.

Two types of liquid-jet injectors are available for delivering soluble-protein crystals. One with a GDVN produces a thin liquid beam from a nozzle with an inner diameter (ID) of 50–150 μm. Figure 2(a) shows a schematic drawing of the injector and a microscopic image of the nozzle tip. A helium gas stream through the outer capillary squeezes the sample beam to a diameter of 4–40 μm. The beam size is varied via the flow rate of the liquid and the stagnation pressure of the helium. In the case of a 10 μm stream from a 150-μm-ID nozzle, for example, a typical flow rate is 0.3 ml·min^{-1}. The other kind of injector is used for circulating a sample suspension with a peristaltic pump (Fig. 2(b)). The liquid-beam diameter is nearly the same as that of the nozzle aperture (100 or 200 μm). The flow rate is typically 1.5 ml·min^{-1} (2.5 ml·min^{-1}) with a 100 μm (200 μm) nozzle.

For crystals in highly viscous carriers, a syringe-pump injector is employed [5]. A carrier medium with crystals is extruded from a syringe needle at a low flow rate, which can be as low as ~0.1 μl·min^{-1}. The standard ID of the needle is 110 μm. Because of the low flow rate, the protein consumption is less than 1 mg in most cases. The flow rate can be further reduced by using a thinner needle, for example, ~0.03 μl·min^{-1} with a 50-μm-ID needle.

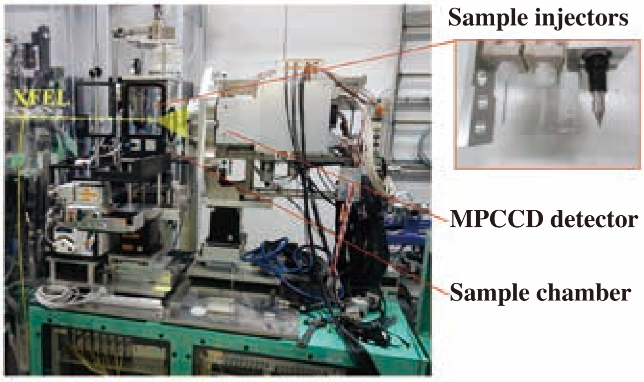

Fig. 1. DAPHNIS system with major components: sample chamber, injectors, and MPCCD detector with eight sensor modules.

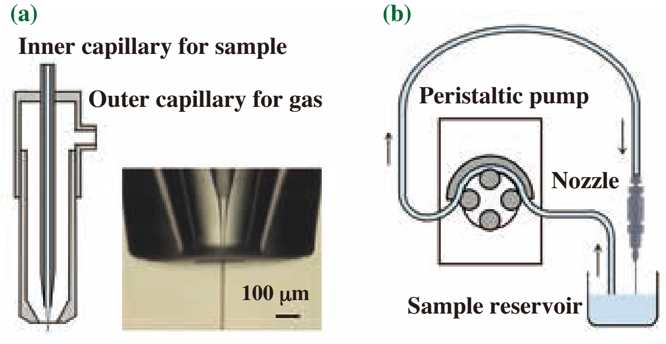

Fig. 2. Liquid-jet injectors. **(a)** Schematic drawing of a liquid-jet injector with a GDVN and a photograph of the nozzle tip. A helium gas stream is provided through the outer capillary to focus a liquid beam ejected from the inner capillary. **(b)** Schematic drawing of a liquid-jet injector with a sample circulator.

The DAPHNIS system was applied to SFX measurements of the model protein lysozyme. The XFEL beam at **BL3** of SACLA had a center photon energy of 10 keV with a bandwidth of 5×10^{-3} (FWHM; full width at half maximum) and an average pulse energy of 110 μJ (7×10^{10} photons/pulse) at the sample position. The repetition rate was 20 Hz. The focal size of the 10 keV beam was 1.5 μm (FWHM) in both the horizontal and vertical directions. The sample chamber was filled with helium gas with a partial pressure of >0.9 atm.

Lysozyme crystals with sizes of about 1 μm were dispersed in an aqueous buffer solution comprising 10% (w/v) sodium chloride and 1.0 M sodium acetate (pH 3.0). The number density of the crystals was $\sim10^9$ ml^{-1}. The crystal suspension was delivered using a liquid-jet injector with a GDVN having a 150 μm ID. The injector provided a 10-μm-diameter sample beam with a flow rate of 0.3 ml min^{-1}. The sample-to-detector distance was ~50 mm. Diffraction patterns were recorded with the MPCCD detector in a shot-by-shot manner.

In one measurement series, 45084 shots were applied to the sample in ~40 min. The 1 μm crystals of lysozyme provided clear diffraction patterns (Fig. 3(a)), 3226 of which were able to be processed for indexing Bragg spots. From the indexed images, 99.8% completeness was achieved at resolutions of 30.0–2.40 Å. An electron density map was successfully refined at a resolution of 2.4 Å (Fig. 3(b)). Higher-resolution data can be obtained by using larger crystals. For example, 7–10 μm crystals provided a structure model with a 2.0 Å resolution [5].

In conclusion, DAPHNIS has been successfully applied to protein SFX at SACLA. Even 1 μm crystals of lysozyme provided a clear electron density map with a 2.4 Å resolution in a measurement time of ~40 min. This result indicates that DAPHNIS can be used for the fast structure analysis of proteins for which large crystals are difficult to obtain. The ambient-pressure operation is useful for preventing fluid samples from freezing. The simple and compact structure of DAPHNIS facilitates future upgrades, for example, it can be easily modified to investigate ultrafast dynamics by a pump-and-probe technique. It is also adaptive to new sample-delivery methods such as pulsed droplet injection as well as the fast scanning of fixed crystal targets.

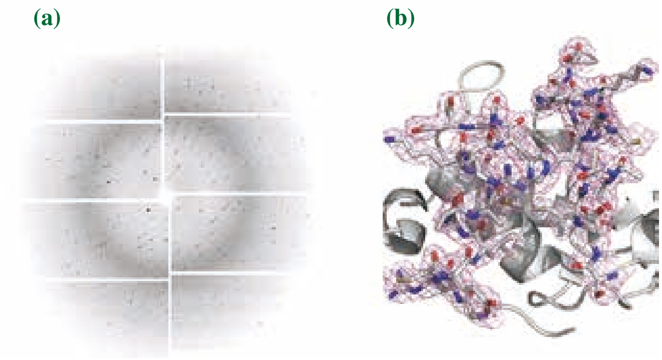

Fig. 3. Results of the SFX measurement of lysozyme. **(a)** One of the diffraction patterns of the 1 μm lysozyme crystals. **(b)** Close-up view of the lysozyme structure with an electron-density map contoured at the 1.0σ level. This figure was drawn with the PyMol program (http://www.pymol.org).

Kensuke Tono[a,b,*], So Iwata[b,c] and Makina Yabashi[a,b]

[a] Japan Synchrotron Radiation Research Institute (JASRI)
[b] RIKEN SPring-8 Center
[c] Department of Cell Biology, Kyoto University

*E-mail: tono@spring8.or.jp

References

[1] H.N. Chapman *et al*.: Nature **470** (2011) 73.
[2] U. Weierstall: Phil. Trans. R. Soc. B **369** (2014) 20130337.
[3] *K. Tono, E. Nango, M. Sugahara, C. Song, J. Park, T. Tanaka, R. Tanaka, Y. Joti, T. Kameshima, S. Ono, T. Hatsui, E. Mizohata, M. Suzuki, T. Shimamura, Y. Tanaka, S. Iwata and M. Yabashi: J. Synchrotron Rad.* **22** *(2015) 532.*
[4] T. Kameshima *et al*.: Rev. Sci. Instrum. **85** (2014) 033110.
[5] M. Sugahara *et al*.: Nat. Methods **12** (2015) 61.

Signal enhancement and Patterson-search phasing for higher-spatial-resolution coherent X-ray diffraction imaging of biological objects

Coherent X-ray diffraction imaging (CXDI) is a lensless imaging technique for the structural analysis of non-crystalline samples typically with micron to submicron dimensions [1]. In CXDI experiments (Fig. 1), spatially coherent X-rays irradiate an isolated sample object, and the Fraunhofer diffraction pattern from the object is recorded on a detector. When the pattern is sampled at a spacing finer than the Nyquist interval (oversampling condition), phase information of the object can be directly recovered from the diffraction pattern with iterative phase retrieval (PR) algorithms. Thereby, we can obtain an electron density map of sample objects projected along the direction of the incident beam. The short wavelength and high penetration depth of X-rays allow visualization of the internal structures of whole objects that are too thick for analysis with electron microscopy with resolution beyond the limit of optical microscopy.

Biological samples are extremely sensitive to radiation, even at cryogenic temperatures, yet need to be imaged with significant doses of X-rays due to their small scattering cross section. X-ray free-electron laser (XFEL) sources have the potential to solve this conflicting problem, since the femtosecond pulse duration and the high photon flux density of XFELs allow the collection of diffraction data before samples are destroyed. So far, XFEL-CDI has visualized large viruses, biological cells and cell components such as chloroplasts and nuclei at resolutions of 30–100 nm.

However, the poor diffraction power of biological objects remains an obstacle to improving the resolution of electron density maps. Another serious problem in CXDI is the quality and incompleteness of experimental diffraction data. Iterative PR calculations starting from a diffraction pattern with poor signal-to-noise ratios and unobserved data (particularly in the area at lowest spatial frequency where there is a beamstop; Fig. 1) often diverge or yield an incorrect solution. A reliable initial phase is extremely helpful for overcoming these problems and can lead to the correct structure.

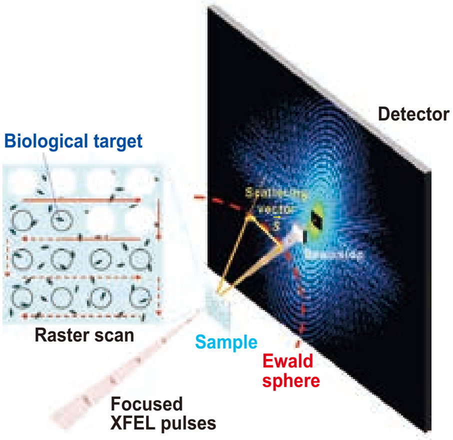

Fig. 1. Schematic illustration of XFEL-CDI experiments. In our scheme, biological targets are embedded in thin amorphous ice and raster-scanned with XFEL pulses. The direct beam transmitted through the sample is blocked by a beamstop, resulting in a lack of diffraction data at lower frequencies.

Recently, we have developed a new method to enhance diffraction signals from biological objects and to derive a reliable initial phase from their diffraction patterns alone [2]. Here, we introduce the concept behind this technique and demonstrate that the resolution is improved by a factor of two or more from a set of calculations based on our XFEL-CDI experiments at beamline **BL3** of SACLA [3,4].

We use colloidal gold (CG) particles and image the particles and biological targets together. Figure 2(a) shows a bacterial cell with four flagella and dispersed CG particles. The irradiation of an XFEL pulse on the whole sample yields an interference pattern between diffraction waves from both the biological target and the CG particles on the detector plane (Fig. 2(b)). Because the average electron density of gold is tenfold higher than that of biological objects, weak diffraction waves from the biological target are effectively enhanced to a detectable level by interference with strong waves from the CG particles. In fact, numerical calculations under the current experimental conditions at SACLA show that the diffraction pattern from the whole sample (Fig. 2(b)) extends to a more than twice wider range of spatial frequency than that of the diffraction pattern from the biological target alone (Fig. 2(c)). The diffraction pattern from the cell-CG model is dominated by the contribution from the CG particles, which display concentric ring patterns, and the interference term enhances the diffraction signals from the biological target by one order of magnitude, except for the valleys in the ring patterns (Fig. 2(d)).

The conventional PR from the diffraction pattern of the cell-CG model (Fig. 2(b)) does not converge to interpretable solutions mainly because of the lack of lower frequency information, which corresponds to the overall shape of the sample. In our scheme, the Patterson-search phasing method is adopted to derive the positions of the CG particles from the diffraction pattern, and the positions can be used in iterative PR calculations as an initial phase. Because of the large

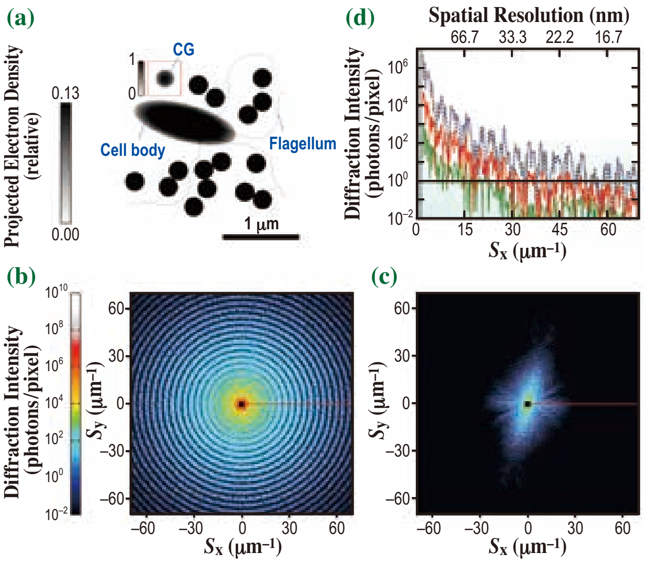

Fig. 2. **(a)** Sample for signal-enhanced XFEL-CDI. **(b)** Diffraction pattern calculated from the whole sample shown in (a). **(c)** Pattern obtained from the bacterial cell including the flagella in (a) alone. Poisson noises are added in (b) and (c). **(d)** Intensity profiles without noises along red horizontal lines in (b) and (c) calculated from the individual components: whole sample, blue solid line; bacterial cell, green solid line; CG particles, yellow dotted line; and magnitude of the interference term, red solid line. The missing region at the center is gray.

contribution from the CG particles (Fig. 2(d)), the initial phase approximates well that of the whole sample, and this leads to reliable reconstruction of the whole sample. This strategy is similar to the heavy atom method used for phasing in X-ray crystallography [5], but the CG particles are more powerful as the scattering from CG is much stronger.

In our calculations, the CG particles yielded clear peaks in a sharpened Patterson map (Fig. 3(a); see also Methods in [2]). Every peak represents the relative position (cross vector) between two gold particles. Then the absolute positions of the CG particles were determined by the Patterson superposition method [5] (Fig. 3(b)). By treating the positions of CG particles as a constraint, we reconstructed a projected electron density map of the CG particles through the PR calculation. Finally, we successfully obtained the map of the whole sample from the initial phase derived from the map of the CG particles (Fig. 3(c)). The reconstruction clearly reveals electron densities corresponding to the cell body and the four flagella, even though the projected electron density of a single flagellum is only 1.1% of that of the CG. In contrast, a map of the biological target reconstructed from the diffraction pattern of the cell alone is somewhat blurred, and the flagella are not correctly resolved (Fig. 3(d)). The spatial resolution of the map of the cell-CG model is estimated to be ~13 nm by Fourier ring correlation analysis, whereas the resolution of the cell-alone model is limited to ~29 nm. Thus, the method described here can improve the spatial resolution more than twofold under the current experimental setup.

As CG is a nonreactive material, this approach is compatible with imaging biological objects under physiological conditions. Flash-cooling of samples can maintain hydrated states and the integrity of cellular and subcellular structures. Thus, the combination of cryo-CXDI [3] and the signal enhancement with CG is well suited for imaging of biological structures. On the basis of the calculations reported here, cryo-XFEL-CDI with CG particles is presently under way, aimed at higher resolution and reliable structure analysis of complex biological targets [4].

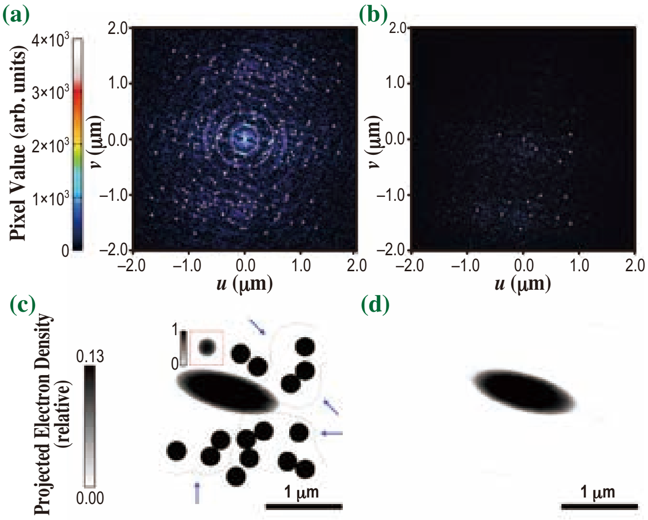

Fig. 3. **(a)** Sharpened Patterson map calculated from the diffraction pattern in Fig. 2(b). **(b)** Superposition minimum function map derived from panel (a) by Patterson search. Clear peaks are found at the positions of the CG particles. **(c)** Projected electron density map of the whole sample reconstructed from the pattern in Fig. 2(b) with the initial phases. **(d)** Map of the bacterial cell alone reconstructed from the pattern in Fig. 2(c).

Yuki Takayama and Koji Yonekura*

RIKEN SPring-8 Center

*E-mail: yone@spring8.or.jp

References

[1] J. Miao *et al.*: Science **348** (2015) 530.
[2] *Y. Takayama, S. Maki-Yonekura, T. Oroguchi, M. Nakasako and K. Yonekura: Sci. Rep.* ***5*** *(2015) 8074.*
[3] M. Nakasako *et al.*: Rev. Sci. Instrum. **84** (2013) 093705.
[4] Y. Takayama and K. Yonekura: Acta Crystallogr. A **72** (2016) 179.
[5] G.M. Sheldrick: Methods in Enzymol. **276** (1997) 628.

Time-resolved hard X-ray photoelectron spectroscopy using SACLA: Investigation of space-charge effects induced with optical pump and X-ray probe pulses

Hard X-ray photoelectron spectroscopy (HAXPES) is well known as a powerful method to study the bulk electronic structure of condensed matter owing to its intrinsic advantages, e.g., element and atomic-site specificity and its large probing depth. In order to extend its capability for investigating the transient electronic states excited in the bulk material, we have established a time-resolved HAXPES (trHAXPES) technique and successfully demonstrated its feasibility at the X-ray free-electron laser (XFEL) facility SACLA [1-3]. In general, time-resolved PES (trPES) is achieved by a pump-probe method, i.e., a target material is photoexcited by an intense pump pulse and the temporal evolution of the transient electronic structure is subsequently probed by a second ultrashort photon pulse.

The use of ultrashort pump and probe pulses with high peak intensities implies a fundamental limitation for trPES: vacuum space-charge effects. Whenever the absorption of a photon pulse leads to the emission of more than one electron into the vacuum, the mutual Coulomb repulsion between the photoelectrons on their passage to the spectrometer may result in distortions of the detected photoelectron spectra, i.e., shifts in the initial kinetic energy and spectral broadenings [4]. Such distortions are essentially unavoidable in pump-probe type PES at high photon energies due to the notoriously low photoionization cross sections and the low repetition rates of the ultrashort-pulsed hard X-ray FEL sources currently available. However, we have found that space-charge effects can be easily moderated by adjusting the experimental conditions. In order to understand the probe and pump pulse-induced space-charge effects, we have carried out systematic studies using the micro-focused and non-focused XFEL beam from SACLA.

In the left panel of Fig. 1, we show typical Ti 1*s* core-level photoemission spectra of $SrTiO_3$, as a function of pulse energy, excited by the micro-focused 8 keV XFEL beam [1]. As can be seen in the figure, the Ti 1*s* HAXPES spectra show drastic spectral changes due to strong space-charge effects with increasing pulse energy. This can be qualitatively understood by N-body numerical simulations [4] shown in the right panel of Fig. 1. Although the peak position of the spectrum simulated for the highest pulse energy (red open triangles) shows a deviation from the measured one, the tendency of the spectral evolution as a function of the pulse energy is explained fairly well. The deviation between measurement and simulation may be attributed to deviations and uncertainties of the used parameters, in particular in the diameter of the XFEL beam. The sharpest spectrum (black curve) at the lowest pulse energy demonstrates that HAXPES using the micro-focused XFEL beam is almost close to being practical because the acquisition time of the spectrum is approximately 40 min at a repetition rate of only 30 Hz.

We have also studied pump pulse-induced space-charge effects, as shown in Fig. 2, by conducting a real pump-probe trHAXPES measurement at a fixed pump-probe delay of –80 ps (probe pulse before pump pulse). A $SrTiO_3$ and a VO_2 sample were excited with optical pump pulses of two different photon energies ($h\nu$ = 1.55 eV and 3.10 eV) with pulse energies in the range of 40-550 μJ corresponding to incident fluences of about 1.6-22.5 mJ/cm^2 (beam diameter ~700 μm), whereas the average XFEL pulse energy was set to about 0.9 μJ/pulse to minimize the space-charge effects induced with the probe pulse. Such strong optical excitation generally leads to the nonlinear emission of a dense disk-like cloud of “slow” photoelectrons, with up to 1.3×10^6 particles in the present case [2], that will interact with the “fast” photoelectron cloud emitted by the non-focused XFEL probe pulse with a spot diameter of approximately 700 μm. Figure 2 demonstrates that the “fast” photoelectron cloud is continuously broadened and shifted toward higher kinetic energies when the pump pulse energy is increased. Energy shifts up to 2 eV are observed. The energy shift induced by space charge is expected to be proportional to the number of pump electrons. This number, however, will depend nonlinearly on the absorbed pump pulse energy because two or more photons have to be absorbed simultaneously for the emission of a photoelectron, i.e.,

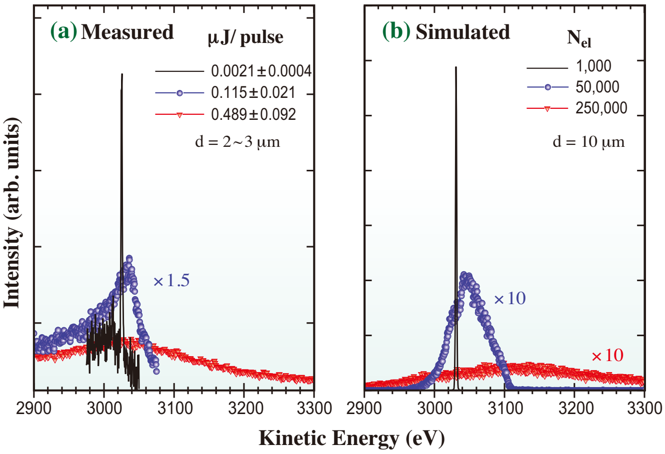

Fig. 1. Measured **(a)** and simulated **(b)** Ti 1*s* HAXPES spectra of $SrTiO_3$ as a function of the micro-focused XFEL pulse energy. N_{el} : Number of electrons in the cloud.

nonlinear multi-photon electron emission has to take place, when the pump photon energy (hν = 1.55 eV and 3.10 eV) is lower than the work function of the target material, e.g., 4.0 ± 0.2 eV for $SrTiO_3$. We have found that the power law dependencies of the pump laser-induced energy shift on the pump pulse energy can be interpreted by regarding the close relationship between the multiphoton electron emission induced by intense pump pulses and the work functions of target materials. Details are described in Ref. 2.

As a first major step to apply trHAXPES to the study of intrinsic material dynamics, we have carried out systematic studies of time-dependent pump laser-induced space-charge effects on core-level photoelectron spectra at SACLA [2,3]. The experimental results of the trHAXPES measurements are plotted in the left panel of Fig. 3 together with the best fits using Voigt profiles. The zero of the horizontal axis is defined by the position of the Ti 1*s* photoemission peak at a blocked pump beam. When pump and probe pulses overlap in time (at zero delay), the maximum spectral shift and broadening are observed. In the right panel of Fig. 3, the extracted time dependence of the Ti 1*s* spectral shift is shown together with the calculations which are obtained from a series of simple mean-field models [2]. In the simplest form of the model, the radial and longitudinal broadening of the charged disk are neglected ('1D model'). In two successive extensions of the model, the radial expansion of the disk is taken into account ('2D model') and the kinetic energy spread of the pump electrons is further incorporated ('Ext. 2D model'). We found that the more realistic model, i.e., extended 2D model, explains the experimental results fairly well. Furthermore, we also found that the sharp peaking of the spectral shift that occurs when pump and probe pulses overlap in time can be used to determine the experimental time zero with a precision of better than ±10 ps.

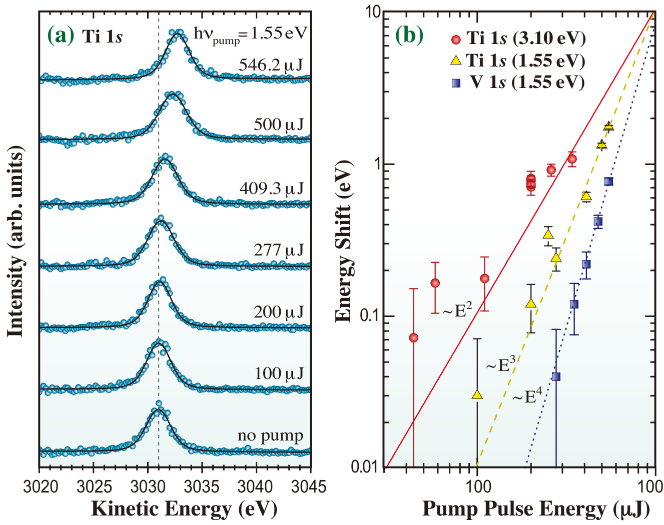

Fig. 2. **(a)** Evolution of Ti 1*s* HAXPES spectra of $SrTiO_3$ as a function of the pump pulse energy. The vertical dashed-line indicates the peak position for a blocked pump beam. **(b)** Spectral shifts of Ti 1*s* emission from $SrTiO_3$ and V 1*s* emission from VO_2 as a function of the pump pulse energy in a log-log plot. The red-filled circles, yellow-filled triangles, and blue-filled squares are experimental data from different experimental runs. The lines indicate fits to the experimental results with the assumption of power law dependences on the pump pulse energy.

As we have shown here, our systematic experimental investigation of space-charge effects in trHAXPES, along with N-body numerical simulations and simple analytic models, has laid the basis for a novel sub-picosecond time-resolved solid-state spectroscopy technique. This technique will become fully practical as soon as the repetition rates of XFELs enter the kHz range.

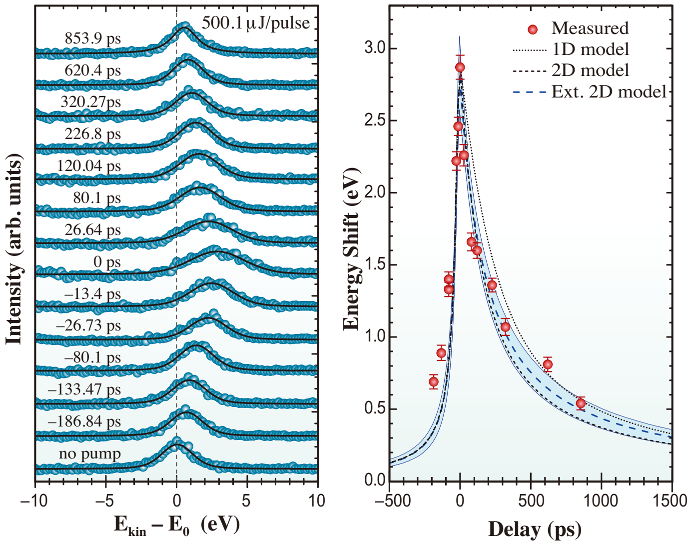

Fig. 3. **(a)** Temporal evolution of Ti 1*s* HAXPES spectra of $SrTiO_3$ as a function of pump-probe delay. The vertical dashed-line shows the peak position for a blocked pump beam (E_0=3030.97±0.3 eV). **(b)** Spectral shift of Ti 1*s* emission as a function of pump-probe delay. The red-filled circles are experimental data. The lines are from different analytic models. For the "extended 2D model", 68.3% confidence bands are also indicated.

Lars-Philip Oloff[a,b], Kai Rossnagel[a,b] and Masaki Oura[b,*]

[a] Institute for Experimental and Applied Physics,
University of Kiel
[b] RIKEN SPring-8 Center

*E-mail: oura@spring8.or.jp

References

[1] *M.Oura, L.-P. Oloff, K. Rossnagel, A. Chainani, and M. Matsunami: J. JSSRR* ***29*** *(2016) 14. (in Japanese)*
[2] *L.-P. Oloff, M. Oura, K. Rossnagel, A. Chainani, M. Matsunami, R. Eguchi, T. Kiss, Y. Nakatani, T. Yamaguchi, J. Miyawaki, M. Taguchi, K. Yamagami, T. Togashi, T. Katayama, K. Ogawa, M. Yabashi, and T. Ishikawa: New J. Phys.* ***16*** *(2014) 123045.*
[3] M. Oura *et al.*: Trans. Mat. Res. Soc. Jpn. **39** (2014) 469.
[4] S. Hellmann *et al.*: Phys. Rev. B **79** (2009) 035402.

FACILITY STATUS

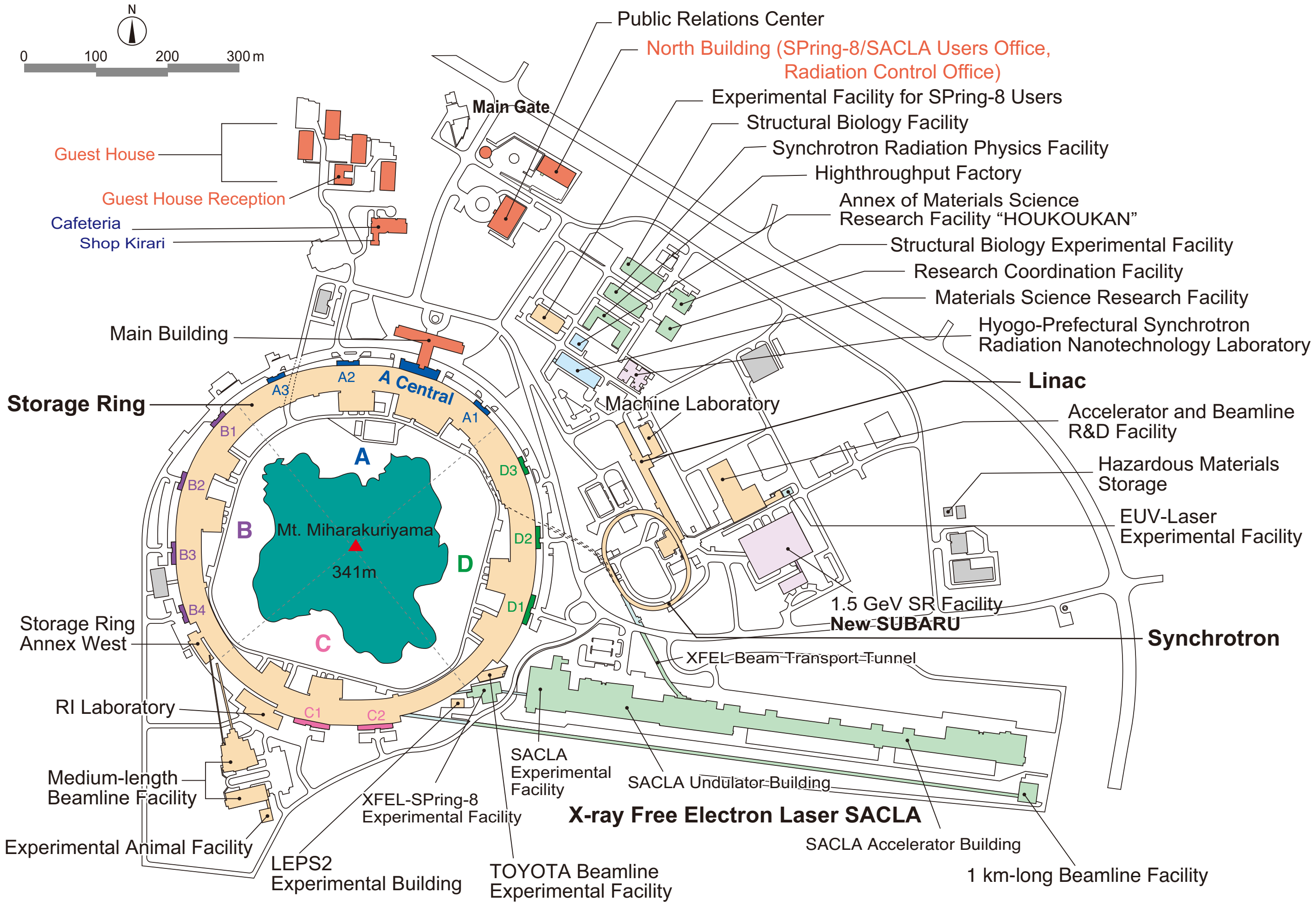

SPring-8

I. Introduction

As of December 2015, the cumulative number of users who visited SPring-8 for their experiments since 1997 was as high as 200,000, showing that SPring-8 has been reliably and continuously contributing to the SR community as a center of advanced photon science. Indeed, as reported in the next section in detail, SPring-8 was stably operated throughout 2015 with the total operation time of the storage ring and the total user beam time of 4805.8 h and 4033.9 h, respectively, with the total down time of 16.8 h. Because of the major renovation of an extra-high-tension power source starting from the end of December 2015 up to the end of March 2016, SPring-8 had to complete all its operations by the middle of December 2015, making the machine schedule quite tight and, thus, challenging.

Regarding its research proposal system, SPring-8 introduced a novel category of proposals for the public beamlines, called Epoch-Making Initiatives Projects, which entails the creation and development of unexplored fields in combined and interdisciplinary research beyond the boundaries of traditional fields and the broadening of the basis for using SPring-8. Concerning the contract beamlines, JAEA Quantum Dynamics (BL11XU), JAEA Materials Science (BL14B1), JAEA Quantum Structural Science (BL22XU), JAEA Actinide Science (BL23SU), Catalytic Reaction Dynamics for Fuel Cell (BL36XU, The University of Electro-Communication), and Hyogo ID (BL24XU, Hyogo Prefecture), have undergone the interim review process for the year 2015 and all their proposals have been approved for continuation.

At the time of writing this report, SPring-8 users number as many as 11,000, all of whom are respected members of the SPring-8 User Community (SPRUC). It is, hence, important for SPring-8 to jointly organize scientific events with SPRUC, such as the SPring-8 Symposium and The Joint Conference on Industrial Applications of SPring-8, to facilitate dialogue between them. In 2015, the SPring-8 Symposium was held on September 13–14, 2015, at Kyushu University with a participant number of 259, and The Joint Conference on Industrial Applications of SPring-8 held on September 3–4, 2015, Kawasaki, had 296 participants. As part of its continuous effort towards the fostering of human resources, SPring-8 organized the 15th SPring-8 Summer School with 66 students of graduate schools nationwide, on cooperation with Hyogo University, Kwansei Gakuin University, the University of Tokyo, Okayama University, and Japan Atomic Energy Agency.

By hosting those delegations from APS, ESRF, and DESY, SPring-8 organized the 15th Three-Way Meeting from February 26, 2015, and lasting three days, to reconsider the raison d'etre of this meeting that has continued for more than twenty years. This latest meeting reconfirmed its significance, and it was decided to hold the next one at DESY in the early autumn of 2016. As in the past years, SPring-8 contributed to the synchrotron radiation community of the Asia-Oceania region by organizing the Cheiron School for young scientists/engineers from this region for the period of September 10–19, 2015. There were 60 participants who joined the school for the year. As an annual event, SPring-8 held its 23rd Open House on Sunday, April 26, 2015, to communicate with the local community. The total number of visitors was 5,634, which provided an excellent opportunity to win public understanding of the highly advanced photon science realized at SPring-8 and SACLA.

The 15th Three-Way Meeting

II. Machine Operation

The operation statistics for the last five fiscal years are shown in Fig. 1. In FY2015, the total operation time of the accelerator complex was 4817.9 h. The operation time of the storage ring was 4804.8 h, 84.0% of which (4033.9 h) was for SR experiments. This excellent figure of user time represents a storage ring availability of 99.45%, which ranks with the best record of 99.46% established last year. The downtime resulting from failure accounted for 0.45% (16.8 h) of the total user time, and no loss of user time exceeding several hours occurred. The intensity of the light source, i.e., the stored current, is kept extremely stable owing to the top-up operation, in which the current is filled up at any time on demand. The dead band of the stored current in the top-up operation is routinely 0.03 mA (0.03%) and the current stayed within 0.1% in 99.5% of the user time in FY2015, which also beats the all-time record of 99.2% in FY2012.

The variety of operation modes is one of the characteristics of SPring-8. The operation modes are grouped into the multibunch mode, several-bunch mode, and hybrid-filling mode. There has been no user operation with the multibunch mode since FY2011. The several-bunch mode consists of equally spaced bunches or bunch trains, i.e., 203 bunches, or 29 trains of 11 bunches, and the hybrid-filling mode is composed of a long bunch train and isolated single bunches, as shown in Table 1, where the share of each operation mode is also shown. An isolated bunch impurity is routinely maintained less than 10^{-8} in the top-up operation by bunch cleaning in the booster. The bunch current is also kept constant within a 1% band by the top-up operation. Table 2 summarizes the beam parameters of the storage ring.

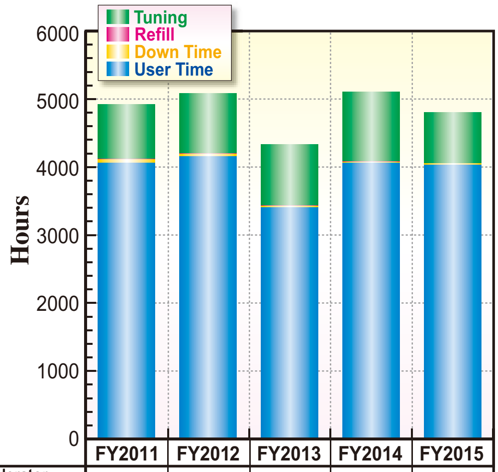

	FY2011	FY2012	FY2013	FY2014	FY2015
Accelerator Operation Time	4918.6	5078.8	4330.0	5099.3	4817.9
Storage Ring Operation Time	4904.2	5063.1	4265.5	5080.7	4804.8
Tuning & Study (Acc. & BL)	803.0	884.0	898.0	1024.7	748.8
Refill	4.4	5.2	3.5	5.1	5.3
Down Time	57.0	39.2	20.0	17.1	16.8
Mean Time Between Failures	117.7	107.7	213.0	163.2	202.8
Achieved User Time	4058.5	4155.6	3408.5	4057.8	4033.9
Planning User Time	4120.0	4200.0	3432.0	4080.0	4056.0
Availability (%)	98.5	98.9	99.3	99.5	99.5

Fig. 1. Operation statistics for most recent five fiscal years.

Table 1. Operation modes in FY2015

	Single bunch current (mA)	Share of operation time (%)
203 bunches		21.3
4 bunch-train × 84		0.0
11 bunch-train × 29		35.5
1/7-filling + 5 single bunches	3	8.9
2/29-filling + 26 single bunches	1.4	6.5
1/14-filling + 12 single bunches	1.6	11.2
4/58-filling + 53 single bunches	1	0.0
11/29-filling + 1 single bunch	5	16.6

Table 2. Beam parameters of the SPring-8 storage ring

Energy [GeV]	8
Number of buckets	2436
Tunes (ν_x / ν_y)	41.14 / 19.34
Current [mA]:	
single-bunch	12
multi-bunch	100
Bunch length (σ) [psec]	13
Horizontal emittance [nm·rad]	2.4 *
Vertical emittance [pm·rad]	4.8 *
Coupling [%]	0.2
RF Voltage [MV]	14.4 ** ~ 16
Momentum acceptance [%]	3.2 (~256 MeV)
Beam size (σ_x / σ_y)* [μm]	
Long ID section	333 / 7
ID section	316 / 5
BM1 section	94 / 12
BM2 section	100 / 12
Beam divergence (σ_x' / σ_y')* [μrad]	
Long ID section	8 / 0.7
ID section	9 / 1.0
BM1 section	58 / 0.5
BM2 section	68 / 0.5
Operational chromaticities (ξ_x / ξ_y)	+2 / +2 ***
Lifetime [h]:	
100 mA (multi-bunch)	~ 250
1 mA (single-bunch)	~ 30
Horizontal dispersion [m]:	
Long ID section	0.153
ID section	0.146
BM1 section	0.039
BM2 section	0.059
Fast orbit stability (0.1 – 200 Hz) [μm]:	
horizontal (rms)	~ 4
vertical (rms)	~ 1

* Assuming 0.2% coupling
** Power saving mode
*** With bunch-by-bunch feedback

III. Beamlines

The SPring-8 storage ring can accommodate up to 62 beamlines: 34 insertion devices, 4 long undulators, and 24 bending magnets. At the time of writing, 56 beamlines were in operation, covering a wide variety of research fields involving synchrotron radiation science and technology. The beamlines are classified into the following four types.

(1) Public Beamlines
(2) Contract Beamlines
(3) RIKEN Beamlines
(4) Accelerator Diagnostics Beamlines

There are now 26 public beamlines in full operation. The beamlines that are proposed and constructed by external organizations, such as universities, research institutes, and private companies, are called contract beamlines and are exclusively used by the contractors for their own research purposes. At present, 19 contract beamlines are in operation. The contract beamlines include the NSRRC BM (BL12B2) and NSRRC ID (BL12XU) beamlines, which were constructed by the National Synchrotron Radiation Research Center of Taiwan. The beamlines constructed by RIKEN are called RIKEN beamlines, and are mainly used for RIKEN's own research activities, with partial availability for public use. RIKEN is now operating 9 beamlines and is reconstructing one beamline. In addition, two accelerator diagnostics beamlines are in operation (BL05SS accelerator diagnostics beamline is also partly available for public use).

To illustrate the beamline portfolio of SPring-8, a beamline map is shown in Fig. 2 together with the beamline classification. The research fields of each beamline are presented in Table 3.

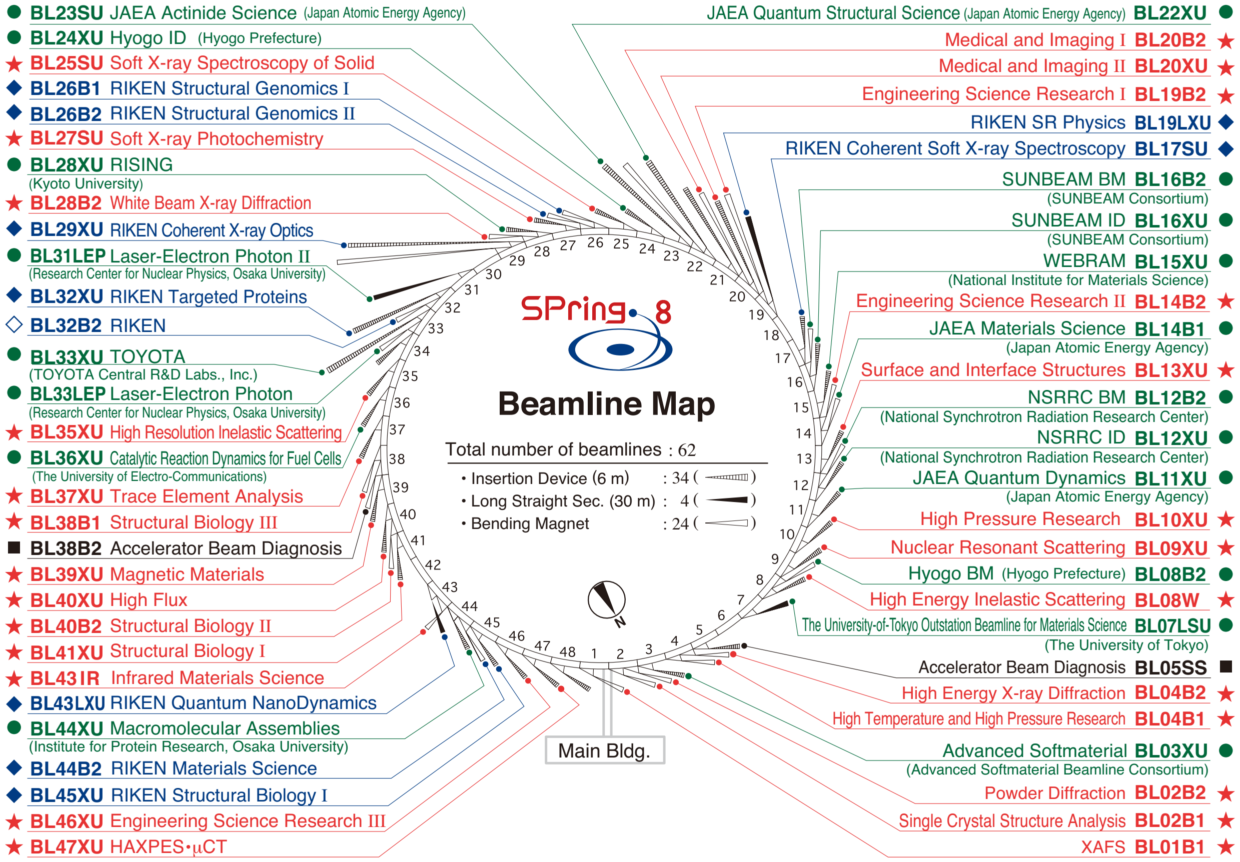

BL: Beamline
B1, B2: Bending Magnets
XU: X-ray Undulator
SU: Soft X-ray Undulator
W: Wiggler

IR: Infrared Radiation
LEP: Laser-Electron Photon
LXU: Long-length X-ray Undulator
LSU: Long-length Soft X-ray Undulator
SS: Straight Section

WEBRAM: Wide Energy Range Beamline for Research in Advanced Materials
NSRRC: National Synchrotron Radiation Research Center, Taiwan
RISING: Research & Development Initiative for Scientific Innovation of New Generation Batteries

★ : Public Beamlines
● : Contract Beamlines
◆ : RIKEN Beamlines
■ : Accelerator Diagnostics Beamlines

◇ : Planned or Under Construction

Fig. 2. Beamline map.

Table 3. List of beamlines

BL #	Beamline Name	(Public Use) or (First Beam)	Areas of Research
	★ Public Beamlines		
BL01B1	**XAFS**	(Oct. 1997)	XAFS in wide energy region (3.8 to 113 keV). XAFS of dilute systems and thin films. Quick XAFS with a time resolution of seconds to tens of seconds.
BL02B1	**Single Crystal Structure Analysis**	(Oct. 1997)	Charge density study and crystal structure analysis from accurate single crystal diffraction measurements. (X-ray energy range: 8 – 115 keV)
BL02B2	**Powder Diffraction**	(Sept. 1999)	Charge density study and phase identification of crystalline materials from accurate powder diffraction measurements. (X-ray energy range: 12.4 – 35 keV)
BL04B1	**High Temperature and High Pressure Research**	(Oct. 1997)	High temperature and high pressure research with the multi-anvil press by powder X-ray diffraction, radiography and ultrasonic measurement.
BL04B2	**High Energy X-ray Diffraction**	(Sept. 1999)	Pair distribution analysis for glass, liquid, and amorphous materials. High-energy X-ray total scattering. Containerless levitation.
BL08W	**High Energy Inelastic Scattering**	(Oct. 1997)	Magnetic Compton scattering. High-resolution Compton scattering. High-energy Bragg scattering. High-energy fluorescent X-ray analysis.
BL09XU	**Nuclear Resonant Scattering**	(Oct. 1997)	Lattice dynamics using nuclear inelastic scattering. Mössbauer spectroscopy, especially for the surface/interface study and under the extreme conditions. Hard X-ray photoelectron spectroscopy (HAXPES). Depth analysis of HAXPES with high flux and energy resolution.
BL10XU	**High Pressure Research**	(Oct. 1997)	Structure analysis and phase transitions under ultra high pressure (DAC experiment). Earth and planetary science.
BL13XU	**Surface and Interface Structures**	(Sept. 2001)	Atomic-scale structural analysis of surfaces and interfaces of crystalline materials, ultra-thin films, and nanostructures. Surface X-ray diffraction (SXRD). Microbeam diffraction.
BL14B2	**Engineering Science Research II**	(Sept. 2007)	XAFS in wide energy region (3.8 to 72 keV). XAFS of dilute systems and thin films.
BL19B2	**Engineering Science Research I**	(Nov. 2001)	Residual stress measurement. Structural analysis of thin film, surface, interface. Powder diffraction. X-ray imaging, X-ray topography. Ultra-small angle X-ray scattering.
BL20XU	**Medical and Imaging II**	(Sept. 2001)	Microimaging. Hard X-ray microbeam/scanning microscopy, imaging microscopy, microtomography, phase-contrast microtomography with Bonse-Hart interferometer, X-ray holography, coherent X-ray optics, and other experiments on X-ray optics and developments of optical elements. Medical application. Microangiography, refraction-enhanced imaging, phase-contrast CT using interferometer. Ultra-small angle scattering.
BL20B2	**Medical and Imaging I**	(Sept. 1999)	Microimaging: microtomography, phase-contrast microtomography with grating interferometer for biological specimen and other kinds of specimen. Evaluation and development of various kinds of optical elements for novel imaging techniques. Large field X-ray topography.
BL25SU	**Soft X-ray Spectroscopy of Solid**	(Apr. 1998)	Study of electronic state of solids by soft X-ray photoemission spectroscopy (PES) including angle-resolved PES (ARPES). Atomic arrangement analysis of surfaces by photoelectron diffraction (PED) technique using two-dimensional photoemission analyzer. Magnetic state analysis by magnetic circular dichroism (MCD) of soft X-ray absorption and its element-specific magnetization curve measurements. Chemical and magnetic imaging by soft X-ray scanning microscopy and photoelectron emission microscopy (PEEM).
BL27SU	**Soft X-ray Photochemistry**	(May 1998)	Ambient atmospheric pressure soft X-ray photoabsorption spectroscopy. Chemical state analysis of light elements in dilute samples (NEXAFS). Elemental and chemical mapping using micro soft X-ray beam. Soft X-ray emission spectroscopy for solids.
BL28B2	**White Beam X-ray Diffraction**	(Sept. 1999)	White X-ray diffraction and topography. Time-resolved energy-dispersive XAFS (DXAFS) for studies of chemical and/or physical reaction process. Biomedical imaging and radiation biology studies.
BL35XU	**High Resolution Inelastic Scattering**	(Sept. 2001)	Materials dynamics on ~meV energy scales using inelastic X-ray scattering (IXS).
BL37XU	**Trace Element Analysis**	(Nov. 2002)	X-ray microbeam spectrochemical analysis. Ultra trace element analysis. High energy X-ray fluorescence analysis.
BL38B1	**Structural Biology III**	(Oct. 2000)	Structural biology. Macromolecular crystallography. Automatic data collection.
BL39XU	**Magnetic Materials**	(Oct. 1997)	X-ray magnetic circular dichroism (XMCD) spectroscopy and element-specific magnetometry under multiple-extreme conditions. XMCD/XAS using a sub-micron X-ray beam. X-ray emission spectroscopy. Resonant X-ray magnetic scattering.
BL40XU	**High Flux**	(Apr. 2000)	Time-resolved diffraction and scattering experiments. Microbeam X-ray diffraction and scattering experiments. X-ray photon correlation spectroscopy. Fluorescence analysis. Quick XAFS. Submicrometer-scale single crystal structure analysis with high flux and zone plate focused X-ray beam. Single shot imaging with X-ray choppers. Laser pump-X-ray probe experiment.
BL40B2	**Structural Biology II**	(Sept. 1999)	Noncrystalline small and wide angle X-ray scattering.
BL41XU	**Structural Biology I**	(Oct. 1997)	Structural biology. Macromolecular crystallography. Microcrystallography. High resolution data collection.
BL43IR	**Infrared Materials Science**	(Apr. 2000)	Infrared microspectroscopy.
BL46XU	**Engineering Science Research III**	(Nov. 2000)	Structural characterization of thin films by X-ray diffraction and X-ray reflectivity measurement. Residual stress measurement. Time resolved X-ray diffraction measurement. Hard X-ray photoemission spectroscopy.
BL47XU	**HAXPES · μCT**	(Oct. 1997)	Hard X-ray photoelectron spectroscopy (HAXPES). Depth analysis of angle resolved HAXPES with wide acceptance lens. Projection type microtomography. Imaging type microtomography. Hard X-ray microbeam/scanning microscopy.

BL #	Beamline Name	(Public Use) or (First Beam)	Areas of Research
			● Contract Beamlines
BL03XU	**Advanced Softmaterial** (Advanced Softmaterial Beamline Consortium)	(Nov. 2009)	Structural characterization of softmaterials using small- and wide-angle X-ray scattering. Grazing-incidence small- and wide-angle X-ray scattering for thin films. X-ray diffraction and reflectivity measurements for softmaterials.
BL07LSU	**The University-of-Tokyo Outstation Beamline for Materials Science** (The University of Tokyo)	(Oct. 2009)	Time-resolved soft X-ray spectroscopy, nano-beam photoemission spectroscopy, ultra high-resolution soft X-ray emission spectroscopy, and any methods requiring the highly brilliant soft X-ray beam.
BL08B2	**Hyogo BM** (Hyogo Prefecture)	(Jun. 2005)	XAFS in a wide energy region. Small angle X-ray scattering for structural analyses of polymer and nanocomposite materials. X-ray topography. Imaging. Powder diffraction with a high angular-resolution.
BL11XU	**JAEA Quantum Dynamics**	(Oct. 1998)	Nuclear scattering. Surface and interface structure analysis with MBE. Inelastic X-ray scattering. XAFS.
BL12B2	**NSRRC BM** (National Synchrotron Rad. Res. Center)	(Oct. 2000)	X-ray absorption spectroscopy. Powder X-ray diffraction. High resolution X-ray scattering. Protein crystallography.
BL12XU	**NSRRC ID** (National Synchrotron Rad. Res. Center)	(Dec. 2001)	High resolution non-resonant or resonant inelastic X-ray scattering. High resolution near-edge X-ray Raman scattering. Phase transitions under high-pressure, low and high temperatures. High-resolution X-ray absorption and emission spectroscopy. X-ray physics and optics.
BL14B1	**JAEA Materials Science**	(Dec. 1997)	Materials science under high-temperature and high-pressure. *In situ* study on catalysis using dispersive XAFS. X-ray diffraction for structure physics.
BL15XU	**WEBRAM** (National Institute for Materials Science)	(Jan. 2000)	Hard X-ray photoelectron spectroscopy. High-precision X-ray powder diffraction.
BL16B2	**SUNBEAM BM** (SUNBEAM Consortium)	(Oct. 1998)	Characterization of secondary battery related materials, semiconductors, fuel cells, catalysts, and several industrial materials using X-ray absorption fine structure measurements, X-ray diffraction (including X-ray reflectivity technique) and X-ray topography.
BL16XU	**SUNBEAM ID** (SUNBEAM Consortium)	(Oct. 1998)	Characterization of secondary battery related materials, semiconductors, fuel cells, catalysts, and structural materials using X-ray diffraction, X-ray microbeam based evaluation techniques (including X-ray magnetic circular dichroism), hard X-ray photoemission spectroscopy and fluorescence X-ray analysis.
BL22XU	**JAEA Quantum Structural Science**	(May 2002)	Materials science under high-pressure. Resonant X-ray scattering. Speckle scattering. Residual stress/strain distribution analysis.
BL23SU	**JAEA Actinide Science**	(Feb. 1998)	Surface chemistry with supersonic molecular beam. Biophysical spectroscopy. Photoelectron spectroscopy. Magnetic circular dichroism.
BL24XU	**Hyogo ID** (Hyogo Prefecture)	(May. 1998)	Surface/interface analysis for industry by fluorescent X-ray analysis, strain measurements and grazing incidence X-ray diffraction. Microbeam formation studies for materials and life sciences. Micro-SAXS for local long-range structure analysis.
BL28XU	**RISING** (Kyoto University) RISING: Research & Development Initiative for Scientific Innovation of New Generation Batteries	(Apr. 2012)	Analysis of rechargeable batteries. X-ray diffraction spectroscopy. Time-resolved X-ray diffraction and XAFS. Hard X-ray photoelectron spectroscopy.
BL31LEP	**Laser-Electron Photon II** (RCNP, Osaka University)	(Oct. 2013)	Production of high intensity GeV photon beam by laser-backward Compton scattering. Hadron physics via photonucleon and photonuclear reactions. Test and calibration of detectors with GeV gamma-ray and converted electrons/positrons.
BL33LEP	**Laser-Electron Photon** (RCNP, Osaka University)	(Jun. 1999)	Meson photoproduction from nucleon and nucleus. Photoexcitation of hyperons, nucleon resonances, and other exotic states. Photonuclear reactions. Beam diagnoses. Test and calibration of detectors with GeV photon beam.
BL33XU	**TOYOTA** (TOYOTA Central R&D Labs., Inc.)	(Apr. 2009)	Time-resolved XAFS. Characterization of industrial materials, such as catalysts, secondary batteries, fuel cells.
BL36XU	**Catalytic Reaction Dynamics for Fuel Cells** (The University of Electro-Communications)	(Jan.2013)	Real time analysis of catalytic reaction dynamics for fuel cells: time resolved XAFS and X-ray diffraction, 2D scanning microscopic XAFS, 3D computed tomography/laminography XAFS, ambient pressure hard X-ray photoelectron spectroscopy.
BL44XU	**Macromolecular Assemblies** (IPR, Osaka University)	(May 1999)	Crystal structure analysis of biological macromolecular assemblies (e.g., membrane protein complexes, protein complexes, protein-nucleic acid complexes, and viruses).
			◆ RIKEN Beamlines
BL17SU	**RIKEN Coherent Soft X-ray Spectroscopy**	(Sept. 2003)	High resolution photoemission spectroscopy. Soft X-ray emission spectroscopy for liquid and biological samples. Soft X-ray diffraction spectroscopy. Surface science.
BL19LXU	**RIKEN SR Physics**	(Oct. 2000)	SR science with highly brilliant X-ray beam.
BL26B1	**RIKEN Structural Genomics I**	(Apr. 2002)	Structural genomics research based on single crystal X-ray diffraction.
BL26B2	**RIKEN Structural Genomics II**	(Apr. 2002)	Structural genomics research based on single crystal X-ray diffraction.
BL29XU	**RIKEN Coherent X-ray Optics**	(Dec. 1998)	X-ray optics, especially coherent X-ray optics.
BL32XU	**RIKEN Targeted Proteins**	(Oct. 2009)	Protein microcrystallography.
BL43LXU	**RIKEN Quantum NanoDynamics**	(Oct. 2011)	High resolution inelastic X-ray scattering for investigating atomic and electronic dynamics.
BL44B2	**RIKEN Materials Science**	(Feb. 1998)	Structural materials science research using powder X-ray diffraction.
BL45XU	**RIKEN Structural Biology I**	(Jul. 1997)	Time-resolved and static structures of non-crystalline biological materials using small-angle scattering and diffraction techniques.
			■ Accelerator Diagnostics Beamlines
BL05SS	**Accelerator Beam Diagnosis**	(Mar. 2004)	Accelerator beam diagnostics. R&D of accelerator components. Nano-forensic science.
BL38B2	**Accelerator Beam Diagnosis**	(Sept. 1999)	Accelerator beam diagnostics.

IV. User Program and Statistics

SPring-8 calls for public use proposals twice a year, in principle. The submitted proposals are reviewed by the SPring-8 Proposal Review Committee (SPring-8 PRC). Since 1997, SPring-8 has accepted a variety of proposals. For the promotion of research on industrial applications at SPring-8, the Industrial Application Division was established in 2005. With consultation support for industrial users provided by the division's coordinators, currently, Industrial Application Proposals account for approximately 20% of the total number of proposals conducted at the public beamlines. In addition, the Measurement Service was introduced in 2007B, wherein the personnel of the Industrial Application Division carry out XAFS measurements on behalf of users at BL14B2. SPring-8 also launched a Protein Crystallography Data Collection Service at BL38B1 and Powder X-ray Diffraction Measurement Service at BL19B2 in 2009B, a Hard X-ray Photoemission Spectroscopy (HAXPES) Measurement Service, and a Thin Film Analysis (GIXD/XRR) Measurement Service at BL46XU in 2012B, and a Small Angle Scattering (SAXS) Measurement Service at BL19B2 in 2014B.

In FY2015, JASRI established the Social Interest Proposals and the Epoch-Making Initiatives Projects, which are new types of proposals at the public beamlines. The purpose of the former is to support research proposals with themes that attract public interest and meet social requirements, and the latter is to establish and develop unexplored fields in combined and interdisciplinary research beyond the boundaries of traditional fields and to broaden the basis for using SPring-8.

In FY2015, JASRI has also improved the beamtime allocation system for research proposals in the field of Life Science(L1)/Protein Crystal Analysis with the use of SPring-8 Public Macromolecular Crystallography Beamlines. These main improvement points are as follows:

(i) The SPring-8 Proposal Review Committee (PRC) will determine only the acceptance or rejection of a proposal and the order of priority.

(ii) The research period for the proposal is one year.

(iii) A questionnaire on the beamtime allocation (the number of shifts, date of use, desired beamline) must be completed by project leaders four times a year.

SPring-8 has consistently provided ~4,000 h of user beamtime per year. Since the start of its operation in 1997, SPring-8 has succeeded in providing users with a total beamtime of 70,797 h. The beamtime available to users, the number of experiments conducted, and the number of user visits at the public and contract beamlines are summarized in Fig. 3. Part of the proposals are for proprietary use, for which refereed reports are not required. More details can be found at ***http://www.spring8.or.jp/en/about_us/spring8data/***.

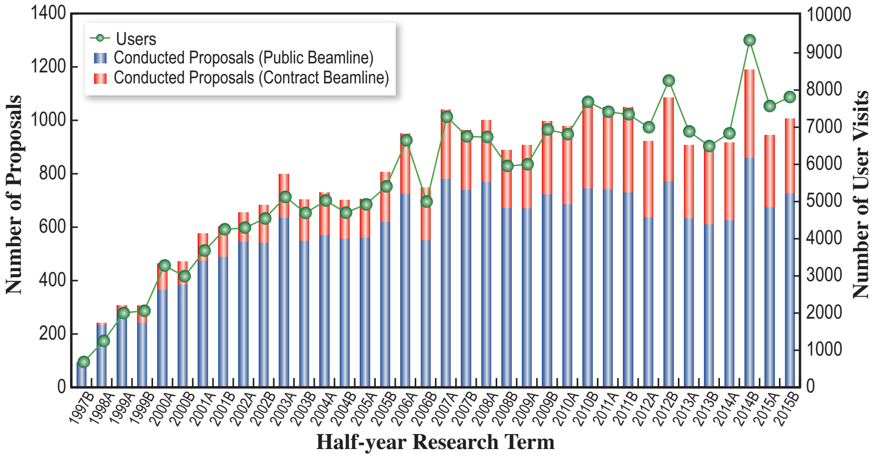

Fig. 3. Numbers of user visits and conducted experiments.

V. Research Outcomes

As of March 2016, the total number of registered refereed papers since the opening of SPring-8 was 11,498, out of which 9,575 papers resulted from the use of public beamlines (including public use at other beamlines), 2,355 papers from that of contract beamlines, 1,151 papers from that of RIKEN beamlines, and 557 papers from hardware/software R&D. The papers resulting from the use of two or more beamlines are counted for each beamline. More details can be found at *http://www.spring8.or.jp/en/about_us/spring8data/* and the publication database is available at *https://user.spring8.or.jp/uisearch/publication2/*.

VI. Budget and Personnel

When SPring-8 started operation in 1997, it was jointly managed by RIKEN, JAERI (now JAEA), and JASRI. However, JAERI withdrew from the management of SPring-8 on September 30, 2005. SPring-8 is currently administered by RIKEN and JASRI in a collaboratively manner.

The total budget for the operation of SPring-8 in FY2015 was 9.259 billion yen. As of October 2015, RIKEN and JASRI have a total of 506 staff members.

VII. Research Complex

The facilities of SPring-8, SACLA, and NewSUBARU form the Center of Excellence (COE) at the SPring-8 campus, where JASRI, public beamline users, the contractors of contract beamlines, RIKEN, and the University of Hyogo work in close cooperation, forming a research complex where each member has their own role in delivering high-quality results in the field of synchrotron radiation science and technology. The organizational charts of RIKEN and JASRI, which are at the center of this research complex, are shown in Fig. 4 and Fig. 5, respectively.

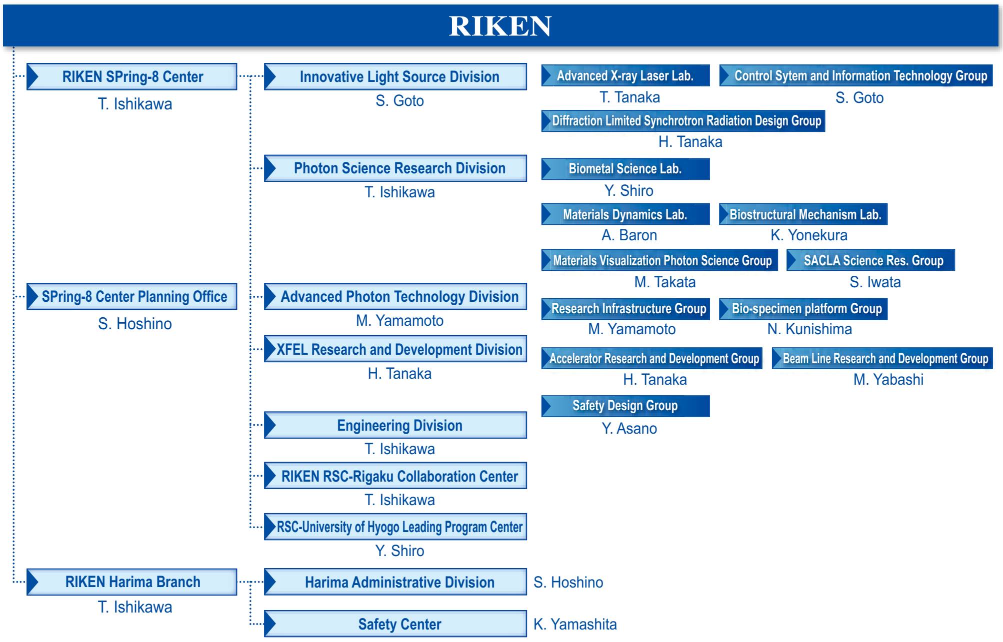

Fig. 4. RIKEN Harima Branch chart as of April 2016.

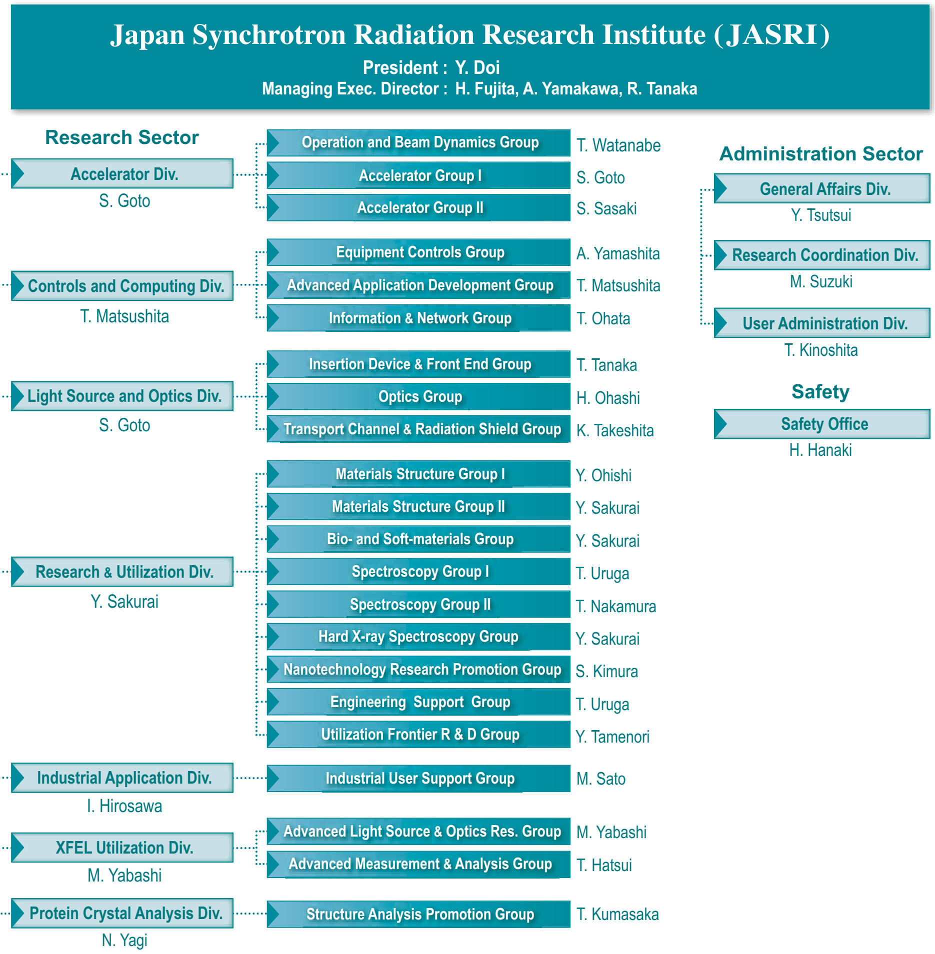

Fig. 5. JASRI chart as of April 2016.

VIII. Users Societies and Other Activities

SPring-8 Users Community (SPRUC)

The SPring-8 Users Community (SPRUC) is a user society that includes not only all users but also potential users who are interested in using SPring-8. In addition to these individuals, representative organizations of about 24 institutes (principal universities, national/international research institutes, industries, beamline consortiums), participate in SPRUC to discuss further promotion of the utilization of SPring-8 from the strategic and perspective viewpoints.

As one of the key activities of SPRUC, the SPring-8 Symposium is held annually at the site of one of the representing organizations jointly with RIKEN and JASRI. SPring-8 Symposium 2015, with the theme "Global Innovation Utilizing Synchrotron Radiation Science-From Global View Point," was held at Kyushu University on September 13 and 14, 2015. SPRUC provides the Young Scientist Award to recognize pioneering achievements in photon science by individual young scientists using SPring-8. The award ceremony and award lecture were held at the SPring-8 Symposium. The SPRUC 2015 Young Scientist Award was conferred to two young scientists (Dr. Kaye Morgan, Monash University and Dr. Satoshi Matsuyama, Osaka University). SPring-8 Symposium 2016 is scheduled to be held on August 29 and 30, at Kwansei Gakuin University.

In accordance with the recommendation by the "WG on Reorganization of SPRUC Research Groups," SPRUC has established "SPRUC multidisciplinary research groups" that work in multidisciplinary research fields in order to promote the use of SPring-8 in the new areas that will be important for future developments in science and technology. This was one of the main activities of SPRUC in 2015. Four multidisciplinary research fields and four program officers, each leading a multidisciplinary research group, were designated following comprehensive advice from the advisors of the SPRUC research groups. For the constant renewal of the system, each multidisciplinary research group works two years and is then expected to organize a new research group. Two multidisciplinary research groups for nanodevice science and application were launched in 2015 through an innovative use of SPring-8 via organic collaboration with JASRI and RIKEN. Two more research groups will start their activities soon. Moreover, research groups were reorganized at the end of March 2016 and new research groups will start from April 2016.

Young Scientist Award
Prof. A. Takahara, Dr. K. Morgan, Dr. S. Matsuyama, and Prof. J. Mizuki

Other Activities

- The 23rd SPring-8 Open House
April 26, 2015 • SPring-8

- The 15th SPring-8 Summer School 2015
July 5 – 8, 2015 • Public Relations Center, SPring-8

- The 9th AOFSRR School - Cheiron School 2015
September 10 – 19, 2015 • Public Relations Center, SPring-8

Cheiron School

Summer School

SACLA

I. Introduction

SACLA is the world's second X-ray free electron laser (XFEL), following the Linac Coherent Light Source (LCLS) in the US. Currently, these are the only two XFELs in operation. SACLA delivers the shortest wavelength XFEL. SACLA achieved its first lasing on June 7, 2011, within three months of electron beam commissioning, and launched user operations from 2012A. Since then, we have operated SACLA in four years with reasonable stability and reliability.

II. Machine Operation & Beamlines

Our fourth year of operations proceeded without any significant issues. Operation statistics are summarized in Table 4. The ratio of downtime to user time was kept below 4%, a reasonably low rate for linac-based light sources.

Table 4. Operation statistics for FY2015

	Time (h)
Total operation time	6483
User time	3924
Facility tuning time	158
Study time	2401
Downtime	154

In 2014, two beamlines, BL3 for XFEL and BL1 for broadband spontaneous light, were open for users, while all experiments were conducted with BL3. As the newest beamline, construction of BL2 was completed during the summer shutdown, and first laser amplification was achieved on October 21. An upgraded beamline for soft X-ray FEL, BL1, which combines the prototype accelerator of SACLA (SCSS), is due to be in operation in 2016. For more details, please refer to SACLA Beam Performance in this volume.

III. User Program and Statistics

SACLA calls for public use proposals twice per year. Proposals fall into two categories: General Proposals for general research with no specific research theme, while Priority Strategy Proposals are on strategic themes that are designated by the national policy. Currently there are two strategic themes: Hierarchical Structure Dynamics of Biomolecules and Pico/Femto Second Dynamic Imaging. Table 5 shows the research themes for each group:

Table 5. Research themes for each group

1. Hierarchical Structure Dynamics of Biomolecules	1-1 Structural Analysis of Drug-targeted Membrane Protein Nanocrystals
	1-2 Imaging of Whole Cell and Its Components in the Living State
	1-3 Single Molecule Structural Analysis of Supramolecular Complex
	1-4 Dynamics Research Combining Single Molecule X-ray Diffraction Experiments and Supercomputer Analysis
	1-5 Dynamic Structural Analysis Using Pump-Probe Techniques
2. Pico/Femto Second Dynamic Imaging	2-1 Gas-Phase/Liquid-Phase/Solid-Phase Reaction Dynamics
	2-2 Ultrafast Interface Reaction Processes
	2-3 Charge Generation/Charge Transfer Dynamics
	2-4 Ultrafast Processes under Extreme Conditions
	2-5 Dynamic X-ray Spectroscopy

Table 6, Figs. 6 and 7 provide statistics on proposals, users, and beamtime.

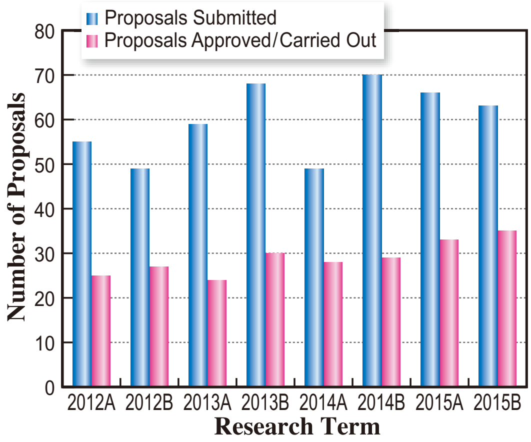

Fig. 6.

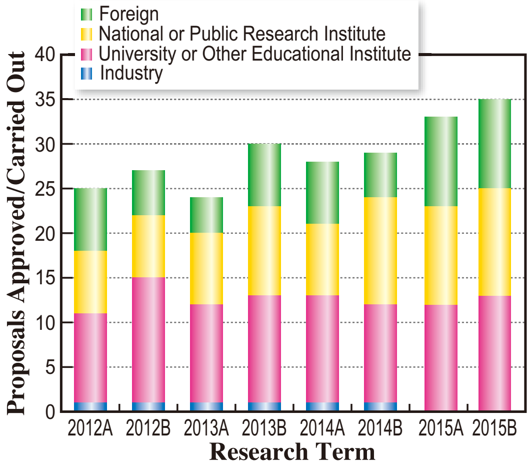

Fig. 7.

Table 6. Number of proposals submitted, proposals approved/carried out, cumulative users and beamtime available by research term

Half-year Research Term	Proposals Submitted	Proposals Approved / Carried Out			Cumulative Users	Beamtime Carried Out (Shifts)
			(Priority Strategy Proposals)	(General Proposals)		
2012A	55	25	(12)	(13)	297	126
2012B	49	27	(19)	(8)	461	154
2013A	59	24	(15)	(9)	268	117
2013B	68	30	(19)	(11)	410	139
2014A	49	28	(20)	(8)	400	147
2014B	70	29	(17)	(12)	430	140
2015A	66	33	(23)	(10)	527	144
2015B	63	35	(23)	(12)	552	152

One shift = 12 hours at SACLA beamlines

IV. Research Outcome

In 2015, more than 30 papers from SACLA were published. These included three papers in Nature. Some of these studies, both scientific and technical, are included in this volume of SPring-8/SACLA Research Frontiers.

NewSUBARU

The NewSUBARU synchrotron light facility is operated by the Laboratory of Advanced Science and Technology for Industry, University of Hyogo. This facility consists of an electron storage ring and nine beamlines. Electron injection is supplied from a 1 GeV linac of the SPring-8 facility. The conceptual layout of the NewSUBARU facility is illustrated below.

(1) BL01 gamma-ray beamline is used for nuclear physics research and the generation of high-energy positrons, which are used for nondestructive material inspections.

(2) BL02 and BL11 are nano-micro manufacturing beamlines using large area X-ray lithography and LIGA technology.

(3) BL03, BL09 and BL10 are beamlines for EUVL and related research. LSI mask inspection technology using coherent scatterometry is being developed.

(4) BL05, BL06, BL07 and BL09 are material analysis beamlines. Soft X-ray spectroscopy technologies (XFAS, XPS, XES) are used.

All NewSUBARU beamlines are open for industrial and sciencific use. The promotion of user use and technical assistants for users are supported by MEXT's "Project for Creation of Research Platforms and Sharing of Advanced Research Infrastructure."

Shuji Miyamoto
Director of LASTI, University of Hyogo

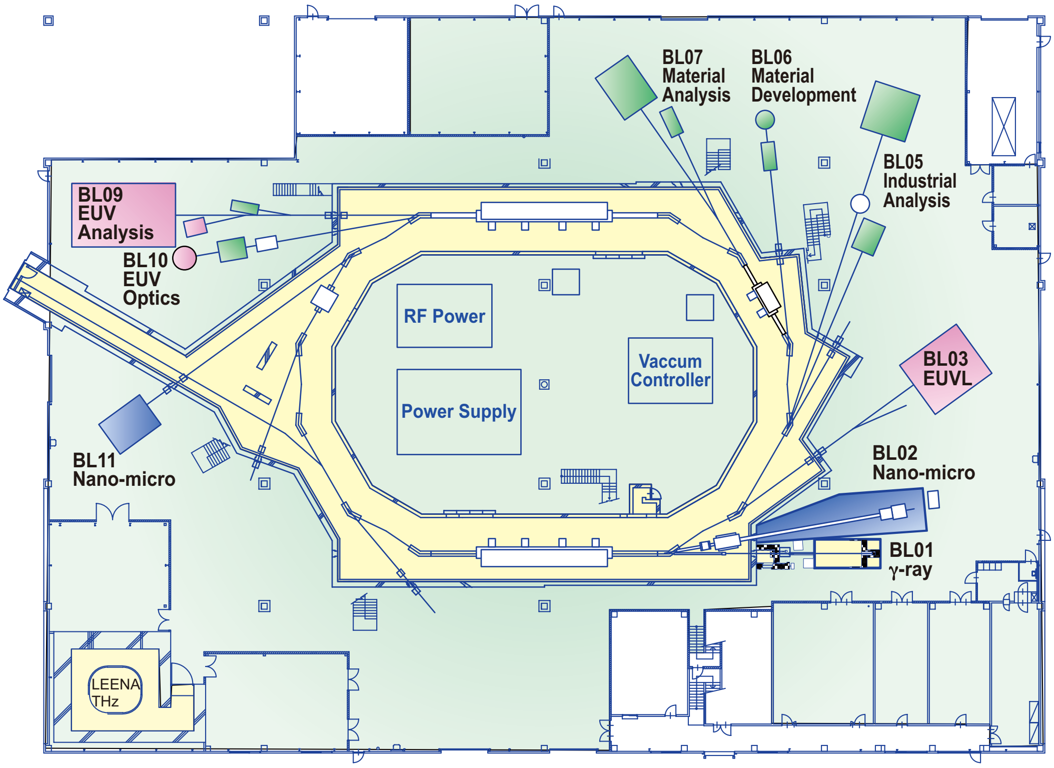

Low energy soft X-ray emission spectrometer at BL-09A in NewSUBARU

Owing to the high brilliance of soft X-ray radiation sources, the study of electronic states by X-ray emission spectroscopy (XES) has recently attracted attention in various research topics such as lithium ion batteries, fuel cells, compound semiconductors, and photocatalysts. Since the penetration depth of soft X-rays is greater than that of electrons, XES is applicable to the electronic state analysis of the bulk and interfacial layers. Because the X-ray emission probability of light elements (Li-F) is low, and decreases with decreasing atomic number [1], an intense excitation light source is necessary for XES measurement. The NewSUBARU synchrotron radiation facility is equipped with a long undulator (LU) with a total length of approximately 11 m [2], and its photon flux density is as high as 1.2×10^{11} photons/s at the sample position. Therefore, it is suitable as an excitation light source for the XES of light elements.

We have focused on the energy region of 50–600 eV and developed XES equipment with high energy resolution at BL-09A. The optical design of the spectrometer is based on a grazing incidence flat-field spectrometer using a valid line-spacing (VLS) grating. Because there is a limitation of the spatial space, the design concept of the HEPA2.5 (High Efficiency Photon Energy Analyzer Ver.2.5) spectrometer [3], which has relatively high resolution for its small size, was adopted for the optical design of the spectrometer. The entrance slit is placed 10 mm from a sample and its opening width can be changed in the range of 5–300 μm from outside of the vacuum chamber. Taking into account the contribution of the electron cloud on CCD, the energy resolution, $E/\Delta E$, was estimated to be greater than 1000 in the energy range of 50–600 eV.

The spectrometer was constructed at the endstation of the beamline in March 2014. Figure 1 shows a photograph of the spectrometer. The spectrometer is composed of three chambers: the sample/slit chamber, the grating chamber, and the CCD chamber, with the grating and CCD chambers held on a plate that is machined in accordance with the optical design. An E2V back-illuminated CCD chip for the soft X-ray detector was fixed on a copper block, which was cooled and controlled to –110°C by liquid nitrogen. In the processing image data, a super-resolution reconstruction algorithm [3] was adopted to obtain the incidence position at a lower spatial resolution than the CCD pixel size.

Adjustment of the spectrometer was started in April 2014, and it is now in operation. Si-L, B-K, C-K, N-K, Ti-L, and O-K emissions of various samples were successfully measured with high energy resolution. Figure 2(a) shows an example of a CCD image of N-K emission from a Si_3N_4 thin film. Horizontally polarized soft X-rays with photon energy considerably above the N1*s* ionization threshold (~400 eV) were irradiated on the sample at a 45° angle of incidence. The typical exposure time for one spectrum was 20 min. The sharp upper line in Fig. 2(a) reflects elastic scattering of the excitation X-rays. The broad lower line in Fig. 2(a) reflects the fluorescent X-rays from the Si_3N_4 sample. The reconstructed spectrum of N-K emission from the Si_3N_4 thin film is shown in Fig. 2(b). The sharp peak at 420 eV corresponds to the elastic scattering of incident X-rays. The broad peaks at approximately 390 eV correspond to the fluorescent X-rays from

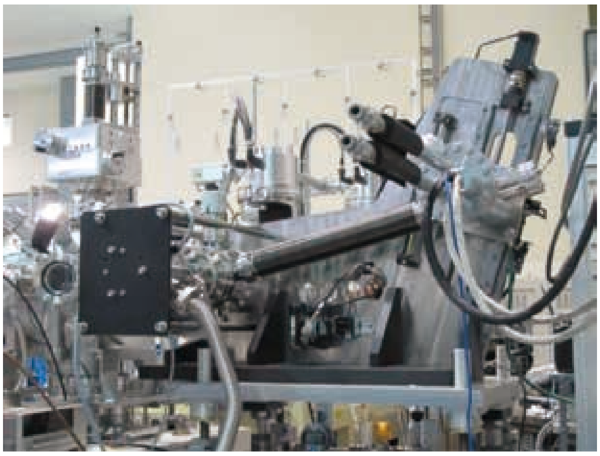

Fig. 1. Soft X-ray emission spectrometer constructed at BL-09A at the NewSUBARU SR facility.

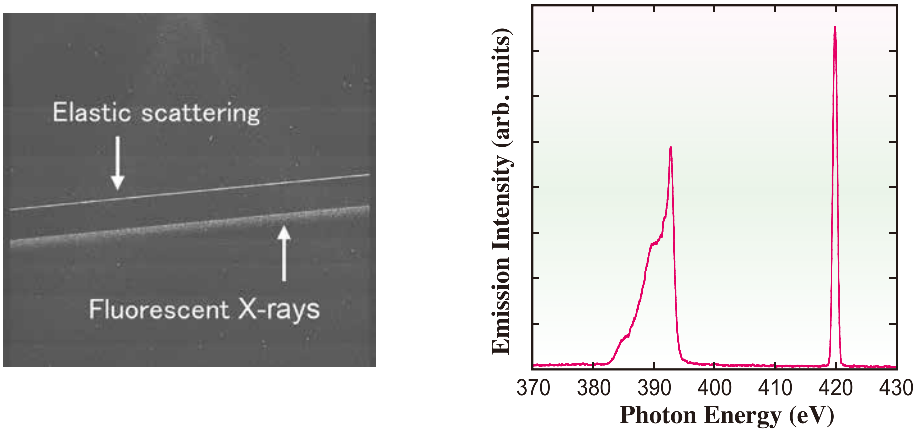

Fig. 2. Example of **(a)** CCD image of N-K emission from a Si_3N_4 thin film and **(b)** spectrum reconstructed from the image.

the Si_3N_4 sample. The shape of the fluorescence peaks is in good agreement with previously reported spectra [4]. The total energy resolution, including the beamline monochromator resolution, was estimated to be E/ΔE ~760 and ~1000 at approximately 400 eV and 300 eV, respectively.

Figure 3 shows the take-off-angle-dependent N-K X-ray emission spectra of hexagonal boron nitride (h-BN) powder. All features of the spectra are very similar to those previously reported using high resolution equipment [5,6]. As shown in the figure, the peak height at 394 eV shows strong angle dependence. Since h-BN powder comprises flat crystalline grains, it has a crystalline orientation when is fixed against an indium plate. Therefore, the $\pi \rightarrow 1s$ emission of the h-BN powder is expected to exhibit significant take-off-angle dependence, similarly to the π^* absorption spectra. Thus, the observed angular dependence of the $\pi \rightarrow 1s$ emission reflects the π electrons of the hexagonal network structure of the h-BN crystal.

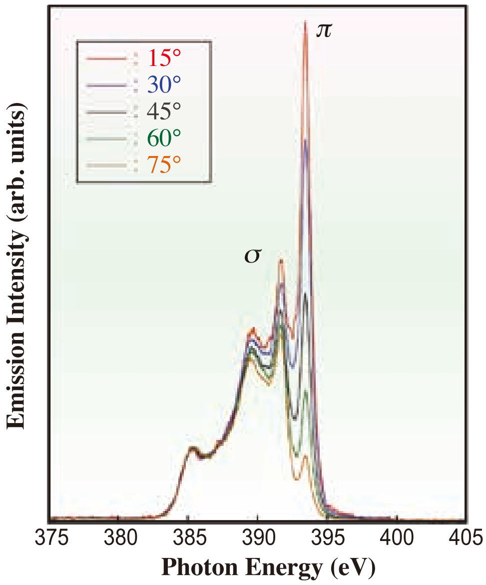

Fig. 3. Measured take-off-angle dependence of N-K X-ray emission spectra of h-BN powder.

Masahito Niibe

NewSUBARU, LASTI, University of Hyogo

E-mail: niibe@lasti.u-hyogo.ac.jp

References

[1] M.H. Chen *et al.*: Phys. Rev. A **24** (1981) 177.
[2] M. Niibe *et al.*: Synchrotron Rad. Instrum., AIP Conf. Proc. **705** (2004) 576.
[3] T. Tokushima *et al.*: Rev. Sci. Instrum. **77** (2006) 063107.
[4] G. Wiech and A. Simunek: Phys. Rev. B **49** (1994) 5398.
[5] A.B. Preobrajenski *et al.*: Phys. Rev. B **77** (2008) 085421.
[6] Y. Harada *et al.*: Rev. Sci. Instrum. **83** (2012) 031116.

Editor
Naoto Yagi
Japan Synchrotron Radiation Research Institute (JASRI)

Editing, Design & Layout
Marcia M. Obuti-Daté
Japan Synchrotron Radiation Research Institute (JASRI)

Printing
ROKKO Publishing & Sale Co.

JASRI
Information & Support System Section
Users Administration Division

1-1-1 Kouto, Sayo-cho, Sayo-gun
Hyogo 679-5198 • JAPAN
Tel. +81-(0)791 58-2797 Fax. +81-(0)791 58-1869

E-mail: frontiers@spring8.or.jp
http://www.spring8.or.jp/

SPring-8 SACLA

http://www.spring8.or.jp

Japan Synchrotron Radiation Research Institute (JASRI)
1-1-1 Kouto, Sayo-cho, Sayo-gun, Hyogo 679-5198, Japan